École doctorale n°531 : Science, Ingénierie et Environnement

Thèse de doctorat

Spécialité : **Sciences et Techniques de l'Environnement**

soutenue par

Cécile Defforge

pour obtenir le grade de docteure délivré par

l'Université Paris-Est

Data assimilation for micrometeorological applications with the fluid dynamics model *Code_Saturne*

---

soutenue le 14 octobre 2019
devant le jury composé de :

Dr Sophie Ricci	CERFACS	**Rapporteure**
Dr Alberto Martilli	CIEMAT	**Rapporteur**
Pr Chantal Staquet	Université Grenoble Alpes	**Examinatrice**
Dr Olivier Talagrand	LMD	**Examinateur**
Dr Bertrand Carissimo	CEREA	**Directeur de thèse**
Pr Marc Bocquet	CEREA	**Co-directeur de thèse**
M. Raphaël Bresson	EDF R&D	**Invité**
Dr Patrick Armand	CEA DAM/DIF	**Invité**

Remerciements

Dans un premier temps, je souhaiterais sincèrement remercier Sophie Ricci et Alberto Martilli pour leur relecture attentive de mon manuscrit ainsi que pour leurs questions pertinentes et leurs remarques constructives. Je tiens également à remercier Chantal Staquet ainsi qu'Olivier Talagrand pour leur participation à mon jury de thèse, leurs questions et remarques sur mes travaux.

Évidemment, je remercie très chaleureusement mes deux directeurs de thèse : Bertrand Carissimo et Marc Bocquet. Ils ont toujours été très disponibles et encourageants tout au long de ma thèse. J'ai beaucoup appris à leurs côtés au cours de ces trois années, aussi bien sur le plan professionnel que personnel. J'ai particulièrement apprécié la complémentarité de leurs domaines d'expertise et toutes les discussions très enrichissantes que j'ai pu avoir avec eux.

J'ai également eu la chance de collaborer avec le CEA grâce à Patrick Armand que je souhaite donc remercier d'avoir suivi assidûment mes travaux et apporté une perspective opérationnelle supplémentaire.

Et "last but not least", je remercie vivement Raphaël Bresson d'avoir partagé ses développements informatiques qui m'ont permis de considérablement progresser en Python, pour son perfectionnisme particulièrement stimulant et pour le temps qu'il m'a accordé pour répondre à mes questions – plus ou moins pertinentes – écouter mes histoires, partager mon chocolat et discuter de choses et d'autres.

En dehors de mon jury de thèse, je souhaiterais adresser des remerciements tout particuliers à tous mes collègues, avec qui j'ai été très heureuse de partager ces trois années. Tout d'abord, je pense à l'ensemble des membres du CEREA : Léa, Guillaume, Éric J., Évelyne, Éric D., Denis, Arièle, Nicolas, Yannick, Sébastien, Dominique, Martin, Cédric, Joffrey, Alban, Lya, Palmira, Carole, Clémentine, Aurélie, Mouhamet, Youngsoeb, Karine, Lydie, Véronique et Pietro.

Mes journées à EDF ont également été égayées par la bibliothèque et tous ses bénévoles : Alain, Franchine, Isabelle, Aurélien, Antoine et Geneviève. Ainsi que par les pauses sportives du mardi avec Marie-Charlotte, Céline, Nelly et Pauline.

Je n'oublie pas les autres doctorants (et anciens doctorants) du groupe MFEE et LNHE avec qui j'ai partagé de très bons moments... et des cours d'anglais : Riccardo, Clément, Thibaut, Lucie, Gaëtan, Germain, William, Li, Hamza, Thomas, Nour et Léo.

Un grand merci donc à toutes ces personnes pour leur présence au quotidien !

Pour finir, je souhaite remercier ma famille et mes amis. Merci Julien pour les pauses café du vendredi, ton écoute attentive et ton émerveillement quasi-systématique devant mes créations couturières. Merci Tanguy de nous avoir montré qu'il est tout à fait possible de partir à l'autre bout du monde une semaine avant sa soutenance, d'avoir partagé un projet entrepreneurial un peu avorté et la mise au point de l'appli Malaussène, de m'avoir donné le conseil très avisé de m'inscrire à des cours de natation et aussi d'être aussi bavard que moi (voire d'avantage ?). Merci Sophie, Justine et Brigitte d'apporter une note féminine dans mon entourage. Merci Basile de rendre ma vie rigolote et de me soutenir dans tout ce que j'entreprends. Merci maman d'être venue à Paris pour ma soutenance, pour ton aide précieuse dans la préparation du pot et surtout pour ton amour inconditionnel. Merci papa d'avoir fait en sorte de pouvoir suivre ma thèse depuis Toulouse. Enfin, un immense merci à tous les autres amis et membres de ma famille que je ne cite pas ici mais qui ont été présents tout au long de ces trois dernières années !

Abstract

Air quality is a major health and environmental issue worldwide. Similarly, the accuracy of wind resource assessment triggers significant economic and environmental repercussions. In order to study these two topics, it is necessary to accurately determine local wind fields using numerical models of micrometeorology. Such simulations are extremely sensitive to meteorological conditions at the domain borders. Up to present, the boundary conditions (BC) were estimated based on the results of larger scale simulations, which provide information that is not accurate enough, or even incomplete, for local scale purposes. As a matter of fact, the lack of knowledge about the BC represents a major source of error and uncertainty for micrometeorological studies.

The potential sites for wind farm installation as well as built environments (urban areas or industrial sites) can be equipped with instruments measuring meteorological variables or pollutant concentration. The observations provided by these instruments represent a second source of information, insufficiently exploited for micrometeorological studies. Indeed, the *in situ* measurements are perturbed by the complex geometrical features on sites and might be difficult to exploit. In order to improve the exactitude and the accuracy of the BC, and consequently of the locale-scale atmospheric simulations, data assimilation (DA) methods, suited to this micrometeorological problem, could be applied to take benefit from the available observations.

So far, DA methods have been mainly developed for large-scale meteorology and employed to correct the initial conditions (IC). In order to broaden the application scope of DA to micrometeorology, existing DA methods must be adapted to be able to correct the BC instead of IC.

Two of the existing DA methods seem compatible with computational fluid dynamics (CFD) models used for micrometeorology over complex geometries: the back and forth nudging (BFN) algorithm and the iterative ensemble Kalman smoother (IEnKS). We have adapted these two methods, from a theoretical perspective, so as to include the BC in the control variables. The performances of the adapted versions of the BFN algorithm and the IEnKS have first been assessed with a simplified, 1D model of atmospheric flow with two layers, based on the shallow-water equations. The BFN algorithm and the IEnKS have then been tested in 2D and 3D with the atmospheric module of the open-source CFD model *Code_Saturne*.

The first study case with *Code_Saturne* corresponds to a real application of wind

resource assessment in a mountainous region with steep topography where three meteorological masts have been installed during a few months and provided in situ wind observations. The second case is a study of pollutant dispersion in an urban area, based on the measurements of wind and pollutant concentration coming from the "Mock Urban Setting Test" field campaign carried out in the USA. In this second case, the turbulence is also included in the BC and thus in the control variables. For both studies, some observations are assimilated and the remaining ones are used to validate the results.

The experiences performed for the wind resource assessment study have revealed that the CFD models present too strong nonlinearities (flow recirculation after obstacles) for the BFN algorithm, which is based on a linearity assumption. However, both cases have shown the ability of the IEnKS to reduce the error and the uncertainty of the BC by assimilating a few observations, with operationally affordable computational costs. Consequently, the simulated wind fields with *Code_Saturne* are also closer to the validation observations and the confidence intervals are reduced. Eventually, the IEnKS allows, in one case to estimate the wind potential, and in the other case to build the pollution maps, with much more exactitude and accuracy.

Keywords

Air pollution, Air quality, Atmospheric dispersion, Back and forth nudging algorithm (BFN), Boundary conditions, Computational fluid dynamics (CFD), Data assimilation, Iterative ensemble Kalman smoother (IEnKS), Local scale simulation, Micrometeorology, Wind potential, Wind resource assessment.

Résumé

La qualité de l'air est un enjeu sanitaire et environnemental majeur. Par ailleurs, l'estimation précise des potentiels éoliens est la source d'importantes retombées économiques et environnementales. Pour étudier ces deux sujets, il est nécessaire de reconstituer précisément les champs de vent locaux grâce à des modèles numériques de micro-météorologie. Ces simulations sont extrêmement sensibles aux conditions météorologiques aux limites du domaine d'étude. Jusqu'à présent, les conditions aux limites (CL) étaient estimées à partir de simulations à plus grande échelle, qui fournissent des informations imprécises, voire incomplètes pour l'utilisation à micro-échelle. Par conséquent, la méconnaissance des CL représente une source majeure d'erreur et d'incertitude dans les études micro-météorologiques.

Les sites susceptibles d'accueillir un parc éolien et les environnements bâtis (quartiers urbains ou sites industriels) peuvent être équipés d'instruments de mesures météorologiques et de concentration de polluants. Les observations fournies par ces instruments constituent une seconde source d'information, jusqu'à ce jour peu exploitée pour les études micro-météorologiques. En effet, étant à l'intérieur du domaine, les observations sont perturbées par la géométrie complexe des sites étudiés. Afin d'améliorer la précision des CL et donc des simulations atmosphériques à l'échelle locale, des méthodes d'assimilation de données (AD) adaptées à cette problématique pourraient permettre de mettre à profit les observations disponibles.

Jusqu'à présent, les méthodes d'AD ont été principalement développées pour répondre aux besoins de la météorologie à grande échelle et donc utilisées pour corriger les conditions initiales (CI). Afin d'élargir le champ d'application de l'assimilation de données aux simulations à l'échelle locale, il faut adapter les méthodes d'AD pour qu'elles permettent de corriger les CL plutôt que les CI.

Parmi les méthodes d'assimilation de données existantes, deux semblent compatibles avec les modèles de mécanique des fluides atmosphérique (CFD) utilisés pour la micro-météorologie en géométrie complexe : l'algorithme de nudging direct et rétrograde (BFN) et le lisseur de Kalman d'ensemble itératif (IEnKS). Nous avons adapté ces deux méthodes d'un point de vue théorique pour inclure les CL dans les variables de contrôle. Les performances des versions adaptées du BFN et de l'IEnKS ont tout d'abord été étudiées avec un modèle simplifié d'écoulement atmosphérique à deux couches en 1D, basé sur les équations de Saint-Venant. Le BFN et l'IEnKS ont ensuite été testés en

deux puis trois dimensions avec le module atmosphérique du modèle open-source de CFD *Code_Saturne*.

Le premier cas d'étude avec *Code_Saturne* correspond à une application réelle d'estimation de potentiel éolien dans une région montagneuse au relief très accidenté où trois mâts de mesure fournissent des observations de vent. Le second cas d'étude correspond à une étude de dispersion de polluants en milieu urbain, basé sur les observations de vent et de concentration, provenant de la campagne de mesures « Mock Urban Setting Test » aux USA. Dans ce second cas, la turbulence est également incluse dans les conditions aux limites. Dans les deux cas, une partie des observations est utilisée pour l'assimilation et le reste pour la validation des résultats.

Les expériences menées sur le premier cas ont révélé que les modèles de CFD présentent des non-linéarités trop fortes (recirculations derrière les obstacles) pour l'algorithme de BFN, fondé sur une hypothèse de linéarité. Les études avec cette méthode n'ont donc pas été poursuivies. En revanche, les deux cas d'étude ont montré la capacité de l'IEnKS à réduire l'erreur et l'incertitude sur les CL grâce à l'assimilation d'une petite dizaine d'observations, en un nombre raisonnable de calculs. Par suite, l'écart entre les champs de vent simulés et les observations de validation est également réduit. De même, l'incertitude sur les simulations est plus faible. Finalement, l'IEnKS permet d'estimer le potentiel éolien dans un cas et les concentrations en polluant dans l'autre, avec beaucoup plus de précision.

Mots clés

Assimilation de données, Conditions aux limites, Dispersion atmosphérique, Estimation de ressource éolienne, Lisseur de Kalman d'ensemble itératif (IEnKS), Micrométéorologie, Mécanique des fluides numérique (CFD), Nudging direct et rétrograde (BFN), Pollution de l'air, Potentiel éolien, Qualité de l'air, Simulation à l'échelle locale.

Assimilation de données pour des applications micro-météorologiques avec le modèle de mécanique des fluides *Code_Saturne*

Introduction

La qualité de l'air urbaine est un enjeu sanitaire et environnemental majeur. Par ailleurs, l'estimation précise des potentiels éoliens présente d'importantes retombées économiques et environnementales. Ces deux exemples d'applications micro-météorologiques requièrent l'estimation précise des champs météorologiques (vent, turbulence, etc.) dans des domaines de quelques kilomètres carrés. Lorsque les domaines étudiés présentent des éléments géométriques complexes (topographie escarpée, présence de bâtiments, etc.), les modèles numériques utilisés pour simuler les conditions météorologiques doivent être suffisamment fins. Le développement de la puissance de calcul permet d'utiliser des modèles de mécanique des fluides numériques (CFD) dans des conditions quasi-opérationnelles. Le module atmosphérique du modèle *open-source* de CFD *Code_Saturne* est utilisé pour de nombreuses applications micro-météorologiques.

L'une des limites des modèles de CFD est leur sensibilité aux paramètres d'entrée, et en particulier aux conditions aux limites (CL). En effet, les limites des domaines étudiés en micro-météorologie sont généralement des frontières ouvertes pour lesquelles il faut définir des CL. De plus, les temps d'intégration caractéristiques à l'échelle locale sont généralement très supérieurs au temps nécessaire aux informations pour se propager dans le domaine. Par conséquent, l'influence des conditions initiales (CI) s'estompe rapidement et ce sont finalement les CL qui déterminent la solution. Les CL représentent donc une source majeure d'incertitudes dans les simulations atmosphériques à l'échelle locale et leur estimation précise est l'un des enjeux majeurs de la micro-météorologie.

Les différentes échelles caractéristiques rencontrées en météorologies interagissent

continuellement. La turbulence qui agit à des échelles très fines affecte les conditions météorologiques à méso-échelle. Réciproquement, les phénomènes météorologiques ayant lieu à méso-échelle influencent l'évolution de la météorologie à l'échelle locale. Par conséquent, les CL doivent refléter à la fois les variations méso-échelles et micro-échelles. Pour ce faire, des méthodes de descente d'échelle ont été mises aux points afin d'estimer les CI et les CL pour les simulations micro-météorologiques à partir de résultats de simulations à méso-échelle. Toutefois, les différences de résolutions spatiales et temporelles entre les domaines à méso- et micro-échelle sont telles que les CI et CL ainsi déterminées peuvent être erronées ou ne pas contenir toute l'information nécessaire (influence des obstacles, relief fin, etc.). Par exemple, les petites échelles de la turbulence sont rarement résolues à méso-échelle alors qu'elles sont nécessaires à la définition des CI et des CL pour les simulations à l'échelle locale. Ainsi, les méthodes de descente d'échelle fournissent une première estimation des CL qui est pertinente et contient des informations liées aux phénomènes météorologiques à grande échelle. Toutefois cela ne permet pas d'estimer suffisamment précisément les CL pour une utilisation à micro-échelle. Il serait donc bénéfique de pouvoir combiner l'estimation obtenue par descente d'échelle avec une autre source d'informations.

Les sites susceptibles d'accueillir un parc éolien, les quartiers urbains et les sites industriels sont généralement équipés d'instruments de mesures météorologiques et de concentrations de polluants. Les observations fournies par ces instruments constituent une seconde source d'information, jusqu'à ce jour utilisée essentiellement pour la validation des modèles et non pour améliorer les simulations micro-météorologiques. En effet, étant à l'intérieur du domaine, les observations sont perturbées par la géométrie complexe des sites étudiés ce qui en complique l'exploitation. Une solution pour tenir compte des observations disponibles au sein du domaine d'étude est d'utiliser des méthodes d'assimilation de données (AD), adaptées à la problématique des simulations atmosphériques à l'échelle locale.

L'AD cherche à combiner de façon optimale les deux sources d'informations disponibles : la première estimation – ou ébauche – fournie par la descente d'échelle, et les observations. Jusqu'à présent, les méthodes d'AD ont été principalement développées pour répondre aux besoins de la météorologie à grande échelle. Or à grande échelle, les simulations atmosphériques sont largement dominées par les CI, de telle sorte que l'AD est généralement utilisée pour corriger les CI. L'enjeu du travail de thèse présenté dans ce document est d'élargir le champ d'application de l'AD aux simulations à l'échelle locale. Pour ce faire, il faut adapter les méthodes d'AD pour qu'elles puissent corriger les CL plutôt que les CI. De façon imagée, il faut que les informations contenues dans les observations, qui peuvent déjà "remonter dans le temps", puissent également "remonter dans l'espace".

Méthodes d'assimilation de données

Après avoir effectué un état de l'art des techniques d'AD existantes, deux méthodes ont été sélectionnées : l'algorithme de nudging direct et rétrograde (BFN) et le lisseur de Kalman d'ensemble itératif (IEnKS). Ces deux méthodes ont été choisies car elles semblent être adaptées à l'utilisation de modèles de CFD pour des simulations à l'échelle locale. En effet, l'utilisation du modèle adjoint n'est pas requise et elles permettent les calculs en parallèle, ce qui est nécessaire pour les simulations atmosphériques qui peuvent être très coûteuses en temps de calcul. Ces deux méthodes ont été adaptées d'un point de vue théorique pour inclure les CL dans les variables de contrôle. Le BFN est une méthode itérative qui consiste à enchaîner des intégrations directes (temps croissant) et rétrogrades (temps décroissant) du modèle, en incluant un terme de nudging dans les deux cas. En considérant le cas particulier des équations de Saint-Venant – qui peuvent être utilisées pour représenter de façon simplifiée l'atmosphère en deux couches – nous avons montré que l'intégration rétrograde peut être effectuée en prenant l'opposé du champ de vitesse et en intégrant le modèle avec des pas de temps positifs. La méthodologie ainsi obtenue a été généralisée aux équations complètes de Navier-Stokes, résolues par le modèle de CFD *Code_Saturne*. Cette généralisation est basée sur une hypothèse de linéarité des équations, qui n'est pas nécessairement vérifiée en pratique.

L'IEnKS est une méthode variationnelle d'ensemble : elle est fondée sur la minimisation d'une fonction de coût – qui mesure la distance à l'ébauche et aux observations – et les statistiques de l'erreur d'ébauche sont représentées par un ensemble. La dérivation de l'IEnKS dans le cas où les variables de contrôle sont les CL est analogue à la dérivation classique pour laquelle les variables de contrôle correspondent aux CI. Si l'IEnKS présente l'avantage de ne faire intervenir que très peu de paramètres, cette méthode reste néanmoins sensible au choix de l'ensemble initial qui représente les statistiques d'erreur d'ébauche. Nous avons proposé une méthode consistant à estimer en premier lieu la matrice de covariance d'erreur d'ébauche à partir d'analyses statistiques de la climatologie (e.g., longues séries temporelles d'observations ou de simulations). L'ensemble initial correspond alors aux modes principaux de cette matrice, qui peuvent par exemple être déterminés grâce à une décomposition en valeurs singulières.

Le 3D-Var est une méthode variationnelle qui est considérée ici comme une référence. Cette méthode est disponible dans le module d'AD ADAO de la plateforme *open-source* SALOME (http://www.salome-platform.org). Le gradient de la fonction de coût est ici estimé par différences finies.

Première étude : les équations de Saint-Venant

Dans un premier temps, nous avons utilisé un modèle simplifié d'écoulement atmosphérique en 1D, gouverné par les équations de Saint-Venant. Ce modèle a permis de tester et comparer l'IEnKS, le BFN ainsi que le 3D-Var sur des cas à une dimension, pour lesquels

la condition à la limite est réduite à une seule valeur de vitesse. Ce premier cas d'étude a permis de valider le bon fonctionnement des méthodes adaptées à la prise en compte des CL et d'effectuer plusieurs analyses de sensibilité. Nous avons ainsi vérifié que le comportement de l'IEnKS et du BFN étaient en accord avec la théorie. En particulier le BFN résout un problème fondamentalement différent de celui résolu par l'IEnKS et le 3D-Var. Ainsi, l'IEnKS et le 3D-Var sont sensibles aux erreurs d'ébauche mais peu aux erreurs d'observation alors que l'analyse donnée par le BFN est indépendante de l'ébauche et est très sensible aux erreurs d'observation.

Les résultats de cette étude ont été publiés dans Defforge et al. (2018).

Deuxième étude : estimation de potentiel éolien

Le BFN et l'IEnKS ont ensuite été testés avec le module atmosphérique de *Code_Saturne* dans le contexte d'une étude de potentiel éolien pour un site à la topographie très escarpée. La météorologie à méso-échelle dans la région englobant le site, simulée avec le modèle WRF, est disponible pour une période de 3 ans. De plus, trois mâts météorologiques étaient présents sur le site entre janvier et décembre 2007, fournissant des observations de vitesse et de direction du vent à différents niveaux verticaux.

Dans un premier temps, nous avons considéré une coupe verticale dans le plan XZ pour laquelle les CL correspondent à un unique profil vertical, défini en 21 niveaux, pour la composante est-ouest du vent. Le vecteur de contrôle est alors de taille 21 et nous avons effecté des expériences jumelles en créant des pseudo-observations à partir d'une simulation de référence. Ce cas en 2D nous a permis de réaliser des analyses de sensibilité aux différents paramètres des méthodes. En particulier, nous avons constaté que la méthodologie mise en place pour le BFN n'est pas adaptée à ce cas où les non-linéarités sont significatives (recirculation derrière les pics du relief). En effet, le fait d'effectuer l'intégration rétrograde en prenant l'opposé du champ de vitesse n'est ici pas équivalent à une intégration en temps rétrograde. Par conséquent nous n'avons pas poursuivi l'étude du BFN et nous nous sommes concentrés sur l'IEnKS.

Dans un second temps, nous avons considéré le domaine entier en 3D et les CL ont été définies en 20 profils verticaux répartis autour du domaine. Chaque profil est défini en 21 niveaux verticaux et contient les deux composantes de la vitesse horizontale. Le vecteur de contrôle en 3D est donc de taille 840. Des expériences jumelles ont été effectuées sur le domaine en 3D avec 30 pseudo-observations situées aux emplacements des trois mâts de mesure et à différents niveaux verticaux.

Pour finir, nous avons reproduit des conditions opérationnelles d'estimation de la ressource en utilisant la méthodologie WRAPP qui consiste à regrouper les situations météorologiques simulées par WRF en un nombre réduit de classes (ici 50). Pour chaque classe, une situation représentative est choisie et simulée avec *Code_Saturne*. Dans l'étude présentée ici, nous avons appliqué l'IEnKS pour chacune des 50 situations représentatives,

l'ébauche étant donnée par les résultats de la simulation WRF correspondante. Nous avons assimilé les 10 observations fournies par deux des mâts et celles provenant du troisième mât ont permis de valider les résultats. Pour chacune des situations représentatives, nous pouvons estimer l'énergie que produirait une éolienne, située à l'emplacement du mât de validation, à partir des observations, de la simulation WRF, de la simulation avec *Code_Saturne* et les CL fournies par WRF, et de la simulation avec *Code_Saturne* et les CL corrigées par l'IEnKS. La moyenne de ces 50 potentiels, pondérés par la taille des classes, donne une estimation du potentiel annuel. Nous avons ainsi mis en évidence que l'utilisation de *Code_Saturne* avec des CL imprécises ne donne pas des résultats significativement différents de ceux obtenus avec WRF. En revanche, l'utilisation de l'IEnKS avec 5 membres et 10 observations permet de nettement améliorer l'estimation du potentiel éolien. De plus, l'IEnKS présente l'avantage de fournir une mesure de l'incertitude sur les résultats après assimilation, donnée par la dispersion de l'ensemble *a posteriori*. Nous avons ainsi montré que l'IEnKS permet également de réduire l'incertitude sur le potentiel estimé.

Les résultats de cette étude ont été publiés dans Defforge et al. (2019a).

Troisième étude : dispersion en milieu bâti

La dernière étude s'inscrit dans un contexte de dispersion atmosphérique en milieu urbain. Nous utilisons les nombreuses observations fournies par la campagne de mesure "Mock Urban Setting Test" qui a été menée dans une ville idéalisée, reconstituée avec des containers, dans le désert de l'Utah en septembre 2001. Le domaine simulé s'étend sur 348m $\times$ 348m $\times$ 50m et est centré sur les containers qui sont disposés selon une grille de 12 par 10 containers, convrant une région de 200m $\times$ 200m. Les CL sont définies en un unique profil vertical, situé en amont du domaine, pour les deux composantes de la vitesse horizontale et l'énergie cinétique turbulente. Le profil est défini en 22 niveaux verticaux de telle sorte que le vecteur de contrôle pour les expériences d'AD est ici de taille 22. Au cours de cette campagne de mesures, plusieurs lâchers d'un gaz inerte (propylène) ont été effectués et observés à l'aide de multiples instruments, mesurant le vent et la concentration de gaz, installés dans et au-dessus de la canopée urbaine. Nous avons étudié deux de ces lâchers correspondant à des conditions atmosphériques neutre et stable. Pour chacun de ces deux cas, nous avons effectué deux expériences d'assimilation : la première consistait à assimiler 14 observations de vent et la seconde 13 observations de concentration. Les observations restantes (une centaine) sont utilisées pour la validation des résultats. L'ébauche est estimée à partir d'observations disponibles à quelques centaines de mètres du domaine simulé.

Cette étude a montré que l'IEnKS avec peu de membres (5 ici) est capable de corriger l'erreur et l'incertitude sur les CL et ainsi d'améliorer les simulations au sein du domaine. L'analyse des deux expériences a montré que les variables assimilées sont mieux corrigées

que les autres. En particulier, assimiler uniquement des observations de concentration en quelques points permet de corriger le champ de concentration, en général en rectifiant la direction du vent, même s'il peut subsister des erreurs dans le champ de vent. Puisque la dispersion du gaz est largement déterminée par le vent, assimiler des observations de vent permet de corriger le champ de vent et donc le champ de concentration. Ainsi, l'assimilation d'observations de vent est plus efficace pour améliorer globalement la simulation. Nous avons également effectué des expériences en assimilant 8 observations de vent et 7 de concentration. Les résultats dans ce cas sont très légèrement meilleurs à ceux obtenus en assimilant des observations de vent uniquement, notamment concernant la turbulence. Dans tous les cas étudiés, la dispersion du gaz – qui est l'objectif final de ce type d'études – est mieux représentée grâce à l'IEnKS.

Une publication est prévue avec les résultats de cette étude (Defforge et al., 2019b).

Conclusions

Les trois études menées dans le cadre de ce travail de thèse ont permis d'évaluer les performances de deux méthodes d'AD pour des applications micro-météorologiques. Nous avons mis en évidence le fait que le BFN (dans sa version proposée ici) ne peut être utilisé dans des cas où les non-linéarités sont trop fortes, par exemple en présence de recirculations après les obstacles. Même si nous n'avons pas poursuivi l'étude de cette méthode, les bons résultats obtenus dans la première étude laissent envisager des perspectives positives pour le BFN. En particulier, une amélioration possible serait d'utiliser une version linéarisée du modèle pour l'intégration rétrograde. Les deux applications réelles ont montré que l'IEnKS peut facilement être adapté à différentes études de micro-météorologie. Cette méthode permet, en un nombre raisonnable de calculs, d'améliorer l'exactitude des simulations en réduisant l'erreur sur les CL. De plus, la dispersion de l'ensemble donne une estimation de l'incertitude sur l'analyse et nous avons montré que l'IEnKS permet de réduire cette incertitude et donc d'améliorer la précision des CL et par suite des simulations. De fait, le potentiel éolien ou les champs de concentration de polluant, estimés à partir des champs de vents simulés par *Code_Saturne*, sont également plus justes et les incertitudes de ces estimations sont réduites.

Plusieurs analyses pourraient être menées pour améliorer encore les performances de l'IEnKS. En particulier, il serait intéressant d'effectuer des analyses de sensibilité à la taille de l'ensemble ou au nombre et à l'emplacement des observations. Par ailleurs, la mise en place de méthodes de localisation pourrait s'avérer nécessaire dans certaines configurations afin de prendre en compte les corrélations spatiales des variables assimilées. Enfin, nous avons considéré ici des CL constantes et des simulations stationnaires. L'utilisation de l'IEnKS pour résoudre des problèmes instationnaires représente un enjeu futur pour cette méthode.

Enfin, l'IEnKS a ici été utilisé pour des applications micro-météorologiques avec

Code_Saturne. Toutefois, l'IEnKS étant non-intrusif, il pourrait tout à fait être appliqué avec d'autres modèles et pour d'autres champs d'application comme les études climatiques régionales, l'hydrologie, les feux de forêts, etc.

Références

Defforge, C. L., B. Carissimo, M. Bocquet, P. Armand, and R. Bresson, 2018: Data assimilation at local scale to improve CFD simulations of atmospheric dispersion: application to 1D shallow-water equations and method comparisons. *Int. J. Environ. Pollut.*, **64**, 90–109. 12

Defforge, C. L., B. Carissimo, M. Bocquet, R. Bresson, and P. Armand, 2019a: Improving CFD atmospheric simulations at local scale for wind resource assessment using the iterative ensemble Kalman smoother. *J. Wind. Eng. Ind. Aerodyn.*, **189**, 243–257. 13

Defforge, C. L., B. Carissimo, M. Bocquet, R. Bresson, and P. Armand, 2019b: Improving dispersion modelling in built environments with CFD using the iterative ensemble Kalman smoother. *To be submitted*. 14

Contents

List of abbreviations

AASQA Official Air Quality Monitoring Associations.

ABL atmospheric boundary layer.

ARL Army Research Laboratory.

ASU Arizona State University.

BC boundary conditions.

BFN back and forth nudging.

BLUE Best Linear Unbiased Estimator.

cdf cumulative distribution function.

CEA Commissariat à l'énergie atomique et aux énergies alternatives.

CEREA Centre d'Enseignement et de Recherche en Environnement Atmosphérique.

CFD computational fluid dynamics.

DA data assimilation.

DAW data assimilation window.

digiPID digital photo-ionization detectors.

DNS direct numerical simulation.

DPG Dugway Proving Ground.

ECMWF European Center for Medium-range Weather Forecasts.

EDA ensemble of variational data assimilation.

EDF Électricité de France.

EnKF ensemble Kalman filter.

EnKS ensemble Kalman smoother.

EWEA European Wind Energy Association.

IC initial conditions.

IEnKF iterative ensemble Kalman filter.

IEnKS iterative ensemble Kalman smoother.

LANL Los Alamos National Laboratory.

LES large eddy simulation.

LIDAR Light Detection And Ranging.

M-O Monin-Obukhov.

MAE mean absolute error.

MCP measure-correlate-predict.

MUST Mock Urban Setting Test.

NWP numerical weather prediction.

pdf probability density function.

PWIDS Portable Weather Information and Display System.

RANS Reynolds-averaged Navier-Stokes.

RMSE root mean square error.

SAMS surface atmospheric measurement system.

SODAR Sound Detection And Ranging.

STD standard deviation.

SVD singular value decomposition.

SWE shallow-water equations.

TKE turbulence kinetic energy.

UU University of Utah.

UVIC ultraviolet ion collector.

List of abbreviations

WMO World Meteorological Organization.

WRAPP Wind Resource Assessment and Power Production.

WRF Weather Research and Forecasting.

List of symbols

Symbols for micrometeorology

ϵ	Dissipation rate of turbulence kinetic energy	m^2/s^3
κ	von Kármán constant	-
ρ	Fluid density	kg/m^3
θ	Potential temperature	K
ζ	Dimensionless height parameter	-
c	Species concentration	ppmv
Fr	Froude number	-
k	Turbulence kinetic energy	m^2/s^2
L	Monin-Obukhov length	m
g	Gravity	m/s^2
g'	Reduced gravity	m/s^2
h	Height above the ground	m
p	Pressure	Pa
t	Time	s
T	Temperature	K
u^*	Surface stress	m/s
u	x-component of velocity	m/s
v	y-component of velocity	m/s
w	z-component of velocity	m/s
z	Absolute height	m
z_r	Topography elevation	m

Symbols for data assimilation

$\mathbf{A}$	Ensemble of anomalies	$\mathbb{R}^{l\times N}$
$\mathbf{B}$	Background error covariance matrix	$\mathbb{R}^{l\times l}$
$\mathcal{F}$	Forward operator	$\mathbb{R}^l \to \mathbb{R}^p$
$\mathcal{H}$	Observation operator	$\mathbb{R}^n \to \mathbb{R}^p$
$\mathbf{K}$	Nudging matrix	$\mathbb{R}^{n\times p}$
$\mathcal{M}$	Model	$\mathbb{R}^l \to \mathbb{R}^n$
$\mathbf{w}$	Weight vector	$\mathbb{R}^N$
$\mathbf{R}$	Observation error covariance matrix	$\mathbb{R}^{p\times p}$
$\mathbf{x}$	System state	$\mathbb{R}^n$
$\mathbf{y}$	Observations	$\mathbb{R}^p$
$\mathbf{z}$	Control vector	$\mathbb{R}^l$

Introduction

Many human activities are influenced by meteorology and it is therefore necessary to fully understand the meteorological processes in order to represent them. For instance, both wind engineering and air quality studies are largely dependant on meteorology at local scale. These two fields of study are of direct relevance to environmental and health issues and will constitute key topics in the near future. Moreover, they both are related to Électricité de France (EDF) activities and future challenges.

Wind represents a clean and renewable source of energy that will largely continue to develop in the coming years to meet the European and World agreements about energy and climate change (e.g., Paris Agreement, signed in 2016, aims at keeping the increase in global average temperature below 2°C above pre-industrial levels). In 2018, the wind power capacity worldwide reached 600GW, after a growth of 10.8% in 2017 and 9.8% in 2018. At the end of 2018, all the wind turbines installed over the world covered nearly 6% of the global electricity demand. The Global Wind Energy Council anticipates that new installations will emerge to rise the global installed capacity to 840GW by 2022. In Europe, the penetration level of wind energy in the electrical mix is of 11.6% and its growth should accelerate in the coming years. Indeed, recent regulatory and economic developments have substantially changed the European perspective for wind energy. According to the European Wind Energy Association (EWEA) Central Scenario, 320GW of wind energy capacity are expected to be installed in Europe by 2030 – 254GW onshore and 66GW offshore (Fig. 1). This would represent a multiplication of the capacity by more than two in comparison with the installed capacity in 2014 (129GW).

The projected development of new wind farms lets us anticipate the need for wind resource assessment of new regions. This first step of any wind project consists in estimating the hypothetical energy production of a future wind farm and it generally determines if the project is economically feasible. As a result, it is crucial to very accurately estimate the wind resource of any prospected site. The accuracy of this estimation is particularly important as it allows to reduce the financial risks – and the related over-costs – associated with the substantial investment necessary for the construction of a wind farm. Wind farms generally extend over a few tens of kilometres and prospected areas for the installation of new onshore farms are often in mountainous regions where the steep relief affects the wind flow. Wind resource assessment for such areas is thus particularly difficult.

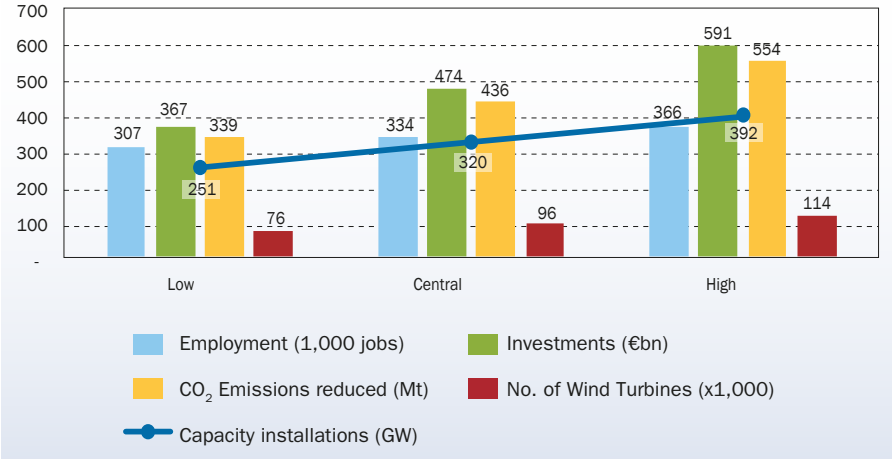

Figure 1: EWEA capacity scenarios and macro-enconomic benefits (source: EWEA, 2015).

Air quality is a major health and environmental issue worldwide and especially in cities. The World Health Organisation estimates that outdoor air pollution was responsible for the premature death of some 4.2 million people worldwide in 2018. Air quality is particularly poor in urban areas, where most of the population lives. Today, 55% of the world population lives in urban areas and, according to the United Nations Organisation, this rate is projected to reach 68% by 2050. As a consequence, the topic of outdoor air quality is of growing interest in the scientific community. Outdoor air pollution might be studied at different scales, both temporally and spatially. The layer of air beneath the mean height of the buildings (resp. trees) constitutes the urban (resp. forest) canopy layer. This layer is significantly affected by the obstacle canopy – defined as the assemblage of buildings, trees, and other objects composing a town. The microscale processes that take place in the urban canopy layer typically extend over a few meters to several hundred meters in the horizontal direction and over a few hundred meters in the vertical direction. The evolution of pollution at local scale is mainly driven by advection – which transports the pollutants – and diffusion – which causes mixing – and pollutant concentration is thus largely determined by the wind flow. As a result, estimating the meteorological variables (wind, turbulence, etc.) inside the urban canopy layer is an essential step to study pollutant dispersion.

Dispersion modelling is also necessary for emergency purposes related to hazardous, and even radioactive, materials. Accidents and malicious activities (e.g., terrorist attacks) might release hazardous materials into the atmosphere. These releases are more likely to occur in industrial neighbourhoods or urban areas and can affect human health through inhalation, ingestion of contaminated food or water, cloud or ground shine. In order to respond to such incidents, governmental agencies – such as the Commissariat à l'énergie atomique et aux énergies alternatives (CEA) in France – must be able to model the

dispersion of the hazardous materials into the atmosphere.

Both wind resource assessment and atmospheric dispersion modelling require the accurate estimation of the wind field – i.e., values of wind speed and direction at every point of the domain – and turbulence, for local-scale domains. These very complex micrometeorological fields are generally simulated with computational fluid dynamics (CFD) models that are very sensitive to input parameters. In particular, atmospheric simulations at local scale are largely determined by the meteorological conditions at the boundaries of the domain: the boundary conditions (BC). Up to now, the BC were estimated from the results of larger-scale models, which provide inaccurate, and sometimes incomplete, information. The insufficient knowledge of the BC represents a major source of uncertainty in micrometeorological studies.

In order to improve the atmospheric simulations at local scale, it is essential to improve the accuracy of the BC. The potential sites for wind power development and the built environments are often equipped with instruments measuring either meteorological variables or pollutant concentrations. The observations supplied by these instruments constitute a second source of information, relatively unexploited until now for micrometeorological studies. Indeed, *in situ* observations are perturbed by the geometrical features of the domain. Consequently, there is considerable scope for developing data assimilation (DA) methods to take benefit from available observations in order to estimate the BC as accurately as possible.

Up to now, DA methods have been mostly developed to meet the needs of large-scale meteorology. However, at such scales the atmospheric simulations are largely driven by initial conditions (IC) – i.e. the state of the meteorological variables at a given time to forecast the state at the next time step. As a matter of fact, DA methods have been mainly used to correct the IC. To date, DA methods allow to bring *back in time* information contained in observations. In the present work, the main objective is to revise such methods so that they bring information "back in space" and consequently extend the use of DA to micrometeorology.

To achieve this goal, the first step consists in choosing one or several DA method(s) appropriate for a use with CFD models in operational conditions. Next, a theoretical study must show that the methods can be adapted to the micrometeorological problems. And lastly, several tests have to be conducted to assess the efficiency of the methods with a CFD model for operational studies.

This document presents in details the context and the results of this work. Chapter 1 describes the lower layer of the atmosphere where micrometeorological processes take place and how these processes are modelled. This chapter also presents the methodologies implemented for wind resource assessment and dispersion modelling. Chapter 2 is an introduction to DA, reviewing the existing methods and the few cases where DA has been applied to micrometeorological problems. In Chapter 3 we describe the two selected DA methods, in their version adapted to atmospheric simulations at local scale. At first, a

validation study for these two methods is conducted with a simple model representing the atmosphere as a two-layers fluid flow, which resolves the shallow-water equations (SWE) in 1D. The results of this study are described in Chapter 4 and have been published in Defforge et al. (2018). The efficiency of the methods is then assessed in a context of wind resource assessment with twin experiments and field observations in a region with very complex topography. The twin experiments are conducted with a 2D domain in the XZ plane and then with the complete 3D domain. Measurements provided by a field campaign are eventually used in a cross-validation process. The object of Chapter 5 is to present this second study and to show the limitations of one of the two methods. The results presented in Chapter 5 have been published in Defforge et al. (2019a). For the second method, another study is described in Chapter 6, which corresponds to dispersion modelling in urban area and uses the observations provided by the Mock Urban Setting Test (MUST) field campaign. The experiments conducted in this urban configuration aim at assessing the ability of the adapted DA method to assimilate a few observations of wind or pollutant concentrations, within the urban canopy. Eventually, the last chapter gives the conclusions of the present work and outline perspectives for future works. Some theoretical developments have been performed in order to derive the adapted versions of the DA methods. Similarly, the SWE have been studied in details to perform the first study. Since these theoretical demonstrations are not essential to the overall understanding of the work and for the sake of clarity of the main manuscript, they have been added as supplementary information in Appendices B and A.

Chapter 1

Micrometeorology

Introduction

Meteorology impacts many human activities and has thus been studied for more than a century. Since atmospheric motions span a wide range of temporal and spatial scales – from hundredths of seconds to thousands of years, and from millimetres to thousands of kilometres – different subdomains of study have emerged. The two applications that interest us in the present study – wind resource assessment and atmospheric dispersion modelling – require accurate estimations of the meteorological variables (e.g., wind field, turbulence, etc.) over domains of a few squared kilometres horizontally and up to a few hundred meters above the ground. They consequently lie in the field of *micrometeorology*, which focuses on the atmospheric phenomena and processes at small spatial and temporal scales (Arya, 1988; Foken, 2017). In a first part, we present the vertical structure of the atmosphere and especially focus on the lowest part, where micrometeorological processes take place. To understand the origin of these processes, we then give the basic laws of thermodynamics and dynamics governing them. Afterwards, We present the different meteorological models, and in particular the atmospheric module of the open-source computational fluid dynamics (CFD) model *Code_Saturne*, and how the models at different scales interact. Eventually, we briefly review the methodologies applied for wind resource assessment and dispersion modelling.

1.1 The atmospheric boundary layer

1.1.1 Structure of the atmosphere

Both wind resource assessment and dispersion modelling focus on domains of a few squared kilometres horizontally. In order to model meteorology in such domains, it is first necessary to estimate the required vertical extent of the studied domains. To do so, one should understand the vertical structure of the atmosphere.

The mass of the atmosphere is mainly concentrated near the ground: half of its mass

is situated below 5500m and 99% are below 30km. This mass distribution justifies the fact that meteorology focuses on the first 20km or so of the atmosphere. The vertical profile of temperature in the atmosphere defines a vertical division of the atmosphere into four layers (Fig. 1.1a).

- The *troposphere* is the lowest layer of the atmosphere, extending between the ground and an altitude of 9km to 16km. In this layer the temperature decreases with height. The troposphere upper limit is called the *tropopause* and its height varies with latitude and weather conditions. Most of the meteorological phenomena occur within the troposphere and almost all the air pollutants are emitted, transported, and dispersed in this layer.

- The *stratosphere*, above the troposphere, extends up to 50km in altitude. Since the temperature increases with height in the stratosphere, this layer is relatively stable and there is little mixing there.

- The *mesosphere* is the region of the atmosphere extending between 50km and 80km. In this layer the temperature decreases again with altitude such that the coldest temperatures in the atmosphere occur at the upper limit of the mesosphere.

- The *thermosphere* is the uppermost layer of the atmosphere where the temperature increases very rapidly with altitude.

The lowest part of the troposphere, which is in contact with the ground, is called the *atmospheric boundary layer (ABL)* (Garratt, 1994) (Fig. 1.1b). The ABL is the scene of the micrometeorological processes: numerous matter, heat, and momentum exchanges, especially between the air and the underlying surface take place there. The ABL structure is determined by both the dynamics and thermodynamics of the lower atmosphere and the physical and thermal properties of the underlying surface. The ABL thickness, commonly referred to as *mixing depth*, varies in space and time between several tens of meters to a few kilometres. The mixing depth depends, in particular, on the topography and land use of the underlying surface as well as the large-scale meteorological conditions.

1.1.2 Dynamics of the atmospheric boundary layer

Dynamics of any fluid flows, such as the air in the atmosphere, is governed by fundamental laws of mass, energy, and momentum balance. Since numerical models of micrometeorology solve the governing equations of the flow it is necessary to derive these laws to understand, and thus properly apply, these models. In what follows, we will give the governing differential equations based on the fundamental laws of dynamics and thermodynamics. Detailed derivation of the conservation equations can be found in books on fluid mechanics, dynamical meteorology, or geophysical fluid dynamics (e.g., Haltiner and Martin, 1957; Pedlosky, 1979; Dutton, 1995).

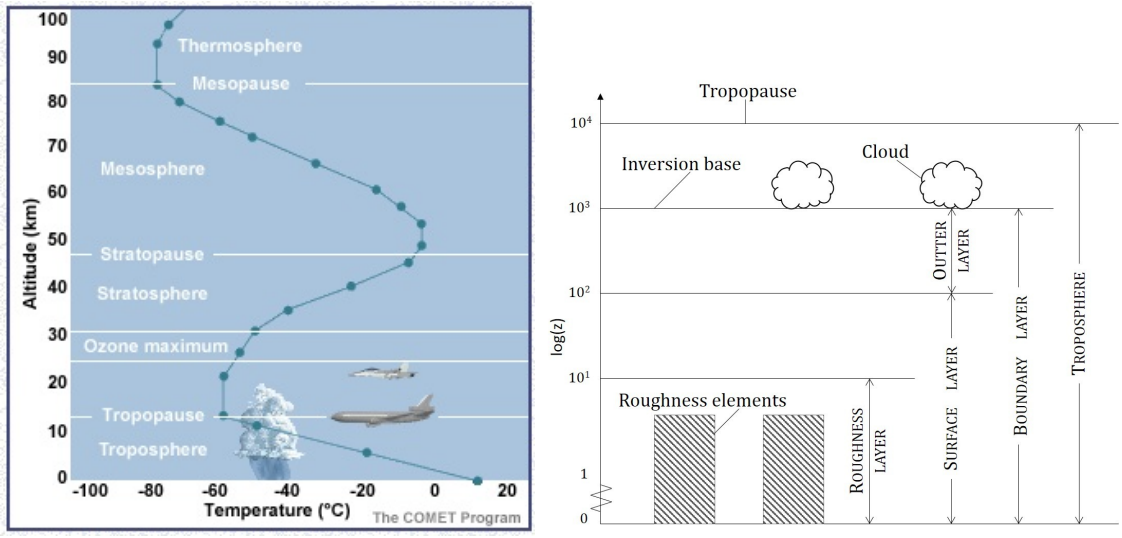

(a) (b)

Figure 1.1: a) Vertical structure of the atmosphere (source: NCSU). b) Vertical structure of the troposphere after (after Arya, 1988).

Conservation of mass

The law of mass conservation states that the mass of a system must be conserved. Applying this law to an elementary volume of air yields the **continuity equation**. Using the Einstein notation, it reads

$$\frac{\partial \rho}{\partial t} + \frac{\partial \rho u_i}{\partial x_i} = 0, \tag{1.1}$$

where u_i is the i-th component of the flow velocity and ρ is the fluid density. This equation mathematically represents the fact that the local rate of change in density must be equal to the divergence of mass in all the directions. At the small scales considered in the present work, the temporal variation of density $\partial\rho/\partial t$ is usually small compared to the other terms and it is therefore neglected (Pielke, 2013). This anelastic approximation allows to filter acoustic waves – which propagate very fast – from the solutions and still take the compressibility of the fluid into account.

When the principle of mass conservation is applied to a particular species i present in the air, one obtains the **diffusion equation** for the concentration of this species (c_i):

$$\frac{\partial c_i}{\partial t} + u_j \frac{\partial c_i}{\partial x_j} = D_{mi} \frac{\partial^2 c_i}{\partial x_j \partial x_j} + R_i(c_1, c_2, ...c_N, T) + S_i, \tag{1.2}$$

where D_{mi} is the diffusion coefficient of species i, R_i is the rate of change of concentration with time due to chemical reactions with other species – which depends on temperature T – and S_i represents other sources or sinks for this species.

Momentum balance

The overall momentum of any solid or fluid in motion must be conserved. The application of this principle to the fluid flow in an elementary volume yields:

$$\frac{\partial u_i}{\partial t} + u_j \frac{\partial u_i}{\partial x_j} = -\frac{1}{\rho}\frac{\partial p}{\partial x_i} + g_i + \frac{1}{\rho}\frac{\partial \tau_{ij}}{\partial x_j} + C_i, \tag{1.3}$$

where p is the pressure, g_i is i-th component of the gravity force, τ_{ij} are the components of the viscous stress tensor, and C_i is the i-th component of the Coriolis force. The left-hand side terms represent the acceleration of the fluid – in a Lagrangian framework – which can be decomposed between the time-dependent – i.e., the Eulerian acceleration – and advection components. The right-hand side terms correspond to the pressure gradient, the gravity force, the viscous effects of air, and the Coriolis effects due to the rotation of the Earth. The system of equations formed by this equation of momentum balance and the continuity equation (1.1) constitutes the **Navier-Stokes equations** which describe the motion of any viscous fluid.

Energy balance

The total energy of a system is conserved, even though the energy can change form (e.g., kinetic energy or heat). In the atmosphere, the source of energy that is mainly studied is heat, which is transferred by conduction, convection, and radiation. The variable commonly used to deal with heat in meteorology is the *potential temperature* θ which allows to compare parcels of air from different heights in the atmosphere and thus quantify the thermal instability of the air. It is defined for a parcel of air, initially at temperature T and pressure p, as the temperature that the parcel would attain if adiabatically brought to a standard reference pressure p_0. The relation between T and θ is given by the following equation:

$$\theta = T\left(\frac{p_0}{p}\right)^{R^*/c_p}, \tag{1.4}$$

where R^* is the gas constant for dry air, c_p is the specific heat capacity at a constant pressure, and p_0 is a reference pressure level, usually set equal to 1000hPa.

To take into account the air moisture, the *virtual potential temperature* is defined as the theoretical potential temperature of dry air that would have the same density as moist air. It is related to the actual potential temperature by

$$\theta_v = \theta\left(1 + 0.61r - r_{\mathrm{L}}\right), \tag{1.5}$$

where r and r_{L} are the mixing ratio of water vapour and liquid water in the air.

The application of the principle of energy conservation to heat in an elementary volume of atmospheric air, written in terms of potential temperature, reads

$$\frac{\partial \theta}{\partial t} + u_j \frac{\partial \theta}{\partial x_j} = \frac{1}{\rho C_p}\frac{\partial}{\partial x_j}\left(\lambda \frac{\partial \theta}{\partial x_j}\right) + S_\theta, \tag{1.6}$$

where C_p is the specific heat at constant pressure, λ is the molecular thermal conductivity, and S_θ is a source (or sink) term, mainly due to the latent heat of any evaporation or condensation in the volume. This equation suggests that the potential temperature of an air parcel is conserved in its motion, as long as only adiabatic transformations (compression or expansion) occur. When diabatic effects are present (e.g., condensation, evaporation) they represent sources (or sinks) of potential temperature.

1.1.3 Atmospheric stability and similarity theory

Atmospheric stability

The potential temperature can be seen as a 'normalized' temperature such that its vertical gradient characterizes the stability of the atmosphere. If we raise a cold air parcel (in terms of potential temperature), initially below warm air, it becomes colder (and thus heavier) than the surrounding air and therefore it goes back down: the atmosphere is stable. On the contrary, if a warm air parcel, initially below cold air, rises, it is found warmer (and lighter) than the surrounding air such that it continues rising: the atmosphere is unstable. Mathematically, this leads to the three following configurations:

- if $\frac{\partial \theta}{\partial z} > 0$, the atmosphere is stable,
- if $\frac{\partial \theta}{\partial z} = 0$, the atmosphere is neutral,
- if $\frac{\partial \theta}{\partial z} < 0$, the atmosphere is unstable.

These classes of stability can be used to classify meteorological situations. The atmospheric stability influences the dispersion of pollutants and the correspondence between the ABL structure and the typical observed plume shapes is schematically shown in Figure 1.2.

Similarity theory

Similarity theories are based on dimensional analysis and provide empirical relationships between variables of interest. Such theories are commonly used in micrometeorology since the relations governing turbulent processes are not always analytically solvable. A very commonly used similarity theory has been proposed by Monin and Obukhov (1954) for stationary and horizontally homogeneous conditions with no radiation. It has been developed to describe the vertical variations of wind speed and temperature, in non-neutral conditions, as a function of the dimensionless height parameter

$$\zeta = z/L, \tag{1.7}$$

where L is the Monin-Obukhov (M-O) length. This length is defined as a combination of the friction velocity (u_*), the surface potential temperature (θ_0), and the kinematic heat flux ($\overline{w'\theta'_0}$):

$$L = -\frac{u_*^3}{\kappa \frac{g}{\theta_0} \overline{w'\theta'_0}}, \tag{1.8}$$

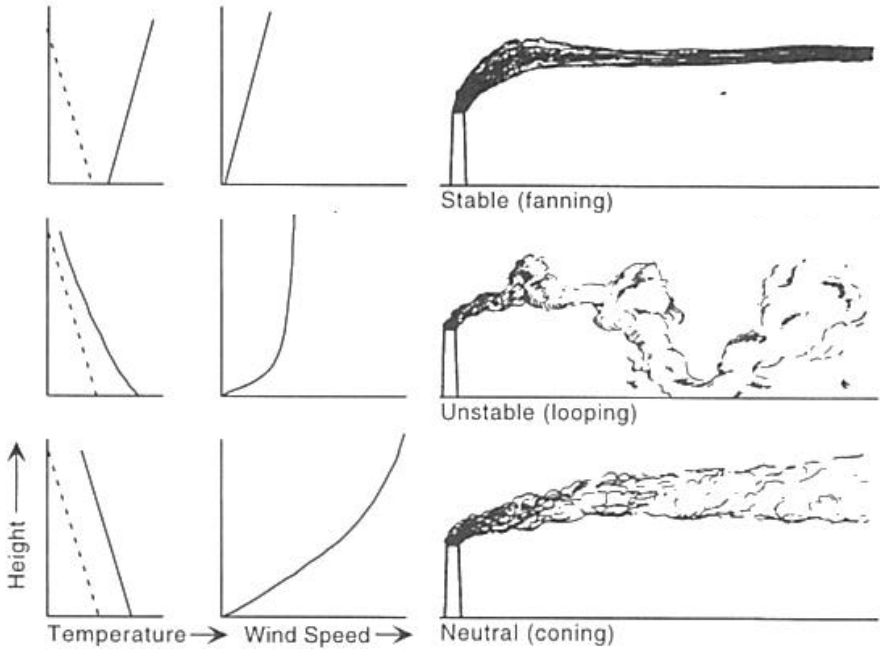

Figure 1.2: Schematic depiction of plume shapes according to the atmospheric stability level and the corresponding wind speed and temperature vertical profiles (source: Arya, 1988).

where $\kappa \approx 0.40$ is the von Karman's constant. The M-O length characterizes the ratio of contributions from buoyant and shear productions to turbulence kinetic energy (TKE). It is also used as a proxy for the stability of the atmosphere: it is unstable when $L < 0$ and stable when $L > 0$. When the atmosphere is neutral, by construction, $|L| \to \infty$.

From a dimensional analysis, the M-O similarity theory defines universal functions that empirically relate the dimensionless parameter ζ and the vertical gradients of velocity and potential temperature:

$$\frac{z}{u_*}\frac{\mathrm{d}U}{\mathrm{d}z} = \frac{1}{\kappa}\phi_m(\zeta), \tag{1.9}$$

$$\frac{z}{\theta_*}\frac{\mathrm{d}\theta}{\mathrm{d}z} = \frac{1}{\kappa}\phi_h(\zeta), \tag{1.10}$$

where U is the mean horizontal wind speed at height z, $\theta_* = -\frac{\overline{w'\theta'_0}}{u_*}$ is the friction temperature, θ is the mean potential temperature at height z, and ϕ_m and ϕ_h are the universal functions of momentum and heat respectively.

The integration of equations (1.9) and (1.10) with respect to z gives the logarithmic vertical profiles of velocity and potential temperature:

$$U = \frac{u_*}{\kappa}\left[\log\left(\frac{z}{z_0}\right) - \psi_m(\zeta)\right], \tag{1.11a}$$

$$\theta = \theta_0 + \frac{\theta_*}{\kappa}\left[\log\left(\frac{z}{z_{0\mathrm{T}}}\right) - \psi_h(\zeta)\right], \tag{1.11b}$$

where z_0 and $z_{0\mathrm{T}}$ are the roughness lengths for momentum and heat and ψ_m and ψ_h are defined as follows:

$$\psi_m(\zeta) = \int_{z_0/L}^{z/L} [1 - \phi_m(\zeta)] \frac{\mathrm{d}\zeta}{\zeta}, \tag{1.12a}$$

$$\psi_h(\zeta) = \int_{z_{0\mathrm{T}}/L}^{z/L} [1 - \phi_h(\zeta)] \frac{\mathrm{d}\zeta}{\zeta}. \tag{1.12b}$$

$$\tag{1.12c}$$

The universal M-O functions are determined using experimental data (e.g., Du Vachat and Musson-Genon, 1982). Several definitions of these functions have been proposed and a review of the different formulations is given in Foken (2006). One of the most commonly used is the one proposed by Businger and Dyer (Businger, 1988):

$$\phi_m(\zeta) = \phi_h(\zeta) = 1 + 5\zeta \qquad \text{if } 0 \leq \zeta < 1, \tag{1.13}$$

$$\phi_m^2(\zeta) = \phi_h(\zeta) = (1 - 15\zeta)^{-1/2} \qquad \text{if } -5 < \zeta < 0. \tag{1.14}$$

From the M-O relations, vertical profiles of TKE $k = \frac{1}{2}\left(\overline{u'^2} + \overline{v'^2} + \overline{w'^2}\right)$ and of its rate of dissipation ϵ can also be derived, as in Duynkerke (1988):

$$k = \frac{u_*^2}{\sqrt{C_\mu}} \left(\frac{\phi_m(\zeta)}{\phi_\epsilon(\zeta)}\right)^2 \tag{1.15a}$$

$$\epsilon = \frac{u_*^3}{\kappa(z + z_0)} \phi_\epsilon(\zeta), \tag{1.15b}$$

where C_μ is a constant and $\phi_\epsilon \approx \phi_m$ (Pahlow et al., 2001).

1.2 Modelling meteorology

The fundamental equations presented in the previous section, which govern the atmospheric processes, are not solvable analytically. However, numerical models have been developed to find approximated solutions to these systems of equations. As mentioned above, atmospheric motions – and thus meteorology – span a wide range of temporal and spatial scales (see Fig. 1.3). Consequently, several models exist and focus on different ranges of scales. We present below the main classes of meteorological models.

1.2.1 Global and regional scale models

Spatial and temporal scales are linked: the phenomena occurring at large horizontal scales generally also span long time scales (see Fig. 1.3). Consequently, global models, which simulate the atmospheric flow over the whole Earth and regional – or continental – models are usually run over long time periods to capture large-scale processes. In order to limit the calculation times, the spatial and temporal resolution of the models must be adapted to the size of the simulated regions. For instance, the global model

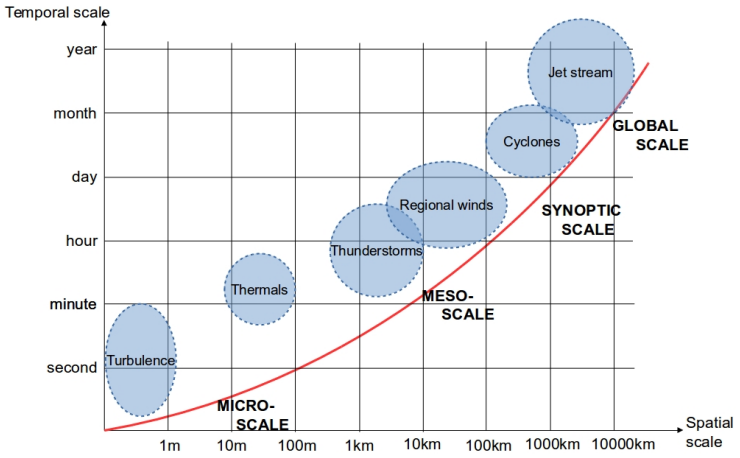

Figure 1.3: Spatial and temporal scales of the atmospheric processes (after R. Gaston).

ARPEGE developed by Météo-France has an average spatial resolution of 16km and a time step of 360s. The regional models AROME and Weather Research and Forecasting (WRF), developed by Météo-France and NCAR respectively, have horizontal grid cells of approximately 1km and a time resolution of 1min or less. The equations solved by the different global and regional models may differ. All the equations are derived from the Navier-Stokes equations but they generally include approximations in large-scale models, in order to reduce the computational cost of the equations resolution. Moreover, when the grid cells are large, the atmospheric phenomena occurring at small scales, compared to the cell size, cannot be explicitly resolved and need to be parametrised. The most common parametrisations include convective clouds, radiative transfers, and cloud microphysics (e.g., Noilhan et al., 1989; Kain and Fritsch, 1993; McFarlane, 2011). Subgrid phenomena might have a substantial influence on the atmospheric flow such that a great research effort is carried out to improve the parametrisations in global and regional models (e.g., Garuma, 2018).

1.2.2 CFD models for local-scale atmospheric simulations

To represent local-scale domains, CFD models are increasingly used. These models directly solve the full Navier-Stokes equations such that they are computationally expensive. The recent increase in computational capacities allows to use CFD models for many atmospheric applications at local scale. Such models are generally used with meshes which horizontal resolution spans from a few tens of meters to several meters and with time steps down to a few seconds. Despite the relatively small size of grid cells used in CFD models, turbulence might occur at scales smaller than the mesh resolution and impact the flow at the scales resolved by the model. Consequently, different methodologies

have been developed through the years to model turbulence, some of which are presented below.

Modelling turbulence

Turbulence corresponds to the fluctuations, in time and space, of velocity, temperature, and scalar concentrations, around their mean values. As the atmospheric motion in the ABL is always turbulent, it is necessary to understand and represent turbulent exchanges and mixing processes to study micrometeorology (e.g., Stull, 1988). We present here, in a qualitative way, the three main techniques for modelling turbulence. These approaches are based on the Navier-Stokes equations, and include more or less approximations.

Direct numerical simulation (DNS) The turbulent processes in the ABL involve a wide range of time and length scales. In theory, it is possible to represent all these scales by a direct simulation of the Navier-Stokes equations (DNS). This method numerically solves the equations of the dynamics for all the scales involved in the turbulent processes. To do so, DNS requires a very fine resolution to explicitly resolve the smallest scales of motion (Kolmogorov length scale, typically 10^{-5}m in the atmosphere) and a a sufficiently large domain to represent the largest scales of interest (typically 10^3m in the atmosphere). As a result, DNS is computationally very expensive and despite the significant increase in computational capacities over the last decades, the DNS technique has only been applied to low Reynolds-number flows, for which the ratio between the largest and smallest scales is limited to a few hundreds. The Reynolds numbers encountered in the ABL is typically of 10^8 such that the number of grid points necessary would be of 10^24 and the computational resources required by DNS would exceed the capacity of the most powerful computers currently available. Still, this technique is very useful for research purposes.

Large eddy simulation (LES) The small scales of motion are the most computationally expensive to resolve. The approach adopted for LES is to spatially filter the meteorological fields in order to remove subgrid scale information and explicitly simulate the larger eddies only. The smaller scales are not resolved but their contribution to energy dissipation and to turbulent processes are parametrised using subgrid models, which are functions of resolved-scale variables. These parametrisations, necessary to close the set of equations, are simpler than Navier-Stokes equations and faster to solve. The effect of the low-pass filtering, applied in the LES approach, can be seen as time- and spatial-averaging. This technique, although less faithful than DNS, requires less computational resources and becomes increasingly popular.

Reynolds-averaged Navier-Stokes (RANS) modelling and turbulence closure models For most of engineering and environmental applications, only the mean fields (velocity, temperature, concentration, etc.) are of interest. The RANS approach is based

on the Reynolds decomposition: each flow variable (x) is separated into its mean value ($\overline{x}$), which represents the large scales, and its fluctuating component with zero mean (x'), which accounts for turbulent small-scale flow:

$$x = \overline{x} + x'. \tag{1.16}$$

The averaging operator used in the previous equation theoretically corresponds to a temporal mean over a given time period. Theoretically, the mean variables should then be time independent. However, the time-dependent terms are generally kept in the derivation of the RANS equations. The retention of these terms can be justified by the ergodicity of turbulent flows and the different time scales involved in the system. According to the ergodicity hypothesis, for statistically stationary processes, the temporal means are equal to the ensemble means, which are time-dependent (Frisch and Kolmogorov, 1995). Moreover, typical time scales of turbulent fluctuations – and thus the averaging period – are generally much smaller than characteristic times of large-scale fluid motions. During such long time periods, the mean variables are not necessarily stationary. These two points can justify the assumed time-dependency of the mean variables considered in RANS equations.

The Reynolds decomposition is applied to all the variables: the three velocity components, the fluid density, the pressure, the potential temperature, and the species concentrations. These variables are replaced by their Reynolds decomposition in the equations of continuity (1.1), momentum conservation (1.3), heat (1.6), and pollutant transport (1.2). The governing equations are then time-averaged to derive the Reynolds-averaged equations:

$$\frac{\partial \overline{\rho}\ \overline{u_i}}{\partial x_i} = 0, \tag{1.17a}$$

$$\frac{\partial \overline{u_i}}{\partial t} + \overline{u_j}\frac{\partial \overline{u_i}}{\partial x_j} = -\frac{1}{\overline{\rho}}\frac{\partial \overline{p}}{\partial x_i} + g_i + \frac{1}{\overline{\rho}}\frac{\partial \overline{\tau_{ij}}}{\partial x_j} + C_i - \frac{\partial \overline{u_i' u_j'}}{\partial x_j}, \tag{1.17b}$$

$$\frac{\partial \overline{\theta}}{\partial t} + \overline{u_j}\frac{\partial \overline{\theta}}{\partial x_j} = \frac{1}{\overline{\rho} C_p}\frac{\partial}{\partial x_j}\left(\lambda \frac{\partial \overline{\theta}}{\partial x_j}\right) + \overline{S_\theta} - \frac{\partial \overline{u_j' \theta'}}{\partial x_j}, \tag{1.17c}$$

$$\frac{\partial \overline{c_i}}{\partial t} + \overline{u_j}\frac{\partial \overline{c_i}}{\partial x_j} = D_{mi}\frac{\partial^2 \overline{c_i}}{\partial x_j \partial x_j} + \overline{S_i} - \frac{\partial \overline{u_j' c_i'}}{\partial x_j}. \tag{1.17d}$$

Supplementary terms ($\overline{u_i' u_j'}$) appear in the equation of momentum conservation (1.17b). These terms are the components of the total stress tensor accounting for turbulent fluctuations in fluid momentum and are called the Reynolds stresses. Due to the nonlinearity of the Navier-Stokes equations, the RANS equations include some terms related to turbulent flux that depend on unknown covariances of two fluctuating variables: $\overline{u_i' u_j'}$, $\overline{u_j' \theta'}$, and $\overline{u_j' c_i'}$. The presence of these terms in the RANS equations constitutes the closure problem of turbulence: there are more unknown variables than the number of equations.

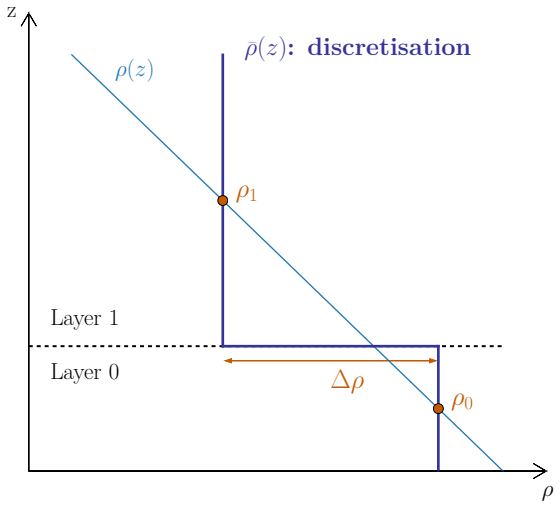

Figure 1.4: The layer system corresponds to a crude discretisation of the troposphere (light blue line) into two layers of constant density (dark blue line). The dynamics in the upper layer is neglected and the bottom layer follows the shallow-water equations (SWE) with a reduced gravity $g' = \frac{\Delta\rho}{\rho_0} g$.

Several models of turbulence have been proposed to solve this closure problem and obtain a closed set of equations.

- The **mixing length model** is a method attempting to describe momentum transfer by turbulence Reynolds stresses within the ABL by means of an eddy viscosity (Prandtl, 1925). It is conceptually analogous to the mean free path in thermodynamics: a fluid parcel will conserve its properties for a characteristic length, L, before mixing with the surrounding fluid.

- The **k-epsilon** model is an improvement of the mixing length model and is now the most common model used in CFD. It focuses on the mechanisms that affect the TKE and consists in a set of two equations: one for the TKE k and one for its dissipation rate ϵ (Launder and Spalding, 1974).

- Other turbulence models exist and research is still ongoing to improve them (e.g., second order closure, Umlauf and Burchard, 2005).

Since RANS models are more computationally efficient than LES models (Rodi, 1997) they are still preferred to simulate the ABL flows over complex terrain and all the CFD simulations performed in the present work use RANS turbulence modelling.

1.2.3 Shallow-layer model of the atmospheric boundary layer

The SWE are derived from the Navier-Stokes equations in the approximation of a small layer height, compared to horizontal spatial scales. These equations can be used to

represent atmospheric flows if the gravity g is replaced by the reduced gravity $g' = \frac{\rho - \rho_a}{\rho} g$ to account for the small difference of density between the simulated ABL (ρ) and the free atmosphere above (ρ_a), as shown on Figure 1.4. Moreover, the discretised 'level' models – which use, for instance, vertical finite-difference approximations – often chosen to simulate continuously stratified fluid, can be shown to be equivalent to multi-layer models – where SWE are applied to each layer (Audusse et al., 2006; Pedlosky, 1979). Therefore the simple model described below can be considered as a crude vertical representation of the atmosphere into two layers: the ABL which satisfies the SWE and the free atmosphere above (see Fig. 1.4).

In one dimension, the two state variables of the SWE are the thickness of the fluid layer (h, here the boundary layer), and the mean horizontal velocity (u) which are related as follows, assuming that ground friction and diffusion are neglected:

$$\frac{\partial \mathbf{X}}{\partial t} + \mathbf{M}\frac{\partial \mathbf{X}}{\partial x} = \mathbf{S}, \tag{1.18}$$

where $\mathbf{X} = \begin{pmatrix} h \\ u \end{pmatrix}$, $\mathbf{M} = \begin{pmatrix} u & h \\ g' & u \end{pmatrix}$, and $\mathbf{S} = \begin{pmatrix} 0 \\ -g'\frac{\partial z_r}{\partial x} \end{pmatrix}$ with z_r the bottom topography. The problem is well-posed if two boundary conditions (BC) are prescribed, one on h and one on u (e.g., Abbott, 1966).

The nature of a flow is determined by the value of the Froude number, which is the ratio of the flow inertia to the external forces: $Fr \equiv \frac{u}{\sqrt{gh}}$. If $Fr < 1$ the flow is subcritical (or fluvial), if $Fr = 1$ it is critical (or torrential), and if $Fr > 1$ the flow is supercritical.

Bernoulli equation

The 1D SWE with topography and without ground friction nor diffusion, equation 1.18, can be solved analytically by the Bernoulli equation (1.19) (e.g., Goutal and Maurel, 1997) which is based on the energy conservation and states that the sum of the specific head ($\mathcal{H}_s \equiv h + \frac{u^2}{2g'}$) and the topographic elevation (z_r) is conserved over the domain:

$$\frac{u^2}{2g'} + h + z_r = \mathcal{H}_0, \tag{1.19}$$

where $\mathcal{H}_0$ is the specific head determined at one point of the domain where the system state is known.

Method of characteristics

In addition to Bernoulli equation, the 1D SWE can be solved using the method of characteristics (Abbott, 1966; Lister, 1960). This method consists in using the two eigenvalues of $\mathbf{M}$ ($\alpha_+ = u + c$ and $\alpha_- = u - c$ where $c = \sqrt{g'h}$ is the wave speed) to

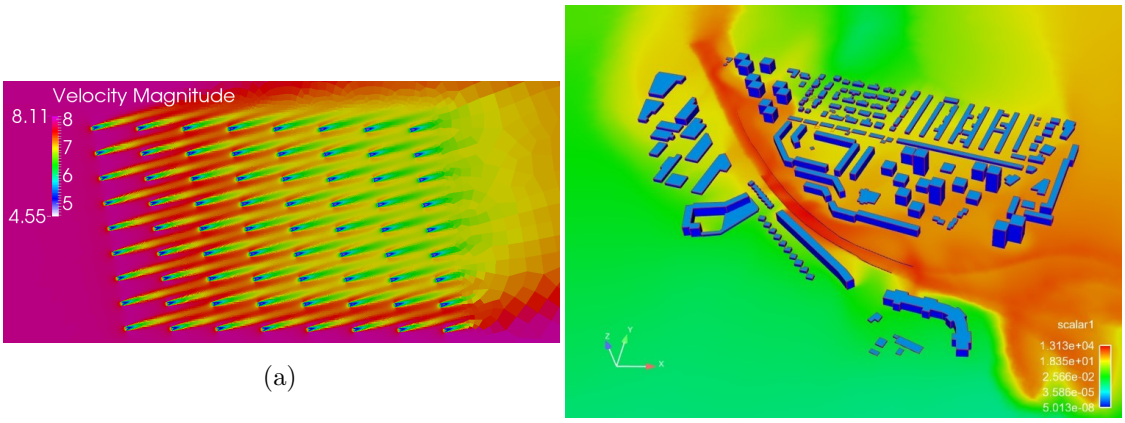

(a) (b)

Figure 1.5: (a) Example of CFD simulation with the atmospheric module of *Code_Saturne* over a wind farm (source: G. Angot). (b) Example of pollutant dispersion modelling in the suburbs of Toulouse's city, France.(source: Z. Gao).

derive a system of conservation equations:

$$\left(\frac{\partial}{\partial t} + \alpha_+ \frac{\partial}{\partial x}\right)(u + 2c) = 0 \iff \left.\frac{\mathrm{d}R_+}{\mathrm{d}t}\right|_{\mathcal{C}_+} = 0, \tag{1.20a}$$

$$\left(\frac{\partial}{\partial t} + \alpha_- \frac{\partial}{\partial x}\right)(u - 2c) = 0 \iff \left.\frac{\mathrm{d}R_-}{\mathrm{d}t}\right|_{\mathcal{C}_-} = 0, \tag{1.20b}$$

where $R_+ = u + 2c$ and $R_- = u - 2c$ are the *Riemann invariants*, conserved along the curves $\mathcal{C}_+$ and $\mathcal{C}_-$ defined by

$$(\mathcal{C}_+) : \frac{\mathrm{d}x}{\mathrm{d}t} = \alpha_+ = u + c, \tag{1.21a}$$

$$(\mathcal{C}_-) : \frac{\mathrm{d}x}{\mathrm{d}t} = \alpha_- = u - c. \tag{1.21b}$$

More details about the derivation of the SWE, their theoretical resolution, and the model used to solve them can be found in Appendix A.

1.2.4 Atmospheric module of *Code_Saturne*

Code_Saturne is a free, open-source software developed and released by Électricité de France (EDF) to solve CFD applications (Archambeau et al., 2004). It solves the Navier-Stokes equations for 2D, 2D-axisymmetric, or 3D flows using a co-located finite volume scheme. *Code_Saturne* can be used for steady or unsteady simulations and to simulate laminar or turbulent flows.

This model has the particularity to handle meshes with any type of cells (e.g., tetrahedral, hexahedral) and any type of grid structure (e.g., unstructured, block structured, hybrid). There are several turbulence approaches available in *Code_Saturne* including the mixing length, $k - \epsilon$, and LES.

The atmospheric module of *Code_Saturne*, has been developed by the Centre d'Enseignement et de Recherche en Environnement Atmosphérique (CEREA) to simulate atmospheric flows in the ABL. It is based on the standard version of *Code_Saturne* to which supplementary developments have been added to model the specificities of the atmospheric dynamics. This module is used for a wide range of quasi-operational applications, including wind resource assessment and pollutant dispersion modelling (see Fig. 1.5).

In the atmospheric module of *Code_Saturne*, the thermal effects in the ABL are taken into account by the resolution of the equation of energy conservation, derived for the potential temperature (see Eq. 1.6). Other thermal processes such as the buoyancy effect (e.g., momentum balance, thermal production of turbulence) are also included. The microphysics of water can also be represented by three variables (virtual potential temperature, number of droplets, and water content) to study, for instance, fog formation or cooling tower plumes (Bouzereau, 2004).

The BC for open boundaries (lateral or top) can be prescribed with different degree of complexity: from simple vertical academic profiles to full 3D fields, interpolated from larger-scale simulations (dynamical downscaling). The interactions with the ground (momentum balance and heat exchange) are modeled and both a forest model (Zaïdi et al., 2014) and an urban canopy model can be used when necessary. In addition, the effect of solar and infrared radiation can be taken into account (Makké et al., 2016).

Code_Saturne offers the possibility to transport scalars, which is particularly useful to study pollutant dispersion (Milliez, 2006). Moreover, modules of gas-phase and particle chemistry are available as well as sedimentation, wet scavenging, and deposition. These options allow to study traffic pollution (Albriet et al., 2010) or air pollution in street canyons (Thouron et al., 2019).

For wind resource assessment studies, it is possible to model the wake effect of wind turbines.

The atmospheric module of *Code_Saturne* is used in the present work to evaluate the performances of the data assimilation (DA) methods in operational conditions (see Chapters 5 and 6).

1.2.5 Relative importance of initial and boundary conditions

The resolution of Navier-Stokes equations requires the knowledge of the initial state of the system – IC – and/or the state of the atmosphere at the domain boundaries – BC. The atmospheric models (except for global models) have open boundaries: the borders of the domain do not correspond to physical limits. Consequently the state of the atmosphere outside the domain impacts its inner state and evolution through these open boundaries. In order to take these mesoscale effects into account, the inner meteorology must be forced by the prescription of BC representative of the mesoscale meteorology.

Depending on the characteristic length- and time-scales of the system, the IC and BC do not equally influence the solution within the domain. In order to understand the

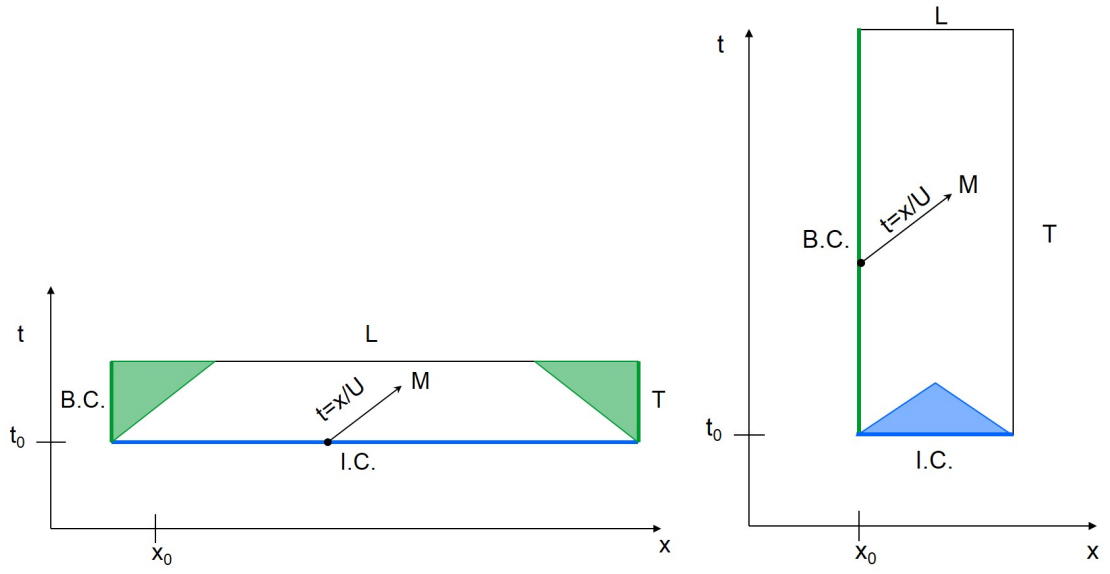

Figure 1.6: Relative importance of initial conditions (IC) and BC for a) large-scale meteorology and b) local-scale meteorology. L, T, and U are typical scales of length, time, and velocity. a) Except for the regions coloured in green, the solution in the domain is mainly influenced by the IC. b) The solution is mainly influenced by the BC, except for the blue region.

relative importance of IC and BC, we use here the method of characteristics previously presented (see Section 1.2.3).

Figure 1.6a shows a schematic representation of a large-scale atmospheric domain in the spatio-temporal space. For atmospheric flows, the wind speed is typically of the order of magnitude of $U \sim 10$m/s. Large-scale domains extend over $L \sim 1000$km and the simulations typically last $T \sim 1$day $\sim 10^4$s such that $T \times U/L \sim 0.1$. Consequently, the spatial extent of the domain is much greater than the typical distance travelled by the flow during a simulation: $L \gg T \times U$. In Figure 1.6a, one of the two characteristic curves is represented by an arrow and indicates that the solution in M depends on the IC. It is similar for most of the points in the domain, except the ones in the two green regions. On the contrary, small-scale meteorology corresponds to spatio-temporal domains longer along the temporal axis than the spatial axis: $L \ll T \times U$. We have seen in Section 1.2.2 that micrometeorological applications are studied over domains of a few kilometres ($L \sim 1$km) and during characteristic time scales of $T \sim 1$h $\sim 10^3$s, such that $T \times U/L \sim 10$. As a result, most of the points in the domain are influenced by BC – except for the blue region – (Fig. 1.6b). Stationary simulations correspond to the limit $T \to \infty$ and the steady-state of the system does not depend on the IC at all.

This schematic representation illustrates the fact that large-scale simulations are largely determined by IC whereas for local-scale models, the solution is mainly influenced

by BC. Note that the two cases presented here are somehow extremes and one could imagine domains for which both the IC and BC substantially influence the inner solution. This heuristic demonstration qualitatively justifies that, in order to improve the accuracy of micrometeorological simulations, the inputs that have to be corrected are the BC.

1.2.6 Combining different scales

Turbulence is an example of how small-scale processes impact larger-scale meteorology; their effects are taken into account through subgrid models or parametrisation (see Section 1.2.2). Similarly, large-scale phenomena and processes impact micrometeorology. For instance, CFD domains generally cover a few kilometres in the horizontal direction and several hundred meters in the vertical direction. The mesoscale atmospheric phenomena that often drive wind patterns occur at larger scales and cannot be captured by local-scale models. Consequently, information from larger-scale meteorology must be provided to CFD models, especially through the definition of the BC.

In order to combine informations from regional- and local-scale simulations, two types of downscaling methods exist: statistical and dynamical.

Statistical downscaling

Statistical downscaling determines (statistical) relationships between predictors available during a long time period (e.g., outputs of large-scale models or observations) and some local-scale predictands (Wilby and Wigley, 1997). There are three categories of statistical downscaling:

- Regression methods seek linear or nonlinear relationships between the predictors and predictants. In wind resource assessment, regression methods are generally called measure-correlate-predict (MCP) methods and are used to infer statistical relations between a reference site where long-term measurements are available and the nearby candidate site (Carta et al., 2013). While regression methods have a low computational cost, they are reliable only for relatively flat regions and require a well-developed measurement network. Moreover they generally underestimate the variability of the predictands and thus poorly assess the impact of extreme events.

- Weather generators generate synthetic time series from realistic high-frequency variablility (Wilks and Wilby, 1999). These stochastic models are generally applied in climate change impact studies.

- Weather classification methods group predictors into a reduced number of classes according to their similarities (e.g., wind speed and direction) during a training period over which both predictand and predictors are available. The classes are then used to reconstruct the long-term time series of predictand values.

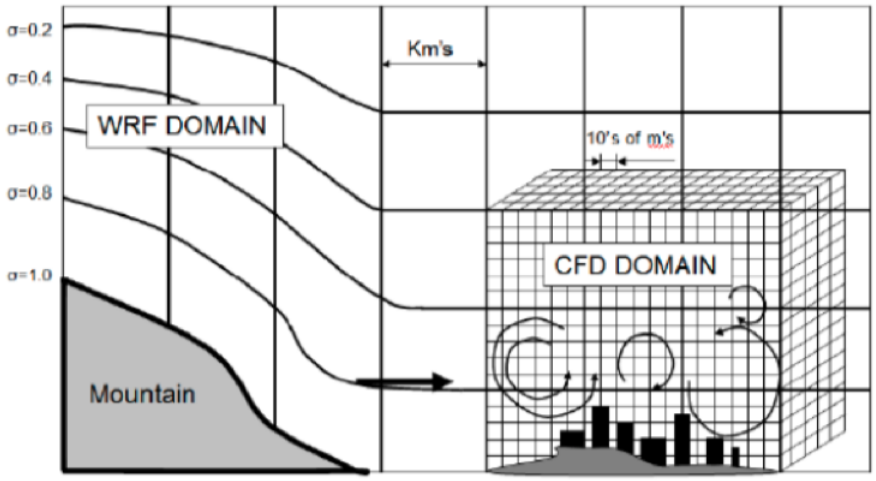

Figure 1.7: Representation of scale imbrication from meso- to local-scale models (source: E. Leblebici).

Dynamical downscaling

Dynamical downscaling – or nesting – can be one-way or two-ways. One-way nesting consists in extrapolating the results of large-scale simulations to force local-scale models, generally through the definition of BC (e.g. Yamada, 2004; Probst and Cárdenas, 2010; Rodrigues et al., 2016) (Fig. 1.7). With such method, the information only goes from the mesoscale to the local-scale model. On the other hand, two-way nesting is based on information sharing between the mesoscale and microscale models in both directions (e.g., Debreu and Blayo, 2008; Zajaczkowski et al., 2011; Chen et al., 2011). Nesting methods are widely used for wind energy applications and urban studies. In both types of studies, the shared information include meteorological variables. In dispersion modelling studies, the pollutant concentration might also be taken into account by downscaling (Stocker et al., 2012; Oldrini et al., 2017).

Although downscaling methods are efficient ways of including large-scale meteorology in microscale simulations, the methods are not always fully satisfactory. For microscale imbrications with CFD models, the difference in spatial and temporal resolution between mesoscale and CFD domains might be very large and gives rise to several issues. The mesoscale outputs might indeed lack accuracy or some information can be missing. The initial guess of BC obtained from mesoscale outputs are generally incorrect and especially near the ground, where the effect of complex terrain – poorly represented at the resolution of mesoscale models – are the most important. Moreover, there might be inconsistencies between the physics of models across scales. For instance, mesoscale models rarely simulate the small scales of turbulence such that the outputs of mesoscale models do not contain enough information about turbulence in the domain of interest (e.g., Muñoz-Esparza et al., 2014). As a result, the state of the variables related to turbulence (e.g., k

and ϵ) which must be provided as BC to CFD models must be empirically reconstructed. Several studies have proposed methods to combine mesoscale and microscale models in terms of turbulence, either for RANS models (Kunz et al., 2000; Baik et al., 2009; Tewari et al., 2010; Castro et al., 2010; Kwak et al., 2015; Balogh and Parente, 2015, e.g.,) and more recently with LES models (e.g., Liu et al., 2012; Nakayama et al., 2012; Michioka et al., 2013).

1.3 Wind resource assessment

Wind resource assessment consists in evaluating the mean annual energy that could be produced if a wind farm was installed at a specific site. The existing methods for assessing the wind resource of a site are generally based on *in situ* measurements, mesoscale or local-scale modelling, or on the use of meteorological reanalyses (Landberg et al., 2003; Probst and Cárdenas, 2010; Blocken, 2014; Sanz Rodrigo et al., 2017).

1.3.1 Site measurements

Historically, the wind potential for a candidate site was assessed through statistical analyses of the available wind measurements, recorded in the area of concern (e.g., Fagbenle et al., 2011). For instance, statistical downscaling methods mentioned in Section 1.2.6 have been widely used to infer wind potential of a given site from observations of a few locations (Sanz Rodrigo et al., 2017). However, due to the relatively high cost of weather stations, the measurement network is generally coarse. Moreover, at least one year of data is required to build climatology of a candidate site and in practice it appears that longer time series are needed to well capture the climatology of a given site. These requirements are not always fulfilled, either for economical or complexity reasons, and the development of computational capacities have lead to the common use of linear and nonlinear numerical models (Ayotte, 2008).

1.3.2 Mesoscale models

Numerical weather prediction (NWP) models generate mesoscale data that can be used in the same way as on-site measurements (Al-Yahyai et al., 2010). Other mesoscale models have been developed, one of the most popular being the WRF model (Skamarock et al., 2005). In particular, this model is used with a resolution of 3km in space and 30min in time to build the New European Wind Atlas which aims at becoming a standard for site assessment (Witha et al., 2019). However, mesoscale models generally have too coarse horizontal resolution, leading to several sources of uncertainties, especially when the prospected site is in complex terrain. In order to accurately capture the effects of complex geometrical features, it is necessary to have a sufficiently fine resolution either in the measurement network or in the model.

1.3.3 Mass-consistent models

Traditionally, microscale wind fields were obtained from mass-consistent diagnostic models (Sherman and Sherman, 1978; Homicz, 2002). These models are based on mass conservation and sometimes include additional parametrisation to represent microscale effects (e.g., thermal slope flows). While these models can give somehow good results in simple cases, they fail in representing some microscale phenomena such as recirculation after obstacles or ABL profiles (e.g., Ehrhard et al., 2000). Mass-consistent models are generally coupled with NWP models which provide an initial guess of the wind field (Barcons et al., 2018).

1.3.4 Linear models

Linear models, such as WAsP CFD (Wind Atlas Analysis and Application Program) which is widely used in the wind energy community (Mortensen et al., 1993), are based on the linearisation of the momentum equation. Such linear models reduce the computational cost of simulations and provide reasonable estimations for flat terrains or with small slopes. However, they are not suitable when the topography is steep as the linearity assumption is not valid any more (Ayotte and Hughes, 2004). Indeed, complex geographical features (topography, buildings, etc.) substantially affect the wind flow, at relatively small scale, and nonlinear models are necessary to better represent their effects.

1.3.5 CFD models

As described in Section 1.2, boundary layer flows can be simulated with CFD models. With the development of computing capacities, the use of CFD modelling at local scale is more and more frequent, especially over complex terrain (Cattin et al., 2006; Palma et al., 2008; Blocken et al., 2015; Dhunny et al., 2017) and in urban areas (Kalmikov et al., 2010; Simões and Estanqueiro, 2016; Wang et al., 2017). Given the large number of parameters and choices required to perform CFD simulations, best practice guidelines for ABL flow modelling as well as validation and verification methodology have been proposed (e.g., Franke et al., 2011; Casey and Wintergerste, 2000; Sanz Rodrigo et al., 2017). One of the major differences between the several CFD models used in wind resource assessment studies come from the model of turbulence as both RANS (e.g., Maurizi et al., 1998; Castro et al., 2003) and LES models (e.g., Uchida and Ohya, 2008) have been applied in previous studies. Such methods provide an approximation of the turbulence inputs which might trigger errors within the simulated domain. However, it is still not practicable to use DNS for operational wind resource assessment studies.

1.3.6 WRAPP methodology

Wind resource assessment might provide the mean spatial distribution of wind conditions. However, it is not realistic, from a computational-cost perspective, to simulate a full year

of meteorology with CFD or to calculate high-resolution maps of wind flow over too large domains. Several methodologies, combining both statistical and physical downscaling (see Section 1.2.6), have thus been developed to reduce the number of CFD simulations to operationally affordable computational costs while being representative of a long-term period (Frey-Buness et al., 1995; Frank and Landberg, 1997; Badger et al., 2014).

EDF R&D has developed a statistical-dynamical downscaling method based on weather classification: the Wind Resource Assessment and Power Production (WRAPP) methodology. It consists in coupling mesoscale model WRF with the atmospheric module of the CFD model *Code_Saturne*. The mesoscale model is run over a large domain which includes the candidate site, for a long period of time (a few years). All the meteorological situations thus simulated are clustered in a few hundreds of statistical classes. The classes must be as homogeneous as possible and with the largest distance between the different classes. The classes are calculated with a k-means clustering method which compares hourly outputs of WRF, based on several variables such as wind speed and direction. The atmospheric stability is also often taken into account by adding the M-O length – or any other variable – as an additional dimension to the classification (e.g., Sanz Rodrigo et al., 2008). For each class, a single situation is selected and considered as representative of the whole class. This situation is then simulated with *Code_Saturne*. The inlet conditions for the CFD simulation are defined from an extrapolation of the WRF results, for the representative situation, to the resolution of the *Code_Saturne* domain (see Section 1.2.6).

The wind potential is evaluated for each of these representative situations and the overall wind potential is calculated as the average over these few representative situations, weighted by the size of the classes. This methodology has been applied in several wind resource assessment studies at EDF R&D (Angot, 2018).

1.4 Atmospheric dispersion modelling

Outdoor air quality is a rising health issue, especially in large cities and developing countries. Atmospheric dispersion modelling is necessary to estimate concentrations of pollutants emitted from various sources and calculate high-resolution maps of pollution over urban neighbourhoods or industrial areas. In turns, these maps are used for many applications: urban environmental planning, emissions management, policy and mitigation strategies evaluation, pollution episodes forecasting, building design, etc.

The flow field, and consequently the pollutant plume, are particularly difficult to simulate in built environment. Indeed, the buildings substantially impact the dynamics and the thermodynamics of the flow, and the dispersion of the pollutants. As a consequence of the complexity of dispersion modelling in built environment, several studies have focused on this topic (Holmes and Morawska, 2006).

Both the flow field and the dispersion might be modelled with different methodologies. The choice of the methodology is generally a compromise between precision

and computation cost. For the flow field, the differences between the several models and studies mainly come from the representation of turbulence. More details about the available options to represent the turbulence in CFD models are given in Section 1.2.2. Regarding the modelling of pollutant dispersion, various approaches also exist (Tominaga and Stathopoulos, 2016). The most popular are box models, Gaussian plume models, Lagrangian models, and Eulerian models, as detailed below.

1.4.1 Box model

Box models consist in treating the simulated domain as a box and applying the conservation of mass inside this box (e.g., Ragland, 1973). These models are based on the assumption of uniform distribution of pollution inside the domain and they thus estimate the volume-averaged pollutant concentration inside the domain, as a function of time. The wind speed and direction are considered constant in time and uniform in space. Despite the simplified treatment of meteorology, box models can include more sophisticated chemical and photochemical modules which better represent the physics and chemistry of particles within the atmosphere. These models are relatively easy to use and may be useful to study simple cases. They have been used in several studies to predict concentrations of ozone and other photochemical pollutants in urban areas (e.g., Soetaert and Herman, 1995; Kunsch and Webber, 2000). However, the assumptions are strong so that box models are imprecise and may be inadequate for several studies, especially in complex environments.

1.4.2 Gaussian plume model

Gaussian models are very widely used in atmospheric dispersion modelling. Under steady conditions and spatial homogeneity, the analytical solution of the transport equation is a pollution plume which follows Gaussian distributions in both vertical and horizontal directions (Bosanquet and Pearson, 1936). The Gaussian models consider that this solution is valid in other situations. The width of the plume depends on vertical and horizontal variances of the Gaussian distributions, determined empirically either by stability classes (Pasquill, 1961) or travel time from the source.

Gaussian plume models assume that during the characteristic time for dispersion (e.g., a few hours), the meteorological conditions and air pollutant emissions are constant. Over complex terrain, under convective conditions, or at local scales, the assumption of horizontal homogeneity of the wind field does not hold any more. In such cases, Gaussian plume models are not appropriate. Moreover, the plume centreline trajectory is assumed straight in Gaussian model, which is not suitable to model dispersion under low wind conditions or too close to the source. Despite the simplicity of the mathematical operations behind Gaussian models, which makes them easy to use – they require a small number of inputs and low computer resources –, their limitations are too significant and

these models are not appropriate for the micrometeorological applications studied in the present work.

1.4.3 Lagrangian model

Lagrangian modelling consists in following pollution plume parcels – also called particles – as they move in the atmosphere (e.g., Stohl et al., 2005). The model calculates the statistics of the trajectories of a large number of particles. The concentration is then a product of the probability density function thus computed and a source term. Lagrangian models rely on a prior estimation of the meteorological fields inside the domain such as the mean fluid velocity, turbulence, and molecular diffusion. These models are well suited for dispersion modelling over flat terrain in steady conditions (Oettl et al., 2001; Raza et al., 2001; Venkatesan et al., 2002; Tsuang, 2003) as well as unsteady conditions with more complex geometries (Du, 2001; Hurley et al., 2003; Jung et al., 2003). However these models might be computationally expensive as the number of particles increases and the interaction between particles are difficult to take into account.

1.4.4 Eulerian model

Unlike Lagrangian models for which the frame of reference moves with the particles, Eulerian models consider a fixed Cartesian frame and 'observe' the particles flowing. In this fixed frame, given the fields of wind and turbulence, Eulerian models solve the equation of advection-diffusion for a scalar, which represents the pollutant concentration (see Equation 1.2). In order to solve this equation for a continuous field, this equation is discretised in time and space. Most CFD models – including *Code_Saturne* – solve the equation of advection-diffusion for scalars, in addition to Navier-Stokes equations, and thus enter in the category of Eulerian models for dispersion. These models provide a complete temporal and spatial description of the meteorology as well as pollutant transportation within the domain. Moreover, as they directly solve the Navier-Stokes equations with only a few approximations, including turbulence modelling, outputs of CFD models are more physically realistic than box or Gaussian plume models. Furthermore, CFD allows to precisely represent the buildings and to simulate the wind field, turbulence, and temperature over complex terrain. Consequently, there is a growing consensus for using CFD models in atmospheric dispersion modelling at local scale (Robins, 2003; Holmes and Morawska, 2006; Blocken et al., 2013). In order to homogenize the results of studies using CFD for dispersion modelling, especially for regulatory purposes, best practices guidelines have been proposed (Franke et al., 2011; Blocken, 2015).

The counterpart of CFD modelling is the computational cost. Indeed, the finer the resolution is, the longer is the computation. Similar to wind resource assessment, the development of computational capacities allows to use CFD models for many dispersion modelling studies. The same limitations hold, and methodologies have been developed to assess air quality with CFD models during long time periods (Parra et al., 2010). Here

again, one of the major issues related to the use of CFD models is the sensitivity to several input parameters, and especially BC (Lateb et al., 2016). Both Eulerian and Lagragian models are available in the atmospheric module of *Code_Saturne*(Bahlali, 2018; Bahlali et al., 2018). In the present study, we use the Eulerian model only and we aim at improving the knowledge of the BC through DA.

One should note that the evolution of pollutants might also include chemical reactions. The dispersion models presented above do not include such phenomena and supplementary models can be used to take them into account (e.g., Polyphemus, Mallet et al., 2007). In the present work, and especially in Chapter 6, we consider inert tracer gases which are only transported by the flow and are not affected by chemical reactions.

Chapter 2

Introduction to data assimilation

Contents

Introduction

Many potential wind farms and built environments are equipped with instruments measuring meteorological variables (wind, turbulence, temperature, etc.) or pollutant concentration. Most of the time, these observation networks do not provide a satisfactory spatial and temporal coverage: they are either permanent but sparse in space or spatially dense but over a short period of time. Moreover, the complex geometrical features of the studied sites might perturb the observations, thus complicating their exploitation. Despite these difficulties, measurements available within the domains of interest represent a great source of information in addition to mesoscale and computational fluid dynamics (CFD) models. In this chapter, we first present the available measurement data for wind resource assessment and dispersion modelling in terms of location, measured variables, and frequency. In the subsequent sections, we introduce the mathematical formalism of data assimilation (DA) and present the main DA methods developed so far. Eventually, we review the application of DA in the context of CFD atmospheric simulations at local scale.

2.1 Available observations

2.1.1 Observations in candidate sites for wind power

As mentioned in Section 1.3, the sites prospected for the installation of wind farms are generally equipped with one or more meteorological (or met) masts which provide wind and turbulence observations at local scale (see Fig. 2.1). The met masts – or towers – are generally between 50m and 120m high, depending on the topography and the vegetation nearby. Instruments are installed at various levels above the ground, one of which, if possible, corresponds to the hub height (between 25m and 100m).

Since the wind speed is faster over the crests, the wind turbines – and thus the met masts – are generally installed on crests and usually equipped with:

- anemometers that measure wind speed. Cup anemometers are historically used to measure horizontal wind speed ($\sqrt{u^2+v^2}$, where u and v are the two velocity components in the horizontal plane). New technologies of sonic anemometers are

now available, which provide localized but very frequent observations of the three velocity components.

- wind vanes are used in combination with cup anemometers to measure the horizontal wind direction.
- pressure, temperature, and relative humidity sensors are sometimes installed on meteorological masts as well.

While traditional met masts have the advantage to be well understood and thus benefit from broad acceptance and confidence for industrials and financiers, they are less convenient to install and maintain. Indeed, met masts often require siting permits which are long to obtain and ideally they should be maintained during at least one year to obtain sufficiently long observed time series. Moreover, they supply very local information about the wind field.

(a) Meteorological mast equipped with anemometers and wind vanes.

(b) Sound Detection And Ranging (SODAR) in hilly terrain.

Figure 2.1: Examples of instruments observing wind and usually installed in the context of wind resource assessment

In the two last decades, remote sensing technologies have been strongly promoted in the wind energy community since they better characterize the spatial wind variability across a site (Clifton et al., 2013). These technologies allow to remotely measure wind speed and direction, using instruments installed on the ground or mounted on airplanes

or satellites. For wind resource assessment, both Light Detection And Ranging (LIDAR) and SODAR technologies are increasingly used (Antoniou et al., 2003; Bingöl et al., 2009). These two instruments are based on Doppler effect: a LIDAR emits pulsed laser light while a SODAR uses sound waves to measure the wind speed. Recently, a new technology named Wind Scanner has been developed to combine several LIDAR in order to synchronously scan the different wind velocity components in every point (Mikkelsen et al., 2008).

While anemometers provide localized, but frequent, observation data, LIDAR and SODAR generally have a greater spatial coverage sampled at a lower frequency. Indeed, remote sensing devices are able to measure wind speed up to 200m above the ground, which is a significant advantage since turbines grow taller. In addition to this better vertical coverage, remote sensing instruments also measure across the full rotor sweep. Such instruments thus provide a much richer data set than met masts. Moreover, remote sensing technologies are relatively easy to deploy leading to lower installation costs compared to met masts, which compensates for higher purchase prices. However, up to present, low confidence is granted to measurements provided by remote sensing technologies and met masts remain the preferred solution for wind resource assessment.

Both met masts and remote sensing instruments provide partial representations of the wind field over regions where wind farms could be installed, that are valuable for wind resource assessment.

2.1.2 Observations in built environment

Measurements have been essential in the development of dispersion models. The observations might come from full-scale field measurements as well as wind tunnels (Robins, 2003; Xia et al., 2014; Lateb et al., 2016). As explained in Section 1.4, meteorological fields represent a critical input for dispersion modelling. As a matter of fact, both wind measurements and pollutant concentration data are useful for atmospheric dispersion studies. During past decades, advances in technologies have provided scientists with more accurate and cheaper instrumentation as well as improved methodologies to store and process the available data (Grimmond, 2006).

Most urban areas do not satisfy the World Meteorological Organization (WMO) requirements for site selection (Jarraud, 2008) due to the presence of buildings which might disturb or obstruct the air flow. New guidelines for meteorological observation, specific to urban areas, have thus been proposed (Oke, 2007). A review of urban meteorological networks is proposed in Muller et al. (2013), who highlight the fact that most small-scale sensor networks are installed in the context of short-term research and are rarely maintained after the end of the projects. Consequently, the measurement data are only available over short periods of time.

If several cities now dispose of a network of air quality monitoring, these networks are usually too coarse to capture the high spatial and temporal variability of pollution within

cities. For instance, in Paris, approximately 70 measurement stations are operated by Airparif over a region extending up to 100km from Paris center. Since the variations of air quality might occur at scales of a few meters, one can understand that this network, though essential, is not fine enough. Similarly, other Official Air Quality Monitoring Associations (AASQA) maintain measurement networks in several urban areas in France.

In addition to these permanent networks, some dedicated field campaigns have been performed in different regions and provide highly dense spatial coverage, either within actual cities (e.g., Moltchanov et al., 2015) or in reconstituted urban areas (Biltoft, 2001; Hanna et al., 2012). Data provided by field campaigns are very valuable for model calibration and methods testing.

In built environment, both meteorological and pollutant concentration observations are available within the urban canopy, and sometimes above. These data provide information about the state of the atmospheric boundary layer (ABL) and the air quality that could be used to improve atmospheric simulations and dispersion modelling.

2.2 Data assimilation problem, definitions, and notation

The goal of DA is to improve the estimate of some control variables using all available information. The control variables can include the state of a system or some model parameters for which an *a priori* value is known, called *background*. The information that is optimally combined by DA generally includes the background, the available observations, the physical model, etc.

In what follows, the control vector of size l – which can correspond to initial conditions (IC), boundary conditions (BC), model parameters, etc. – will be referred to as $\mathbf{z}$, and its first estimate or background is $\mathbf{z}^{\mathrm{b}}$. The departure of the background from the true value of the control vector corresponds to the background error ϵ^{b}:

$$\epsilon^{\mathrm{b}} = \mathbf{z}^{\mathrm{b}} - \mathbf{z}^{\mathrm{t}}, \tag{2.1}$$

where the superscript 't' refers to the (unknown) truth. The background error is assumed unbiased and only the random component of the error is considered here. The background error covariance matrix $\mathbf{B}$ at time k is then defined by

$$[\mathbf{B}_k]_{ij} = \mathbb{E}\left[[\epsilon^{\mathrm{b}}]_i [\epsilon^{\mathrm{b}}]_j\right], \tag{2.2}$$

where $\mathbb{E}$ represents the expectation operator. This matrix of $\mathbb{R}^{m\times m}$ is symmetric and positive semi-definite by construction.

The control vector at time k ($\mathbf{z}_k$) is related to the system state $\mathbf{x}_k$ of size n by a model $\mathcal{M}_k$ which may be nonlinear and vary in time:

$$\mathbf{x}_k = \mathcal{M}_k(\mathbf{z}_k). \tag{2.3}$$

This model is usually assumed perfect, though recent studies take the model errors into account (e.g., Trémolet, 2006; Sakov et al., 2018).

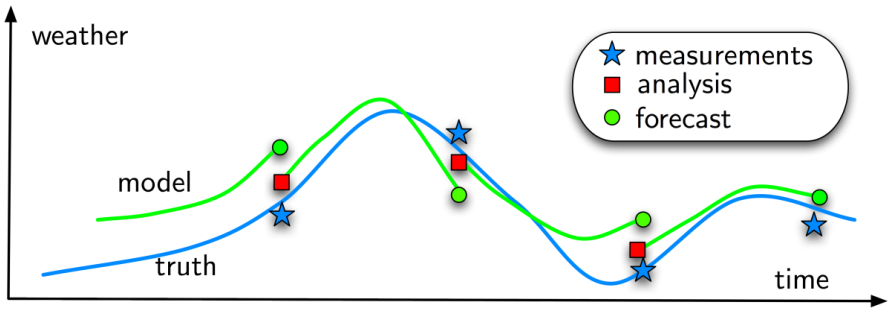

Figure 2.2: Example of DA process when the control vector corresponds to the IC: the analysis optimally combines the pieces of information provided by the background and the observations. The state of the system obtained from the numerical integration of the model, initialised with the analysis IC is the background of the next analysis cycle (source: Naratip Santitissadeekorn).

An observation operator $\mathcal{H}_k$, which may also be nonlinear and vary in time, projects the state's space into the observation's space. The available observations at t_k ($\mathbf{y}_k$) are related to the true state of the control vector by

$$\mathbf{y}_k = \mathcal{H}_k(\mathbf{x}_k^{\mathrm{t}}) + \epsilon_k^{\mathrm{o}}, \tag{2.4}$$

where the vector of available observations is of size p and ϵ_k^{o} is the observation error. The observation error includes the instrumental errors, induced by the measurement process, and the representativeness errors, due to the fact that $\mathbf{x}_k$ is a discrete representation of the system state. The observation error is also assumed unbiased and the observation error covariance matrix is defined in $\mathbb{R}^{p\times p}$ by

$$[\mathbf{R}_k]_{ij} = \mathbb{E}\left[[\epsilon^{\mathrm{o}}]_i[\epsilon^{\mathrm{o}}]_j\right]. \tag{2.5}$$

This matrix contains information about the uncertainty of the observations and possible correlations between errors. In practice, $\mathbf{R}$ is often diagonal – thus assuming uncorrelated observation errors – and constant in time.

Given the background and the observations, characterized by the background and observation error covariance matrices, DA seeks to optimally combine these two sources of information, from a mathematical perspective (Fig. 2.2).

2.3 Nudging methods

One of the first and most basic DA method is *nudging*, which consists in adding a relaxation term to the dynamical equations (e.g., Section 5.2.2 of Kalnay (2003), Chapter 4 of Asch et al. (2016)). The relaxation, or feedback term is proportional to the distance between the observations and the projection of the system state onto the observation space:

$$\mathbf{x}_k = \mathcal{M}_k(\mathbf{z}_k) + \mathbf{K}_k\left[\mathbf{y}_k - \mathcal{H}_k \circ \mathcal{M}_k(\mathbf{z}_k)\right], \tag{2.6}$$

where $\mathbf{K}_k$ is a gain matrix to be determined. An improvement of this method has been recently developed: the back and forth nudging (BFN) algorithm which consists of consecutive iterations of forward and backward integrations with nudging (Auroux and Blum, 2005, 2008; Auroux et al., 2013). The BFN algorithm has been tested and proved to converge on simple models where the control variables are the IC (Auroux and Blum, 2008; Auroux et al., 2011; Auroux and Nodet, 2012). More details about the BFN algorithm will be given in Section 3.2.

2.4 Variational methods

Apart from nudging, DA techniques developed so far and operationally implemented are generally divided into two classes: statistical (or filtering) methods and variational methods. Filtering methods seek to minimise the analysis error variance while variational methods aim at minimising a constrained cost function. In what follows, we present the variational approach, based on optimal control theory.

The cost function which is minimised by the variational methods, such as 3D-Var or 4D-Var (e.g. Kalnay, 2003; Asch et al., 2016), measures misfit of the state's vector to the available data (e.g., the departure of the control variable from the background estimate and from the observations). We present in what follows the Bayesian derivation of the 3D-Var cost function.

2.4.1 Bayesian derivation of the cost function

DA might be formulated in a Bayesian framework, giving – in some sense – a consistent theoretical answer to DA theory. Since 3D-Var performs analysis at a given time step and for the sake of simplicity, we omit the subscript k referring to the time step in this section.

In the Bayesian framework, the goal of variational methods is to maximise the probability density function (pdf) – or likelihood – of the control vector, conditional to some observations:

$$p(\mathbf{z}|\mathbf{y}). \tag{2.7}$$

To express the filtering or smoothing pdf in terms of known variables, the control vector is assumed to follow a Gaussian distribution with mean $\mathbf{z}^{\mathrm{b}}$ and the background error covariance matrix is $\mathbf{B}$:

$$p(\mathbf{z}) = n\left(\mathbf{z}|\mathbf{z}^{\mathrm{b}}, \mathbf{B}\right), \tag{2.8}$$

where $n(\mathbf{a}|\overline{\mathbf{a}}, \mathbf{A})$ is the normal distribution centred on $\overline{\mathbf{a}}$ with covariance matrix $\mathbf{A}$.

As mentioned above, the model is often assumed perfect and this assumption holds in all the present work. We thus deduce the pdf of $\mathbf{x}$ conditional to $\mathbf{z}$:

$$p(\mathbf{x}|\mathbf{z}) = \delta\left[\mathbf{x} - \mathcal{M}(\mathbf{z})\right], \tag{2.9}$$

where δ is the Dirac distribution defined here in $\mathbb{R}^n$.

Given the state of the system, $\mathbf{x}$, the observations are also assumed to follow a Gaussian distribution:

$$p(\mathbf{y}|\mathbf{x}) = n\left(\mathbf{y} - \mathcal{H}(\mathbf{x})|0, \mathbf{R}\right). \tag{2.10}$$

Bayes' rule describes the likelihood of an event A, conditional to another event B and is stated mathematically as follows:

$$p(A|B) = \frac{p(B|A)p(A)}{p(B)}. \tag{2.11}$$

Using Bayes' rule and equation (2.9), the pdf of $\mathbf{z}$ conditional to $\mathbf{y}$ reads

$$\begin{aligned} p(\mathbf{z}|\mathbf{y}) &\propto p(\mathbf{y}|\mathbf{z})p(\mathbf{z}) \\ &\propto p\left(\mathbf{y}|\mathbf{x} = \mathcal{M}(\mathbf{z})\right) p(\mathbf{z}). \end{aligned} \tag{2.12}$$

A cost function can be derived from this pdf, satisfying:

$$p(\mathbf{z}|\mathbf{y}) \propto \exp\left(-\mathcal{J}(\mathbf{z})\right). \tag{2.13}$$

The assumption of Gaussian distributions (Eq. 2.8 and 2.10), combined with the equation (2.12), gives the expression of the cost function, written in the control space:

$$\mathcal{J}(\mathbf{z}) = \frac{1}{2}\|\mathbf{z} - \mathbf{z}^{\mathrm{b}}\|^2_{\mathbf{B}^{-1}} + \frac{1}{2}\|\mathbf{y} - \mathcal{F}(\mathbf{z})\|^2_{\mathbf{R}^{-1}}, \tag{2.14}$$

where we use the notation $\|\mathbf{x}\|^2_{\mathbf{A}} = \mathbf{x}^{\mathrm{T}}\mathbf{A}\mathbf{x}$ and $\mathcal{F} = \mathcal{H} \circ \mathcal{M}$ is the forward operator.

2.4.2 3D-Var

3D-Var algorithm corresponds to the minimisation of the cost function $\mathcal{J}$ given by Equation (2.14). As mentioned above, 3D-Var is used when the observations are available at the same time than the system state given by $\mathcal{M}(\mathbf{z})$. Note that in the case where $\mathbf{z}$ corresponds to the IC, the model $\mathcal{M}$ coincides with identity and the forward operator is simply equal to the observation operator.

If the forward operator is linearised in the vicinity of $\mathbf{z}$, to obtain the matrix $\mathbf{F}$ (which depends on $\mathbf{z}$ if $\mathcal{F}$ is nonlinear), the gradient of the cost function reads

$$\nabla\mathcal{J}(\mathbf{z}) = \mathbf{B}^{-1}(\mathbf{z} - \mathbf{z}^{\mathrm{b}}) - \mathbf{F}^{\mathrm{T}}\mathbf{R}^{-1}\left(\mathbf{y} - \mathcal{F}(\mathbf{z})\right). \tag{2.15}$$

In the case where $\mathcal{F}$ is linear, the cost function is convex and thus admits a minimum reached for $\mathbf{z}^{\mathrm{a}}$ such that $\nabla\mathcal{J}\left(\mathbf{x}^{\mathrm{a}}\right) = 0$. The estimate of the control vector that minimises the cost function corresponds to the optimal control vector and is called the *analysis*. All the variables related to the analysis are referred to with the superscript 'a' in what follows. The 3D-Var analysis in a linear case is given by

$$\mathbf{z}^{\mathrm{a}} = \mathbf{z}^{\mathrm{b}} + \left(\mathbf{B} + \mathbf{F}^{\mathrm{T}}\mathbf{R}^{-1}\mathbf{F}\right)^{-1}\mathbf{F}^{\mathrm{T}}\mathbf{R}^{-1}\left(\mathbf{y} - \mathcal{F}(\mathbf{z}^{\mathrm{b}})\right) \tag{2.16}$$

and is equivalent to the Best Linear Unbiased Estimator (BLUE) which is derived from a statistical approach. The analysis error covariance matrix is then equal to the inverse of the Hessian of the quadratic cost function, $\mathbb{H}$:

$$\mathbb{H}^{-1} = \left(\mathbf{B}^{-1} + \mathbf{F}^{\mathrm{T}}\mathbf{R}^{-1}\mathbf{F}\right)^{-1}. \tag{2.17}$$

When the control variables are the IC, the analysis state $\mathbf{z}^{\mathrm{a}}$ can be propagated in time by the model to give a first estimate for the next analysis cycle (see Fig. 2.2). Similarly, the analysis error covariance matrix calculated at the end of an analysis provides an estimate of the background error covariance matrix for the next cycle.

2.4.3 4D-Var

The difference between 3D- and 4D-Var comes from the length of the data assimilation window (DAW): 3D-Var assimilates observation at only one time step – and thus looks for the optimal value of the control vector at this unique time – whereas 4D-Var takes into account observations from a whole DAW – and seeks the trajectory of several values of the control vector that best fits the background and these observations.

Let us assume that observations are available between times $t = 0$ and $t = L$: $\{\mathbf{y}_l\}_{l=0\ldots L}$. The *filtering* pdf is defined as the pdf of the control vector at the end of the DAW ($\mathbf{z}_L$), conditional to past observations:

$$p(\mathbf{z}_L|\mathbf{y}_0, \ldots, \mathbf{y}_L). \tag{2.18}$$

The *smoothing* pdf is the pdf of the control vector at any intermediate time k conditional to past and future observations:

$$p(\mathbf{z}_k|\mathbf{y}_0, \ldots, \mathbf{y}_L), \tag{2.19}$$

for any $0 \leq k \leq L$. Smoothing might also be performed over the whole DAW, leading to the smoothing pdf

$$p(\mathbf{z}_0, \ldots, \mathbf{x}_L|\mathbf{y}_0, \ldots, \mathbf{y}_L). \tag{2.20}$$

Following a similar derivation as for 3D-Var, the 4D-Var cost function related to the smoothing pdf (2.19) reads

$$\mathcal{J}(\mathbf{z}_k) = \frac{1}{2}\|\mathbf{z}_k - \mathbf{z}_k^{\mathrm{b}}\|^2_{\mathbf{B}_k^{-1}} + \frac{1}{2}\sum_{l=0}^{L}\|\mathbf{y}_l - \mathcal{F}_l(\mathbf{z}_k)\|^2_{\mathbf{R}_l^{-1}}, \tag{2.21}$$

where $\mathcal{F}_l = \mathcal{H}_l \circ \mathcal{M}_{k:l}$ with $\mathcal{M}_{k:l}$ the model propagating the control vector at time k to the system' state at time l.

Once again, linearising the forward operator $\mathcal{F}_l$ in the vicinity of $\mathbf{z}_k$ to obtain the matrix $\mathbf{F}_l$, the gradient of the cost function is given by

$$\nabla\mathcal{J}(\mathbf{z}_k) = \mathbf{B}_k^{-1}(\mathbf{z}_k - \mathbf{z}_k^{\mathrm{b}}) - \sum_{l=0}^{L}\mathbf{F}_l^{\mathrm{T}}\mathbf{R}_l^{-1}\left(\mathbf{y}_l - \mathcal{F}_l(\mathbf{z}_k)\right). \tag{2.22}$$

The inverse of the Hessian of the cost function reads:

$$\mathbb{H}^{-1} = \left(\mathbf{B}_k^{-1} + \sum_{l=0}^{L} \mathbf{F}_l^{\mathrm{T}} \mathbf{R}_l^{-1} \mathbf{F}_l \right)^{-1} . \tag{2.23}$$

If the forward operator is linear, the minimisation of the cost function is a quadratic problem which is solved by

$$\mathbf{z}_k^{\mathrm{a}} = \mathbf{z}_k^{\mathrm{b}} - \mathbb{H}^{-1} \nabla \mathcal{J}(\mathbf{z}_k). \tag{2.24}$$

In such a linear case, the statistical equivalent to 4D-Var is the Kalman filter (Kalman, 1960) which consists in a succession of BLUE analyses.

2.4.4 Minimization of the variational cost function

When the forward operator is not linear, the cost function in 3D-Var or 4D-Var algorithm is numerically minimised, usually with a descent-based optimization method. Such method require the estimation of the cost-function gradient, which corresponds to the derivative of the cost function relative to an arbitrary perturbation. Once the gradient is estimated, it is used to identify a direction that leads to lower cost.

The simplest method to estimate the gradient is based on finite differences, which is easy to implement and does not depend on the dynamical model. For instance, the ADAO module of the SALOME open-source platform (http://www.salome-platform.org) offers the possibility to run 3D-Var with a finite-difference approximation of the gradient. However, since the gradient must be calculated in all possible perturbation directions, finite-increment methods are inefficient if the size of the control vector is large. Indeed, the finite-difference approximation requires as many model integrations as control variables (or twice for central differences).

A less expensive way to estimate the gradient of the cost-function is the adjoint approach. The linearisation of the forward operator, introduced in equations (2.15) and (2.22), corresponds to the tangent linear model of the forward operator ($\mathbf{F}_k$), defined as follows:

$$\delta \mathbf{y}_k = \mathbf{F}_k \delta \mathbf{z}_k = \frac{\partial \mathcal{F}}{\partial \mathbf{z}}|_{\mathbf{z}_k} \delta \mathbf{z}_k. \tag{2.25}$$

The adjoint of the linear operator $\mathbf{F}$ is the linear operator $\mathbf{F}^\star$ such that, for any $\mathbf{z}_1$, $\mathbf{z}_2$,

$$< \mathbf{F}\mathbf{z}_1, \mathbf{z}_2 > = < \mathbf{z}_1, \mathbf{F}^\star \mathbf{z}_2 >, \tag{2.26}$$

where $<,>$ represents the inner product. For the inner product in the Euclidean space, the adjoint model is equal to the transpose of the tangent linear:

$$\mathbf{F}^\star = \mathbf{F}^{\mathrm{T}}, \tag{2.27}$$

which is the case in the derivation of the gradient of the cost function in Equations (2.15) and (2.22). Consequently, running the adjoint model backward in time allows to explicitly

calculate the gradient of the cost function with respect to any variable (Le Dimet and Talagrand, 1986).

While the adjoint approach is relatively efficient (it only requires one integration of the adjoint model), it involves the derivation and maintenance of the tangent linear and the adjoint of the forward operator. Consequently, if these two operators are not available – which is generally the case for CFD models – and the control vector is too large to consider finite difference gradient estimation, variational methods are not appropriate.

2.5 Ensemble variational methods

Variational methods, such as 3D-Var or 4D-Var, have many advantages. By construction, 4D-Var seeks a trajectory that best fits all the observations available within the DAW and is thus able to assimilate asynchronous observations. Variational methods can also handle fully nonlinear analysis. However, we have previously highlighted that they require the use of the tangent linear and adjoint models which are very expensive in terms of working force. Each evolution of the direct model must be equivalently reported in the adjoint model, such that the development and maintenance of adjoint models require as many developers as direct models.

In the case where the observation operator is linear, 3D-Var is equivalent to the optimal interpolation, which is a filtering method. If the model is also linear, 4D-Var is equivalent to the Kalman filter at the end of the DAW and to the Kalman smoother (Cohn et al., 1994) otherwise. These statistical methods also have advantages and especially since the development of ensemble-based methods. The ensemble Kalman filter (EnKF) has been first proposed by Evensen (1994) and consists in representing the error statistics by an ensemble of N different estimations of the control vectors. As a result, the error statistics are dynamically propagated by the model. Similarly, the ensemble Kalman smoother (EnKS) has been proposed by Evensen et al. (2000) for smoothing problems. The ensemble subspace corresponds to all the vectors $\mathbf{z}$ of the form:

$$\mathbf{z} = \mathbf{z}^{\mathrm{b}} + \mathbf{A}\mathbf{w}, \tag{2.28}$$

where $\mathbf{A}$ is the matrix of anomalies, defined as the departure of each ensemble member from the ensemble mean – which is equal to $\mathbf{z}^{\mathrm{b}}$ – and $\mathbf{w}$ is a vector of coefficients of size N. While variational methods use a full-rank representation of all errors – since they deal with the full error covariance matrices – the counterpart of ensemble-based methods is that the errors are only partially represented. Indeed, the size of the ensemble, used to represent the error statistics, is generally smaller than the size of the control space, leading to rank-deficiency. Consequently, only the leading modes of the error covariance matrices are taken into account and the analysis is restricted to the subspace spanned by these few modes.

The comparative studies between variational and ensemble methods have not shown significant differences for synoptical meteorology (e.g., Lorenc, 2003; Kalnay et al., 2007;

Yang et al., 2009). In fact, the EnKF slightly outperforms 4D-Var for small DAW because the error estimates dynamically evolve with EnKF analyses. However, for longer DAW, the evolution is less linear and 4D-Var gives better results than the EnKF (Bocquet and Sakov, 2013).

Recently, ensemble variational methods have been developed, combining the advantages of both variational and ensemble-based methods. A comprehensive review of the ensemble variational methods can be found in Chapter 7 of Asch et al. (2016) and we qualitatively present here the main idea of these methods.

Hybrid methods

Hybrid methods combine existing methods by running simultaneously two methods – one statistical and one variational – and exchanging information between them, especially regarding the error statistics. Consequently, it is mainly the error covariances that are hybridized: one part is static as in 3D- or 4D-Var, and the other part comes from an ensemble method such as the EnKF. One example of hybrid EnKF-3D-Var has been introduced by Hamill et al. (2000). These methods avoid the rank-deficiency of the EnKF, mentioned above, and still allow a dynamical evolution of the errors, yet they require the development of two DA methods.

Ensemble of variational data assimilation

Ensemble of variational data assimilation (EDA) – or EnsVar – consists in running several occurrences of a same variational method (e.g. 4D-Var) while perturbing the model, the observations, and/or some model inputs that are not included in the control variables. This method is the variational counterpart of the stochastic EnKF. The EDA provides an ensemble of analyses from which flow-dependent error statistics can be estimated. These ensembles can also be used to initialize the following analysis cycles or ensemble predictions. EDA has been proved to be a successful deterministic and probabilistic estimator in linear and nonlinear conditions with the Lorenz-90 chaotic model (Jardak and Talagrand, 2018a,b). EDA methods have been operationally implemented in NWP centers with 3D- and 4D-Var (Buehner et al., 2010b,a). For instance, Météo-France (Berre et al., 2015) and the European Center for Medium-range Weather Forecasts (ECMWF) (Bonavita et al., 2011, 2012) have setup an EDA system with their already available 4D-Var algorithm, in order to incorporate flow dependence of the errors. Consequently, EDA systems overcome one of the two major limitations of variational methods. The second limitation is the necessity to derive and maintain the tangent linear and the adjoint. Since EDA systems are based on 4D-Var, they do not overcome this issue.

4DEnVar

Some ensemble-based methods, such as the EnKF, do not require the tangent linear of the observation operator as all the coefficients involving the tangent linear are estimated from the ensemble. Similarly, the sensitivities of the simulated values within the DAW to the control variables can be estimated using the ensemble (Liu et al., 2008). As a consequence, the variational optimisation of 4D-Var can be performed in the ensemble subspace defined by Equation (2.28) and thus avoid the use of the model adjoint. The 4DEnVar is based on such a preconditioning for the minimisation. An ensemble of initial perturbations is propagated within the DAW and the adjoint is estimated as the transpose of the matrix that represents the effect of the direct model in the ensemble subspace. This DA method has been operationally implemented at Environment and Climate Change Canada (Buehner et al., 2015).

The iterative ensemble Kalman smoother

The iterative ensemble Kalman smoother (IEnKS) is a four dimensional ensemble variational method heuristically derived from Bayes' rule (Bocquet and Sakov, 2014). It is an extension of the iterative ensemble Kalman filter (IEnKF) (Sakov et al., 2012) to assimilate asynchronous observations. Both the IEnKF and IEnKS are mathematically justified, which is not always the case of the previously mentioned ensemble variational methods that have been developed for operational purposes. The rigorous mathematical justification ensures that the approximations and limitations of the methods are well understood at a theoretical level. The IEnKS is based on the iterative minimisation, for instance using Gauss-Newton algorithm, of a cost function defined in the ensemble subspace. It allows both to propagate the errors thanks to the ensemble and to perform a 4D-variational analysis. By construction, it thus outperforms the EnKF, the EnKS, and 4D-Var, which has been verified on several models (Bocquet and Sakov, 2013, 2014; Haussaire and Bocquet, 2016). Moreover, the IEnKS can easily be parallelized. More details about the derivation of the IEnKS will be given in Section 3.3.

2.6 Data assimilation for CFD atmospheric simulations at local scale

Up to now, DA methods have generally been developed in the framework of large scale meteorology (e.g., Kalnay, 2003; Asch et al., 2016). Since large scale simulations are largely influenced by IC, DA methods are mostly used to improve the accuracy of this model input. We have highlighted in Section 1.2.5 that local scale atmospheric simulations are mainly determined by BC which are generally provided by larger scale models (see Section 1.2.6) and thus might lack accuracy. In order to broaden the field of application of DA to micrometeorology, the existing methods must be adapted to take BC into

account. To make it simple, this comes to invert space and time: existing DA methods are already able to propagate information back in time, while for micrometeorology we would like to propagate information 'back in space'.

In DA literature, BC are rarely considered as control variables. In the field of wind resource assessment, several studies have combined information from CFD models and field measurements, though not using DA methods. For instance, in Tang et al. (2019) the results of CFD simulations are used to infer statistical relations for wind speed and direction between different locations. The on-site measurement data then provide dynamical corrections to the reference solutions obtained from CFD simulations. Song et al. (2014) have used the measurement from a single *in situ* anemometer to estimate the boundary velocity that produces a flow field, simulated with a CFD model, the most in agreement with the observation. This method requires the preliminary CFD computation – and storage – of flow field with several possible values of inflow velocity. Moreover the BC are defined by a unique value of velocity in this study. Similarly, Yan and Li (2016) validate CFD simulations with on-site measurements and then combine the CFD results for several wind directions with statistical meteorological data to produce a regional wind map.

Recently, some aeronautic studies have applied DA methods with CFD simulations to estimate some inflow parameters (Misaka et al., 2008; Kato et al., 2015). In other CFD studies, simple nudging has been used for downscaling from mesoscale to microscale atmospheric models (Zajaczkowski et al., 2011; Duraisamy et al., 2014), though differences in resolution between the models might be problematic. More recently, Mons et al. (2017) and Sousa et al. (2018) have used ensemble-based DA methods to estimate the incoming wind direction and velocity used as inputs for CFD simulations, including only two variables in the control vector.

In the present work, we propose to describe the BC with several vertical profiles of velocity and turbulence, which correspond to hundreds of control variables. We thus use DA to enhance the accuracy of CFD atmospheric simulations at local scale through the correction of a large control vector of BC. In order to do so, and in light of the above, we have selected both the BFN algorithm and the IEnKS to be adapted to microscale atmospheric simulations.

Chapter 3

Data assimilation methods adapted to local-scale atmospheric simulations

Contents

3.1 Introduction

In the context of local-scale atmospheric simulations with computational fluid dynamics (CFD) models for operational purposes, several constraints limit the choice of data

assimilation (DA) method. First, the adjoint model is rarely available for CFD models, and in particular for the atmospheric module of *Code_Saturne*. Moreover, the DA method must be adapted to parallel computation and to nonlinear systems. Since both the back and forth nudging (BFN) algorithm and the iterative ensemble Kalman smoother (IEnKS) seem to fulfil these conditions they have been chosen here to perform DA with the atmospheric module of *Code_Saturne* at local scale. In the present chapter, we give the theoretical derivation of these two methods, adapted to include, as control variables, the boundary conditions (BC) prescribed at the limits of the CFD domain. We also briefly present how 3D-Var is used in the present work as a reference method for comparison purposes. We recall that we consider the DA problem defined by

- a control vector $\mathbf{z} \in \mathbb{R}^l$ corresponding to the BC,
- a background $\mathbf{z}^{\mathrm{b}} \in \mathbb{R}^l$,
- a vector of available observations $\mathbf{y} \in \mathbb{R}^p$,
- a forward operator $\mathcal{F} = \mathcal{H} \circ \mathcal{M}$ which combines the model $\mathcal{M} : \mathbb{R}^l \mapsto \mathbb{R}^n$, where $\mathbf{x} = \mathcal{M}(\mathbf{z}) \in \mathbb{R}^n$ is the system state, and the observation operator $\mathcal{H} : \mathbb{R}^n \mapsto \mathbb{R}^p$.

The three methods described in the following sections are *a priori* appropriate to solve this problem.

3.2 Back and forth nudging algorithm

3.2.1 Description of the method

The BFN algorithm has been developed by Auroux and Blum (2005, 2008) as an evolution of the simple nudging (see Section 2.3). This algorithm has been tested and proved to converge on simple cases of shallow water model (Auroux, 2008), diffusion (Auroux et al., 2011), and transport (Auroux and Nodet, 2012) when the control variables correspond to initial conditions (IC). In the present section, we give a derivation of the BFN, adapted to take BC into account. To perform this derivation, we consider a simple model which solves the 1D shallow-water equations (SWE) (see Eq. 1.18).

The relaxation term added to the dynamical equations in the nudging algorithm, is proportional to the distance between the observations and the projection of the system state into the observation space. The system of SWE thus becomes

$$\frac{\partial \mathbf{X}}{\partial t} + \mathbf{M}\frac{\partial \mathbf{X}}{\partial x} = \mathbf{S} + \mathbf{K}\left[\mathbf{y} - \mathcal{H}(\mathbf{X})\right], \tag{3.1}$$

where $\mathbf{K}$ is a gain matrix.

The BFN algorithm is an iterative algorithm: iterations of forward and backward integrations, both with nudging, are performed over a time period T during which

observations are available. The evolution of the system is governed by the two following equations:

$$\begin{cases} \textbf{(F)} \quad \frac{\partial \mathbf{X}_k^{(\mathrm{f})}}{\partial t} + \mathbf{M}^{(\mathrm{f})} \frac{\partial \mathbf{X}_k^{(\mathrm{f})}}{\partial x} = \mathbf{S} + \mathbf{K}\left[\mathbf{y} - \mathcal{H}(\mathbf{X}_k^{(\mathrm{f})})\right] & \text{for} \quad 0 \leq t \leq T,\ \delta t > 0, \\ \textbf{(B)} \quad \frac{\partial \mathbf{X}_k^{(\mathrm{b})}}{\partial t} + \mathbf{M}^{(\mathrm{b})} \frac{\partial \mathbf{X}_k^{(\mathrm{b})}}{\partial x} = \mathbf{S} - \widetilde{\mathbf{K}}\left[\mathbf{y} - \mathcal{H}(\mathbf{X}_k^{(\mathrm{b})})\right] & \text{for} \quad T \geq t \geq 0,\ \delta t < 0, \end{cases} \tag{3.2}$$

where $\mathbf{K}$ and $\widetilde{\mathbf{K}}$ are gain matrices, the superscripts (f) and (b) refer to forward and backward variables, and the subscript 'k' refers to the index of the BFN iteration (Auroux and Blum, 2005).

For the SWE considered here, we perform the following changes of variables

$$\widetilde{t} = T - t, \tag{3.3a}$$

$$\widetilde{u} = -u, \tag{3.3b}$$

$$\widetilde{\mathbf{X}} = \begin{pmatrix} h \\ \widetilde{u} \end{pmatrix}, \tag{3.3c}$$

$$\widetilde{\mathbf{M}} = \begin{pmatrix} \widetilde{u} & h \\ g & \widetilde{u} \end{pmatrix}. \tag{3.3d}$$

As a result, the backward equation is exactly the same as the forward equation (1.18) where u is formally replaced with $\widetilde{u} = -u$. As a matter of fact, the backward integration is similar to forward integration except that the velocity has to be 'inverted'. With this convention, the time step δt is positive in both forward and backward integrations. Consequently, this implementation of the BFN algorithm has the great advantage that the same solver is used for the forward and backward integrations.

3.2.2 Prescription of boundary conditions in the BFN algorithm

For local-scale simulations, we have seen that the DA methods must be adapted to correct the BC instead of the IC (see Section 1.2.5). Here we use the method of characteristics, presented in Section 1.2.3, to show how BC have to be handled in both forward and backward integrations of the BFN algorithm. The following demonstration is performed in the simple case of unidimensional domain with only two layers of fluid (Fig. 1.4) and neglecting both the Coriolis effect and the friction forces.

The method of characteristics allows to determine the input information that must be prescribed to solve the SWE. In the present study, we consider flows that are subcritical – or fluvial –, meaning that their velocities are smaller than the interface wave velocity. For such flows, the information is propagated downstream and also upstream by the two characteristic curves $\mathcal{C}_+$ and $\mathcal{C}_-$ (Fig. 3.1a). Consequently, for the forward integration of the BFN algorithm, it is necessary to specify a BC on each side of the domain of size L

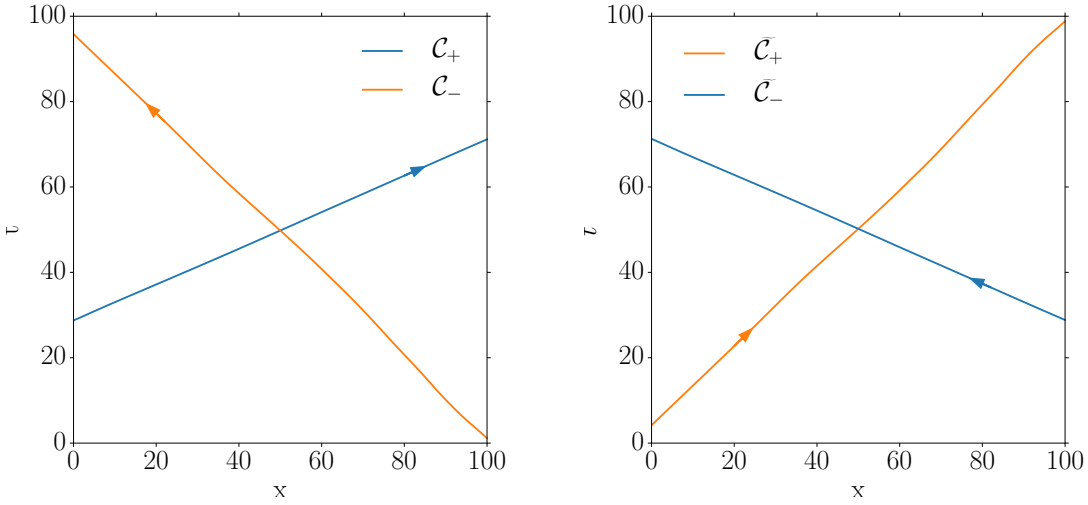

Figure 3.1: Characteristic curves along which the Riemann invariants are conserved in the resolution of the SWE. a) Forward and b) backward integration of the SWE. The blue curves ($\mathcal{C}_+$ and $\widetilde{\mathcal{C}}_-$) transport the same invariant $R_+ = -\widetilde{R}_-$ from the upstream boundary. The orange curves ($\mathcal{C}_-$ and $\widetilde{\mathcal{C}}_+$) transport the same invariant $R_- = -\widetilde{R}_+$ from the downstream boundary. These characteristic curves are computed for a shallow flow over a flat terrain, initially still with a constant inflow prescribed upstream and a constant height downstream.

(e.g., Alcrudo and Garcia-Navarro, 1993). We prescribe here the upstream velocity (u_L on the left of the domain) and the downstream fluid height (h_R on the right).

For the backward integration, we can demonstrate with the method of characteristics that the Riemann invariants $\widetilde{R}_+ = -u + 2\sqrt{gh} = -R_-$ and $\widetilde{R}_- = -u - 2\sqrt{gh} = -R_+$ are conserved along $\widetilde{\mathcal{C}}_+$ and $\widetilde{\mathcal{C}}_-$, respectively defined by

$$\begin{aligned} \widetilde{\mathcal{C}}_+ : \frac{\mathrm{d}x}{\mathrm{d}\widetilde{t}} &= \widetilde{\alpha}_+ = -u + \sqrt{gh}, \\ \widetilde{\mathcal{C}}_- : \frac{\mathrm{d}x}{\mathrm{d}\widetilde{t}} &= \widetilde{\alpha}_- = -u - \sqrt{gh}. \end{aligned} \tag{3.4}$$

The curves $\widetilde{\mathcal{C}}_+$ and $\mathcal{C}_-$ (resp. $\widetilde{\mathcal{C}}_-$ and $\mathcal{C}_+$) are symmetrical with respect to the abscissa axis and they transport the same Riemann invariant (Fig. 3.1).

This demonstration suggests that the BC that is prescribed on the left of the domain in the forward integration (here u_L) must be prescribed on the right in the backward integration (here $\widetilde{u}_\mathrm{R}$). Similarly, the BC prescribed on the right in the forward integration (here h_R) must be prescribed on the left in the backward integration (here h_L). We consider positive values of velocity in the forward integrations, such that the BC that is prescribed on the left of the domain is upstream of the flow. Since the velocity field is inverted between the forward and the backward integrations, the upstream BC is on the

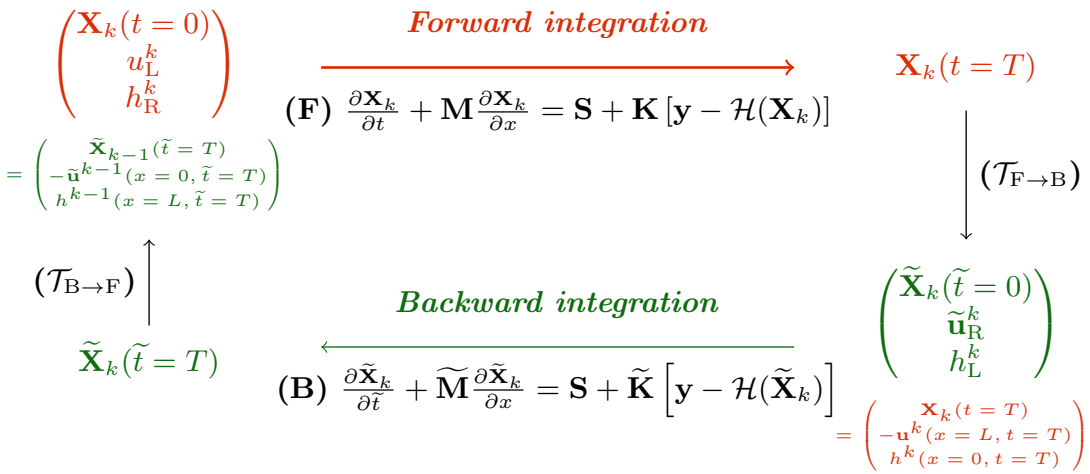

Figure 3.2: Diagram of the k-th iteration of the BFN algorithm. The transformations $(\mathcal{T}_{\mathrm{F}\to\mathrm{B}})$ and $(\mathcal{T}_{\mathrm{B}\to\mathrm{F}})$ shift from forward system to backward system and vice versa. They include a change of variable $\widetilde{t} = T - t$ and an inversion of BC. In the case of SWE, the backward integration is equivalent to performing an integration with positive time steps but with $\widetilde{\mathbf{u}} = -\mathbf{u}$.

right of the domain in the backward integration. Consequently, the velocity is prescribed upstream and the height downstream in both forward and backward integrations.

3.2.3 Updating the boundary conditions with the BFN algoritm

The BC values for the k-th backward integration ($\widetilde{u}_{\mathrm{R}}$ and h_{L}) are given by the system state on the right and left of the domain, respectively, at the end of the k-th forward integration:

$$\widetilde{u}_{\mathrm{R}}^k = -u^k(x = L, t = T), \tag{3.5}$$

$$h_{\mathrm{L}}^k = h^k(x = 0, t = T). \tag{3.6}$$

Similarly, before the $(k+1)$-th forward integration, the BC are updated (and velocity is reversed) according to the state of the system at the end of the k-th backward integration (Fig. 3.2).

At each iteration of BFN – defined as the succession of a forward and a backward integrations – the control variables that are the BC (here u_{L} and h_{R}) are revised. After a sufficient number of BFN iterations, the system converges toward an analysis state, which depends in particular on the nudging matrices. The proof of convergence of the BFN algorithm for the linearized SWE can be found in Appendix B.2. It is important to note that the BFN algorithm does not solve the same problem as 3D-Var or the IEnKS. In fact, the BFN algorithm assimilates several times each observation in order to correct the system state. Except initially, it does not take into account any information on the background statistics of errors. In theory, the analysis state obtained at convergence is

independent of the background state (Auroux and Blum, 2005), whereas 3D-Var and the IEnKS seek an optimal combination of the background *and* observations.

3.2.4 Length of the data assimilation window

During each integration (either forward or backward), a conflict might appear between the prescribed external BC – i.e. the background – and the internal dynamic of the system, modified by the nudging (see Appendix B.1 for more details). Moreover, the shallow layer model used here does not have perfectly transparent boundaries, such that the waves created by the nudging are spuriously reflected. To avoid these two problems, the length of the period of model integration, T, has been chosen equal to the time needed for the nudging information to propagate throughout the domain.

We have determined that the best practice consists in choosing the data assimilation window (DAW) length equal to the time needed for the information coming from the boundary and the nudging to propagate into the whole domain. For instance, let us consider that the nudging is applied on u only, and that there are 5 observations in $x = \{16, 32, 48, 64, 80\}$. The effect of the nudging from the first observation ($x_1 = 16$m) takes $T_1 = \int_{x=x_1}^{x=L} \frac{\mathrm{d}x}{u+\sqrt{g'h}}$ to reach the right boundary. Because nudging is applied at every time step, the characteristic from (x_1, $t = 0$) to ($x = L$, T_1), in dashed, blue in Figure 3.3a, carries the information from all the other observations. Similarly, the information from the 5 observations reach the left boundary in $T_2 = \int_{x=x_2}^{x=L} \frac{\mathrm{d}x}{u-\sqrt{g'h}}$ where $x_2 = 80$m is the abscissa of the rightmost observation. The characteristic carrying upstream the information from all the observations is the dashed, orange line in Figure 3.3a.

The characteristics starting from the points ($x = 0$, T_2) and ($x = L$, T_1), in blue and orange respectively in Figure 3.3a, carry the information from both the observations and the BC. These two characteristics intersect at $t = T$, time after which any point (x, t) of the domain is influenced by all the observations, as well as the prescribed BC. In fact, at least one characteristic passing through (x, t) carries information from all the observations and one BC.

We want the DAW to be long enough to let the information coming from the nudging spanning the whole domain but not too long to avoid mismatch between the prescribed BC (strong constraint) and the forcing produced by the nudging. Consequently, the length of the period of model integration has been chosen equal to the time needed for the nudging information to propagate throughout the domain (T). The iterations of forward and backward integrations are performed over this time period.

We can see in Figure 3.3a that in the experiment described above $T_1 = 1.4$s, $T_2 = 1.6$s, and $T = 2.4$s. The value of 2.4s is verified numerically as shown in Figure 3.3b: it is the DAW for which the BFN converges the most rapidly.

We have verified this method to determine the best DAW length in other configurations: with topography (bump, real profile) and for 1, 2, and 5 observations.

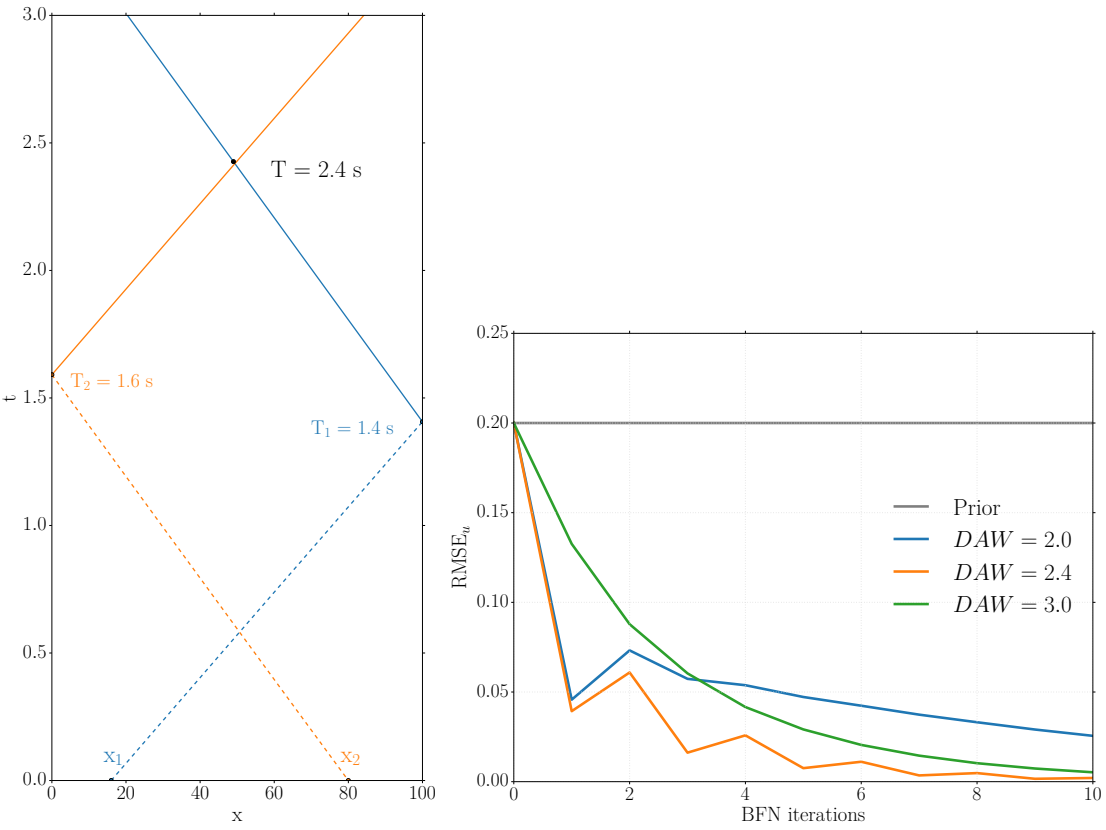

(a) Characteristics transporting nudging information over the domain.

(b) Evolution of the relative RMS error with BFN iterations for different values of the DA window (DAW) in second.

3.2.5 Implementation of the BFN algorithm with *Code_Saturne*

Simple nudging

A nudging algorithm has been implemented in *Code_Saturne* to assimilate observations of any variable simulated by the model (except the pressure): velocity components, turbulence variables (k, ϵ), scalar variables, etc. In order to perform nudging toward a full 3D field – instead of punctual observations – this DA is a two-step process:

1. a first step consists in computing the analysis state given by the Best Linear Unbiased Estimator (BLUE) (see Eq. 2.16)

2. afterwards, the meteorological field simulated by *Code_Saturne* is nudged toward the analysis state obtained at the end of the first step.

This methodology is similar to the 'analysis nudging' available in the Weather Research and Forecasting (WRF) meso-scale model.

For stationary flows, the first step of the method is performed only once, at a time t_0 indicated by the user and the nudging is applied at each subsequent steps. During the spin-up period – defined as the period between the initial time and t_0 – the model is

integrated without nudging. After t_0, nugding is included at every time step and during the whole DAW, whose length is also indicated by the user.

The first step consists in a BLUE analysis, for a different DA problem compared to the one discussed up to present (see the Introduction of the present chapter). The DA problem solved in this first step is the following:

- the control vector corresponds to the system state ($\mathbf{x} \in \mathbb{R}^n$),
- the background is the result of the *Code_Saturne* simulation at time t_0,
- the observation operator is based on the linear interpolation of the simulated field $\mathbf{x}$ in the cell containing the observation to the exact location of the observation.

The background error covariance matrix $\mathbf{B}$ associated with the meteorological field simulated by *Code_Saturne* ($\mathbf{x}$) is very large ($n \times n$). Consequently, it cannot be stored and it is here parametrised by the Cressman function. Each coefficient is thus equal to

$$\mathbf{B}_{i,j} = (1 + r_{i,j}/R)\exp(-r_{i,j}/R), \tag{3.7}$$

where $r_{i,j}$ is the distance between the points i and j and R is the radius of correlation. This radius is specified by the user and may differ in the horizontal and vertical directions.

Back and forth nudging algorithm

The derivation of the BFN algorithm adapted to take the BC into account, presented in Section 3.2.1 is specific to the 1D SWE. However, we keep the same methodology when applied with the full Navier-Stokes equations with *Code_Saturne*. Namely, both the forward and backward integrations are performed with the nudging method explained in the previous section. However, the velocity field is reversed for the backward integrations, i.e., we perform a change of variable $\widetilde{\mathbf{u}} = -\mathbf{u}$ before between each forward and backward integration. The BC are then updated at each BFN iteration, as explained in Section 3.2.3.

The principle of performing the backward integration with the same model as the forward integration, while only reversing the velocity field, has been obtained for the 1D SWE and extended to the Navier-Stokes equations. Theoretically, for the full Navier-Stokes equations it is not equivalent and this assumption could be source of issues. Moreover, we have already highlighted the fact that the BFN algorithm does not solve the same DA problem as 3D-Var and the IEnKS since the background is not taken into account and the observations are assimilated multiple times.

Despite these *a priori* limitations of the BFN algorithm, its relative simplicity, the availability of the nudging algorithm in *Code_Saturne*, as well as its intuitive functioning make this algorithm very attractive. Consequently, the following chapters of this work have tried to evaluate the ability of this method to assimilate *in situ* observations in order to improve the accuracy of local-scale atmospheric simulations with *Code_Saturne*.

3.3 The iterative ensemble Kalman smoother

The IEnKS (Bocquet and Sakov, 2014) is an ensemble variational method of DA. As a variational method, it is based on the minimisation of a cost function and as an ensemble-based method, the analysis error space is spanned by a limited number of vectors: the ensemble members. Since we consider stationary BC and we assume that the model is perfect, there is here no difference between the filtering (IEnKF, Sakov et al., 2012) and smoothing (IEnKS) formulations. Anticipating future applications with unsteady BC, we will consider the smoothing method in what follows, keeping in mind that it is here strictly equivalent to the filtering method. The IEnKS cost function is the same as the one obtained in the derivation of 3D-Var (see Eq. 2.14 in Section 2.4.1), however considered in the ensemble subspace. We give below the derivation of the cost function in the ensemble subspace and its minimisation avoiding the use of the adjoint model.

3.3.1 Derivation of the cost function in the ensemble space

Similarly to the derivation in Sakov et al. (2012) and Bocquet and Sakov (2014), we consider a background ensemble of N members: $\mathbf{E}^{\mathrm{b}} = \left\{\mathbf{z}_{[i]}\right\}_{i=1..N}$, where index $[i]$ refers to the member index in the ensemble. Each member corresponds to a vector of BC.

The background ensemble is centred on the background vector of BC:

$$\mathbf{z}^{\mathrm{b}} = \overline{\mathbf{z}} = \frac{1}{N}\mathbf{E}^{\mathrm{b}}\mathbf{1}, \tag{3.8}$$

where $\mathbf{1}$ is a vector of size N with all components equal to one. The (normalised) anomaly matrix for $\mathbf{z}$ is defined in $\mathbb{R}^{l\times N}$ as the departure of each member from the ensemble mean ($\mathbf{z}^{\mathrm{b}}$):

$$\mathbf{A} = \frac{1}{\sqrt{N-1}}\left[\mathbf{z}_{[1]} - \mathbf{z}^{\mathrm{b}}, \mathbf{z}_{[2]} - \mathbf{z}^{\mathrm{b}}, ..., \mathbf{z}_{[N]} - \mathbf{z}^{\mathrm{b}}\right]. \tag{3.9}$$

The background error covariance matrix is then estimated from the ensemble using the previously defined anomaly matrix:

$$\mathbf{B} = \mathbf{A}\mathbf{A}^{\mathrm{T}}. \tag{3.10}$$

In fact, the spread of the background ensemble around its mean represents the uncertainty of the background.

The ensemble space is smaller than the state space such that it is generally interesting and more efficient to seek a solution to the DA problem in the ensemble space rather than in the state space. The IEnKS seeks the linear combination of the ensemble members that best describes the analysis BC. The coefficients of this linear combination are stored in the weight vector $\mathbf{w}$ of size N. In practice, for a given value of the weight vector, the corresponding vector of BC is

$$\mathbf{z} = \mathbf{z}^{\mathrm{b}} + \mathbf{A}\mathbf{w}. \tag{3.11}$$

Replacing (3.10) and (3.11) in (2.14) and using the notation $\|\mathbf{x}\|^2 = \mathbf{x}^{\mathrm{T}}\mathbf{x}$, the cost function in the ensemble space reads

$$\widetilde{\mathcal{J}}(\mathbf{w}) = \frac{1}{2}\|\mathbf{y} - \mathcal{H} \circ \mathcal{M}(\mathbf{z}^{\mathrm{b}} + \mathbf{A}\mathbf{w})\|^2_{\mathbf{R}^{-1}} + \frac{1}{2}\|\mathbf{w}\|^2. \tag{3.12}$$

The cost function derived here is the same as that obtained in previous DA schemes (e.g., Bocquet and Sakov, 2014), albeit replacing the IC by the BC.

3.3.2 Minimisation of the cost function in the ensemble space

In the following, the cost function (3.12) is minimized in the ensemble space following the Gauss-Newton algorithm. In theory, it is equivalent to use other minimisation schemes such as L-BFGS-B or Levenberg-Marquardt (Björck, 1996). In the present study, we assume that the results are somehow insensitive to the minimisation scheme. A great advantage of working in the ensemble space is that the calculation of the gradient of the cost function does not require the full (in state space) adjoint nor the tangent linear of the forward operator $\mathcal{F}$. It is replaced by the use of the ensemble, thanks to the pre-conditioning by $\mathbf{A}$ as in Liu et al. (2008) and Gu and Oliver (2007). Therefore, one only requires the tangent linear of the operator transporting from the ensemble space to the observation space:

$$\mathbf{Y}^{(j)} = [\mathcal{F}]'_{|\mathbf{z}^{(j)}}\,\mathbf{A}, \tag{3.13}$$

where $\mathbf{z}^{(j)} = \mathbf{z}^{\mathrm{b}} + \mathbf{A}\mathbf{w}^{(j)}$, the index '$(j)$' refers to the iteration index in the Gauss-Newton algorithm, and $[\mathcal{F}]'_{|\mathbf{z}^{(j)}}$ represents the adjoint of the forward operator.

The gradient and the approximate Hessian of the cost function are then given by

$$\nabla\widetilde{\mathcal{J}}_{(j)} = \mathbf{w}^{(j)} - \left(\mathbf{Y}^{(j)}\right)^{\mathrm{T}}\mathbf{R}^{-1}\left[\mathbf{y} - \mathcal{F}(\mathbf{z}^{(j)})\right] \text{ and} \tag{3.14a}$$

$$\mathbb{H}_{(j)} = \mathbf{I}_N + \left(\mathbf{Y}^{(j)}\right)^{\mathrm{T}}\mathbf{R}^{-1}\mathbf{Y}^{(j)}. \tag{3.14b}$$

Using the ensemble, the matrix $\mathbf{Y}^{(j)}$ can be directly estimated, without the need for the estimation of $[\mathcal{F}]'_{|\mathbf{z}^{(j)}}$. Moreover, the matrix $\mathbf{Y}^{(j)}$ is of size $p \times N$ and since p and N are generally small (especially in the cases we are interested in), the computation of $\mathbf{Y}^{(j)}$ and $\left(\mathbf{Y}^{(j)}\right)^{\mathrm{T}}$ is not too expensive.

Using previously defined notation, the Gauss-Newton algorithm reads

$$\mathbf{w}^{(j+1)} = \mathbf{w}^{(j)} - \mathbb{H}^{-1}_{(j)}\nabla\widetilde{\mathcal{J}}_{(j)}\left(\mathbf{w}^{(j)}\right), \tag{3.15}$$

where $\nabla\widetilde{\mathcal{J}}$ is the gradient and $\mathbb{H}$ is the approximation of the Hessian of the cost function.

At each step of this iterative algorithm, the ensemble anomalies must be rescaled such that the propagated ensemble is representative of the current estimate of the state error. There are two methods to do so (Sakov et al., 2012; Bocquet and Sakov, 2012). In the *bundle* variant, the ensemble is shrunk by a small factor ϵ then propagated and

eventually inflated by $1/\epsilon$, which lead to

$$\mathbf{Y}^{(j)} = \mathcal{F}\left(\mathbf{z}^{(j)}\mathbf{1}^{\mathrm{T}}\epsilon\mathbf{A}\right)\left(\mathbf{I}_N - \frac{\mathbf{1}\mathbf{1}^{\mathrm{T}}}{N}\right)\frac{1}{\epsilon}. \tag{3.16}$$

In the *transform* variant, the ensemble is transformed before its propagation using the ensemble transform matrix obtained at the previous iteration:

$$\mathbf{T}_{(j)} = \left(\mathbf{I}_N + \left(\mathbf{Y}^{(j-1)}\right)^{\mathrm{T}}\mathbf{R}^{-1}\mathbf{Y}^{(j-1)}\right)^{-\frac{1}{2}}, \tag{3.17}$$

where $\mathbf{I}_N$ is the identity matrix of size $N \times N$. The propagated ensemble is then rescaled using the transform inverse to (3.17), which gives

$$\mathbf{Y}^{(j)} \approx \mathcal{H} \circ \mathcal{M}\left(\mathbf{z}^{(j)}\mathbf{1}^{\mathrm{T}} + \sqrt{N-1}\mathbf{A}\mathbf{T}_{(j)}\right)\left(\mathbf{I}_N - \frac{\mathbf{1}\mathbf{1}^{\mathrm{T}}}{N}\right)\frac{\mathbf{T}_{(j)}^{-1}}{\sqrt{N-1}}. \tag{3.18}$$

Since the two approaches give very similar results (Bocquet and Sakov, 2012), we use the *transform* method in the present work.

In the two first studies (Chapters 4 and 5), to compute the gradient $\nabla\widetilde{\mathcal{J}}$, we assume that averaging the ensemble of simulated observations is equivalent to applying the forward operator to the mean BC:

$$\mathcal{F}\left(\mathbf{z}^{(j)}\mathbf{1}^{\mathrm{T}} + \sqrt{N-1}\mathbf{A}\mathbf{T}_{(j)}\right)\frac{\mathbf{1}\mathbf{1}^{\mathrm{T}}}{N} \approx \mathcal{F}(\mathbf{z}^{(j)}). \tag{3.19}$$

This linearity assumption is too strong when the observations correspond to values of pollutant concentration such that in the last study (Chapter 6) we explicitly simulate the mean of the ensemble ($\mathcal{F}(\mathbf{z}^{(j)})$).

The solution of the cost function minimisation is referred to as $\mathbf{w}^{\mathrm{a}}$ and the optimal vector of BC, according to the previously defined DA problem, is given by

$$\mathbf{z}^{\mathrm{a}} = \mathbf{z}^{\mathrm{b}} + \mathbf{A}\mathbf{w}^{\mathrm{a}}. \tag{3.20}$$

A posterior ensemble is obtained at the end of the analysis and its spread is informative about the uncertainty of the analysis:

$$\mathbf{E}^{\mathrm{a}} = \mathbf{z}^{\mathrm{a}}\mathbf{1}^{\mathrm{T}} + \sqrt{N-1}\mathbf{A}\left(\mathbb{H}^{\mathrm{a}}\right)^{-\frac{1}{2}}\mathbf{U}, \tag{3.21}$$

where $\mathbf{U}$ is an orthogonal matrix of size $N \times N$ satisfying $\mathbf{U}\mathbf{1} = \mathbf{1}$, used to keep the ensemble centred on the analysis (here we set $\mathbf{U} = \mathbf{I}_N$).

The pseudo-code of Algorithm 1 details one analysis cycle of the IEnKS using the *transform* variant and the Gauss-Newton minimisation algorithm, which is schematically represented in Figure 3.4.

An analysis cycle corresponds to the assimilation of one vector of observations to correct one control vector. In the present work, we consider a control vector of steady BC such that we perform only one analysis cycle and stop the algorithm at this point.

In an unsteady context, several analysis cycles could be performed consecutively to assimilate several vectors of observations and correct several control vectors (see Fig. 2.2). In such cases, the results obtained at the end of the minimisation ($\mathbf{z}^{\mathrm{a}}$, $\mathbf{E}^{\mathrm{a}}$, etc.) could be used as background information for a subsequent analysis cycle.

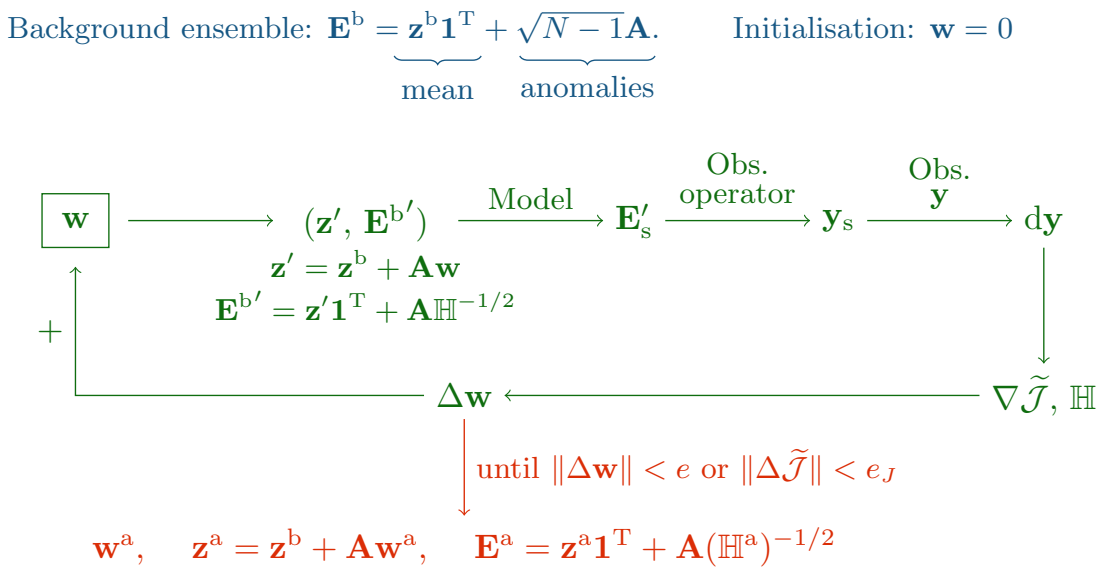

Figure 3.4: One analysis cycle of the IEnKS. The background ensemble $\mathbf{E}^{\mathrm{b}}$ is either obtained by a forecast ensemble from the previous analysis cycle or given as an input of the method. The best estimate of the weight vector $\mathbf{w}^{\mathrm{a}}$ is obtained by minimising the cost function $\widetilde{\mathcal{J}}$ as shown by the cycle on the figure: for each value of $\mathbf{w}$, a new ensemble of BC ($\mathbf{E}^{\mathrm{b}\prime}$), centred on $\mathbf{z}'$, is generated using the *transform* method. The model and the observation operator are applied to this ensemble, which gives an ensemble of simulated observations with mean $\mathbf{y}_{\mathrm{s}}$ that can be compared to the observations $\mathbf{y}$. The increment $\mathrm{d}\mathbf{y} = \mathbf{y} - \mathbf{y}_s$ and the spread of the ensemble of simulated observations around the mean are used in the estimation of the gradient and Hessian of the cost function. The weight $\mathbf{w}$ is thus updated following Gauss-Newton algorithm until the convergence criterion is reached. At the end of the analysis, the best estimate of the control vector $\mathbf{z}^{\mathrm{a}}$ and the analysis ensemble $\mathbf{E}^{\mathrm{a}}$ can be used as a first guess for the next analysis cycle.

Algorithm 1 A cycle of transform/Gauss-Newton IEnKS

Require: Transition model from BC ($\mathbf{z}$) to steady state ($\mathbf{x}_s$): $\mathcal{M}$, observation operator: $\mathcal{H}$, observation vector: $\mathbf{y}$, background ensemble: $\mathbf{E}^{\mathrm{b}}$, and algorithm parameters: e_J, j_{max}. $\mathbf{U}$ is an orthogonal matrix of size $N \times N$ satisfying $\mathbf{U1} = \mathbf{1}$.

1. $j = 0$, $\mathbf{w} = \mathbf{0}$
   $\mathbf{T} = \mathbf{I}$
2. $\mathbf{z}^{\mathrm{b}} = \overline{\mathbf{z}} = \mathbf{E}^{\mathrm{b}}\mathbf{1}/N$
3. $\mathbf{A} = \frac{1}{\sqrt{N-1}}\left(\mathbf{E}^{\mathrm{b}} - \mathbf{z}^{\mathrm{b}}\mathbf{1}^{\mathrm{T}}\right)$
4. **repeat**
   5. $\mathbf{z} = \mathbf{z}^{\mathrm{b}} + \mathbf{A}\mathbf{w}$
   6. $\mathbf{E}_0 = \mathbf{z}\mathbf{1}^{\mathrm{T}} + \sqrt{N-1}\mathbf{A}\mathbf{T}$
   7. $\mathbf{E}_s = \mathcal{M}\left(\mathbf{E}_0\right)$
   8. $\bar{\mathbf{y}}_s = \mathcal{H}\left(\mathbf{E}_0\right)\mathbf{1}/N$
   9. $\mathbf{Y} = \left(\mathcal{H}\left(\mathbf{E}_s\right) - \bar{\mathbf{y}}_s\mathbf{1}^{\mathrm{T}}\right)\frac{\mathbf{T}^{-1}}{\sqrt{N-1}}$
   10. $\nabla\widetilde{\mathcal{J}} = \mathbf{w} - \mathbf{Y}^{\mathrm{T}}\mathbf{R}^{-1}(\mathbf{y} - \bar{\mathbf{y}}_s)$
   11. $\mathbb{H} = \mathbf{I}_N + \mathbf{Y}^{\mathrm{T}}\mathbf{R}^{-1}\mathbf{Y}$
   12. Solve $\mathbb{H}\Delta\mathbf{w} = \nabla\widetilde{\mathcal{J}}$
   13. $\mathbf{w} := \mathbf{w} - \Delta\mathbf{w}$
   14. $j := j + 1$
   15. $\mathbf{T} := \mathbb{H}^{-1/2}$
   16. $\mathcal{J} = \mathbf{w}^{\mathrm{T}}\mathbf{w} + (\mathbf{y} - \bar{\mathbf{y}}_s)^{\mathrm{T}}\mathbf{R}^{-1}(\mathbf{y} - \bar{\mathbf{y}}_s)$

   until $\frac{|\Delta\mathcal{J}|}{\mathcal{J}^{(0)}} < e_J$ **or** $j \geq j_{\max}$
17. $\mathbf{z}^{\mathrm{a}} = \mathbf{z}^{\mathrm{b}} + \mathbf{A}\mathbf{w}^{\mathrm{a}}$
18. $\mathbf{E}^{\mathrm{a}} = \mathbf{z}^{\mathrm{a}}\mathbf{1}^{\mathrm{T}} + \sqrt{N-1}\mathbf{A}\left(\mathbb{H}^{\mathrm{a}}\right)^{-\frac{1}{2}}\mathbf{U}$

3.3.3 Criterion of convergence of the IEnKS inner minimisation algorithm

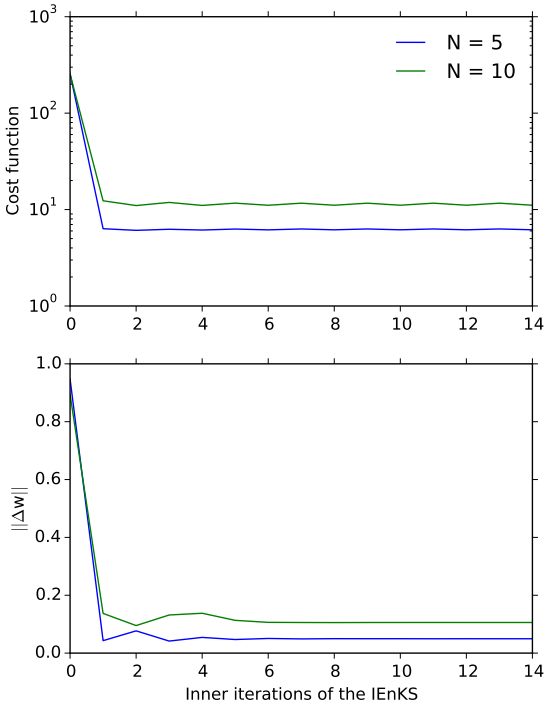

Figure 3.5: Evolution of (upper) the cost function ($\mathcal{J}$) and (lower) the norm of the weight vector increment $\|\Delta\mathbf{w}\|$ with the inner iterations of the IEnKS for the 2D twin experiment with 5 (blue) and 10 (green) members.

The IEnKS cost function is here minimised using a Gauss-Newton algorithm. The convergence criterion for this iterative algorithm is usually defined by the fact that the root mean square of $\mathbf{w}^{(j+1)} - \mathbf{w}^{(j)}$ is smaller than a predefined precision level e: $\|\Delta\mathbf{w}\| < e$.

With the CFD model *Code_Saturne*, the cost function defined in 3.3.1 does not show a clear global minimum. In fact, due to some model imprecisions, there is a small region in the ensemble subspace where the cost function is minimal and nearly constant. When the IEnKS has reached this region, the vector $\mathbf{w}$ might change more than a typical value of $e = 10^{-3}$ while the cost function is nearly constant (Fig. 3.5). In this case the algorithm does not converge according to the criterion on $\|\Delta\mathbf{w}\|$, whereas the minimum of the cost function has been reached. Consequently, we have defined a new criterion of convergence related to the change in the value of the cost function, between two consecutive iterations, relative to the initial value of the cost function. The algorithm is here stopped when $\frac{|\mathcal{J}^{(j+1)} - \mathcal{J}^{(j)}|}{\mathcal{J}^{(0)}} < e_\mathrm{J}$. In all the experiments discussed in this work, $e_J = 10^{-2}$.

Note that, since the cost functions considered in the present work are not perfectly convex, another possibility to find its minimum is inspired from simulated annealing

methods. It consists in running $j_{\max}$ iterations of the IEnKS, and selecting the best configuration, i.e., the value of the control vector which gives the smaller evaluation of the cost function. This methodology has been applied in the last study of this work, presented in Chapter 6.

3.4 3D-Var: a well-known method for comparison purposes

3D-Var is based on the minimisation of the same cost function than the IEnKS, though considered in the control space rather than in ensemble subspace (see Section 2.4.2). This method has been widely used in data assimilation studies and is here used for comparison purposes.

In the present study, the gradient of the cost-function is estimated using finite-difference approximation of the gradient. The ADAO module of the SALOME open-source platform (http://www.salome-platform.org) offers the possibility to run 3D-Var with this approximation and minimises the cost function with a L-BFGS-B nonlinear, constrained optimisation algorithm (Byrd et al., 1995). Since estimating the gradient with finite differences is very computationally expensive, 3D-Var has been only used when the size of the control vector remains small in Chapters 4 and 5.

Chapter 4

Application of data assimilation to 1D shallow-water equations and comparison of the different methods

Contents

4.1 Introduction

To first test the two data assimilation (DA) methods previously described, we use a simple representation of the atmospheric boundary layer (ABL) and the free troposphere above

into two layers, using the shallow-water equations (SWE) which are an approximation of the Navier-Stokes equations for shallow flows (see Section 1.2.3).

The equivalence between 'level' models and 'layer' models, together with the relative simplicity of the SWE, motivate the use of a shallow-layer model to first test the DA methods for atmospheric local-scale simulations, before applying them to computational fluid dynamics (CFD) models. We acknowledge that the shallow-water model used here is quite simple and that it is only a first step in the validation process of the methods, that will be later tested on more complex cases.

In Section 4.2 we introduce the shallow-water model used to represent the atmosphere and test the DA methods in the present study. We also present the experimental setup applied here.

In Section 4.3 we show the results obtained with the three DA methods (the back and forth nudging (BFN) algorithm, the iterative ensemble Kalman smoother (IEnKS), and 3D-Var) with perfect observations. Afterwards, we compare the performances of the methods, in particular their sensitivities to observation errors and to background errors. In the last Section, we give some concluding remarks on this study and perspectives for the subsequent one.

The results presented in this chapter have been published in Defforge et al. (2018).

4.2 Methods

4.2.1 Resolution of the shallow-water equations

In the present study, we consider flows that are subcritical and we prescribe the velocity on the left of the domain: $u(x = 0) = u_{\mathrm{L}}$, and the fluid height on the right: $h(x = L) = h_{\mathrm{R}}$. These boundary conditions (BC) are here considered constant in time and we look for the steady state obtained with these BC.

The 1D SWE with topography and without ground friction nor diffusion (Eq. 1.18) can be solved analytically by the Bernoulli equation (Eq. 1.19) (see Section 1.2.3). The resolution of the Bernoulli equation is used to determine the steady state with two given BC, when no other forcing than the topography takes action. When nudging is added to the SWE, they are solved numerically by a finite-volume method (see Appendix A.4.1).

Figure 4.1 shows the results of the 1D SWE with the following BC: $u_{\mathrm{L}} = 5.5\mathrm{m/s}$ and $h_{\mathrm{R}} = 154\mathrm{m}$. This figure illustrates the steady state that is considered as the reference for the DA experiments.

4.2.2 Experimental set-up

3D-Var, the BFN algorithm and the IEnKS are tested on a shallow-layer system with one-dimensional twin experiments (synthetic observations are extracted from the reference simulation). The experiments correspond to a channel of length $L = 2500\mathrm{m}$ with a

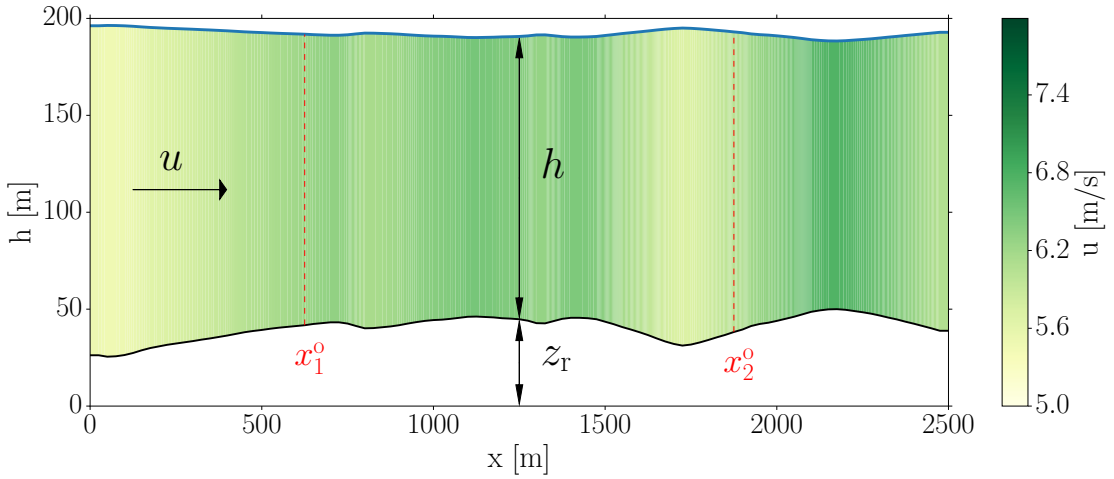

Figure 4.1: Results of the 1D SWE over a realistic topography. The topography (z_r) is shown in black and the absolute height of the fluid ($z_r + h$) is shown in blue. The fluid area is coloured according to the vertical mean of the horizontal velocity (u). The vertical dashed, red lines show the locations of the two velocity observations assimilated in the following experiments.

realistic topography profile but without diffusion nor ground friction. The reduced gravity is equal to $g' = 0.5g = 4.905\text{m/s}^2$, which corresponds to a ABL twice as dense as the free atmosphere above. The reference state is shown in Figure 4.1 and the first guess (or background) corresponds to the BC value $u_L^b = 4.4\text{m/s}$, i.e. a background error of 20%.

The value of the downstream BC ($h_R = 154\text{m}$) is unchanged between the reference simulation and the background. In all the cases, we consider the steady state obtained with constant BC. The initial state for the DA experiments is the steady state obtained with the *a priori* BC: in Sections 4.3.1 and 4.3.2 the same initial state is used for all the DA experiments ($u_L^b = 4.4\text{m/s}$ and $h_R = 154\text{m}$), while in Sections 4.3.3 the background u_L^b differs between the realizations and the initial state varies accordingly. It is noteworthy that for simulations performed until convergence, the initial conditions (IC) does not influence the results, i.e. the steady state.

Two observations of the velocity, located at $x_1^o = 625\text{m}$ and $x_1^o = 1875\text{m}$ (see Fig. 4.1), are extracted from the reference simulation and are kept exact, i.e. noise-free, in Section 4.3.1 while they are noisy in Sections 4.3.2 and 4.3.3.

As noted in Section 3.2, the BFN does not have the same objective as 3D-Var and the IEnKS. To allow a quite fair comparison between these methods, we consider cases for which the uncertainty of the background is substantially larger than of the observations. For 3D-Var and the IEnKS, the background error covariance matrix ($\mathbf{B}$) and the observation error covariance matrix ($\mathbf{R}$) have been chosen diagonal with variances of $1\text{m}^2/\text{s}^2$ and $10^{-6}\text{m}^2/\text{s}^2$ respectively. In all the DA experiments with either 3D-Var or the IEnKS, for each value of the left BC, the steady state is obtained analytically by the

resolution of the Bernoulli equation (Eq. 1.19), without using the numerical modelling. Equivalently, we could have integrated the numerical model during a long enough time until reaching a steady state. For the IEnKS, the background ensemble of 2 members corresponds to the two leading modes of the background error covariance matrix equal to identity, obtained with a singular value decomposition (SVD). The 2 members are recentred such that the ensemble mean is u^{b} (see Fig. 4.2a). The convergence criteria is set to $e = 10^{-3}$.

For the BFN algorithm, the forward and backward integrations with nudging are performed over a time period T, which corresponds to the time needed for the information coming from the observations to reach the BC (see Section 3.2.4). Using the method of characteristics we have estimated this time period to be $T = 30\mathrm{s}$. The nudging is applied every time step ($\delta t = 0.5\mathrm{s}$) and the nudging matrices are the same in the forward and backward integrations: $\mathbf{K} = k\mathbf{H}^{\mathrm{T}}$ where $k = 1\mathrm{s}^{-1}$. This definition of nudging matrices is equivalent to $\mathbf{H}^{\mathrm{T}}\mathbf{R}^{-1}$, often used in nudging studies. In fact, here the observations are independently perturbed by noise such that $\mathbf{R}$ is proportional to the identity matrix: $\mathbf{R} = r\mathbf{I}$. On the other hand, the numerical scheme used to solve the SWE is explicit such that the nudging coefficient must be smaller than one. In the present study, $r = 10^{-6}$ and 0.25 (without and with noise respectively), in which case r^{-1} is too large. Consequently we take the largest possible value for k, which is 1.

We assume that the BFN algorithm has converged when the relative variation of the control vector (here the BC u_{L}) between two consecutive iterations is smaller than 0.05% during 5 consecutive iterations.

4.3 Results

4.3.1 Results with perfect observations

Figures 4.2a and 4.2b show the background in blue, the reference simulation in dashed black, and the observations as red dots.

Figures 4.2a shows the steady state corresponding to the BC of the 2 ensemble members (dotted, blue curves) and of the one calculated by the IEnKS analysis (orange curve). In this simple case the IEnKS perfectly recovers the value of the BC, so does 3D-Var (not shown on the figure).

Figure 4.2b shows the steady state corresponding to the BC obtained after 1, 15, and 33 BFN iterations in the experiment with perfect observations. A BFN iteration is defined as one forward and one backward integrations. The BFN algorithm has converged after 33 iterations, i.e. 66 model integrations over a period of $T = 30\mathrm{s}$, and the BC obtained is $u_{\mathrm{L}}^{\mathrm{a}} = 5.54\mathrm{m/s}$. The relative RMSE between the true state and the state obtained with this value of BC is equal to 0.68%, when evaluated over the whole domain.

The results of both the IEnKS and 3D-Var are very good, though these methods have a slightly higher computational cost. In fact, here the resolution of the Bernoulli

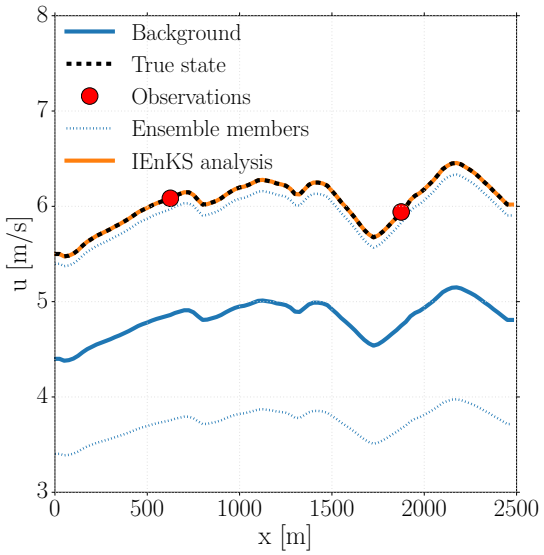

(a) Results of the IEnKS with perfect observations

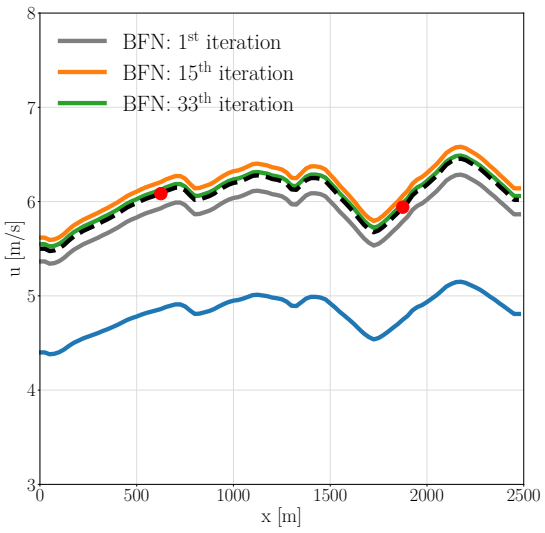

(b) Results of the BFN algorithm with perfect observations

Figure 4.2: Profiles of velocity obtained (a) at the end of the IEnKS analysis and (b) after 1, 15, and 33 BFN iterations for the experiment with perfect observations. The simulations are performed with a shallow-layer model without diffusion nor ground friction.

equation (1.19) is not costly but in general cases – where no analytical solution is available – the model should be integrated over a time window long enough to reach the convergence, and consequently longer than the period T used in the BFN algorithm. In fact, each iteration of the BFN algorithm (i.e. one successive forward and backward integrations) requires nearly 30 times less computational resources than one analysis cycle of IEnKS with two members or one finite-difference calculation for 3D-Var minimisation. However, the IEnKS and 3D-Var can be partially parallelised, unlike the BFN algorithm. The IEnKS is here still more efficient than 3D-Var as the minimisation of the cost function only requires 2 iterations of the Gauss-Newton algorithm, i.e. this method requires 4 model integrations as we consider 2 ensemble members. In comparison, 3D-Var in ADAO estimates the gradient by finite-differences such that each iteration of the optimisation algorithm requires 2 model integrations. Here, 6 iterations are necessary to reach the minimum of the cost function, which corresponds to 12 model integrations.

4.3.2 Results with noisy observations

In real studies, the observations are never perfect. Consequently, we have analysed the ability of the DA methods to assimilate noisy observations.

We have generated an ensemble of 50 pairs of observation errors following a Gaussian distribution with zero mean and a covariance matrix equal to $0.25\mathbf{I}$, where $\mathbf{I}$ is the 2×2

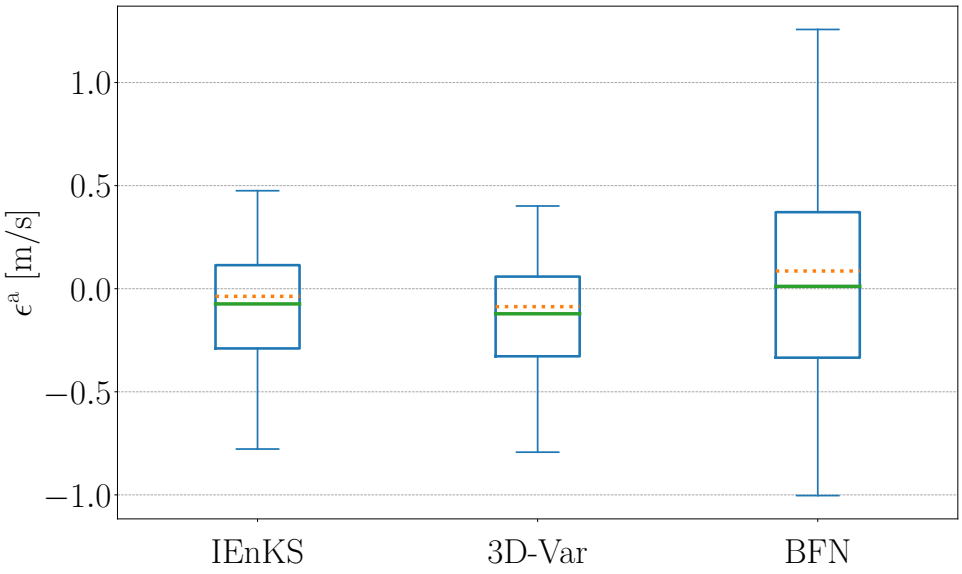

Figure 4.3: Boxplots corresponding to the analysis errors obtained with 50 pairs of noisy observations using the IEnKS, 3D-Var, and the BFN algorithm. The bottom and top of the boxes represent the 1st and 3rd quartiles, the green line corresponds to the mean, the dashed orange line to the median, and the ends of the whiskers represent the minimum and maximum of all the data.

identity matrix. For 3D-Var and the IEnKS, we thus set the observation error covariance matrix to $\mathbf{R} = 0.25\mathbf{I}$ in what follows.

Figure 4.3 shows boxplots corresponding to the distribution of the analysis errors for the 50 cases with noisy observations, for each DA method. The analysis error is defined as the difference between the value of the BC given by the analysis and the true value of the BC:

$$\epsilon^{\mathrm{a}} = u_{\mathrm{L}}^{\mathrm{a}} - u_{\mathrm{L}}^{\mathrm{t}}. \tag{4.1}$$

We observe that the three methods have small mean analysis errors (green line) and quite small dispersions of the errors (blue boxes). The IEnKS and 3D-Var give good results with small mean analysis errors (respectively -0.07m/s and -0.12m/s) and small standard deviation (both 0.27m/s). The BFN algorithm gives the smallest mean analysis error (0.01m/s) though the standard deviation around this mean is larger than for the two other methods (0.5m/s). This larger variability shows that the BFN algorithm is more sensitive to observation errors. It is consistent with the definition of the BFN, which gives a large importance to observations. If observations are not perfect, the BFN algorithm nudges the system toward a state that is close to these observations and which might be different from the true state.

A useful measure of the uncertainty on the analysis is the precision, which is defined

as the inverse of the analysis error variance:

$$p^{\mathrm{a}} = \frac{1}{\sigma_{\mathrm{a}}^2}. \tag{4.2}$$

Theoretically, the analysis precision is the sum of the precisions of the background and of the observations (Section 5.4.1 in Kalnay, 2003). The adjoint of the forward operator $\widetilde{\mathbf{H}}$ can be estimated by the IEnKS and 3D-Var using either the ensemble or finite differences. From this estimate, we deduce the precision of the observations: $p^{\mathrm{o}} = \widetilde{\mathbf{H}}^{\mathrm{T}}\mathbf{R}^{-1}\widetilde{\mathbf{H}} \approx 39\mathrm{s}^2/\mathrm{m}^2$. In this section, we analyse the sensitivity to the observation errors only and the background is the same for the 50 experiments. Consequently, we compare the analysis precisions to the observation precision. Both the IEnKS and 3D-Var give precisions of $14\mathrm{s}^2/\mathrm{m}^2$ which is smaller than the theoretical value, especially because the statistical assumptions are not perfectly satisfied. However, the precisions are not too low neither, indicating that the methods are not very sensitive to the observation errors. In particular, for these two methods, the absolute value of the analysis error is smaller than the background error ($|\epsilon^{\mathrm{b}}| = |u_{\mathrm{L}}^{\mathrm{b}} - u_{\mathrm{L}}^{\mathrm{t}}| = 1.1\mathrm{m/s}$) for all the experiments. This shows that the DA methods always help correct the BC. As mentioned above, the BFN algorithm is intrinsically more sensitive to observation errors, which is consistent with the smaller analysis precision of $4\mathrm{s}^2/\mathrm{m}^{-2}$.

4.3.3 Analysis of sensitivity to the background error

We have also analysed the sensitivity of the DA methods to the first guess $u_{\mathrm{L}}^{\mathrm{b}}$. Similar to the sensitivity analysis to observation error, we have generated an ensemble of 20 background errors, following a Gaussian distribution with zero mean and a variance of $\sigma_{\mathrm{b}}^2 = 1\mathrm{m}^2/\mathrm{s}^2$, symmetrical with respect to zero. We have also generated 10 pairs of observation errors, as in Section 4.3.2. The three DA methods have been tested on these 200 cases.

Figure 4.4 shows the analysis error against the background error for the IEnKS (blue squares), 3D-Var (orange triangles), and the BFN algorithm (green dots). The markers represent the absolute analysis error, averaged over the 10 pairs of noisy observations for a same background error, and the errorbars indicate the standard deviation around these mean values. The absolute values of the background error are represented by the grey line ($y = |x|$): in the dotted areas the analysis error is greater than the background error, indicating that the DA method does not help correct the simulations.

We observe in Figure 4.4 that the mean analysis errors of 3D-Var and the IEnKS (blue squares and orange triangles) are proportional to the background error. This is consistent with the Bayesian framework of these methods. We can also verify that the sensitivity of the IEnKS and 3D-Var to the background error is quite small here, which is in agreement with the fact that the background precision is here substantially smaller than the observation precision. By construction, the BFN algorithm does not depend on the background and we can verify here that the mean analysis error (green circles)

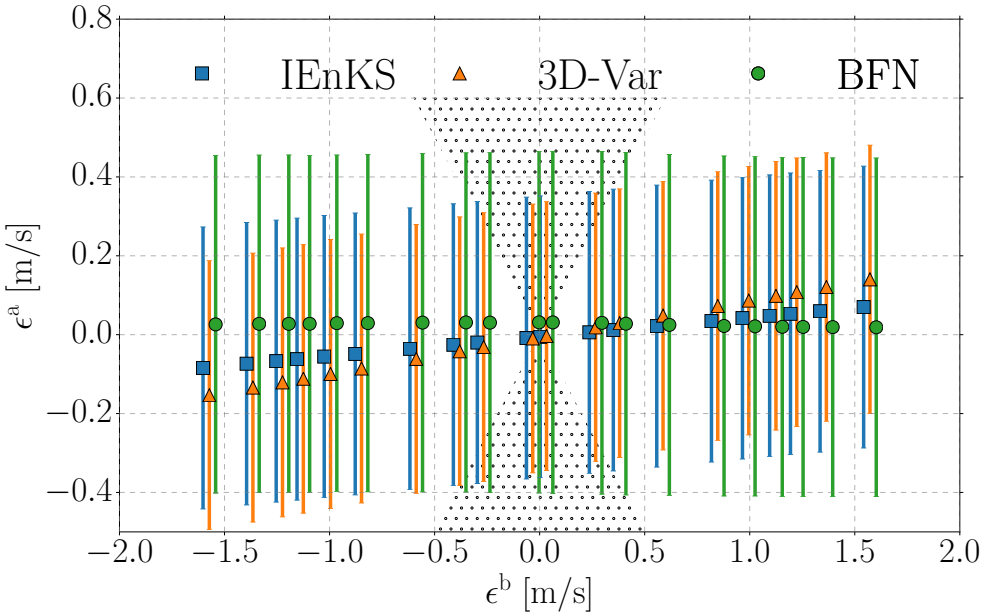

Figure 4.4: Analysis error against background error for 20 values of background error and for the three DA methods: the IEnKS (blue squares), 3D-Var (orange triangles), and the BFN algorithm (green circles). The errorbars are centred on the mean analysis error and show the standard deviation, calculated over 10 experiments with different pairs of observation errors and a given background error. The dotted areas correspond to absolute values of analysis error larger than the background error, i.e. the DA method has increased the error.

is nearly constant. For neither of the three methods does the sensitivity to observation error – represented by the length of the blue, orange, and green errorbars – depend on the background error. We can verify here again that the green error bars are longer than the blue and orange ones, indicating that the BFN algorithm is more sensitive to observation errors than 3D-Var and the IEnKS.

Except for very small absolute background errors (< 0.4m/s), all the errorbars are below the grey line (Fig. 4.4), indicating that in nearly all the cases, the three DA methods help reduce the error on the BC. The cases with very small absolute backward error ($|\epsilon^b|$) correspond to cases for which the values of the background are very close to the true state. However, the background error variance is still larger than the observation error variance ($\sigma_b^2 = 1\text{m}^2/\text{s}^2 > \sigma_o = 0.5\text{m}^2/\text{s}^2$), which means that the confidence placed in the background is smaller than the confidence in the noisy observations. Consequently, in 3D-Var and the IEnKS a smaller weight is given to the background compared to the one given to the observations. As the observations are noisy, the optimal control vector – relative to the DA problem – might be further away from the true state than the background. Consequently, the analysis error is somewhat larger than the background error and in Figure 4.4 the errorbars go over the edges of the dotted region.

The results with the BFN algorithm are consistent with the independence of the analysis to the background error and with the quite large sensitivity to observation error, highlighted in the previous section.

Another way to measure the sensitivity of the methods to background error is to look at the mean analysis error and the standard deviation in the ensemble of 20 experiments for each pair of noisy observations. The IEnKS analysis error depends little on the background value: for each pair of noisy observations, the mean analysis error is smaller than 0.5m/s and the standard deviation around this average value is smaller than 0.05m/s. 3D-Var gives similar results to the IEnKS, even though the standard deviations are slightly larger, indicating that the method is somehow more sensitive to the background error. This is consistent with Figure 4.4 in which the orange triangles follow a line with a larger slope than the blue squares.

With this measure we can also confirm that the BFN algorithm is more sensitive to observation error but less to background error than the two variational methods. In fact, depending on the pair of observations considered, the mean analysis error - calculated over the 20 analyses obtained with different background errors - vary from 0.12m/s to 1m/s. The standard deviations around theses means are all around 0.005m/s.

The analysis precision (Eq. 4.2) is a measure of the confidence in the analysis: the higher the precision is, the lower is the uncertainty on the analysis. In this section, both the background and the observations vary, thus the analysis precision should be the sum of the precisions of the background ($p^{\mathrm{b}} = \frac{1}{\sigma_{\mathrm{b}}^2} = 1\mathrm{s}^2/\mathrm{m}^2$) and the precision of the observations ($p^{\mathrm{o}} = 39\mathrm{s}^2/\mathrm{m}^{-2}$, Section 4.3.2). Consequently the analysis precision should theoretically be equal to $p^{\mathrm{a}} = p^{\mathrm{b}} + p^{\mathrm{o}} = 40\mathrm{s}^2/\mathrm{m}^2$ which gives an estimation of the standard deviation for the analysis velocity at boundary: $\sigma_{\mathrm{a}} = \sqrt{\frac{1}{40}} = 0.16\mathrm{m/s}$. Overall, considering all the 200 simulations for each method, the mean absolute analysis error is equal to -0.007m/s for the IEnKS and 3D-Var and 0.026m/s for the BFN algorithm with precisions of $8\mathrm{s}^2/\mathrm{m}^2$ for the IEnKS and 3D-Var and $5\mathrm{s}^2/\mathrm{m}^2$ for the BFN algorithm. The analysis precisions of all the three methods are greater than the background precision, which confirms that DA methods improve the estimation of the control vector.

Regarding computational efficiency, the BFN algorithm is always the most cost-effective because it is not integrated until convergence. The IEnKS is more effective than 3D-Var in these cases since only two or three iterations of the Gauss-Newton algorithm are necessary to minimise the cost function whereas for 3D-Var the minimisation by finite differences requires at least 5 iterations.

4.4 Conclusions

The shallow-layer model offers an interesting representation of geophysical flows and is often used for simple numerical experiments in meteorology and hydrology. In the present study, we consider a 1D shallow-layer model in order to validate the numerical

behaviour of the modified DA methods (the BFN algorithm, 3D-Var, and the IEnKS) before applying them to more complex model and cases.

The first results presented here show the efficiency of these methods to assimilate a few observations on cases with a complex one-dimensional geometry. The three methods help correct the BC, and thus obtain a state that is closer to the true state than the first guess. It has been shown that even if the observations are noisy and for a quite large range of background errors, the three methods are nearly always able to improve the estimation of the BC.

The IEnKS and 3D-Var depend little on the observation error but depend linearly on the background error. The BFN algorithm is more sensitive to the observation errors but not to the background. The behaviour of the three methods is in good agreement with the theory and highlights the fundamentally different DA problem solved by 3D-Var and IEnKS on one hand and the BFN algorithm on the other hand. Furthermore, the BFN algorithm has the disadvantage of being sensitive to parameters such as the nudging matrix, the length of the integration time window, and the location of the observations. Here we have used a very simple nudging matrix and further investigation could be performed to develop more complex observers, as in Auroux and Bonnabel (2011), Apte et al. (2018) or Krstic et al. (2009), in order to correct fluid height with velocity observations.

In this simple example, the IEnKS is the most efficient DA method as it gives the smallest analysis error, with the greatest precision, and it requires less model integrations than 3D-Var. However, the 1D case analysed in the present study is quite simple and the control vector considered is a singleton. Further investigation on more complex cases, especially with two horizontal dimensions and vertical profiles of velocity will be performed in the following chapters to analyse the performances of the methods on larger control vectors. Eventually, we will apply these methods to more realistic cases with the CFD model *Code_Saturne*.

Chapter 5

Improving CFD atmospheric simulations at local scale for wind resource assessment using data assimilation

Contents

5.1 Introduction

Wind resource assessment is increasingly based on atmospheric simulations with computational fluid dynamics (CFD) models (Landberg et al., 2003; Franke et al., 2004; Blocken, 2014), especially over complex terrain (e.g., Cattin et al., 2006; Palma et al., 2008; Blocken et al., 2015) and in built environment (e.g., Kalmikov et al., 2010; Simões and Estanqueiro, 2016; Wang et al., 2017). We have largely explained in Chapter 1 the fact that local-scale atmospheric simulations are very sensitive to geometrical features such as topography, and boundary conditions (BC) (Yang et al., 2009). In fact, the time needed for any information to propagate into a small-scale domain is much smaller than the

characteristic integration time scale. Consequently, the influence of initial conditions (IC) quickly vanishes with integration time, and the BC eventually control the solution. The BC thus account for a major source of uncertainty in local-scale atmospheric simulations and it is a challenge to accurately estimate them, especially for wind resource assessment.

To first estimate the IC and BC for CFD simulations at small scale, the results of mesoscale simulations are generally used (e.g. Yamada, 2004; Probst and Cárdenas, 2010). However, due to the large difference in spatial and temporal resolution between mesoscale and CFD domains the BC provided by mesoscale simulations are generally incorrect and do not always contain all the information, such as turbulence estimations (see Section 1.2.6). Consequently, mesoscale simulations provide useful information that is not sufficient and should be combined to another source of information, if available, to estimate the BC as accurately as possible.

The prospective sites for implantation of wind farms are often equipped with meteorological instruments, such as anemometers or Light Detection And Ranging (LIDAR), which supply wind measurements inside the domain of interest (Landberg et al., 2003) (see Section 2.1.1). These observations provide supplementary information that could be used with data assimilation (DA) methods to improve the knowledge of BC, and thus increase the precision of atmospheric simulations over small domains.

We have previously explained that, among the existing DA methods, the back and forth nudging (BFN) algorithm and the iterative ensemble Kalman smoother (IEnKS) seem well suited to be applied with CFD simulations for operational purposes. Both methods, in their versions adapted to correct the BC, have already been tested with a 1D shallow-layer model and proved to help correct BC in a simple case (Defforge et al., 2018) (see Chapter 4).

The goal of the study presented in this chapter is to assess the ability of the adapted version of the IEnKS and the BFN algorithm to improve 3D wind simulations. The methods are evaluated in a context of wind resource assessment, by assimilating a few *in situ* observations. We consider a real domain with very complex topography prospected for the installation of a wind farm. This domain has already been studied at EDF R&D for wind resource assessment and mesoscale simulations with the model Weather Research and Forecasting (WRF) are available for three years in the same region. In addition, a field campaign of wind observations has been performed on this site during a few months (Fig. 5.1). In Section 5.2 we introduce the experimental set-up and define the control vectors considered for the DA experiments. The 3D-Var method, which is usually considered as a reference, is here applied with finite differences for comparison purposes. We thus verify that this method can be applied to the CFD simulations with *Code_Saturne*. Then we explain the method used to estimate the background error covariance matrix related to the control vector of BC. We first present the results obtained over a 2D section of this domain in the vertical plane, with twin experiments (Section 5.3). Besides reducing the computation cost – and thus allowing us to perform more sensitivity test –

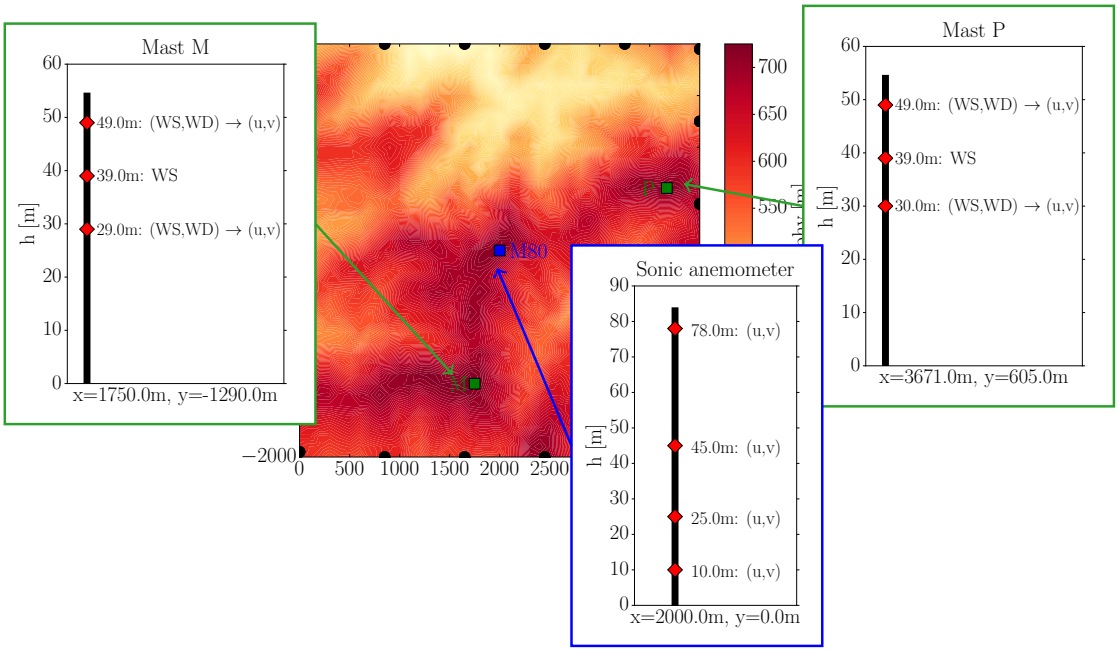

Figure 5.1: Topography of the studied site and location of the three meteorological masts, with the vertical position of the instruments. The black dots along the borders represent the vertical profiles of BC included in the 3D control vector.

this 2D case has the advantage to require the definition of BC on one side only and to allow comparison with 3D-Var. In a second time, we consider the whole 3D domain with four lateral boundaries. To gradually increase the complexity of the DA problem, the IEnKS is tested over this 3D domain with twin experiments (Section 5.4) and then with real observations in a cross validation process (Section 5.5). Eventually, some conclusions are drawn from this study and perspectives for the following work are given.

The results presented in this chapter have been published in Defforge et al. (2019a).

5.2 Methods

5.2.1 Definition of the 2D and 3D control vectors

In this study, we consider stationary BC and steady-state wind fields simulated with the CFD model *Code_Saturne*. At first, we consider a 2D domain in a XZ plane for which the vector of BC corresponds to the vertical profile of wind speed in the plane of the domain, prescribed at the western boundary. We assume that, at the boundary, the wind is only horizontal, such that we only analyse the west-east component of the velocity, referred to as u. The control vector of BC corresponds to the values of u defined in 21 vertical levels.

For 3D studies, several vertical profiles along the four lateral boundaries – West, South, East, and North - are required. Each border of the 3D *Code_Saturne* domain is 4km long, which corresponds to 6 grid points in the WRF domain (green squares in

Fig. 5.3a). In order not to overestimate the horizontal correlations between the vertical profiles, we only consider 6 vertical profiles of BC for each border, equally distributed (red circles in Fig. 5.3a). In total, 20 vertical profiles are included in the control vector and analysed. In 3D, both the west-east (u) and the south-north (v) components of the wind velocity are considered and each profile is defined in 21 vertical levels, such that the control vector in 3D is of size: $l = 20 \times 21 \times 2 = 840$.

5.2.2 Gradient tests for the tangent linear estimation for 3D-Var

To assess the performance of the minimisation algorithm, we have verified that the tangent linear of the forward operator ($\mathcal{F}'$) is correctly estimated with finite differences:

$$\mathcal{F}'_{|(\mathbf{z})}\mathrm{d}\mathbf{z} \approx \frac{\mathcal{F}\left(\mathbf{z}+\alpha\mathrm{d}\mathbf{z}\right)-\mathcal{F}(\mathbf{z})}{\alpha}. \tag{5.1}$$

By construction of the cost function, if the tangent linear is well estimated, then the cost function is analytically well calculated. It is thus equivalent to perform the following test with the tangent linear of the forward operator or with the cost function.

At first, we consider the Taylor residue for the tangent linear:

$$R(\alpha) = \frac{\|\mathcal{F}\left(\mathbf{z}+\alpha\mathrm{d}\mathbf{z}\right)-\mathcal{F}(\mathbf{z})-\alpha\mathcal{F}'\mathrm{d}\mathbf{z}\|}{\|\mathcal{F}(\mathbf{z})\|} = O(\alpha^2). \tag{5.2}$$

This residue should decrease as α^2 when α decreases, until the machine precision is reached.

The second test considers a residue ρ which is the ratio between a perturbation of the forward operator and the tangent linear estimate (Zou et al., 1997; Li et al., 1993; Koohkan, 2012):

$$\rho(\alpha) = \frac{\|\mathcal{F}(\mathbf{z}+\alpha\mathrm{d}\mathbf{z})-\mathcal{F}(\mathbf{z})\|}{\|\alpha\mathcal{F}'\mathrm{d}\mathbf{z}\|} = 1 + O(\alpha). \tag{5.3}$$

When α tends to zero, $\rho(\alpha)$ should linearly converge towards unity.

Figure 5.2a shows the decrease of $R(\alpha)$ with respect to α and Figure 5.2b shows the difference between the residue $\rho(\alpha)$ and 1, with respect to α. In both figures, the results are presented for three different values of the differential increment ($\mathrm{d}\mathbf{z}$), which is used in the finite-difference calculation. The point (in the space of dimension $\mathbb{R}^l$) around which the tangent linear is approximated, corresponds to the reference value of the 2D control vector (see Section 5.2.1). In this case $l = 21$.

From Figs. 5.2a and 5.2b, one can see that a differential increment of 10^{-2} gives goods results: the decrease of $R(\alpha)$ is close to α^2 and the decrease of $1-\rho(\alpha)$ is nearly linear until it reaches a constant value. Thus the differential increment has been set to $\mathrm{d}\mathbf{z} = 10^{-2}$ for all the tests with 3D-Var in the present study.

5.2.3 Estimation of the background error covariance matrix

One of the major issues raised by DA methods is that they require the estimation of the background and observation error covariance matrices. For ensemble-based methods,

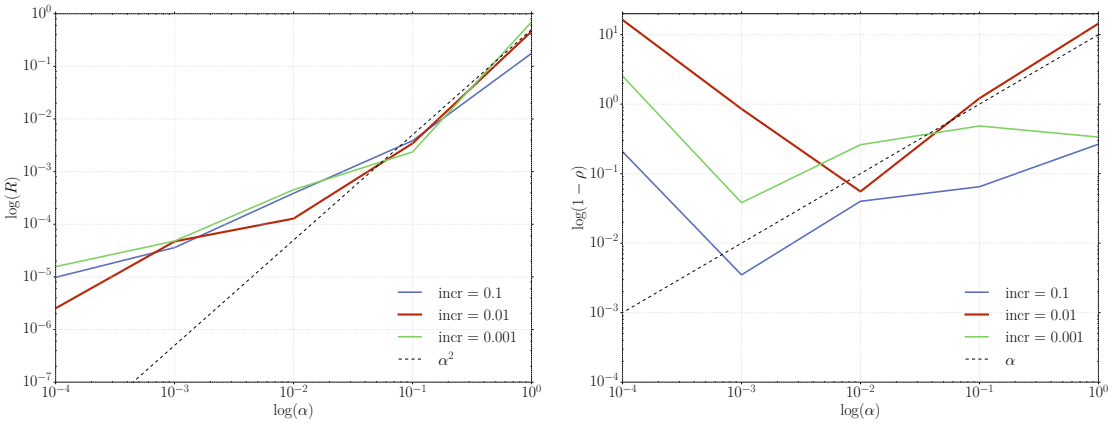

(a) Evolution of the Taylor residue with respect to the multiplication factor α.

(b) Evolution of the difference between the ratio $\rho(\alpha)$ and 1, with respect to α.

Figure 5.2: Verification tests of the tangent linear estimation for three values of the differential increment, used in the finite difference approximation: 10^{-1}, 10^{-2} and 10^{-2}.

such as the IEnKS, the background error statistics are represented by a limited number of vectors – the ensemble members – and the problem is to chose the background ensemble for the first analysis cycle. In fact, for subsequent analysis cycles, the analysis ensemble obtained at the end of a cycle can be used as the background ensemble for the next analysis cycle. In the present study, we only consider one analysis cycle such that it is crucial to appropriately choose the initial background ensemble.

In the present study, we first estimate the background error covariance matrix, associated with the BC of the local-scale domain, in order to construct the background ensemble. In fact, once the background error covariance matrix is known, the background ensemble might either be randomly sampled, according to this matrix, or it might consist of the eigenvectors associated with the largest eigenvalues of this matrix. The estimation of the background error covariance matrix is here based on the statistical analysis of a time series of the control vector associated with the BC. Such a time series is estimated using the results of three years of simulation with the mesoscale model WRF (Skamarock et al., 2005) at the location of the CFD domain. We thus quantify the uncertainty of inflow BC using the results of the mesoscale model WRF, similar to what has been done in García-Sánchez and Gorlé (2018). In what follows, we explain how we use three years of WRF simulations to obtain a series of realisations of the 2D and 3D control vectors and in particular how the profiles are extrapolated near the ground. Eventually, we present the method used to construct the background error covariance matrix from these time series.

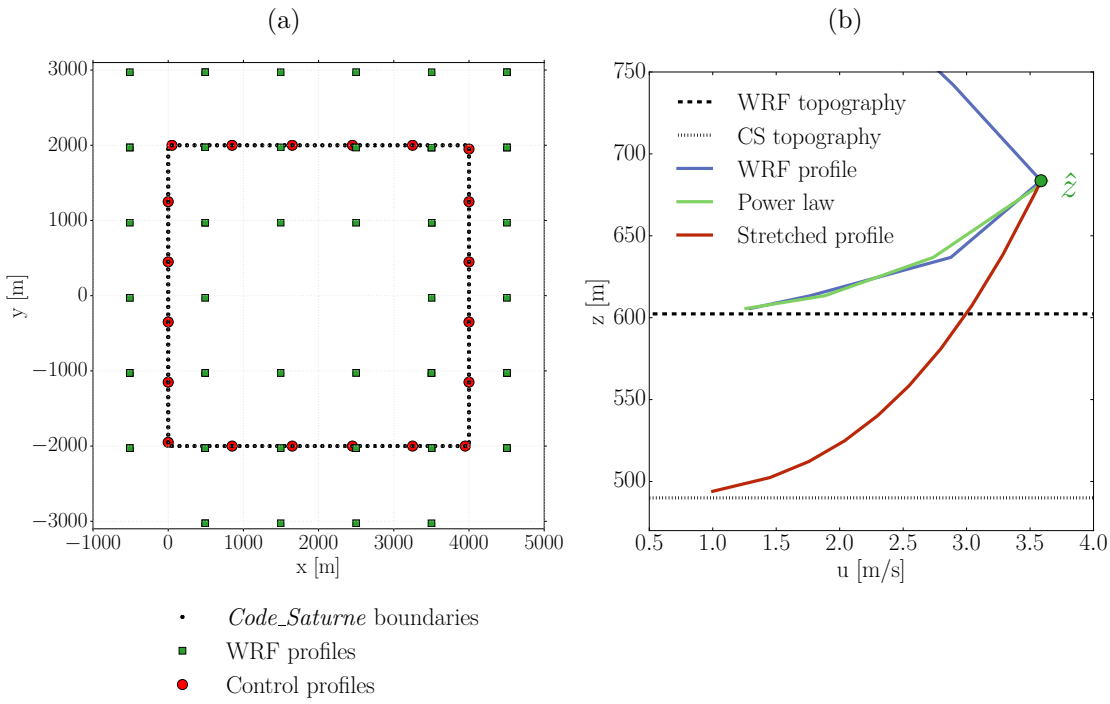

Figure 5.3: Methodology of the adaptation of WRF simulation results to estimate the BC prescribed for *Code_Saturne* simulations. a) View from above of the *Code_Saturne* boundaries of the 3D domain. They correspond to 160 vertical profiles shown as black dots. The control vector only includes 6 vertical profiles per border, equally distributed, shown as red disks on the figure. The wind speed values at each red disk is obtained from a bilinear interpolation of the four closest WRF profiles (green squares). b) Example of profile stretching near the ground, required due to the differences of topography resolution between WRF and *Code_Saturne* domains. The WRF profile (blue) is kept above $\hat{z}$ and replaced by the stretched power law (red) below.

From WRF results to time series of control vector estimates

The WRF simulations cover a mesoscale domain of 54km × 54km, with a horizontal resolution of 1km. Vertically, the domain extends up to 19km above the ground with variable vertical resolution from 15.1m near the ground to 1.7km at the top of the domain. The WRF simulations are available every hour and cover a three-year period. The local scale domains used for *Code_Saturne* simulations are much smaller. The 2D domain extends over 8km along x-direction with a 25m horizontal resolution. In 3D the domain extends over 4km × 4km with a horizontal resolution of 100m. The vertical resolution is finer in *Code_Saturne* than in WRF, especially near the ground: the first 100 meters are described by only 4 vertical levels in WRF and 7 levels in *Code_Saturne*.

To estimate the value of the control vector for each WRF result, we proceed in two steps. First, we perform a horizontal bilinear interpolation from the four closest WRF profiles to the location of each BC profile. Second, we perform specific processing of the lowest vertical levels of the profile obtained after the first step. Indeed, the topography is less precise in the WRF domain than in the *Code_Saturne* domain, such that the wind profiles do not necessarily cover the same vertical region in WRF and in *Code_Saturne*. The *Code_Saturne* topography, which is more accurate, might be locally higher or lower. In the 2D case studied here, the interpolated WRF profile starts at an absolute height of 605m while the *Code_Saturne* profile starts at 490m. The first 8 levels of *Code_Saturne* (out of 21 levels in total) are not covered by the WRF domain. The horizontally interpolated WRF profiles – obtained after the first step – have to be vertically stretched to fit the *Code_Saturne* grid near the ground. One should note that the reverse situation where the *Code_Saturne* topography is higher than the WRF topography might also occur, in which case the WRF profiles should be contracted. The methodology used to do so is detailed in the next paragraph.

We apply the two steps explained above to all the WRF results to obtain a series of more than 2×10^4 realisations of the control vector. Figure 5.4a shows an example of 50 values of the 2D control vector. This time series is used to construct the background error covariance matrix, as explained in the last paragraph of this section.

Stretching (or contraction) of WRF profiles near the ground

In order to stretch (or contract) the WRF profiles on the *Code_Saturne* grid, we assume that the wind velocity profiles near the ground follow a power law, which is a commonly used relationship between height above the ground and wind speed (Peterson et al., 1978):

$$u(h) = u_{\mathrm{R}} \left(\frac{h}{h_{\mathrm{R}}} \right)^{\alpha}, \tag{5.4}$$

where u_{R} is the wind speed at a reference height h_{R} and α is a coefficient which depends on the stability of the atmosphere. One can easily prove that u_{R} and h_{R} are linked such that we set $h_{\mathrm{R}} = 500$m in what follows and the power law is determined by two

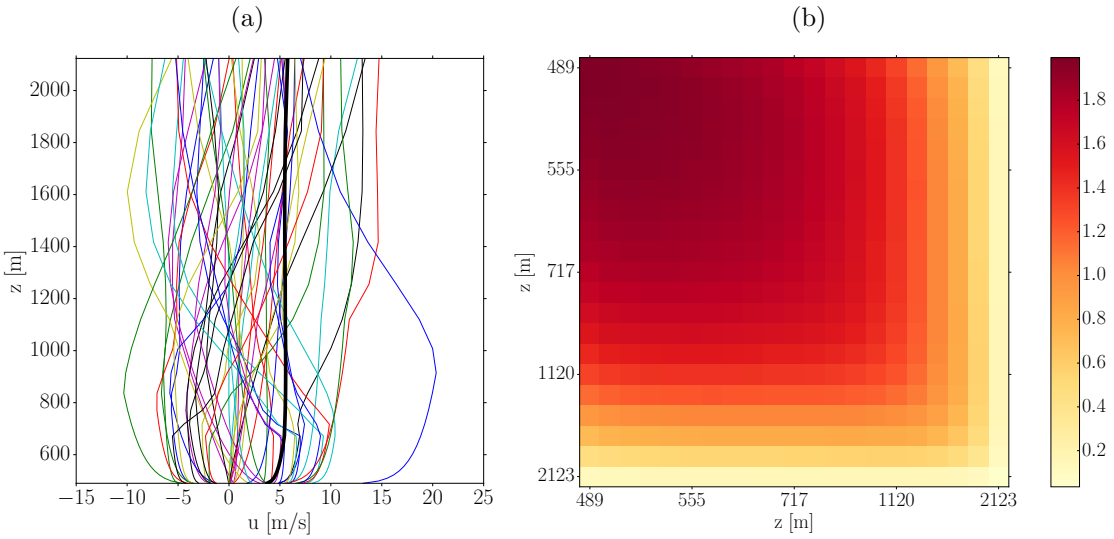

Figure 5.4: a) Example of 50 vertical profiles of wind velocity obtained from WRF results interpolated to the location of the western boundary of the 2D *Code_Saturne* domain and stretched near the ground using a power law. The thicker, black line shows the vertical profile of mean absolute velocity, averaged over the 2.10^4 profiles obtained from 3 years of WRF simulations. b) Background error covariance matrix for the vector of BC prescribed for the 2D *Code_Saturne* simulations. The correlations are estimated from the climatological variability and the variances correspond to the mean WRF simulation error.

independent parameters: u_{R} and α. Note that we always refer to relative height above the ground as h whereas z represents absolute altitude.

For each WRF simulation, we find the power law that best fits the wind profile below $\hat{h}^{\mathrm{w}}$, where the superscripts 'w' and 's' refer to the variables in the WRF and *Code_Saturne* domains respectively and the variables with hat correspond to the values at the level where the profiles must match. The level $\hat{h}^{\mathrm{w}}$ is estimated for each profile as the height below which the WRF velocity increases with height. We thus obtain a couple of parameters $(u_{\mathrm{R}}^{\mathrm{w}}, \alpha)$ such that for any $h^{\mathrm{w}} < \hat{h}^{\mathrm{w}}$ the wind velocity simulated by WRF $(u(h^{\mathrm{w}}))$ approximately follows the power law:

$$u(h^{\mathrm{w}}) \approx u_{\mathrm{R}}^{\mathrm{w}} \left(\frac{h^{\mathrm{w}}}{h_{\mathrm{R}}^{\mathrm{w}}} \right)^{\alpha}. \tag{5.5}$$

Figure 5.3b shows an example of WRF profile (blue) which is approximated by a power law (green) below $\hat{z} = \hat{h}^{\mathrm{w}} + z_0^{\mathrm{w}}$, where z_0^{w} refers to the elevation of WRF topography there.

To project the vertical wind profiles on the *Code_Saturne* grid, we keep the same power-law exponent α but we recalculate the reference velocity $u_{\mathrm{R}}^{\mathrm{s}}$ such that the new power-profile $u^{\mathrm{s}}(h^{\mathrm{s}})$ matches the WRF profile at $\hat{z}$, where the simulated wind speed is $\hat{u}$.

Written in the frame relative to the *Code_Saturne* topography, this junction height is $\hat{h}^{\mathrm{s}} = \hat{h}^{\mathrm{w}} + \Delta z_0$ where $\Delta z_0 = (z_0^{\mathrm{w}} - z_0^{\mathrm{s}})$ is the difference in topography between WRF and *Code_Saturne*. Consequently, we must have

$$u^{\mathrm{s}}(\hat{h}^{\mathrm{s}}) = u_{\mathrm{R}}^{\mathrm{s}} \left(\frac{\hat{h}^{\mathrm{w}} + \Delta z_0}{h_{\mathrm{R}}} \right)^{\alpha} \equiv \hat{u}, \tag{5.6a}$$

$$\Leftrightarrow u_{\mathrm{R}}^{\mathrm{s}} = \hat{u} \left(\frac{h_{\mathrm{R}}}{\hat{h}^{w} + \Delta z_0} \right)^{\alpha}. \tag{5.6b}$$

Using the couple of parameters $(u_{\mathrm{R}}^{\mathrm{s}}, \alpha)$ thus obtained, we can compute the wind velocity profile for all the *Code_Saturne* vertical levels below $\hat{z}$, shown on red in Figure 5.3b. We eventually obtain a full vertical profile by keeping the result of WRF simulation above $\hat{z}$ (blue curve in Fig. 5.3b) and completing it with the stretched power law below (red curve in Fig. 5.3b).

Construction of the background error covariance matrix

We hypothesise that the background error covariance matrix, related to the vector of BC, is a combination of the climatological variability in WRF simulations and of the mean error made by WRF at a given height. We thus estimate the correlations of the background error covariance matrix $\mathbf{B}$ from a climatological covariance matrix ($\mathbf{V}$) and the variances of $\mathbf{B}$ correspond to the estimated WRF errors ($\boldsymbol{\lambda}$). Each coefficient of the background error covariance matrix $\mathbf{B}$ is thus given by:

$$B_{i,j} = \frac{V_{ij}}{\sqrt{V_{ii} V_{jj}}} \sqrt{\lambda_i \lambda_j}. \tag{5.7}$$

The climatological covariance matrix is estimated from the series of control vector estimates, obtained from WRF simulations as explained in the previous section (Fig. 5.4a). The matrix $\mathbf{V}$ thus represents the climatological variability of velocity, in time, simulated by WRF and is very informative with respect to the patterns of covariances.

In order to get a background error covariance matrix that represents well the confidence given in WRF results, we set the variances of $\mathbf{B}$ equal to the mean error made by WRF. This error mainly depends on the distance to the ground (Shimada et al., 2011, Fig. 3a) and increases with height. In fact, the influence of topography is smaller at higher levels such that the WRF simulations are generally more precise there. From data shown in Shimada et al. (2011), we can deduce an approximate expression of the mean absolute WRF error as a function of height:

$$\epsilon_{\mathrm{w}}(h) = \begin{cases} |2 - 3 \times \frac{h}{2500}| & \text{if } h < 2500\text{m}, \\ 1 & \text{if } h > 2500\text{m}. \end{cases} \tag{5.8}$$

For each of the l control variables, defined at the vertical level h_i, we compute the coefficient $\lambda_i = \epsilon_{\mathrm{w}}(h_i)$.

Figure 5.4b shows the background error covariance matrix associated with the error for the background vector of BC, estimated using equation (5.7).

5.2.4 Experimental set-up

At first we consider a 2D vertical section of the domain over realistic topography (Fig. 5.5). The wind field is simulated over this 2D domain with the open-source CFD model *Code_Saturne*. In all the atmospheric simulations performed with *Code_Saturne* in this chapter, the flow is considered steady, the density is assumed constant, and turbulence is modelled by a constant mixing length equal to 10m. The RANS closure model is used such that the simulated variables, and therefore the velocity components, correspond to temporal means (see Section 1.2.2). Symmetric BC are set for lateral faces (South and North), the top boundary is an inlet and the eastern face is a free outlet. The inlet vertical wind profile is prescribed at the western boundary. It is this vertical profile defined in 21 vertical levels that we try to retrieve with DA. The BC are constant in time and the simulations are run over a sufficiently long time for steady state to be reached.

A reference simulation is performed with a prescribed boundary profile, considered as the truth, shown in Figure 5.5. We can see that horizontal wind accelerates over crests, which therefore represent a preferred location to install wind turbines. Wind speed values are observed at $x = 1800$m, corresponding to a local crest (dashed line in Figure 5.5), and at five different heights above the ground: 10m, 25m, 50m, 75m, and 100m. These wind speed values constitute pseudo-observations used in the DA process. To account for instrumental errors, which are generally of the order of magnitude of a few centimetres per second, Gaussian white noise with a variance of $10^{-3}\text{m}^2/\text{s}^2$ is added to these pseudo-observations. Observation error includes the instrument error and the representativeness error which we represent by a diagonal observation error covariance matrix

$$\mathbf{R} = r\mathbf{I} \tag{5.9}$$

with $r = 0.1\text{m}^2/\text{s}^2$. Note that the observation error includes the representativity error in addition to the instrumental error, which explains that r is larger than the variance of the white noise added to the synthetic observations.

The departure of the background from the true profile of inlet wind velocity is consistent with the background error covariance matrix $\mathbf{B}$ defined in Section 5.2.3. Note that the largest eigenvalue of $\mathbf{B}$ is equal to $29.5\text{m}^2/\text{s}^2$.

For 3D-Var, the increment used in the finite difference approximation is set to 10^{-2}. The control space, in which the cost function is minimised, corresponds to the vector of BC, defined in 21 vertical levels.

For the IEnKS and 3D-Var, the same criterion of convergence is defined for the cost function: the minimisation algorithm stops when the change in the cost function, relative to the initial value of $\mathcal{J}$, is smaller than $e_\text{J} = 1\%$.

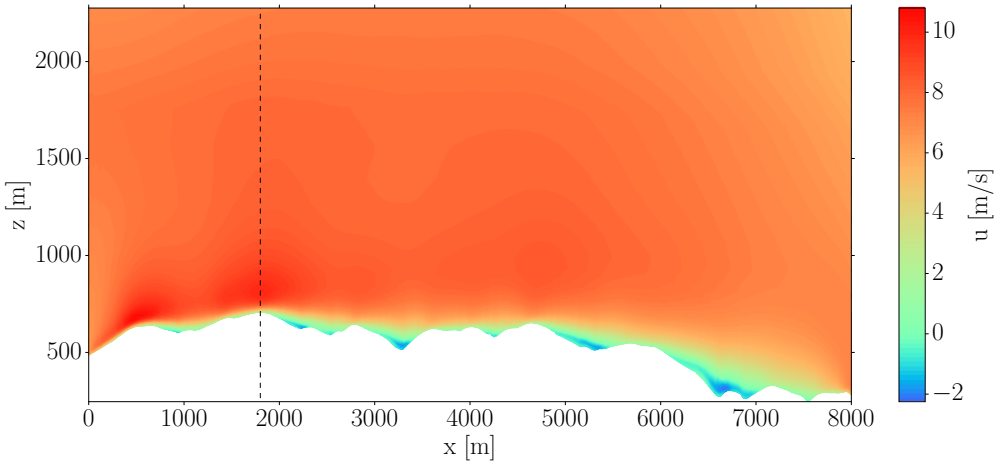

Figure 5.5: Wind field simulated with *Code_Saturne* over the 2D vertical domain. The vertical dashed line shows the location of the virtual instrumented mast which provides synthetic observations for the twin experiments.

5.3 Results of twin experiments in 2D

5.3.1 Results with the BFN

Parameters for the BFN algorithm

As explained in Section 3.2.5, the BFN algorithm can be applied with *Code_Saturne*. Each forward or backward integration includes nudging toward an analysis state, computed as the Best Linear Unbiased Estimator (BLUE). This first step (BLUE) requires the definition of a few parameters, and the values used in the present work are given below. First, as explained in Section 3.2.4, we set the length of the spin-up period to 500 time steps, where the time step varies in space and time between 0.1s and 100s. The length of the data assimilation window (DAW) is also equal to 500 time steps, such that each integration corresponds to 1000 time steps.

The background error covariance matrix for the BLUE analysis is parametrised by a Cressman function with a given radius of influence. In the present study, we take the horizontal radius equal to $L_{\mathrm{H}} = 5000\mathrm{m}$ and the vertical one is set to $L_{\mathrm{z}} = 200\mathrm{m}$ (Duraisamy et al., 2014). As mentioned in Section 4.2.2, the nudging matrix should be of the same order of magnitude as $\mathbf{R}^{-1}$. Since $\mathbf{R}$ eigenvalues are equal to $r = 0.1\mathrm{m}^2/\mathrm{s}^2$, the nudging matrices applied in both forward and backward integrations are equal to $\mathbf{K} = k\mathbf{I}$ with $k = 10\mathrm{s/m}$ and $\mathbf{I}$ the identity matrix.

Nonlinearity issue

Applying the BFN algorithm to the simulation with *Code_Saturne* in 2D over complex topography, we have faced an issue of non-reversibility of the integrations. In fact, if the nudging term is set to zero, the sequential integration of the forward and backward

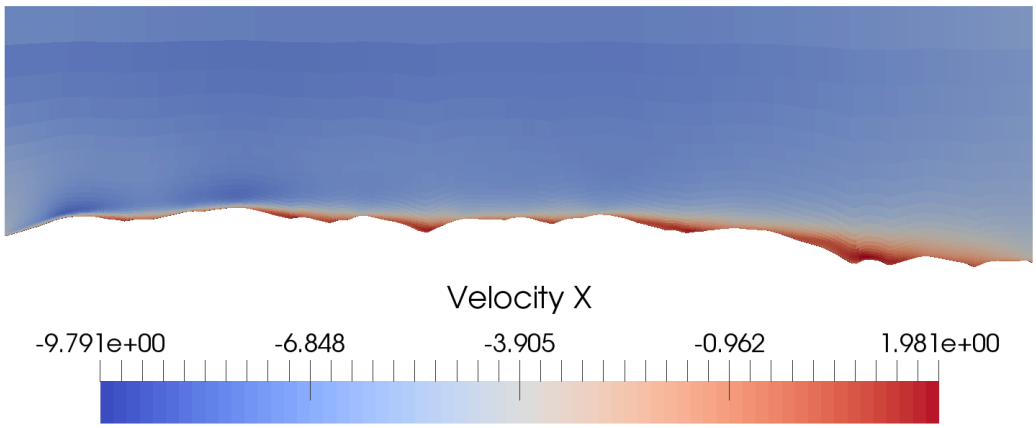

(a)

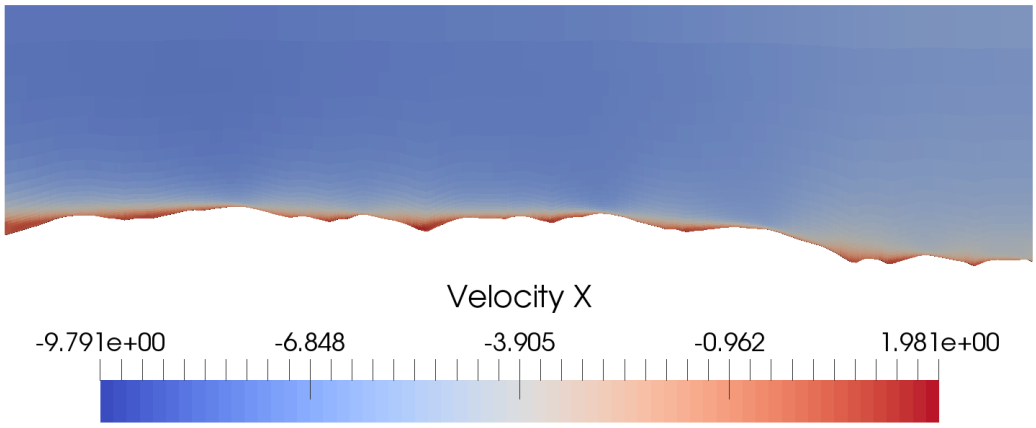

(b)

Figure 5.6: Velocity field (a) at the beginning of the backward integration, obtained by reversing the flow field obtained at the end of the forward integration and (b) at the end of the backward integration. Both integrations are performed without nudging.

equations should bring the system back to its initial state.

We have tested if this reversibility condition is satisfied with *Code_Saturne* following the methodology previously presented (see Section 3.2.5). The nudging coefficient is thus set to $k = 0$s/m for this test. The system state obtained after one iteration – i.e. successive forward and backward integrations – appears to be different from the initial state. The observed differences mainly come from the nonlinearity effects of topography, i.e. the recirculation after topography peaks.

In the backward integration, as the velocity field is reversed, the left side of any topography peak – which corresponds to the upwind side in the forward integration – becomes downwind. Consequently spurious recirculation form on the left side of the topography peaks in the backward integration, whereas they should be on the right. We can see in Figure 5.6 that the recirculation that is downwind at the end of the forward integration – and thus upwind at the beginning of the backward integration – move downwind during the backward integration. In particular, the left border of the domain is near a peak and a recirculation form there. As a matter of fact, when the result of the backward integration along the left border is used to prescribe the upstream BC for the next forward integration, this spurious recirculation dramatically affects the vertical profile of velocity (see Fig. 5.7). Consequently, the reversibility condition of the BFN algorithm without nudging – in its version applied here – is not satisfied.

This experiment highlights that the nonlinearities induced by the steep topography (recirculation after the peaks) are too strong and the backward integration cannot be performed by simply reversing the flow. Consequently, the BFN algorithm that has been developed for the 1D shallow-water equations (SWE) and presented above cannot be applied in cases with strong linearity effects.

Sensibility analyses

We have performed sensibility analyses to assess the effect of several parameters on the BFN results. First, we have tried to increase the vertical extent of the domain in order to have the highest levels unperturbed by the nonlinear effects due to steep topography. Even though the values of BC are kept unchanged at these high levels, the lowest levels – which are the most important for the micrometeorological applications studied here – are largely affected by the recirculation. Consequently this approach does not solve the non-reversibility issue.

In a second time, we have varied the mixing length between $L = 1$m, $L = 50$m, and $L = 100$m without any clear effect on the results. The length of the spin-up period as well as the DAW have also been changed, differently for the forward and backward integrations. We have also performed some sensibility analyses to the radius of influence using in the Cressman function, both in the horizontal and vertical direction, and to the nudging matrices. Here again, we have not found any clear consequence of varying these two parameters.

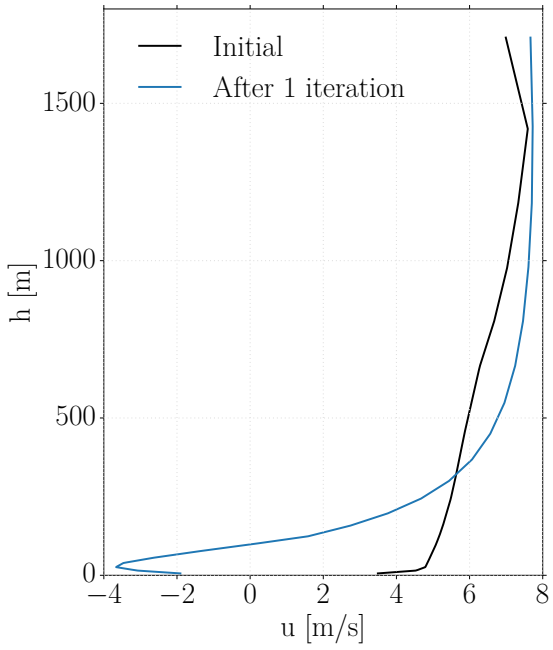

Figure 5.7: Left BC prescribed for the first forward integration and obtained after a one forward and one backward integration, without nudging.

Perspectives for the BFN algorithm

The inadequacy of the revised version of the BFN algorithm to nonlinear cases have lead us to put this method aside and to not test further this method. Some perspectives have been foreseen, though we have not been able to implement them. First, the domain could be extruded with flat topography on each side of the domain. This would prevent from having recirculation affecting the downstream BC. Another possibility could be to develop a linear version of the model that would be applied for the backward integration. This solution would be similar to the adjoint approach for which the model used to integrate the equations backward in time is a linearised version of the forward model.

5.3.2 Results with the IEnKS in 2D

In order to analyse the results obtained with DA methods, we consider two statistical indicators. First, the *error* refers to the departure from the truth as defined in equation 2.1, and corresponds to the ensemble mean. Second, the *uncertainty* is related to the ensemble spread and refers to the confidence interval of the BC estimate, and of the resulting wind field simulations. We also compute the root mean square error (RMSE) of the simulated wind field with a given set of BC, compared to the wind field obtained when the reference BC are prescribed.

With the 2D configuration presented above, we perform a sensitivity analysis to the number of members and to the method used to generate the initial ensemble (not shown). We consider ensembles of 2, 3, 5, 8, 10, and 20 members. For each ensemble size, we

consider two methods of ensemble generation. In one case, the members correspond to the eigenvectors associated with the largest eigenvalues of the singular value decomposition (SVD) of the background error covariance matrix. The second method consists in randomly sample the members, according to the background error covariance matrix. With this second method, we repeat the experiment 15 times for each ensemble size. In both cases, the ensembles are recentred to ensure that the anomaly matrix has zero mean.

With the first method of ensemble generation based on SVD, the error in the analysis BC and the global RMSE of the simulated wind field depend very little on the number of members (not shown). Even with very small ensembles, the IEnKS is able to correct the BC and to reduce the error in the simulated wind field. This is consistent with the fact that the control variables are highly correlated in the vertical.

With random samplings of the ensemble members, on average, the error in the BC and the RMSE of the wind field do not depend much on the number of members. However, the variability of results obtained with the 15 ensembles of same size is quite large, especially for small ensembles (2 or 3 members). With both methods of ensemble generation, the IEnKS always converges in 2 or 3 iterations. The observed sensitivity to random sampling for a given ensemble size motivates us to choose the method based on SVD for the following experiments. Since the results are not sensitive to the number of members with this method, we decide to keep 3 members for what follows.

We also verify that in the lower atmosphere ($z < 800$m), the analysis is nearly insensitive to the background. We have randomly drawn 15 values for background error, according to the same background error covariance matrix, and we assimilate the same observations. The analysis profiles of BC are quite similar to each other below 800m, whereas in the upper layers of the atmosphere, the analysis depends more on the background. These results are consistent with the fact that observations are only available below 800m and that a large weight is given to the observations ($\mathbf{R}$ is much smaller than $\mathbf{B}$). In all the cases, the RMSE computed over the whole domain is smaller for the analysis than for the background and the analysis RMSE is smaller than 0.5m/s for the 15 experiments.

Finally, we perform a sensitivity analysis to verify that the results do not depend on the parameters of the CFD simulations. In twin experiments, the results are almost insensitive to the mixing length or to mesh resolution.

5.3.3 Comparison between the IEnKS and 3D-Var in 2D

The IEnKS and 3D-Var are both used to solve the DA problem defined in Section 5.2.4. The control vector contains the 21 values of horizontal velocity, constituting the vertical wind profile prescribed as western BC.

Figure 5.8 shows the results obtained with the IEnKS and 3D-Var in this 2D case. The first panel (Fig. 5.8a) shows the vertical profiles of BC for the reference simulation

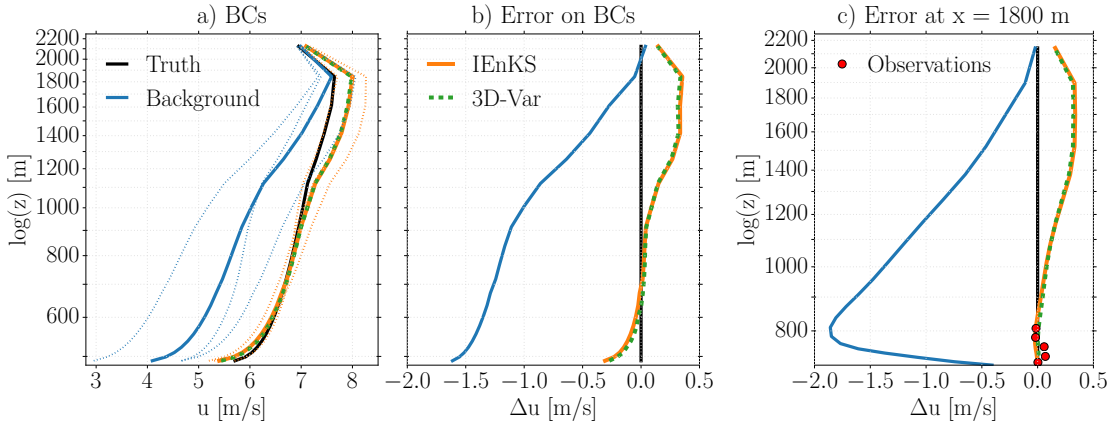

Figure 5.8: Results in 2D with the IEnKS (ensemble of 3 members) and 3D-Var. a) Vertical profile of velocity used as BC in 2D: truth (black), background (blue), and analysis (IEnKS: orange and 3D-Var: dashed, green) profiles. The background (dotted blue) and analysis (dotted orange) ensembles of the IEnKS are also shown. b) Departure from the truth of the background and analysis vertical profiles of velocity used as BC in 2D. c) Departure from the true vertical profile of velocity simulated at the location of observations, $x = 1800$m, for the background and analysis profiles. The noisy observations (red dots) are also shown.

(black), the background (blue), and the analyses obtained with the IEnKS (orange) and 3D-Var (green). The background (dotted blue) and analysis (dotted orange) ensembles are also shown. To better show the impact of the DA methods, the true values of velocity are subtracted to present the background and analysis errors in the BC (Fig. 5.8b). Similar errors are shown at the location of observations ($x = 1800$m) at the end of the simulation (Fig. 5.8c). It can be seen that with both methods the error is largely reduced for the BC, and thus within the domain, especially where observations are available. The two methods give very similar results, which is consistent with the fact that they minimize the same cost function.

Table 5.1 presents the error in the BC and the subsequent error in the simulated velocity field. The maximum error and the mean absolute error (MAE) are given for the BC. Regarding the error of the velocity field, we give the local maximum and the RMSE computed over the whole 2D domain. These error statistics are given for the background and for the analyses obtained with the IEnKS and 3D-Var. We can see from this table the large sensitivity of the velocity field to BC. The error in the background BC is of 1.07m/s on average and smaller than 1.61m/s for all the control variables. However, it triggers errors in the domain that locally reach 2.48m/s. The results presented in Table 5.1 show that the two DA methods have the same capacity to greatly reduce the error in the BC and thus in the whole velocity field.

In the table, we also give the number of integrations needed for the methods to converge. The inner algorithm of the IEnKS converges in 2 iterations and we consider

	Error in BC(m/s)		Error in simu. velocity field (m/s)		STD of simu. ensemble (m/s)		Nb of integ.
	max	MAE	max	RMSE	max	mean	
Background	1.61	1.07	2.48	1.06	1.39	0.59	
IEnKS	0.35	0.14	0.35	0.15	0.28	0.13	6
3D-Var	0.34	0.13	0.34	0.15			110

Table 5.1: Results in 2D with the IEnKS (ensemble of 3 members) and 3D-Var on the same case (same background and same observations). Error in the BC (maximum error and mean absolute error - MAE), error in the simulated velocity field (local maximum and root mean square error - RMSE), standard deviation (STD) of the ensemble of simulated velocity fields (local maximum and average over the whole 2D domain), and the number of model integrations necessary to obtain the analysis.

an ensemble of $N = 3$ members, such that the IEnKS requires only 6 integrations of *Code_Saturne*. The minimisation algorithm used for 3D-Var requires 5 iterations which correspond to more than 100 integrations. In fact, for each iteration, $l + 1$ integrations are required to estimate the gradient of the cost function by finite differences, where $l = 21$ is the size of the control vector. In this case, the IEnKS is thus much more efficient regarding computational cost.

The spread of the background ensemble, used in the IEnKS, characterizes the estimated uncertainty of the background BC. Similarly, the spread of the updated ensemble, at the end of the IEnKS analysis, provides a diagnostic of the posterior error for the BC. For each ensemble member – which corresponds to a profile of BC – we run the CFD model *Code_Saturne* forced with these BC. We thus obtain background and analysis ensembles of simulated wind fields. The spread of these ensembles characterise the accuracy of the simulated wind field. Figure 5.9a shows the standard deviation (STD) of the ensemble of simulated wind fields. The larger the STD is, the less precise is the velocity field, simulated with the ensemble mean (here the background) prescribed as BC. We can see that the STD is particularly large between 50m and 100m above the ground, especially over local crests, where it is the most crucial for wind resource assessment. Figure 5.9b shows the STD of the analysis ensemble which is everywhere smaller than the background STD. As an example, we analyse more precisely the vertical profile of STD above a local crest ($x = 3600$m, shown by the green triangle in Figure 5.9a). The vertical profiles of STD of the background and analysis ensembles of simulated wind fields are shown in Figure 5.9c. We can observe that thanks to the IEnKS, the uncertainty is largely reduced near the ground – where observations are available – and that the influence of observations vanishes with height. Even at high altitudes the IEnKS helps to reduce the uncertainty in the simulations. This vertical pattern of analysis STD is observed in all the 2D domain. It is observed that for 90% of the grid points, the STD is divided by

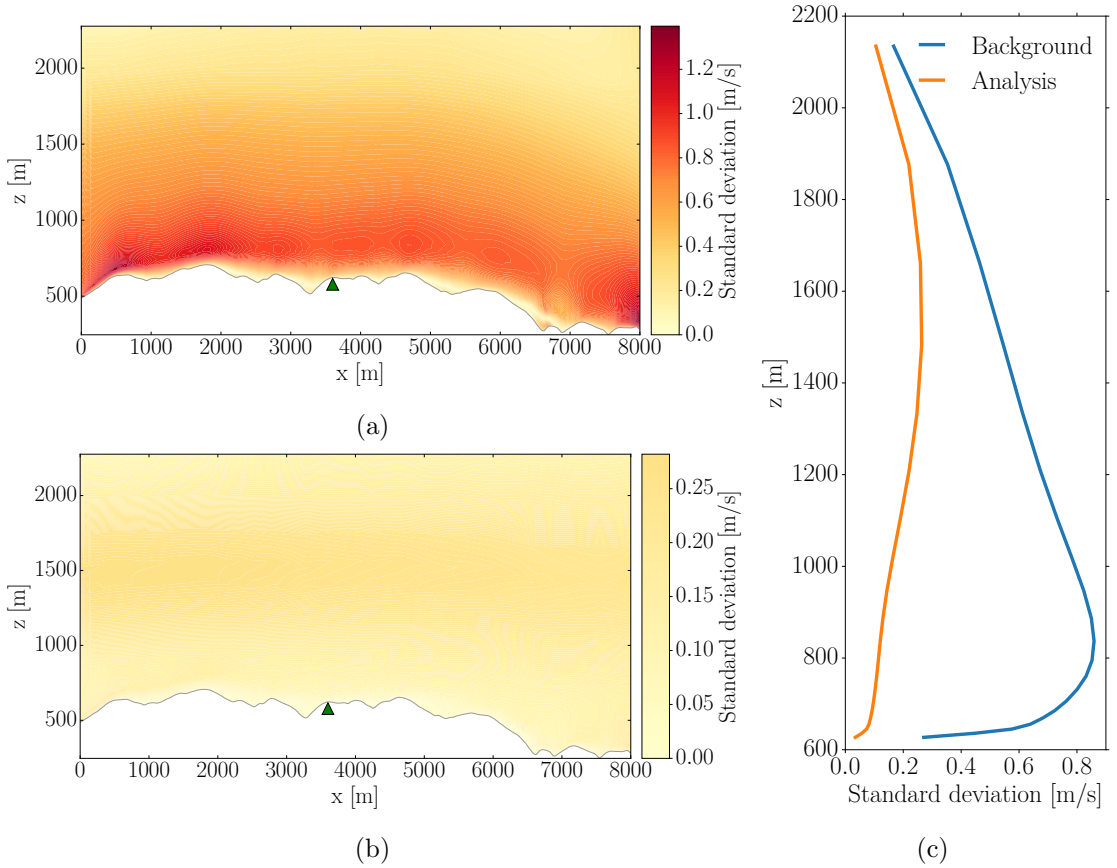

Figure 5.9: Standard deviation of the ensemble of 2D velocity fields simulated with a) the background ensemble members prescribed as BC and b) the analysis ensemble members. c) Vertical profile of background (blue) and analysis (orange) uncertainty on u at a local crest ($x = 3600$m, green triangle on panel a). The uncertainty corresponds to the STD of the ensemble of simulated velocity fields.

more than 1.6 between the background and the analysis. The points where the STD is not reduced are points where the background STD is already small. Table 5.1 gives the local maximum of STD and its average value computed over the whole 2D domain. The large decrease in these values of STD proves that, besides decreasing the mean error in the BC, the IEnKS helps to increase the accuracy of the control vector estimate and consequently of the simulated wind field.

The twin experiments performed in 2D have allowed to compare the performances of the IEnKS with 3D-Var. In order to gradually increase the complexity of the test cases, we first perform twin experiments with the 3D domain (Section 5.4) and then we assimilate field measurements (Section 5.5).

5.4 Results of twin experiments in 3D

5.4.1 Experimental set-up

We consider in this section a 3D domain which extends from $x = 0$m to $x = 4$km, from $y = -2$km to $y = 2$km, and from $z = 288$m to $z = 2318m$. As explained in Section 5.2.1, the control vector in 3D is of size $l = 840$, which corresponds to 20 vertical profiles for u and v, defined in 21 vertical levels (Fig. 5.3a). This control vector is too large to use 3D-Var with finite differences, consequently we only use the IEnKS in this 3D case.

The reference value of the control vector corresponds to one of the WRF results projected on the finer, local grid, as explained in Section 5.2.3. The background is obtained as a perturbation of this true vector of BC. The departure of the background from the truth is randomly sampled from the background error covariance matrix $\mathbf{B}$, defined in Section 5.2.3.

We consider synthetic observations coming from 3 virtual instrumented masts located at:

- $x = 2000$m and $y = 0$m (mast M80),
- $x = 1750$m and $y = -1290$m (mast M),
- $x = 3670$m and $y = 605$m (mast P).

For each mast, pseudo-observations of u and v are extracted at 10, 25, 50, 75, and 100m above the ground. Consequently, 30 observations are extracted from the reference simulation and Gaussian white noise is added to them. The observation error covariance matrix is $\mathbf{R} = 0.1\mathbf{I}\text{m}^2/\text{s}^2$.

The precision required for the IEnKS algorithm to stop is set to $e_\text{J} = 1\%$.

5.4.2 Results with the IEnKS

The IEnKS has been tested on the 3D case with ensembles of 2, 5, 10, 15, 20, 30, and 50 members, all other things remaining equal – such as the background and the noisy observations. We compare the analysis BC and the steady wind field, obtained when these BC are prescribed, to the reference BC and wind field. In particular, we compute the MAE of the BC and the RMSE of the wind field over the whole domain. The sensitivity of the results to the number of members is rather small (not shown). The MAE and the RMSE slightly decrease from 2 to 10 members and then increase again. This could be explained by the fact that increasing the ensemble size increases the number of degrees of freedom which is beneficial between 2 and 10 ensemble members. The slight deterioration of the results with ensembles larger than 10 could be explained by overfitting. In fact, the background error covariance matrix is not perfectly known and increasing the ensemble size tends to represent more precisely the incorrect background

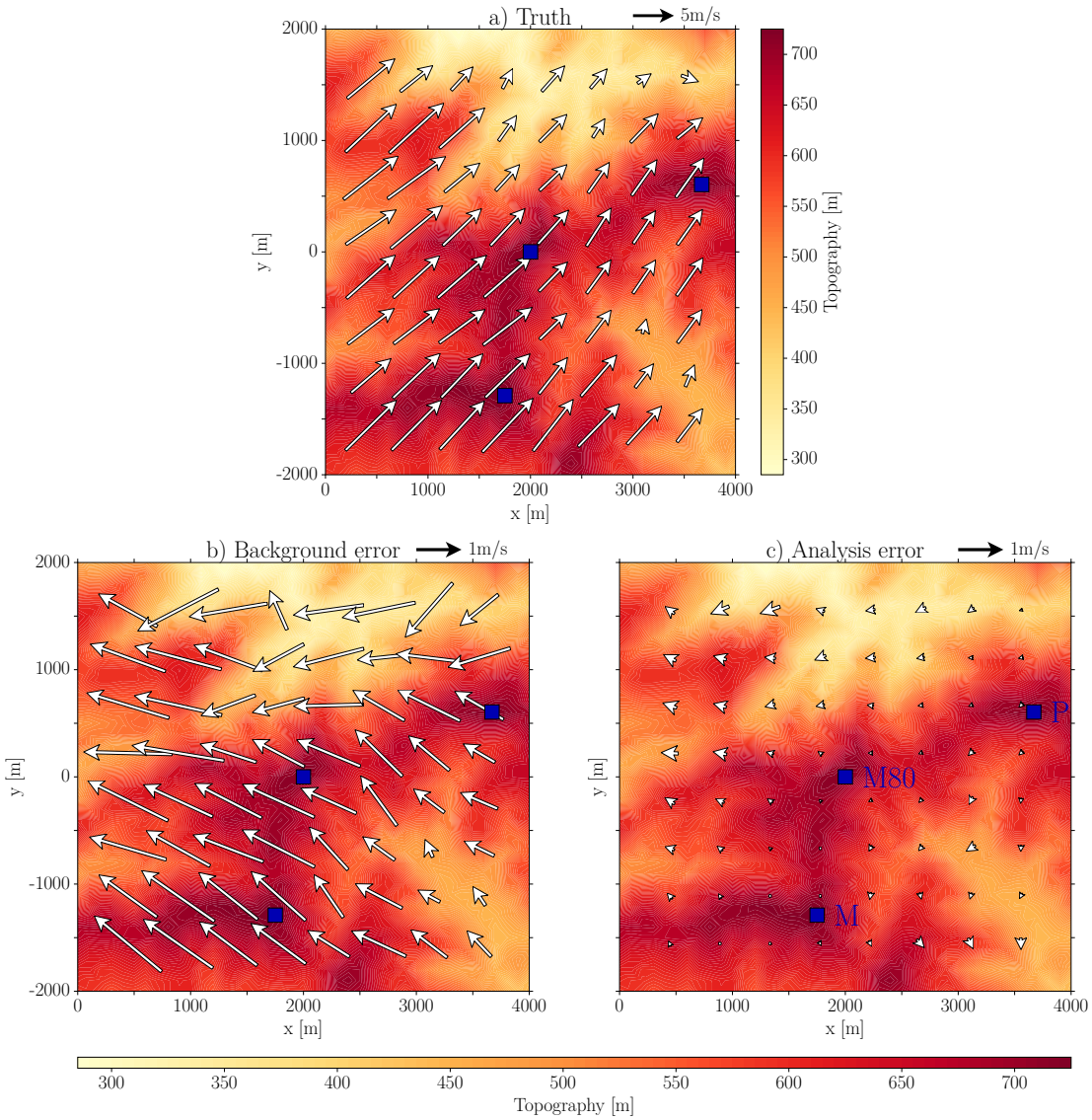

Figure 5.10: Results of the IEnKS in 3D with 5 members. Relief (shaded) and horizontal velocity field (arrows) in the plane of constant height above the ground $h = 80$m. The blue squares represent the location of the three virtual masts providing pseudo-observations. For the sake of visibility, only 3% of the horizontal velocity vectors are shown in the figures. a) Reference velocity field obtained with true BC. b) Background error in the velocity field. c) Analysis error in the velocity field.

	Error in BC (m/s)		Error in simulated velocity field (m/s)		STD of simulated ensemble (m/s)			
					u		v	
	max	MAE	max	RMSE	max	mean	max	mean
Background	2.96	0.96	3.40	0.89	1.28	0.41	1.25	0.41
IEnKS	2.00	0.40	1.90	0.20	0.68	0.10	0.38	0.11

Table 5.2: Results in 3D with the IEnKS (ensemble of 5 members). Error in the BC (maximum error and mean absolute error - MAE), error in the simulated velocity field (local maximum and root mean square error - RMSE), and standard deviation (STD) of the ensemble of simulated velocity fields for u and v (local maximum and average over the whole 3D domain).

error statistics. Consequently the analysis is negatively affected. For the sake of numerical efficiency we thus adopt an ensemble of 5 members in what follows.

Table 5.2 presents some statistics for the background and analysis errors. We can see that the IEnKS helps to divide by more than 2 the MAE of the BC and thus to divide by more than 4 the RMSE of the velocity field simulated in the whole domain. In this case the IEnKS has converged in 3 iterations such that it has required 15 integrations of *Code_Saturne*.

Figure 5.10 shows the results obtained with an ensemble of 5 members, in the surface defined by $h = 80$m, where h is the relative height above the ground. This height is chosen because it corresponds to a typical hub height of wind turbine. The background colors represent the topography of the domain, above which the arrows represent the horizontal velocity field (only a subset is shown). Figure 5.10a shows the reference wind field obtained with the true BC and Figure 5.10b and c show the departure from this wind field for the background and the analysis. We can see in Figure 5.10b that the background error is larger over higher topography. Figure 5.10c shows that the IEnKS allows to largely reduce the error in the wind field, especially near the available observations.

Figure 5.11a shows the true, background, and analysis values of the vertical profile of u prescribed as BC at $x = 0$m and $y = -350$m. Figure 5.11b shows the background and analysis errors for this same profile of BC and Figure 5.11c shows the vertical profile of u simulated at the location of the mast M80 ($x = 2150$m and $y = 0$m). We can see that the analysis error at this location is greatly reduced thanks to the IEnKS. Note that Figure 5.11 only shows the u velocity component for one of the 20 vertical profiles included in the control vector. However, the conclusions drawn for this particular case also hold for the v velocity component and for the other vertical profiles.

Figure 5.11a and b also show the background and analysis ensemble members. The analysis ensemble is narrower than the background ensemble, meaning that the confidence in the analysis has improved over that in the background. The STD of the velocity fields obtained when the different members of the background ensemble are prescribed as BC

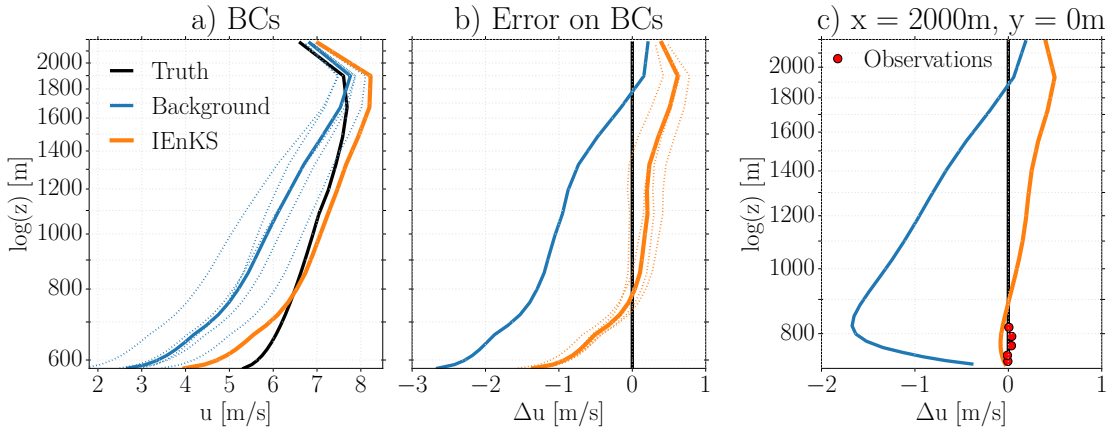

Figure 5.11: Same as Fig. 5.8, for the 3D twin experiment. A logarithmic scale is used for the vertical axis. a) Vertical profile of the BC on u located at $x = 0$m and $y = -350$m, in the middle of the western boundary. The dotted, blue curves correspond to the background ensemble members. b) Departure from the true profile of BC for u. The dotted, orange curves correspond to the analysis ensemble members. c) Error in the vertical profile of velocity simulated at the location of the mast M80 ($x = 2000$m and $y = 0$m).

is indicative of the uncertainty in the background wind field. Figure 5.12a shows the values of this background STD, for the u-component of velocity, for all the points in the plane of constant height above the ground $h = 80$m (colors). The topography is also shown (contours) and we can observe that the STD is generally larger above the crests. This pattern of uncertainty is largely smoothed by the IEnKS, and the values of STD for u and v are divided by more than 2 for 90% of the grid points between the STD of the background and the analysis ensemble (see Fig. 5.12b). The local maxima of STD for u and v and the mean calculated over the whole domain are given in Table 5.2. Globally, the STD of the simulations with the analysis ensemble is smaller than 0.68m/s for u and than 0.38m/s for v. Since the operational objective of DA in the present study is mainly to improve the wind estimate above local crests – where wind turbines might be installed – we present in Figure 5.12c the vertical profile of STD over a crest at $x = 800$m and $y = -1400$m (green triangle on Fig. 5.12a). Figure 5.12c shows the vertical profile of STD for u (solid line) and v (dashed line), simulated with the background (blue) and analysis (orange) BC. For both velocity components, the IEnKS helps to largely reduce the uncertainty in the simulated velocities, and especially near the ground where observations are available.

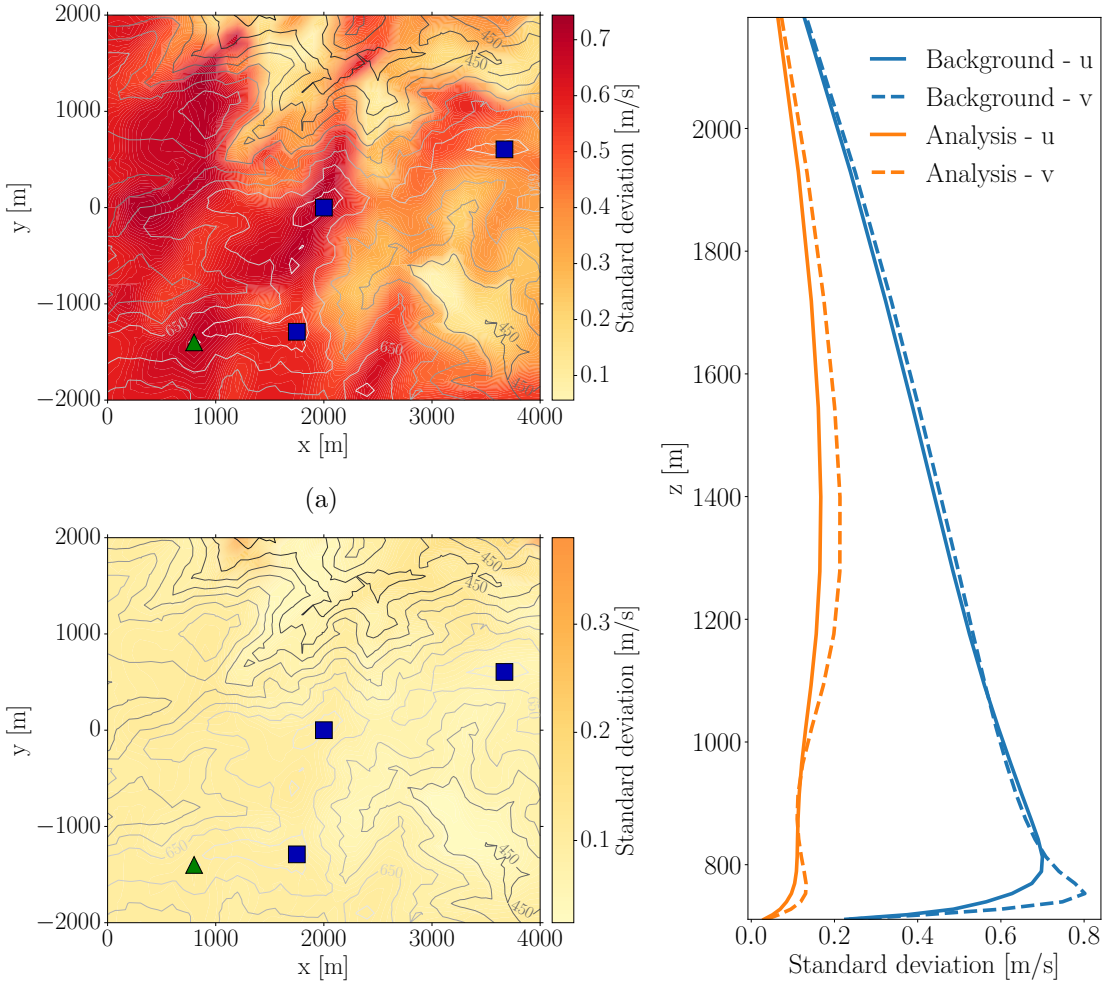

Figure 5.12: a) and b) are similar to Fig. 5.9a and Fig. 5.9b but for the 3D domain. Here we show the STD in the plane of constant height above the ground $h = 80$m, for the u-component of velocity only. The contours show topography. The blue squares represent the locations of the three masts. c) Same as Fig. 5.9c but for the results in 3D for u and v at $x = 800$m and $y = -1400$m, shown by the green triangle on panel a.

5.5 Results with field measurements in 3D

5.5.1 Experimental set up

A field campaign has been performed over the 3D domain as described in Section 5.4.1, between August and December 2007. The observations are available every 10 minutes at 3 masts (M80, M, and P) whose location are given in Section 5.4.1 and shown in Figure 5.10. We use here these observations in a cross-validation procedure: we assimilate the observations provided by the masts M and P (classical cup anemometers and vanes usually available for wind farms), and we compare the results to the observations provided by the mast M80 (sonic anemometer).

The available observations at M and P are:

- wind speed at 30, 39, and 49m above the ground,
- wind direction at 30 and 47m above the ground.

Assimilating observations of wind direction is quite complex, especially because the wind direction is not well defined for small wind speeds. Since wind direction does not change much with altitude, we consider that the observations of wind direction at 47m are still valid at 49m. Consequently, we convert the observations of wind speed and direction to u and v values at 30 and 49m. At 39m we assimilate directly observations of wind speed, as nonlinear observation operator is well handled by the IEnKS. In the following experiments we thus assimilate 10 observations: the 2 wind components (u and v) at 2 heights (30 and 49m) and the wind speed at 1 height (39m) for the 2 masts (M and P).

To validate the results we use the sonic measurements available at the location of the mast M80 and at 4 different heights above the ground (10, 25, 45, and 78m). The sonics have a sample rate of 10 Hz and here we use the values averaged over 10 minutes.

To test the IEnKS in different meteorological situations and with different background errors, the results of WRF simulations are clustered following the Wind Resource Assessment and Power Production (WRAPP) methodology (see Section 1.3.6). The variables considered here in the clustering method are the wind speed, the wind direction, and the departure of the WRF results from the sonic observations. Using a k-means clustering method, 18221 hourly WRF results are clustered in 50 classes and one representative date and time is selected for each class (hereafter referred to as 'representative time'). We thus perform the cross validation process for each of these 50 representative times. The background corresponds to the result of the WRF simulation, projected on the *Code_Saturne* grid as explained in Section 5.2.3.

All the other parameters used in the IEnKS experiments are the same as for the 3D twin experiments (Section 5.4.1).

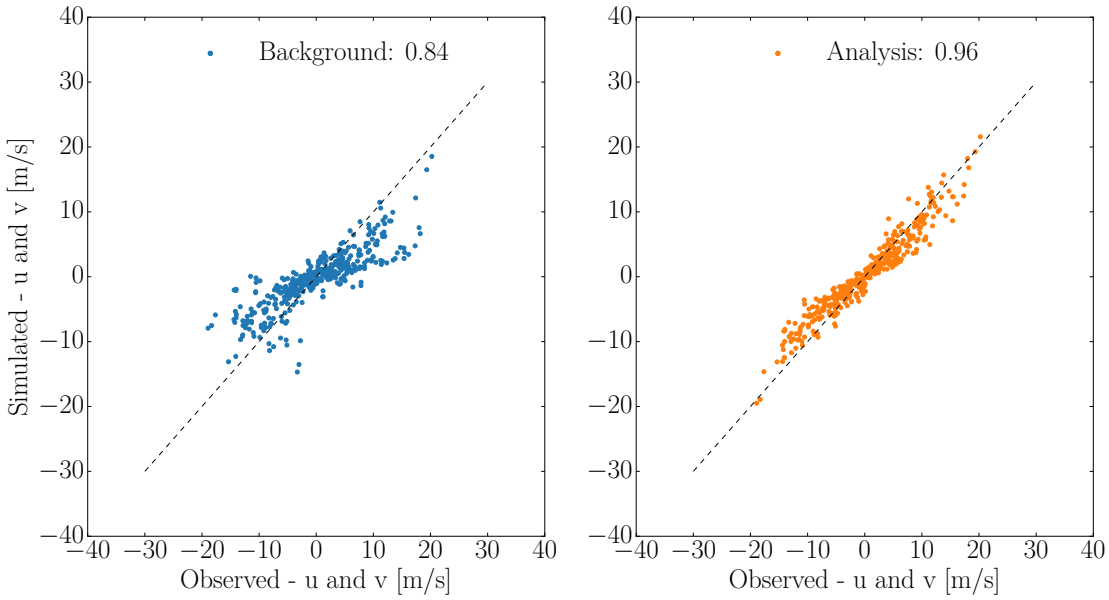

Figure 5.13: Scatter plot of observed versus simulated values for u and v at the location of the mast M80 with (left) the background BC and (right) the analysis BC for the 50 representative situations. The Pearson coefficient is given in the legend.

5.5.2 Results of cross validation

We have performed an analysis cycle of the IEnKS for each of the 50 representative times. The IEnKS generally converges in 4 to 6 iterations. The wind field simulated with the analysis BC thus obtained are compared with the observations from the sonic anemometers. Figure 5.13 shows that the agreement between the simulated and the observed values of u and v at the location of the mast M80 is significantly better with the analysis BC.

Figure 5.14a shows the analysis error – computed by comparing the simulations to the observations at M80 – against the background error for the 50 representative times. The size of the circles is proportional to the size of the class. We also show the linear regression of the points (dashed orange). We can see that the IEnKS helps reduce the error, except in some cases for which the background error is already small. The regression line indicates that the larger the background error is, the larger the error reduction – in average – by the IEnKS. This figure suggests that if the error between WRF simulations and the available observations in the domain is quite small (< 1.5m/s) it might not be beneficial to resort on DA.

Figure 5.14b shows the histograms of the errors of WRF simulations at the location of the mast M80, when compared to sonic observations (green). The histograms are representative of the 18221 situations as the representative times are duplicated according to the class size. Similar histograms are shown for the error made by *Code_Saturne* simulations when the WRF results are used as BC (blue). These BC – and the simulations

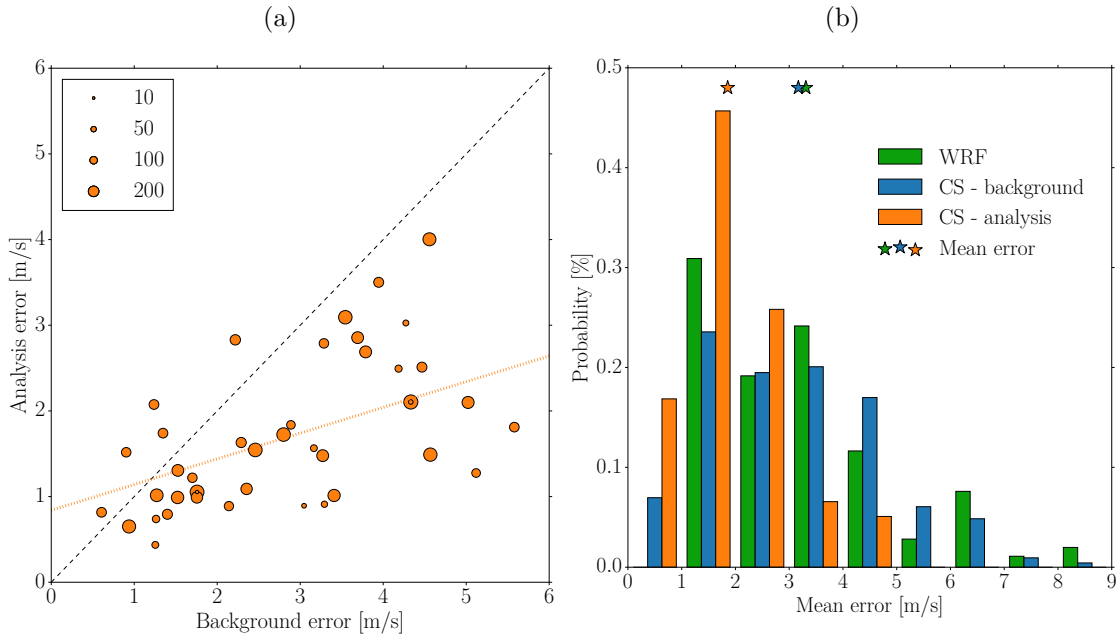

Figure 5.14: a) Analysis error versus background error for the different meteorological situations representative of the 50 classes. The size of the circles represent the class size. b) Histograms of the difference between simulation results and sonic observations.

– correspond to the background of the DA experiment. At the end of the IEnKS analysis, the simulations with *Code_Saturne* forced by the analysis BC are compared to the sonic observations at M80 to obtain the orange histogram in Figure 5.14b. The mean error made by WRF (green), *Code_Saturne* before DA (blue), and *Code_Saturne* after DA (orange) are shown by the stars at the top of the figure. We can see that the use of CFD model does not reduce much the error if the BC are imprecise. However, after a cycle of the IEnKS, the distribution of the errors is largely shifted toward smaller errors and the mean error is divided by 1.7.

To estimate the impact of DA in a context of wind resource assessment, we assume that a unique wind turbine of 6MW wind turbine is installed at the location of the mast M80. For each representative situation, we consider the wind speed, at 78 m above the ground, given by: the sonic anemometer, WRF simulations, *Code_Saturne* simulations with the BC provided by WRF (referred to as CS^b), and *Code_Saturne* simulations with the BC corrected by DA (referred to as CS^a). Using the power curve of a 6MW, we can estimate the corresponding power for each representative time. Eventually, we average the 50 power values by weighting them according to the size of the classes. We thus obtain a potential power for the wind turbine installed there. The wind power potential computed from the measurements is equal to 2993kW, WRF results lead to an estimation of 2098kW, CS^b gives 1737kW, and CS^a gives 2701kW (see Fig. 5.15). The wind potential estimated with WRF results is underestimated by 30%, with CS^b it is

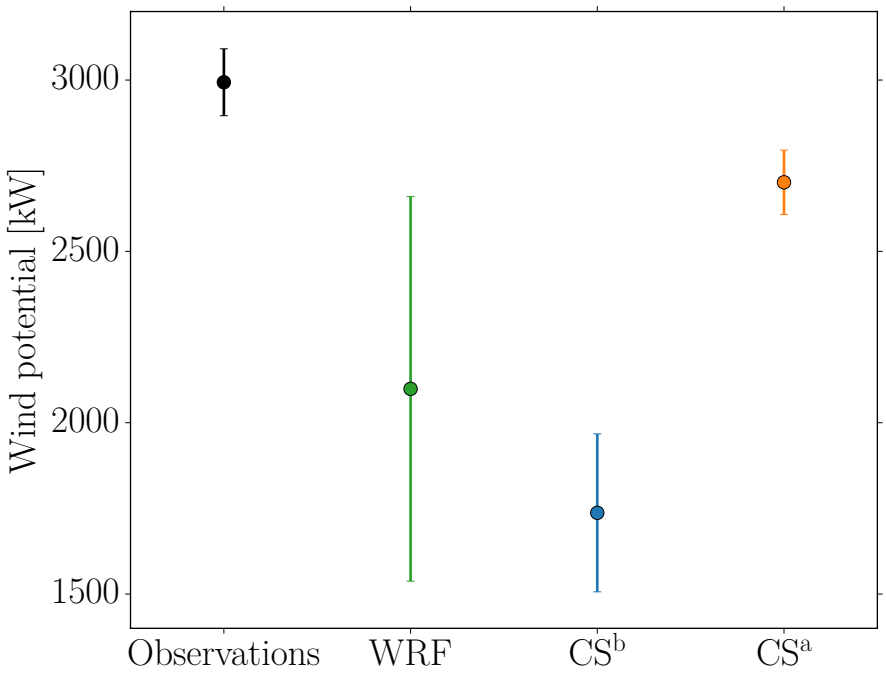

Figure 5.15: Wind potential estimated for one 80m hub height wind turbine installed at the location of the mast M80 from the sonic anemometers observations, WRF simulations, *Code_Saturne* simulations forced with background BC (CS^b), and *Code_Saturne* simulations forced with analysis BC (CS^a). The errorbars represent the difference between the minimum and maximum estimated potentials. For the observations (black) the two estimations come from the observations provided by the sonic anemometer and the cup anemometer. For the WRF simulations, they correspond it correspond to the image by the power curve of the uncertainty on WRF wind fields. And for CS^b and CS^a we take the maximum and minimum among the ensembles.

underestimated by 42%, and with CS^a by less than 10%. Moreover, the uncertainty on the wind resource estimate – which corresponds to the STD of the ensemble – is reduced from 4.7% with CS^b to 1.3% with CS^a. Consequently, the use of the IEnKS to correct the BC of the 50 representative times allows to largely reduce the error of the wind potential estimation as well as the uncertainty in this estimate.

One can note that CS^b gives worse results than WRF, whereas the mean error made by WRF is larger than the one made by CS^b. This might be explained by the nonlinearity of the power curve and especially the effect of cut in (the wind turbine is cut if the wind speed is smaller than 3m/s). Another source of explanation could be that WRF errors are especially large in situations of strong wind, but the power curve reaches a plateau after 13m/s such that these errors do not impact the wind potential computation.

Note that the observations, and thus all this study, are not available during a full year but only for 8 months. Consequently these estimations are not perfectly representative of the potential of this site. Moreover, a mast equipped with cup anemometers is located

just next to the sonic anemometer. If the observations from the cup anemometer is used to estimate the wind power potential, we obtain a value of 2895kW. The difference with the value given previously, obtained with the sonic anemometer measurements, indicates that the observations are not perfect and that the confidence interval is approximately equal to 100kW.

5.6 Conclusions

In the present chapter, we have evaluated the performances the IEnKS and the BFN algorithm in their versions adapted to take BC into account, instead of IC as in their original derivation.

These new versions of the DA methods are tested here with twin experiments in two and three dimensions. In 2D (vertical plane), the BC correspond to the vertical profile of the east-west component of velocity prescribed on one side of the domain. The control vector corresponds to the values of velocity defined in the 21 vertical levels. Both the BFN algorithm and the IEnKS are tested in a configuration with 5 pseudo-observations. In this configuration, we have highlighted that the revised version of the BFN algorithm cannot be applied for this wind resource assessment application. Indeed, the generalisation of the methodology – which has been developed for the SWE – to the Navier-Stokes equations is based on a linearity assumption which is not satisfied in presence of complex geometrical features (such as steep topography). Further investigation could be performed to better quantify the limits of the BFN algorithm.

On the other hand, the IEnKS has been proved to be easily adapted to this wind resource application. With an ensemble of 3 members it allows to divide by more than 7 the mean absolute error of the BC which leads to a large reduction of the global error of the simulated wind field. Moreover, the IEnKS has the great advantage to provide an uncertainty estimate for the analysis, thanks to the ensemble. We thus show that the IEnKS helps to increase the accuracy of the BC and consequently of the wind field simulated over the whole domain. 3D-Var is also used on this 2D case to provide a comparative basis. In fact, the IEnKS and 3D-Var theoretically minimize the same cost function, albeit for 3D-Var it is minimised in the control space whereas for the IEnKS the cost function is defined and minimised in the ensemble space. Both methods give very similar results, though the IEnKS is more efficient in this case, from a computational-cost perspective.

Twin experiments are also performed with a complete 3D domain of 4km$\times$4km$\times$2030m. In this case the control vector corresponds to the BC of wind velocity (both u and v components) defined on the four sides of the domain. The control vector is here of size 840 and we consider 30 synthetic observations extracted from 3 virtual masts in the domain. With a quite small ensemble (5 members), the IEnKS helps to improve the estimate of BC and thus to reduce the global error inside the domain, by decreasing both

the absolute error and the uncertainty in the estimate.

Finally, observations from a field campaign are used in a cross-validation process: the observations from 2 masts are assimilated and the results are compared to the observations provided by a third mast. We have shown that the use of the IEnKS with 5 members helps to reduce the error in most cases. The mean error is then largely reduced which triggers a better estimation of the wind potential of this site. The results have shown that in cases with a small background error (i.e. when the CFD simulations with BC provided by mesoscale outputs are already close to observations), it might not be beneficial to perform DA. Consequently a good practice could be to use DA only in situations for which the background error is quite large (here larger than 1.5m/s).

In the three cases studied here, the IEnKS adapted to BC is proved to enhance the accuracy of local scale atmospheric simulations in operationally affordable conditions. In fact, thanks to the IEnKS, the absolute error of the wind field is reduced as well as the uncertainty associated with this error. As a consequence, the wind potential is significantly better estimated thanks to the use of the adapted IEnKS. In the wind resource assessment study presented here, the meteorological simulations are clustered in 50 classes, which is smaller than the usual practice at EDF R&D of using approximately 200 classes. It would be interesting to assess the sensitivity of the wind potential to the number of classes. Moreover, since using the IEnKS increases the number of model integrations by approximately 20, an interesting perspective would be to compare the results obtained with 1000 classes without DA and with 50 classes and DA.

Chapter 6

Improving dispersion modelling in built environments with CFD using the iterative ensemble Kalman smoother

Contents

6.1 Introduction

Atmospheric dispersion modelling is used for numerous applications: air quality assessment, exposure indicators, support to air quality planning and directives, or in case of nuclear emergency such as accident or malicious activities (e.g., Hanna et al., 2006; Kumar et al., 2011; Benamrane et al., 2013). Many of these applications occur at local scale in urban areas or around industrial sites where the presence of buildings makes the domain geometry more complex. Since the evolution of pollutants in the atmosphere is mainly driven by wind, dispersion modelling requires the knowledge of the meteorology over small domains. As mentioned in Section 1.4, the micrometeorological inputs necessary to study the aforementioned applications are often obtained as outputs of computational fluid dynamics (CFD) models (e.g., Tominaga and Stathopoulos, 2013). Such models generally offer the possibility to transport passive scalars and thus represent the evolution of non-reactive tracers concentration. In order to represent reactive pollutants, the CFD models can be coupled to chemistry or aerosol models (Albriet et al., 2010).

The CFD models used for dispersion modelling are very sensitive to input parameters, related to the pollutant source term (location and mass rate) and to the meteorology. In particular, we have discussed in Section 1.2.5 that the boundary conditions (BC) have a substantial impact on the accuracy of the local-scale atmospheric simulations (Srebric et al., 2008).

Observations are widely used for dispersion studies but mainly for validation purposes. Up to present, the exploitation of observations through data assimilation (DA) has mostly been performed to solve inverse problems for source identification (e.g., Krysta et al., 2006; Davoine and Bocquet, 2007; Winiarek et al., 2012). In such studies, the assimilated observations are pollutant concentration measurements and the typical spatial scales are much larger than those considered in micrometeorology. So far, the wind and turbulence observations available within built environments have rarely been included to improve micrometeorological simulations. While these observations might be perturbed by the geometrical features of the domain, they still contain useful information which could be taken into account through DA. We have seen in Chapter 5 that the iterative ensemble Kalman smoother (IEnKS) can be used to assimilate wind observations available within prospected sites for the installation of wind farms and thus improve the accuracy of the wind resource assessment.

In the present chapter, we evaluate the ability of the IEnKS to assimilate *in situ* wind and concentration observations, perturbed by obstacles, to correct the meteorological

BC prescribed for atmospheric simulations with a CFD model. To achieve this goal, we use the measurements provided by the Mock Urban Setting Test (MUST) campaign, described in Section 6.2. In Section 6.3 we present the experimental set-up and the methods used to apply the IEnKS to this study. Section 6.4 summarises the results obtained with the IEnKS by assimilating first wind observations, and then concentration observations. Eventually, the conclusions of the present study are given in Section 6.5.

6.2 The MUST campaign

The MUST campaign was conducted in September 2001 at the U.S. Army Dugway Proving Ground (DPG) Horizontal Grid test site (Biltoft, 2001; Yee and Biltoft, 2004). The aim of this field campaign was to provide well-documented cases of urban dispersion by acquiring both meteorological and dispersion observations. These datasets have been widely used for urban model development and validation (e.g. Milliez and Carissimo, 2007, 2008; Winiarek, 2014; Bahlali, 2018).

The site is located in the Utah desert where containers form a regular array over a 200m square area. The containers are aligned on a 12 by 10 grid and each container is 12.2m long, 2.42m wide, and 2.54m high. Several trials have been performed and each of them consists in a 15min release of a tracer gas (propylene) from a fixed position, either within or immediately outside the container array, at a height between 0.15m and 5.2m. Biltoft (2001) and Yee and Biltoft (2004) give a comprehensive description of the experimental set-up and analyses of the results. Numerous instruments have been provided by several organisations, such as the Army Research Laboratory (ARL), Arizona State University (ASU), the DPG, the Defence Science Technology Laboratory, Los Alamos National Laboratory (LANL), and the University of Utah (UU).

6.2.1 Meteorological measurements

Many meteorological instruments have been installed within and outside the MUST array during the release experiments. Figure 6.1 is a view from above of the MUST domain with the container array and the meteorological instruments within the domain.

Within the domain, numerous 2D and 3D sonics have been set up and provide observations of mean wind speed and turbulence at a frequency of 10Hz. Information about these instruments are given in the legend of Figure 6.1 and more details are available in Biltoft (2001). As in Milliez (2006), for 2D sonics we estimate the 3D turbulence kinetic energy (TKE) from its 2D value using the similarity theory as follows:

$$k_{3\mathrm{D}} = 1.3 k_{2\mathrm{D}}. \tag{6.1}$$

For each 15-min trial, Yee and Biltoft (2004) have extracted one 200-s quasi-steady period during which meteorological variables as well as gas plume are nearly constant. In the present study, we aim at representing the wind and concentration fields during

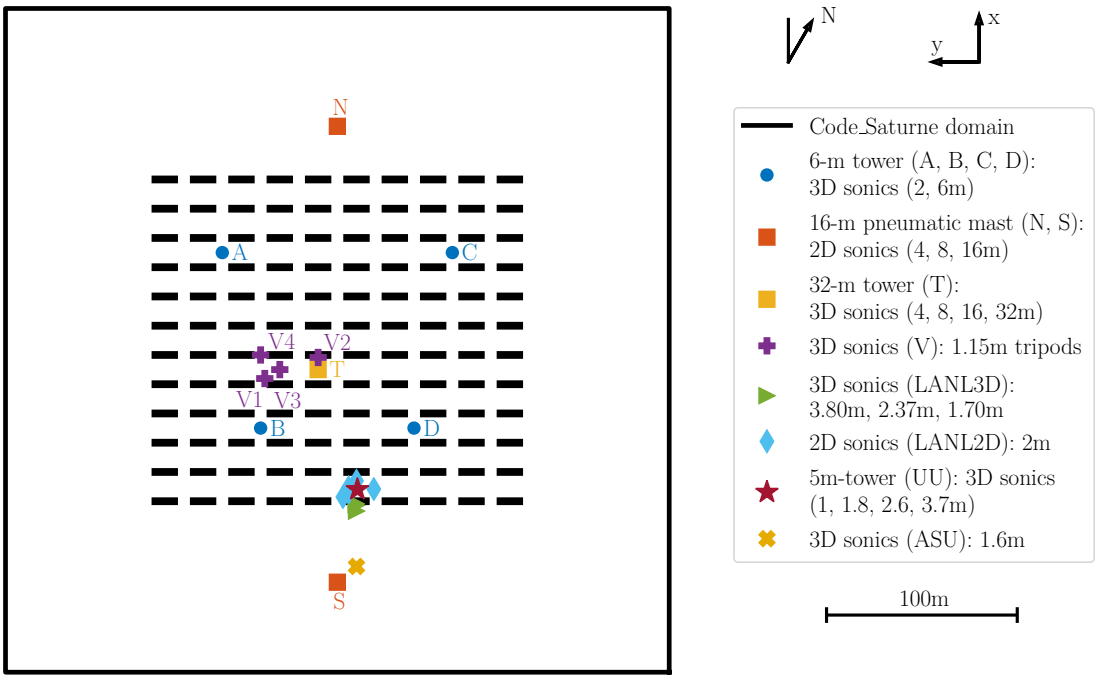

Figure 6.1: Representation of the MUST array within the domain used for *Code_Saturne* simulations. The location of all meteorological instruments is also shown.

two of these periods as stationary simulations. The observations assimilated correspond to the mean values, averaged over the 200-s period (i.e. 2000 sonic observations).

Other instruments are permanently installed in the vicinity of the MUST array and provide supplementary information. In the present study we use observations provided by a PWIDS and a SAMS, located less than 2km upwind of the containers array. A SODAR system, located 400m north-east of the domain, also provides wind and turbulence measurements, especially in upper layers of the atmosphere (see Fig. 6.2). These instruments provide observation of the two components of the horizontal velocity (u, v) at 2m above the ground for the PWIDS, at 10m for the the SAMS, and at several levels between 15m and 200m above ground level in 5-m intervals for the SODAR.

6.2.2 Gas concentration measurements

In addition to the meteorological measurements, instruments measuring gas concentration have been installed in the domain. These instruments are of two types:

- ultraviolet ion collector (UVIC) installed on the 6-meter towers, near the 32-meter tower and at the center of the array. These instruments were calibrated over a range of 0.01 to 1000ppmv.
- digital photo-ionization detectors (digiPID) located on the 32-meter tower and

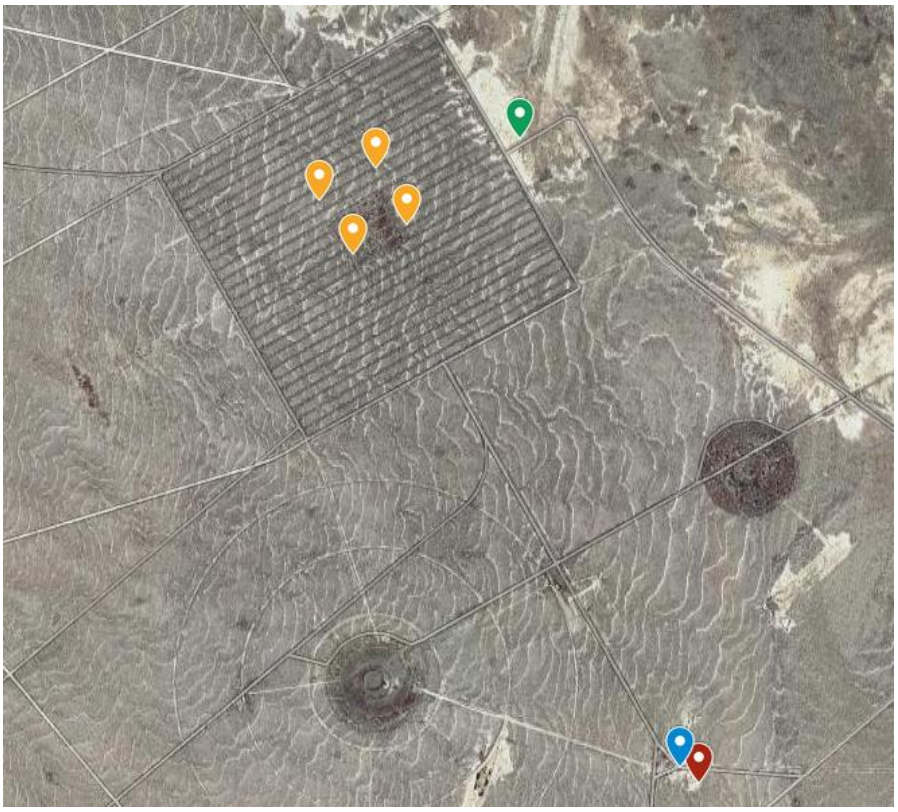

Figure 6.2: Map of the site around MUST array. The light orange pins represent the corners of the container array. The location of the surface atmospheric measurement system (SAMS) #8 (red), the Portable Weather Information and Display System (PWIDS) M6 (blue), and the Sound Detection And Ranging (SODAR) (green) are also shown.

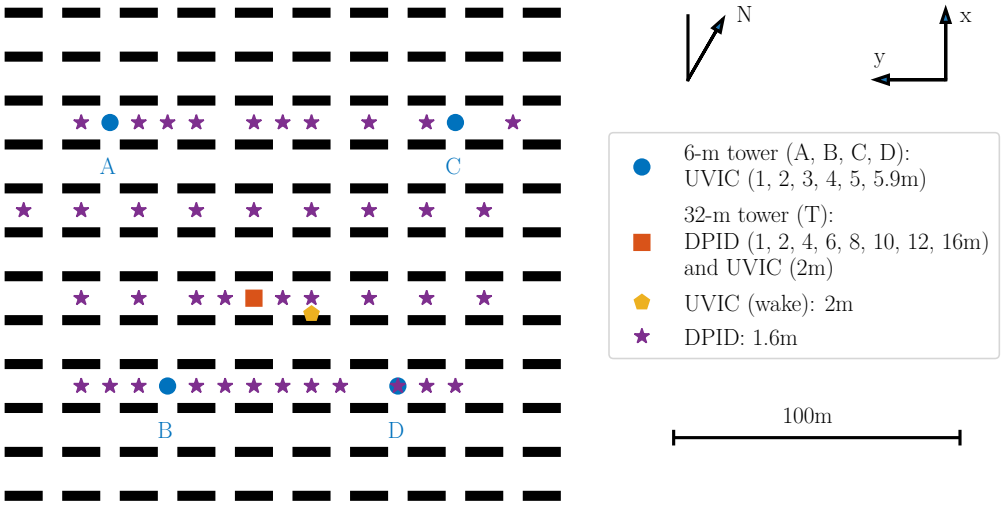

Figure 6.3: Representation of the MUST array with the location of the instruments measuring gas concentration.

along 4 east-west lines inside the containers array with a calibrated operating range of 0.04 to 1000ppmv.

Figure 6.3 shows the location of the 48 digiPID and 26 UVIC. The observations of gas concentration are available during all the 15-min trials with a frequency of 50Hz such that the assimilated values are averaged over 10 000 observations (200s).

6.3 Methods

6.3.1 Experimental set-up

The meteorological field in the region containing the MUST array is simulated using the atmospheric module of *Code_Saturne* (see Section 1.2.4). The domain used for the simulations is of size 348m × 348m horizontally and extends up to 50m in the vertical. The domain is centred on the container array and includes a band of flat terrain outside the array (77m on eastern and western sides and 87m on northern and southern sides). The horizontal resolution is somehow coarse outside the MUST array ($\Delta x = \Delta y = 4$m) and refined inside the containers array up to 0.5m. The vertical resolution decreases with altitude: from $\Delta z = 0.25$m near the ground to $\Delta z = 7.8$m for the uppermost layer (see Fig. 6.4).

The turbulence is modelled using the $k - \epsilon$ model where k is the TKE and ϵ its dissipation rate.

The BC correspond to one vertical profile, located in the middle of the southern border or the domain. The profile is defined by 22 vertical levels for the 3 variables: u, v,

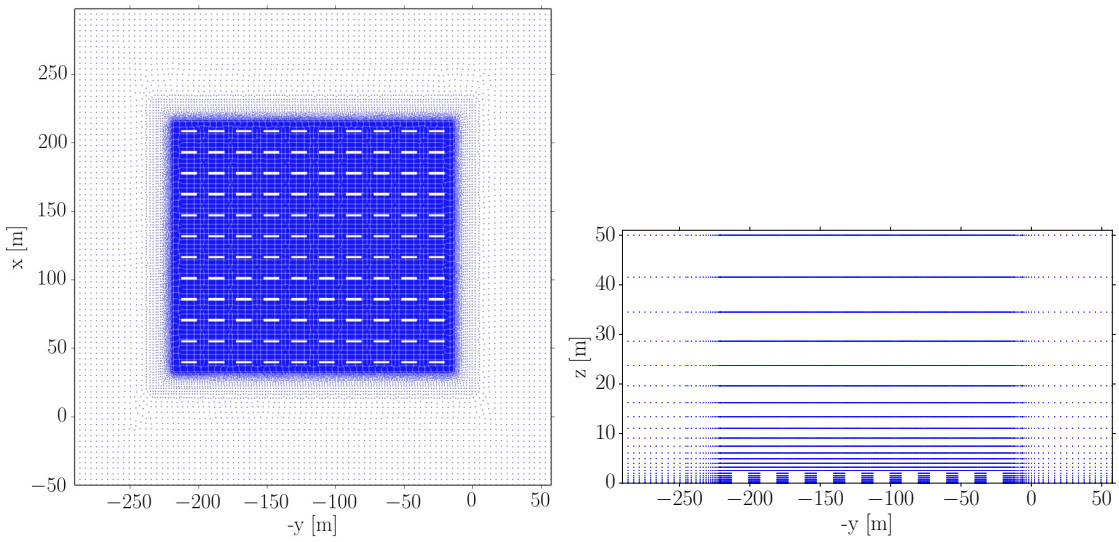

Figure 6.4: Mesh used for the *Code_Saturne* simulations. The points represent the cell edges. (left) Slice at constant $h = 1.5$m and (right) slice a constant $x = 115.5$m.

and k. At the first time step of the model, the field of ϵ is computed in order to ensure the equilibrium between turbulence production and dissipation. The values calculated at the boundaries of the domain are kept as BC of ϵ for the next steps. The model is integrated for 5000 iterations with a fixed time step of 0.1s, which is enough to reach a steady state (Bahlali, 2018).

We consider two different trials of the MUST campaign:

- Neutral case which has been performed the 25^{th} of September 2011 at 18:29 (2681829). The meteorological conditions at this time corresponded to neutral stability conditions with an estimated Monin-Obukhov (M-O) length of $L = 28000$ (Yee and Biltoft, 2004). The pollutant source is located between two containers in the bottom-left corner, at $h = 1.8$m above the ground.

- Stable case which has been performed the 26^{th} of September 2011 at 21:57 (2692157). The conditions were stable with an estimated M-O length of $L = 130$ (Yee and Biltoft, 2004). The tracer gas is released from the roof of the first container in the bottom-right corner, at $h = 2.6$m above the ground.

6.3.2 Anamorphosis for the turbulence kinetic energy

In the DA experiment, the control vector corresponds to the BC. While the two components of the horizontal velocity, u and v, can be considered as Gaussian variables, it is certainly not a valid hypothesis for the TKE. Indeed, the TKE is always positive and analysing observations of k during all the trials shows that the probability density function (pdf) of the TKE approximately follows an exponential distribution (see Fig. 6.6b).

The cumulative distribution function (cdf) of the exponential distribution is

$$F(k) = 1 - \exp(-\lambda k), \tag{6.2}$$

where λ is the rate parameter. Since the IEnKS assumes the Gaussianity of the control variables, we must use *anamorphosis* for the TKE.

The principle of anamorphosis is to find a bijection between the cdf of a non-Gaussian variable (here k) and a Gaussian variable which is included in the control vector in place of the non-Gaussian variable (Cohn, 1997; Bertino et al., 2003). We thus define a new, non-physical variable γ following the normal law $n(0, \sigma_\gamma)$ and its cdf is $G(\gamma)$ such that

$$k = F^{-1} \circ G(\gamma) \tag{6.3}$$

$$\gamma = G^{-1} \circ F(k). \tag{6.4}$$

The choice of the variance for γ (σ_γ) does not affect the DA experiment in general. Here, as we apply an ensemble-based DA technique, the construction of the ensemble, and especially its spread, depends on this variance. Consequently we chose it carefully and more details will be given in the next section.

The control vector considered in the present study includes the 22 values of u, v, and γ and its total size is $l = 66$. The dynamical model $\mathcal{M}$ includes one more step to convert the values of γ into TKE values, then prescribed as BC for k.

6.3.3 Estimation of the background error variances and correlations

In order to construct the background ensemble necessary for the DA experiment with the IEnKS, we first estimate the background error covariance matrix, $\mathbf{B}$. The ensemble anomalies are then determined as the leading modes of this matrix. The coefficients of the background error covariance matrix are decomposed as the product of correlation coefficients $C_{i,j}$ and standard deviation of the individual background errors σ_i:

$$\mathbf{B}_{i,j} = C_{i,j}\sigma_i\sigma_j. \tag{6.5}$$

Correlation coefficients

In order to determine these $C_{i,j}$ and σ_i coefficients, we have analysed the measurements available for all the trials within the domain and above the containers. Indeed, as the containers array is quite small, we can assume that the meteorological variables above the urban canopy are homogeneous in the 348m $\times$ 348m region simulated with *Code_Saturne*. Consequently, we assume that the values of wind and turbulence measured above the containers within the domain are representative of the values at the border of the domain at the same vertical level.

We thus study the observations provided by:

1. the 6-m towers A, B, C, and D at 6m,

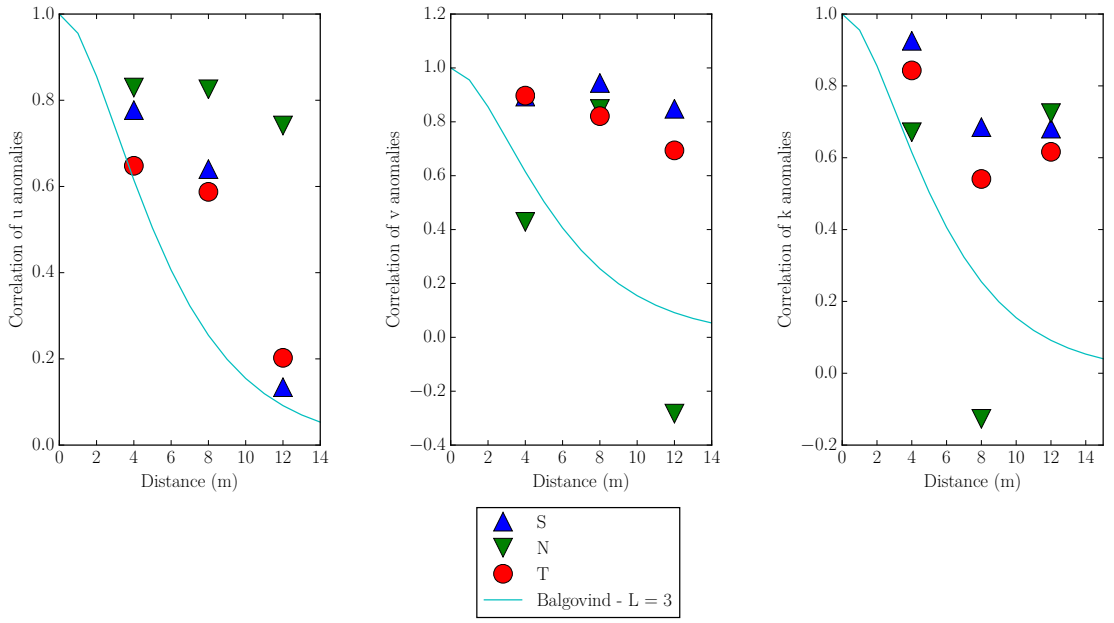

Figure 6.5: Vertical correlations estimated from the horizontal anomalies of u, v, and k for the South (S) and North (N) 16-m masts and the 32-m tower (T). Assuming that the climatological correlations slightly overestimate the background error correlations, we set the correlation length of the Balgovind function to $R = 3$m.

2. the 16-m towers North and South at 4m, 8m, and 16m,

3. the 32-m tower T at 4m, 8m, 16m, and 32m.

In order to estimate vertical and horizontal correlations that are representative of the background error, we have analysed the horizontal anomalies of velocity (A_u and A_v). The horizontal anomalies are defined as the departure of each observation from the spatial mean computed at the same vertical level:

$$A_{x^j} = x_i^j - \frac{1}{N^j} \sum_{i=1}^{N^j} x_i^j, \tag{6.6}$$

where x can be u or v, the superscript 'j' refers to a given height above the ground (4m, 6m, 8m, or 16m), x_i^j is the measurement of the i-th instrument at the j-th height, and N^j is the number of available observations at this height. The values of standard deviation (STD) observed for these horizontal anomalies of velocity and k are relatively small, thus confirming the assumption that the meteorological variables are somehow homogeneous over the small domain considered here. It is important to recall that all the trials have been selected with south-east to south-west wind. Consequently the asymmetric results obtained for the u- and v-components of velocity can be explained by this bias in the selection of the meteorological conditions for which the releases have been performed.

Figure 6.5 shows the vertical correlations evaluated for u, v, and k horizontal anomalies from the observations provided by the towers N, S, and T at 4m, 8m, and 16m. The

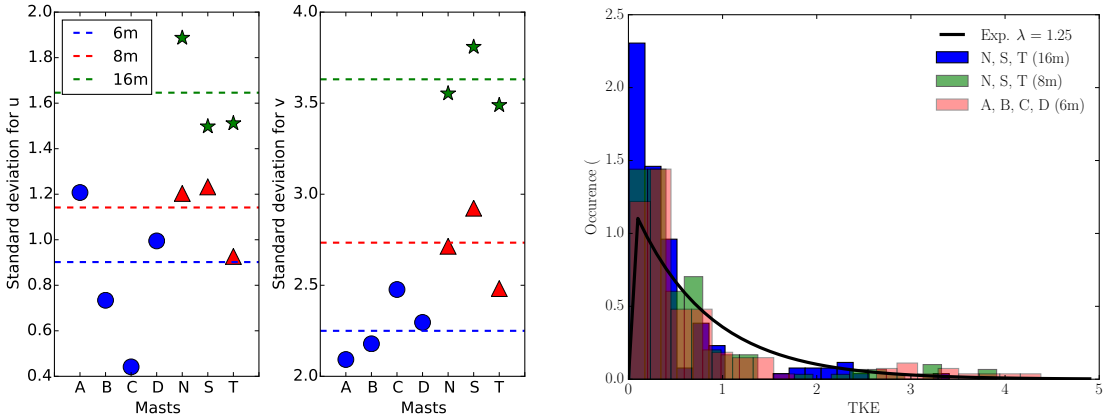

(a) Values of standard deviation estimated from the observations of u and v above the canopy, during all the trials. The dashed lines correspond to the standard deviation calculated for each level, merging all the available observations at this height.

(b) Pdf of the observed values of TKE during all the trials and pdf of the exponential law with $\lambda = 1.25\text{s}^2/\text{m}^2$.

Figure 6.6: Statistical analyses of the climatology used to determine the background error variances.

horizontal anomalies of u and v show a light correlation in the vertical. We chose to describe the vertical correlations with a Balgovind function (Balgovind et al., 1983) which is usually applied to represent the spatial structure of error statistics (Winiarek, 2014). The correlation coefficient C_{ij} between two vertical levels i and j of the same profile is hence assumed to be

$$C_{ij} = \left(1 + \frac{d_{ij}}{R}\right) \exp\left(-\frac{d_{ij}}{R}\right), \tag{6.7}$$

where d_{ij} is the distance between the two levels and R is the correlation length to be determined.

In the light of the correlations observed among the horizontal anomalies, and assuming that the climatological correlations underestimate the background error correlations, we have chosen a correlation length $R = 3\text{m}$ for the three variables u, v, and k. The corresponding Balgovind function is shown in Figure 6.5. We further assume that the different variables (u, v, and k) are not correlated. Using this hypothesis and the Balgovind correlation function (Eq. 6.7) with the correlation length given above, we can construct the background error correlation matrix. This matrix must be multiplied by the variances associated with each variable to get the background error covariance matrix.

Background error variances

The background error variances represent the uncertainty of the first estimate. Consequently, these values may depend on the sources of information used to estimate the background BC. In the present study, we try to recreate operational conditions where the first estimate of the BC is quite poor whereas the observations are very accurate. However, the MUST case is very specific and does not correspond to operational conditions. Indeed, the trials have been performed in particular meteorological conditions – not necessarily representative of the climatology in this region. Moreover, the container array is installed in the middle of a desert area, such that the meteorological conditions outside the domain are not perturbed by any geometrical features and remain spatially homogeneous. As a result, we assume that the climatological variations observed during the several trials for the velocity components and turbulence slightly underestimate the background error variances. Using the climatological analyses (see Fig. 6.6a) and expert judgement, we have set the background error variance for u and v to $\sigma^{\mathrm{b}}_{uv} = 5\mathrm{m/s}$. For the TKE, we have estimated the rate parameter to be $\lambda_k = 1.25\mathrm{s}^2/\mathrm{m}^2$ (see Fig. 6.6b). We set the variance of the anamorphosis variable γ to $\sigma^{\mathrm{b}}_{\gamma} = 5$ to give as much weight to the velocity components as TKE in the DA experiment.

Eventually, we obtain an estimate of the background error covariance matrix used to define the background ensemble. The background ensemble corresponds to the $N-1$ leading modes of the background error covariance matrix – i.e., eigenvectors associated with the largest eigenvalues– with a N-th member necessary to recentre the ensemble. The ensemble of N members thus formed is rotated using a random rotation matrix to avoid having the N-th member too different from the other ones.

6.3.4 Observation error covariance matrix

The observation error covariance matrix $\mathbf{R}$ is diagonal, and the coefficients on the diagonal are equal to

$$(\sigma^{\mathrm{o}})^2 N_{xy} \tag{6.8}$$

where $(\sigma^{\mathrm{o}})^2$ is the variance associated with the observation error and N_{xy} is the number of observations available – and assimilated – at the same horizontal position but different heights. This scaling factor aims at giving similar weight in the cost function to the different areas of the domain and not favour regions that are more observed. Since the extra-diagonal terms of $\mathbf{R}$ are assumed null – i.e., the observations are not correlated –, with this form for $\mathbf{R}$ (Eq. 6.8) the part of the cost function associated with the

observations reads

$$\mathcal{J}^{\mathrm{o}} = \frac{1}{2}\|\mathbf{y} - \mathcal{F}(\mathbf{z})\|^2_{\mathbf{R}^{-1}} \tag{6.9a}$$

$$= \sum_{i=1}^{p} (\mathbf{R}^{-1})_{ii} (\mathrm{d}\mathbf{y}_i)^2 \tag{6.9b}$$

$$= \sum_{j} \frac{\sum_{i=1}^{N_{x_j,y_j}} (\mathrm{d}\mathbf{y}_i)^2}{(\sigma^{\mathrm{o}})^2 N_{x_j,y_j}}, \tag{6.9c}$$

where d$\mathbf{y}$ is the innovation term and the sum over j represents the different horizontal positions where observations are available. Consequently, the cost function associated with the observations is a sum of innovations, averaged for each horizontal position over the different measurements there.

For wind observations, the STD of the observation error is set to $\sigma^{\mathrm{o}}_{uv} = 0.2$m/s and for concentration observations (after applying the logarithmic transformation defined by Equation (6.17)) we set $\sigma^{\mathrm{o}}_{c} = 0.05$.

6.3.5 Estimation of the background boundary conditions

Estimation from PWIDS, SAMS, and SODAR observations

The first estimate of the profile of BC for the wind speed (U) is assumed to follow the semi-logarithmic profile given by the M-O similarity theory (see Section 1.1.3) (Stull, 1988):

$$U(z) = \frac{U_L}{\kappa}\left(\log\left(\frac{z+z_0}{z_0}\right) + 5\frac{z}{L}\right), \tag{6.10}$$

where $\kappa = 0.4$ is the vón Karman constant, z_0 is the roughness length which is set to 0.04m in the MUST domain (Yee and Biltoft, 2004), and L is the M-O length. The local stress U_L is estimated from the boundary layer height h_{ABL} and the surface stress u^*:

$$U_L = u^*\left(1 - \frac{z}{h_{\mathrm{ABL}}}\right). \tag{6.11}$$

In Garratt (1994), the height of the boundary layer is estimated as follows: in neutral conditions

$$h_{\mathrm{ABL}} = 0.2u^*/|f|, \tag{6.12}$$

and in stable conditions

$$h_{\mathrm{ABL}} = 0.4\sqrt{u^* L/|f|}, \tag{6.13}$$

where f is the Coriolis frequency, equal to $f = 9.4 \cdot 10^{-5}$rad/s here.

We also assume that the profile of TKE is consistent with the M-O similitude theory, as given in Launder and Spalding (1974):

$$k = \frac{U_L^2}{\sqrt{C_\mu}}, \tag{6.14}$$

$$\epsilon = \frac{U_L^3}{\kappa}\left(\frac{1}{z} + \frac{4}{L}\right). \tag{6.15}$$

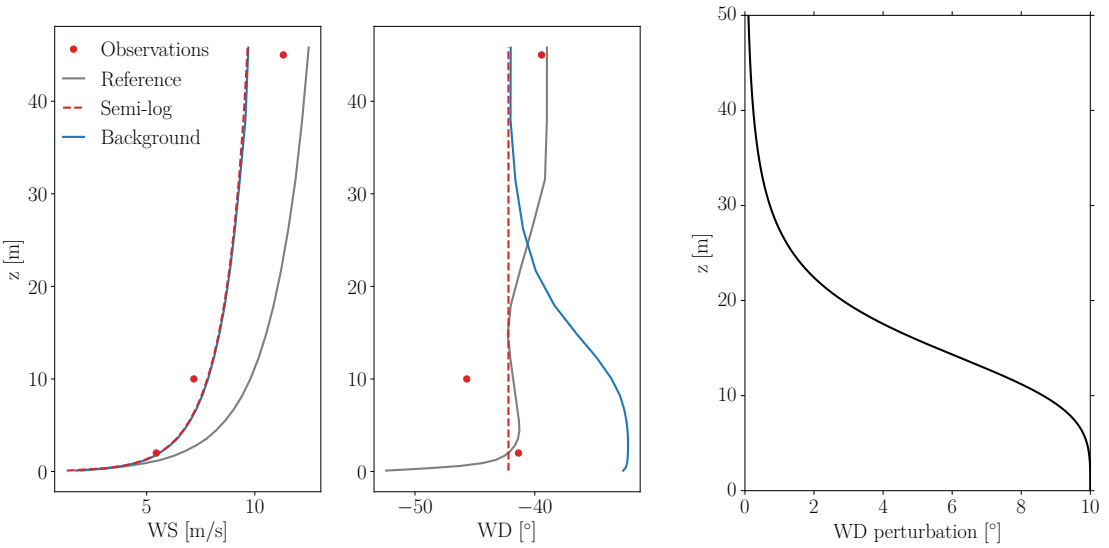

(a) Vertical profiles of wind speed (WS) and wind direction (WD) for the Neutral case. The reference BC, the semi-logarithmic profile reconstructed from the PWIDS, SAMS, and SODAR observations, and the background BC (obtained by perturbing the semi-logarithmic profile) are shown.

(b) Vertical profile of perturbation, added to the profile of wind direction to construct the background BC.

Figure 6.7: Construction of the background BC: (a) the wind speed profile is given by the semi-logarithmic law of M-O similitude theory. The constant profile of wind direction (obtained from the average over the observed values) is perturbed by (b) a function which decreases with altitude.

This scheme has been proved to be well suited for the MUST case (Milliez, 2006).

We first find the value of the surface stress u^* that best fits the observations of wind speed (see Table 6.1 for more details about the observations used to determine u^*). The wind direction is assumed constant over the vertical profile, and the wind direction value is obtained as an average over the available observations. For the Neutral case, we find $u^* = 0.57$m/s, which corresponds to an atmospheric boundary layer (ABL) high of $h_{\mathrm{ABL}} = 1.21$km, and the mean wind direction is equal to $-42.2°$ (with a STD among the observations of 2.6°). For the Stable case, the estimated surface stress is $u^* = 0.40$m/s, $h_{\mathrm{ABL}} = 298$m, the wind direction is estimated to 45.4° (with a STD among the observations of 4°). Figure 6.7aa shows in dashed, red the profiles of wind speed and direction estimated from the observations (red dots) in the Neutral case.

Perturbation of the boundary conditions

As previously mentioned, the MUST case is very specific since the area surrounding the container array is a flat desert and in absence of obstacle the wind field is spatially homogeneous. As a matter of fact, the vertical profile of wind and turbulence observed

by the PWIDS, SAMS, and SODAR – even though these instruments are quite far from the container array – is a very good estimate of the BC. In fact, when the prescribed BC are estimated as explained above, the mean error on the wind field inside the domain – computed as the mean absolute error, compared to the available wind observations – is smaller than 1.1m/s. This error is somehow smaller than what is usually encountered in operational studies.

In order to make this study representative of an operational application, we empirically perturb the BC according to the function

$$\delta X = \delta X_0 \frac{\alpha}{(h/h_L)^4 + \alpha}, \tag{6.16}$$

where δX is the perturbation for the variable X, δX_0 is the maximum perturbation near the ground, h is the elevation, h_L is the level at which the perturbation is equal to $p_L \delta X_0$, and $\alpha = \frac{p_L}{1-p_L}$ (Fig. 6.7b). This function perturbs more the profile near the ground than in the upper layers, which is representative of a typical background error. In operational studies, the background is generally estimated from mesoscale simulations or from observations nearby the domain under scrutiny.

Mesoscale models generally provide poorer estimations of the meteorological fields near the surface, where the effect of topography – inaccurately represented in such models – is greater. As a result, if mesoscale results are used to estimate the background, it is likely that the background error is larger near the ground than in upper layers. Similarly, the variability in time and space of the meteorological variables is greater in the lower levels than in the uppermost ones. Consequently, the observations provided by instruments a few hundred of meters away from the domain of interest, can generally be considered as a good estimation of the BC above a few tens of meters from the ground – even for cases where geometrical features perturb the wind field outside the studied domain. However, in the lower levels, the background provided by such observations is very likely to be wrong.

In order to be consistent with typical background errors, the perturbation that we apply is larger near the ground and vanishes to zero with altitude (see Eq. 6.16). In the present study, we perturb only the wind direction with different amplitudes and with $p_L = 0.01$ and $h_L = 50$m (see Fig. 6.7a).

6.3.6 Assimilating observations of concentration

Values of gas concentration are always positive, such that the distribution of the observation errors cannot be considered as Gaussian. This issue can be overcome by assuming that the observation error for concentration observations follow a log-normal distribution, like in Liu et al. (2017). This study has also highlighted that the logarithmic function might give too much weight to small concentration values. That is why they proposed to add a threshold – constant – value c_t in the logarithmic function. The innovation vector

thus becomes

$$\mathrm{d}\mathbf{y} = \ln\left(c_t + \mathbf{y}\right) - \ln\left(c_t + \mathcal{H} \circ \mathcal{M}(\mathbf{z})\right). \tag{6.17}$$

In the DA experiments involving concentration observations, we have set $c_t = 0.05$ppmv.

6.3.7 Reference simulations

The MUST campaign has already been used in previous studies for validation purposes (Milliez, 2006; Winiarek, 2014; Bahlali, 2018). The CFD simulations performed in these studies corresponded to the 200s quasi-steady periods for each 15-min experiment, selected by Yee and Biltoft (2004). The BC were estimated from the observations provided by the sonic installed on the 16-m tower, at the southern edge of the domain (see Fig. 6.7a). Since the tower is very close to the location where the BC are prescribed, the simulation obtained with these BC are very close to the observations within the domain. The departure from the wind observations assimilated is smaller than 0.5m/s in both the Neutral and Stable cases. Consequently, these simulations are considered as references and the results obtained with the IEnKS are compared to these references.

6.4 Results with the IEnKS and field measurements

6.4.1 Experimental set-up

As previously detailed, the domain used for the CFD simulations with *Code_Saturne* is of size 348m × 348m × 50m with unstructured mesh. The control vector considered in the present chapter corresponds to a vertical profile of BC located in the middle of the southern boundary of the domain. The profile is defined by 22 vertical levels, for three variables: u, v, and γ (which is the anamorphosis variable representing k). Consequently the control vector is of size $l = 66$.

The Neutral and Stable cases have been treated slightly differently and the differences of parametrisation are summarised in Table 6.1.

For both Neutral and Stable cases, we show the results of two DA experiments aiming at correcting the BC related to u, v, and k.

1. The first experiment consists in assimilating 14 observations of the two components of the horizontal velocity (u, v). The analysis obtained in this first experiment is referred to as 'Analysis W'.

2. In the second experiment, the IEnKS is applied to assimilate 13 observations of tracer gas concentration. The analysis of this second experiment is named 'Analysis C'.

The selected measurements for these two experiments, in the Neutral and Stable cases, are detailed in Table 6.1.

	Neutral	**Stable**
Observations for background construction	PWIDS (2m), SAMS (10m), and SODAR (45m)	SAMS (10m) and SODAR (20 and 45m)
WD perturbation	$\delta\text{WD}_0 = -10°$	$\delta\text{WD}_0 = -10°$
u, v assimilated obs. (1st exp.)	Tower A at (2, 6m), Sonic V3 (1.15m), 5-m tower (1, 1.8, 2.6, 3.7m)	Tower C (2, 6m), Sonic V3 (1.15m), 5-m tower (1, 1.8, 2.6, 3.7m)
c assimilated obs. (2nd exp.)	Towers C (1, 2, 3m) and D (1, 2, 3m), 32-m tower (1, 2, 4, 6, 8, 10m), DPID #26 (1.6m)	Towers A (1, 2, 3m) and B (1, 2, 3m), 32-m tower (1, 2, 4, 6, 8, 10m), DPID #23 (1.6m)

Table 6.1: The background BC are estimated by fitting a semi-logarithmic velocity profile to the observations provided by the instruments indicated in the first row (see Section 6.3.5). The vertical profile of wind direction (WD) is perturbed following equation (6.16) with a perturbation near the ground given by the second row (see Fig. 6.7b). The wind observations assimilated in the first experiments are given in the third row and the second experiments assimilate concentration observations provided by the instruments listed in the last row.

As mentioned in Section 6.3.3, the background error covariance matrix has diagonal values equal to $(\sigma_{uv}^{\text{b}})^2 = 25\text{m}^2/\text{s}^2$ and the observation error covariance matrix is diagonal with $\sigma_{uv}^{\text{o}} = 0.2\text{m/s}$ in the first experiments and $\sigma_c^{\text{o}} = 0.05$ in the second ones (see Section 6.3.4). These choices lead to give more weight to the observations than the background.

For all the experiments, the ensemble considered is composed of 5 members and the convergence criterion is set to $e_J = 0.01$, which means that the iterative minimisation algorithm is stopped when the variation of the cost function between two iterations is smaller than 1% of the initial value of the cost function. If this criterion is not reached after $j_{\max} = 10$ iterations, the algorithm is stopped anyway. The analysis is set equal to the value of the control vector which leads to the minimum of the cost function within the available iterations – 10 or less if the algorithm has converged before.

The cross-validation is performed with all the wind, turbulence, and concentration observations available during the studied trials and that are not assimilated in any of the two experiments. These observations are referred to as 'validation observations' in what follows. For the Neutral case, there are 24 validation observations for u, 24 for v, 29 for k, and 40 for c. For the Stable case, there are 24 validation observations for each of u and v, 30 for k, and 44 for c. The small difference comes from some instruments that were not working during the Neutral trial.

We present in what follows the results obtained for the two studied cases (Neutral and Stable) and each of the two different experiments.

6.4.2 Neutral case

With the BC perturbed as explained above, the departure of the simulated wind field to the available u and v observations – selected for DA (see Table 6.1) – is in average of 1.44m/s. With the parametrisation given in Table 6.1, the optimal BC are obtained after 8 IEnKS iterations in the first experiment, and 4 in the second one.

Figure 6.8a and 6.9a show, for the reference simulation, the horizontal wind fields (arrows) and the concentration fields (colors) at two constant heights above the ground: $h = 4$m and $h = 1$m respectively. Note that, for the sake of clarity, arrows are represented every 10m in Figure 6.8a and every 2m in Figure 6.9a. For similar reasons, we have represented the concentration field in logarithmic scale. The Figures 6.8b, c, and d show the error fields at $h = 4$m for the background, and the analyses of the two experiments.

We can see in Figure 6.8b that the background error for velocity is mostly along the y axis. This means that the background velocity field underestimates the v-component of the velocity and slightly the u-component. As a result, the incidence angle is larger than the reference simulation (a) and the wind flow is less aligned with the containers. Moreover, the wind speed is slightly smaller in the background simulation than in the reference one. Consequently, the gas is less diluted by the wind and the concentration in the plume is larger, which is shown by the highest positive values of error than negative ones in Figure 6.8b. In addition, the background pollutant plume, which is somehow aligned with the wind direction at this height, goes more to the left than the reference plume. Consequently, the concentrations are overestimated on the left side of the plume and underestimated on the right side.

We can observe in Figure 6.9a that the presence of obstacles tend to slow down and tilt the wind flow to the right – in the alignment of the container array. Figure 6.9b shows a similar view as Figure 6.9a but for the background simulation. The larger departure between the background incidence angle and the alignment of the containers triggers a greater effect of the obstacles on the background wind field: the wind speed decelerates more within the container array in the background simulation than in the reference one. Moreover, we can observe that the deviation of the wind flow due to the obstacles is stronger, which results in recirculation near the source. In this regions (bottom-left corner), the gas is thus propagated toward the south in the background simulation, whereas this effect is lighter in the reference simulation. As a consequence, the background simulation substantially overestimates the concentrations in this region.

Figure 6.8c shows that the error for the velocity field is largely reduced as compared to the background simulation. As a result, the pollutant plume is more similar to the reference and the error for the concentration field is also reduced to very small values. Figure 6.9c shows the concentration and velocity fields within the urban canopy for the Analysis W. We can see here again that the Analysis W is in very good agreement with the reference in terms of wind direction, wind speed, and concentration values.

Figure 6.8d and Figure 6.9d show that for the Analysis C, the picture is more mixed.

(a) Reference

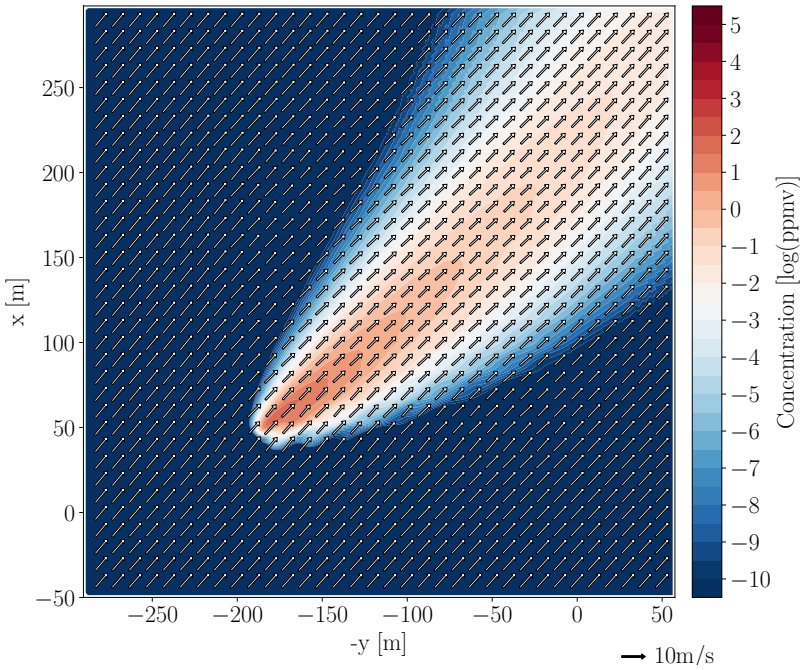

(b) Background (departure from reference)

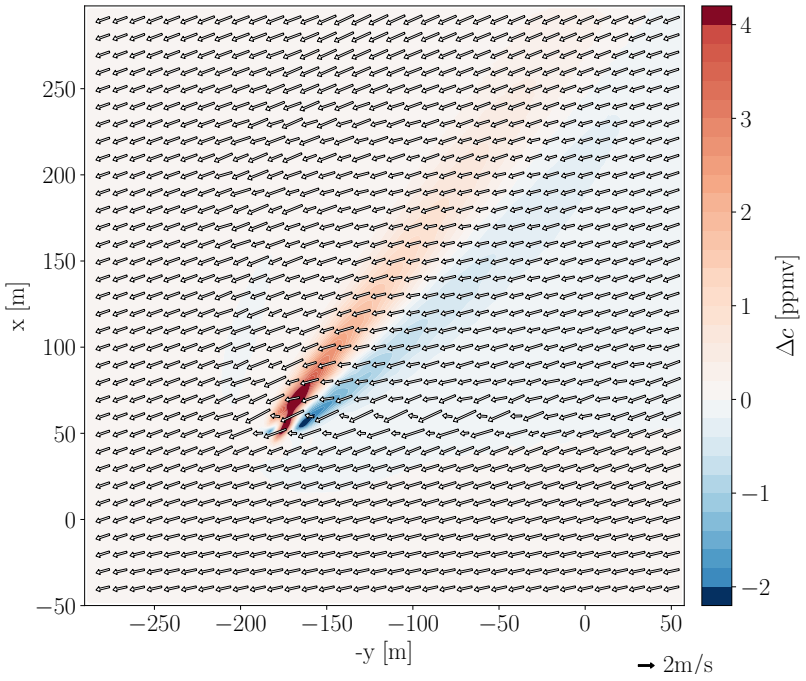

(c) Analysis W (departure from reference)

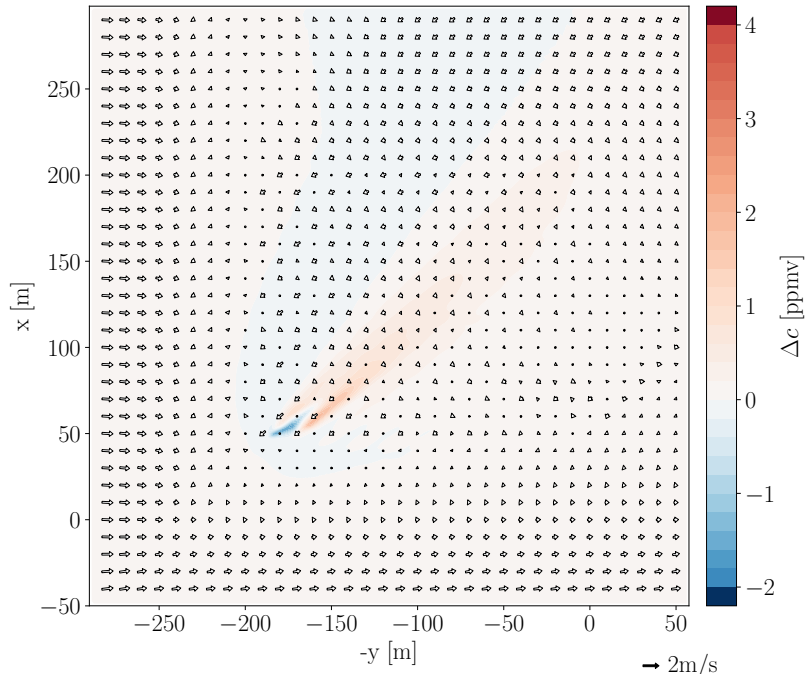

(d) Analysis C (departure from reference)

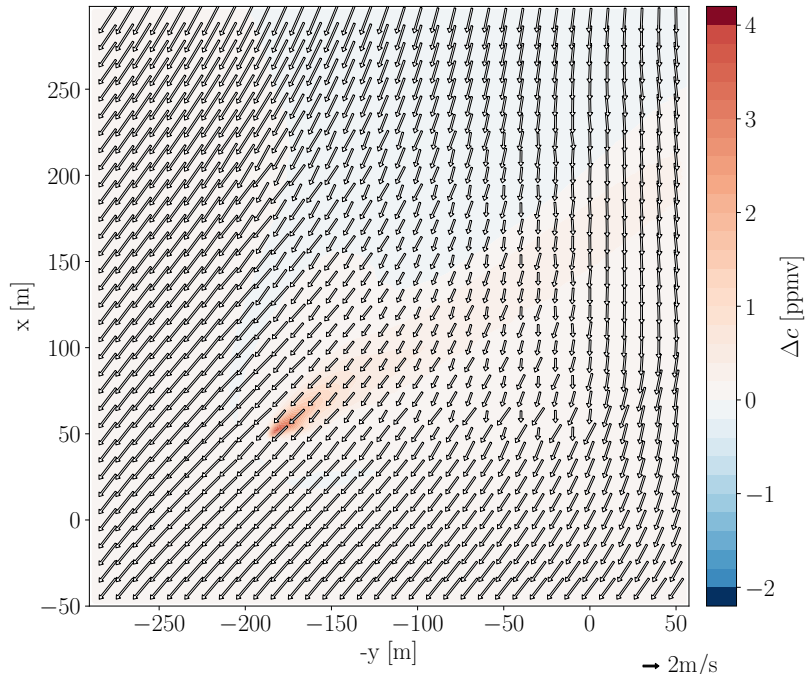

Figure 6.8: Results for the Neutral case. (a) View from above of the concentration field in logarithmic scale (colors) and the velocity field (arrows) at $h = 4$m for the reference simulation. (b) Departure of the background simulation from the reference regarding the concentration field (colors) and the velocity field (arrows). Similar plots are shown for (c) Analysis W and (d) Analysis C. Note that for the sake of visibility, an arrow is plotted every 10m only.

(a) Reference

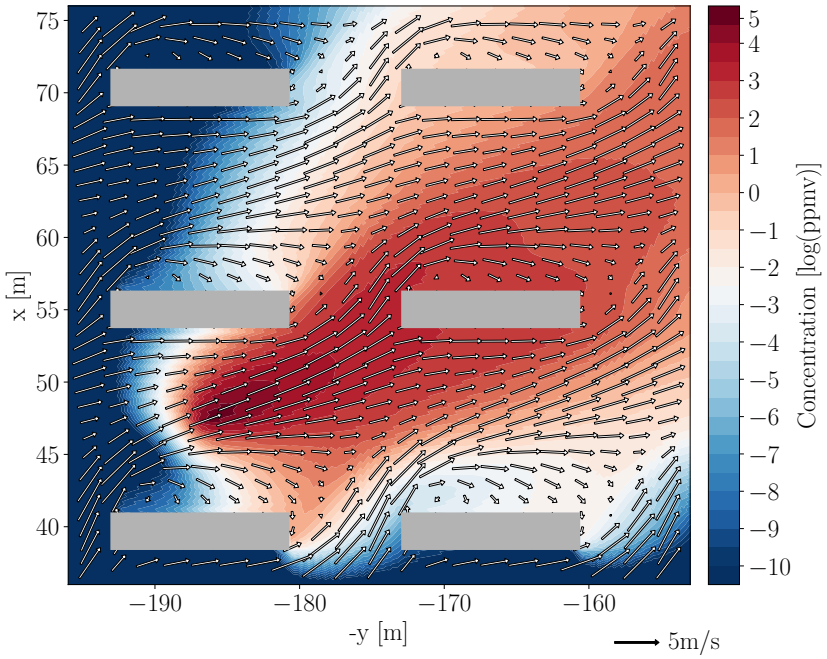

(b) Background

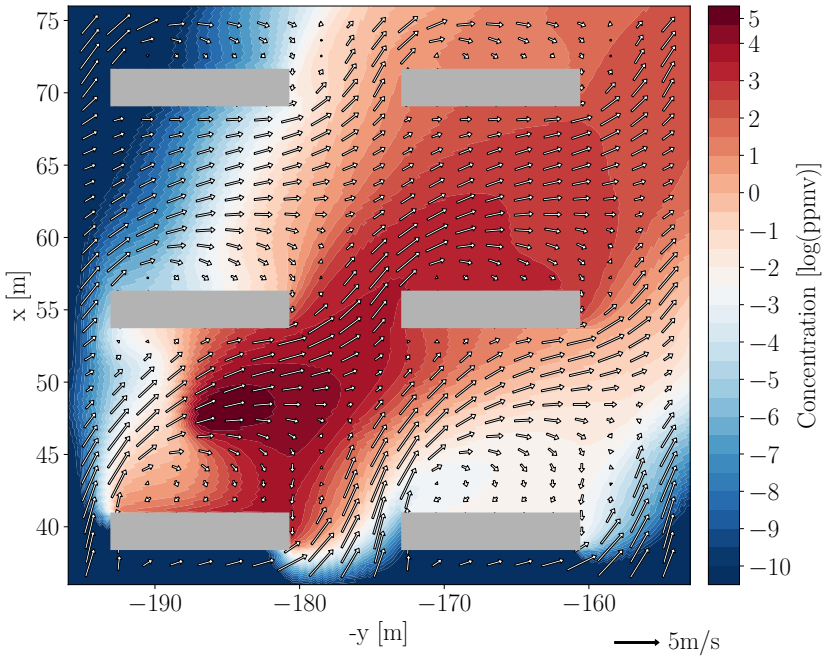

(c) Analysis W

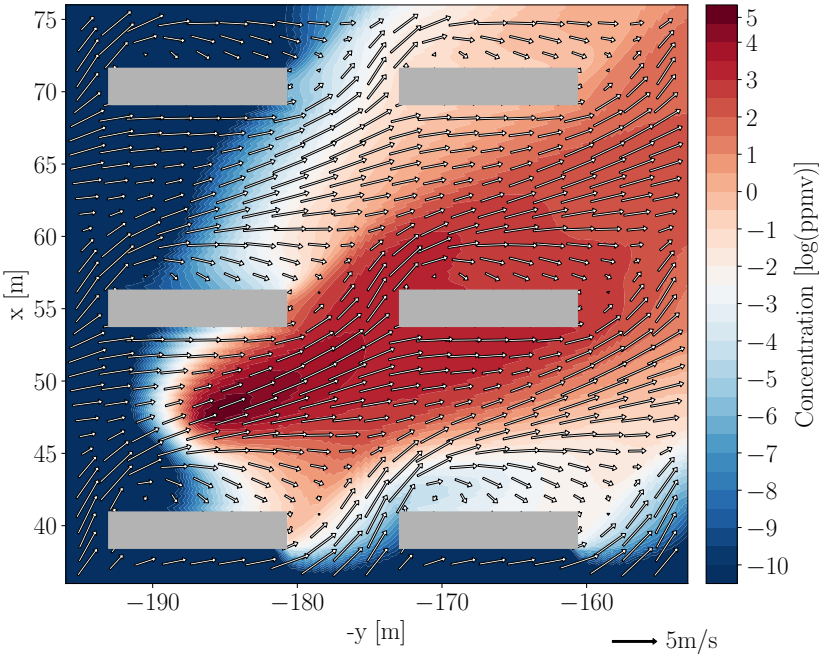

(d) Analysis C

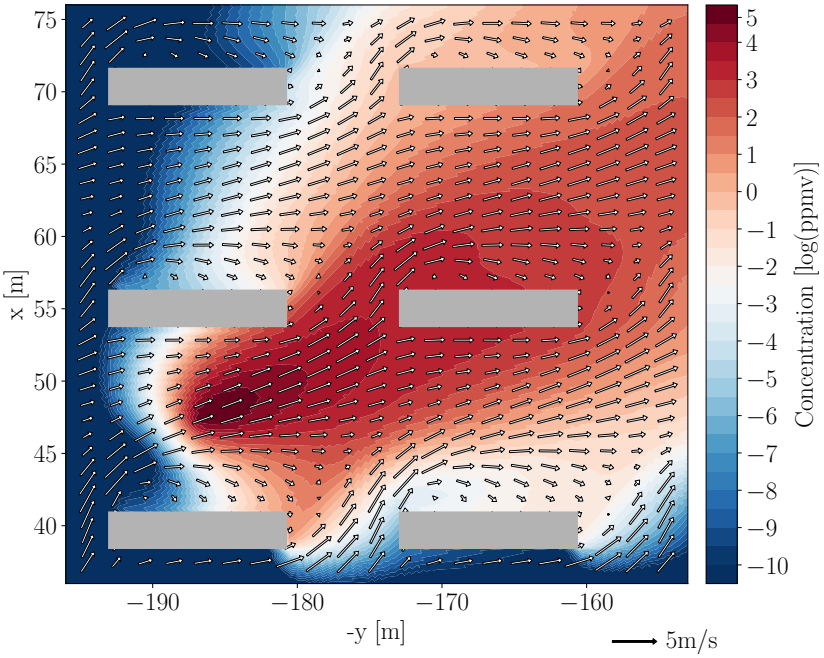

Figure 6.9: Results for the Neutral case near the pollutant source and at $h = 1$m. The concentration (logarithmic scale, colors) and velocity (arrows) fields are shown for (a) the reference simulation, (b) the background, (c) Analysis W, and (d) Analysis C. The horizontal velocity vectors are represented every 2m only.

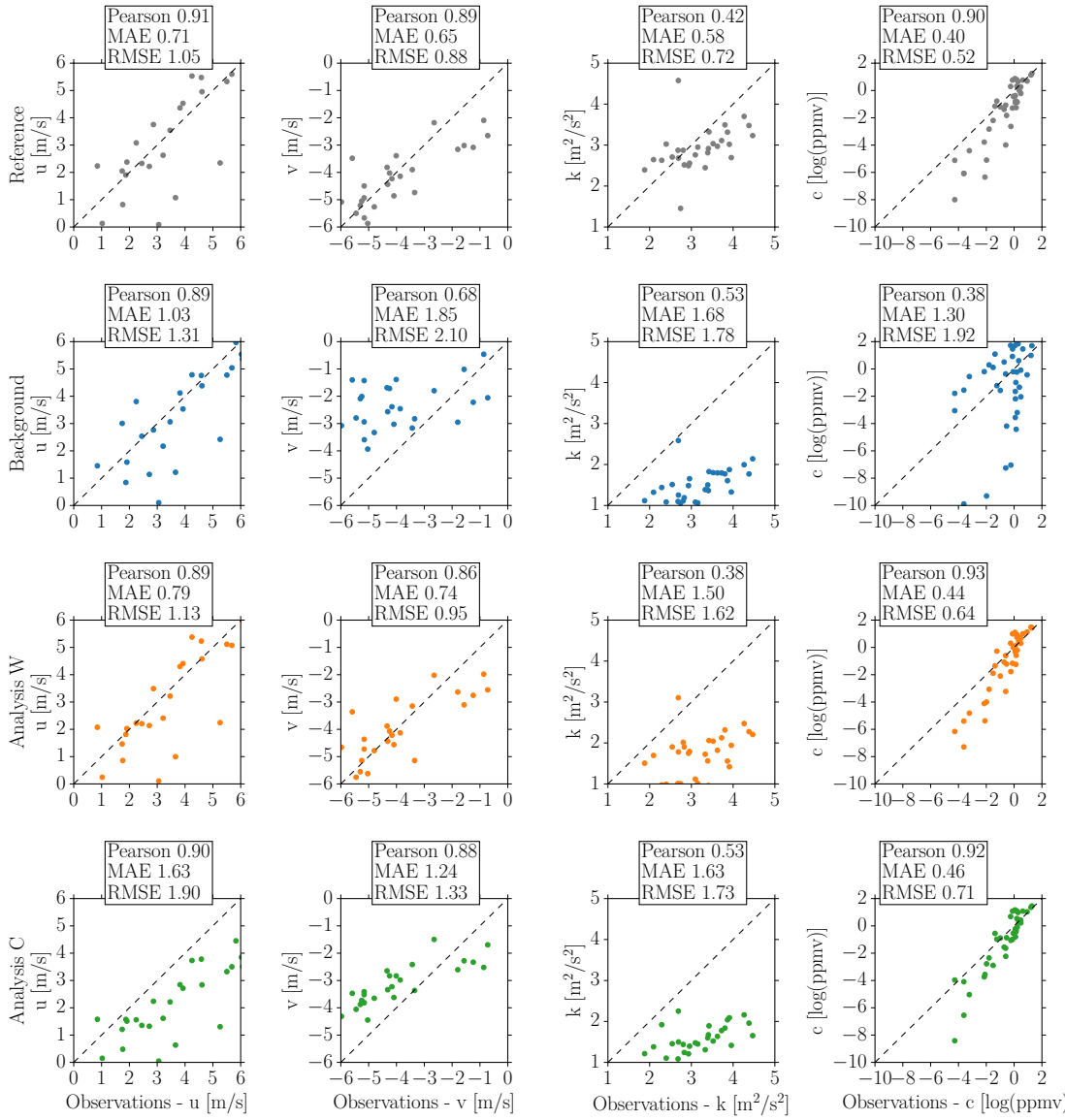

Figure 6.10: Simulated versus observed values for the reference simulation (first row), the background (second row), Analysis W (third row), and Analysis C (fourth row) for the Neutral case. The scatter plots are shown for the two components of the horizontal velocity (u, v), the TKE (k), and the concentration of the tracer gas (c). The Pearson coefficient, the mean absolute error (MAE), and the root mean square error (RMSE) are also calculated for each variable and simulation. All the available observations are plotted and taken into account in the statistics calculations.

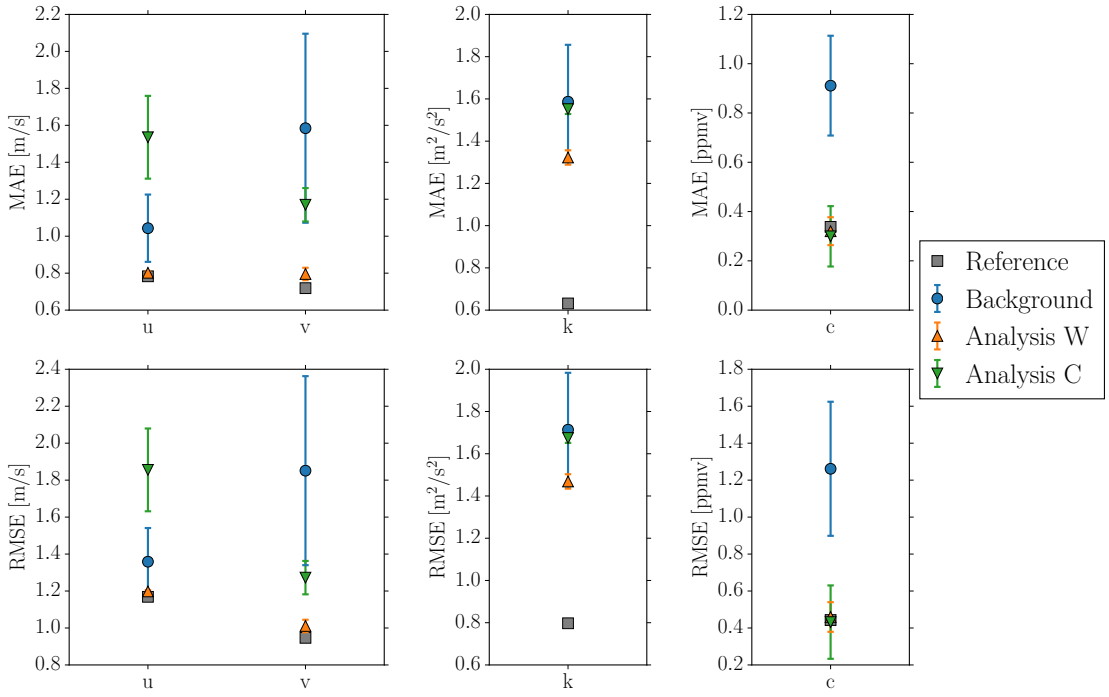

Figure 6.11: MAE and RMSE calculated over the validation observations of u, v, k, and c within the urban canopy ($h < 2.5$m) for the reference, background, and analyses W and C in the Neutral case. The mean values are calculated as an average over the errors, weighted by the inverse of the number of observations available at the same location. Errorbars represent twice the standard deviation of the background and analysis ensembles.

Upstream, the error of velocity, shown in Figure 6.8d, is somehow aligned with the mean flow. This means that the wind direction has been rectified in the BC. However, the wind speed is still underestimated. Downstream, the downward arrows indicate that the error for the v-component of velocity has been reduced but the error for u has increased. As a result, the incidence angle of the wind flow is now too small and the pollutant plume far from the source goes more to the right than the reference simulation. The remaining errors for the wind speed and direction, or alternatively for u and v, explain the light overestimation of the concentrations on the right side of the plume. Still, the errors for concentrations are largely reduced between the background and Analysis C.

Figure 6.9d shows that near the pollutant source, the wind speed is still underestimated though the effect of buildings is here less pronounced – due to the better alignment of the wind flow with the containers. As a result of the faster wind speed, the concentrations are slightly overestimated but the shape of the pollutant plume is very similar to the reference within the canopy. In particular, the concentrations decrease with distance from the source at a similar rate and, in the vicinity of the source, the recirculation has vanished.

In order to further evaluate the benefit of the DA process, Figure 6.10 shows the simulated versus observed values for the two wind components, the TKE, and tracer concentration. These scatter plots are presented for the reference simulation, the background, and analyses W and C. All the available observations – even those assimilated – are represented. Some error statistics – MAE, RMSE, and Pearson coefficient – are also shown.

The error statistics shown in Figure 6.10 are calculated over all the available observations, taking into account all the observations – even the assimilated ones – and without any specific averaging. However, some masts provide several observations at the same horizontal location but at different vertical levels. In order to avoid giving more weight to these well-observed locations, the errors are multiplied by a coefficient equal to the inverse of the number of available observations (for the same variable) at the same horizontal position. With this averaging convention, and considering only the validation observations, we compute the MAE and the RMSE for all the ensemble members, the background, and the analyses. Figure 6.11 shows the MAE and the RMSE, for the background and analyses W and C, and the STD calculated over the background and analysis ensembles (errorbars).

From Figures 6.10 and 6.11, we can confirm the conclusions drawn from the previous analysis of the velocity and concentration fields. In the first experiment, the assimilation of wind observations allows to largely reduce the error for u and v to levels very close to that obtained with the reference simulation. As a result of a better estimation of the wind field, there is a better agreement between observed and simulated values of concentration and the error for c is significantly reduced.

On the other hand, assimilating observations of concentration do not necessarily

improve the knowledge of the velocity field. In the present example, the error for v is reduced whereas the error for u – which was quite small in the background simulation – is increased. We can see again in Figure 6.10 that the velocities simulated with Analysis C are underestimated. As mentioned above, even though errors subsist in the velocity field, the dispersion is well represented. Consequently, the error of concentration estimations is largely reduced.

In all the simulations – background and both analyses – the turbulence is underestimated though the IEnKS helps slightly reduce this error. The small impact of the IEnKS on turbulence BC (not shown) and consequently on the field of simulated TKE suggests that in the present case the inflow turbulence does not impact much the gas dispersion. In fact, most of the turbulence is formed due to the presence of obstacles.

Figure 6.11 also shows the STD of the ensembles, which provide a measure of uncertainty for the simulated values of u, v, k, and c. We can see that assimilating observations of wind, besides decreasing the error, also reduces the uncertainty of u, v, and c. Assimilating observation of concentrations helps to substantially reduce the uncertainty of the simulated concentrations, however the uncertainties of u and v remain quite large.

Comparing the results obtained for the two experiments, one can see that assimilating observations of wind velocity allows to better reduce the error and uncertainty of wind values than assimilating observations of concentration. Since dispersion is mainly driven by the wind flow, the error and uncertainty of concentrations are also significantly reduced through the DA process. Assimilating observations of wind allows to better recover the full state of the system and it is thus somehow more efficient than assimilating observations of concentration.

6.4.3 Stable case

For the stable case, the BC first estimated from the observations provided by the SAMS and the SODAR give particularly good results. The mean departure of the simulated wind field with these BC, compared to the available observations, is equal to 0.6m/s. In fact, as the meteorological conditions are stable, we can guess that the wind profile varies very little spatially and the conditions observed a few hundreds of meters away from the *Code_Saturne* domain give a very good estimation of the BC.

Even with the background BC perturbed as explained in Section 6.3.5, the MAE to the available observations, averaged over u and v observations is of 0.73m/s only in the first experiment, and in the second experiment, the departure from the concentration observations is initially equal to 1.3ppmv.

Figures 6.12a and 6.13a show the velocity and concentration fields simulated with the reference BC. Figure 6.12b shows the departure from this reference simulation above the containers ($h = 4$m). The field of velocity error is oriented toward the left, which indicates that the background error is here again mainly along the v-component. In

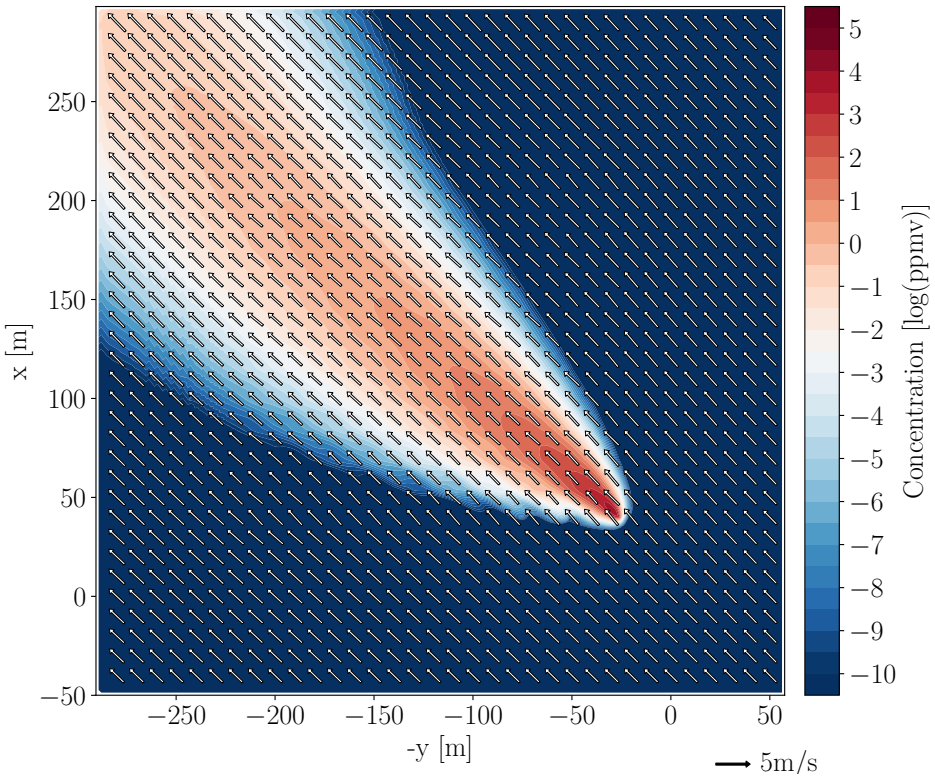

(a) Reference

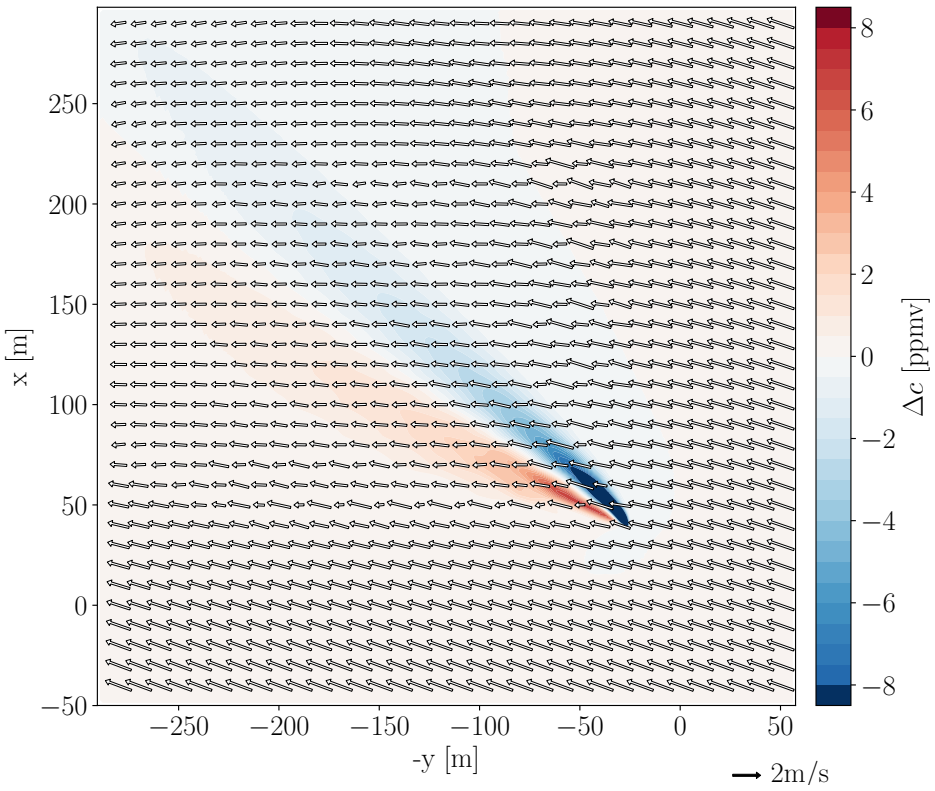

(b) Background (departure from reference)

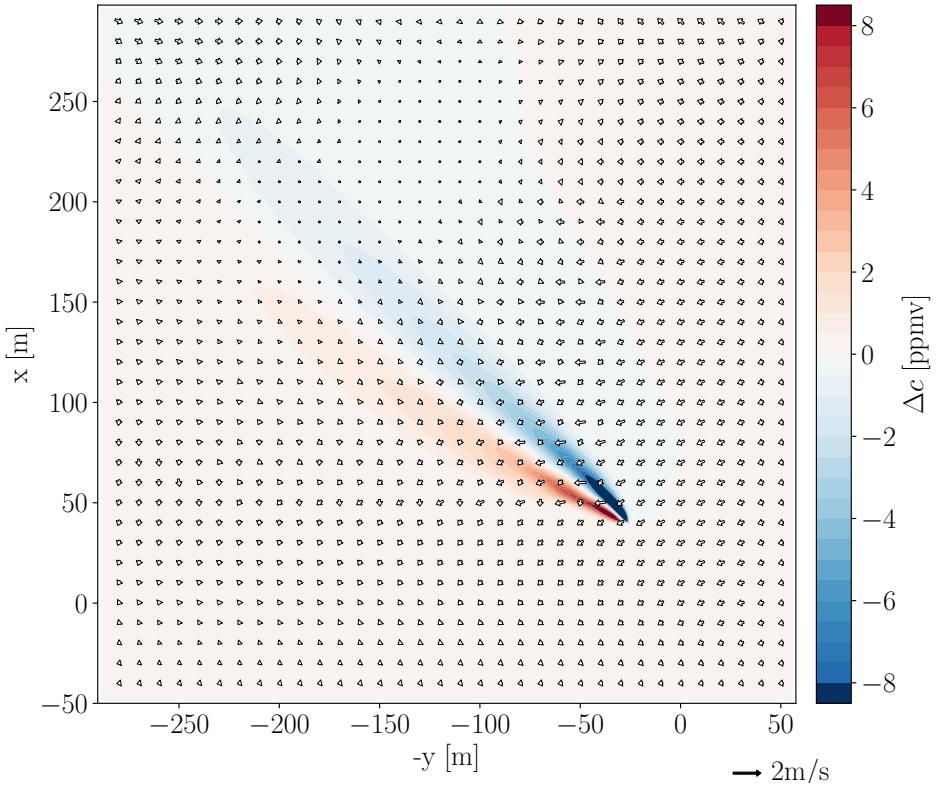

(c) Analysis W (departure from reference)

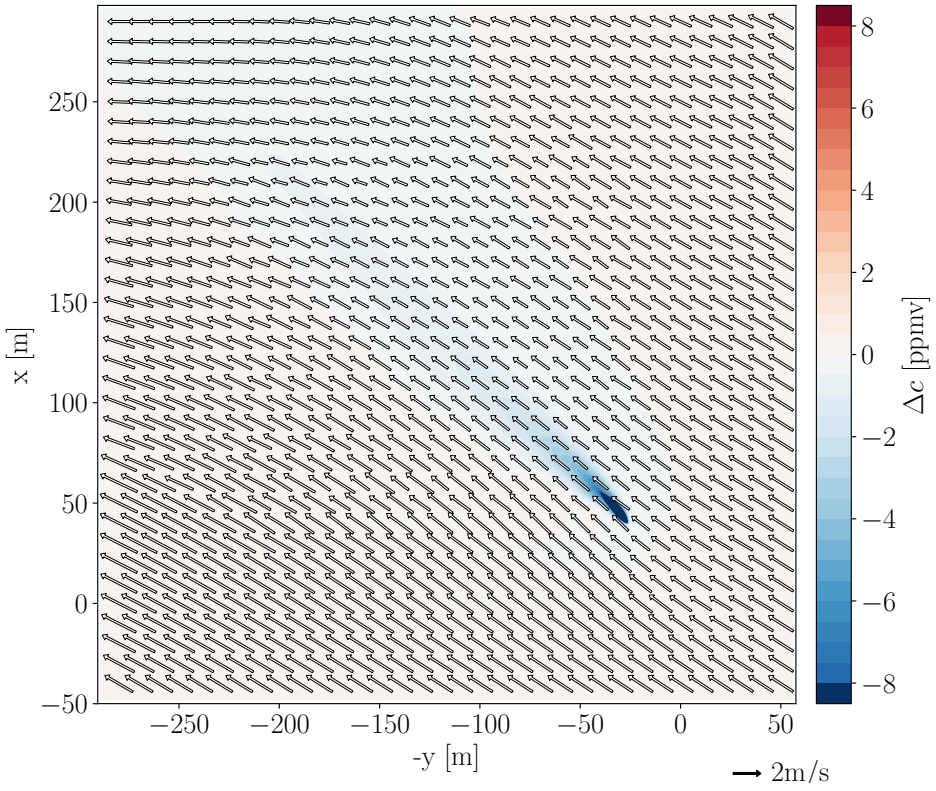

(d) Analysis C (departure from reference)

Figure 6.12: Same as Figure 6.8 but for the Stable case.

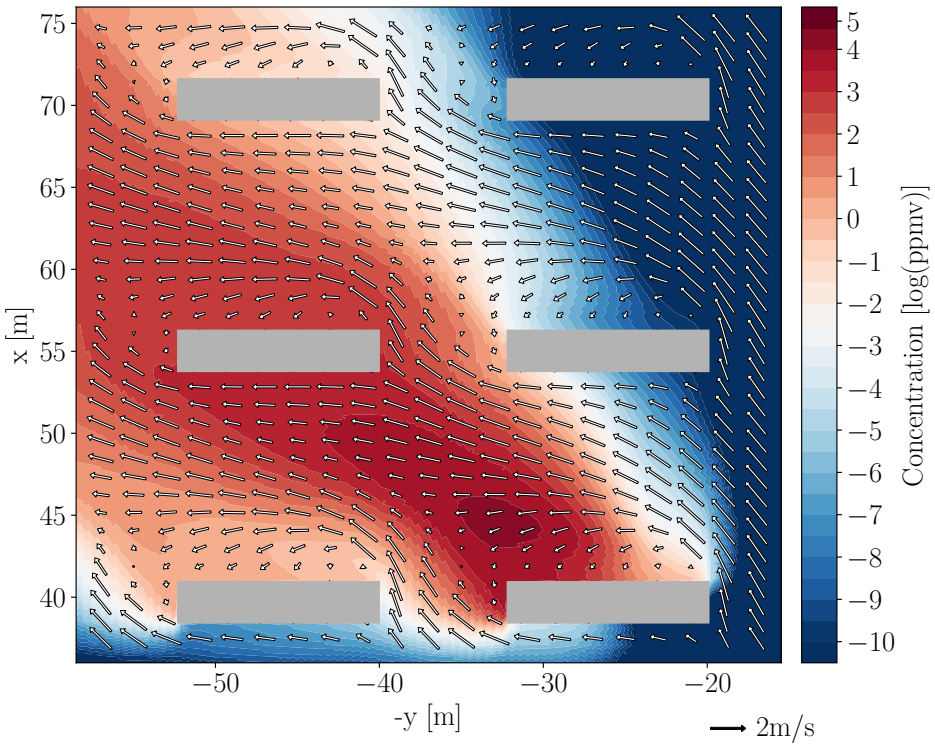

(a) Reference

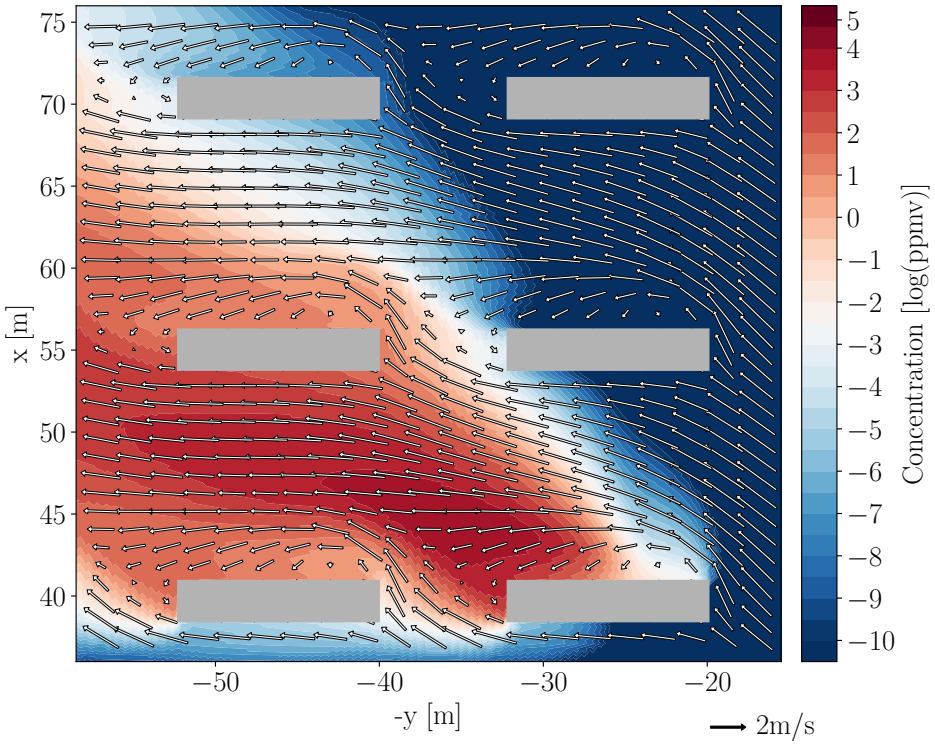

(b) Background

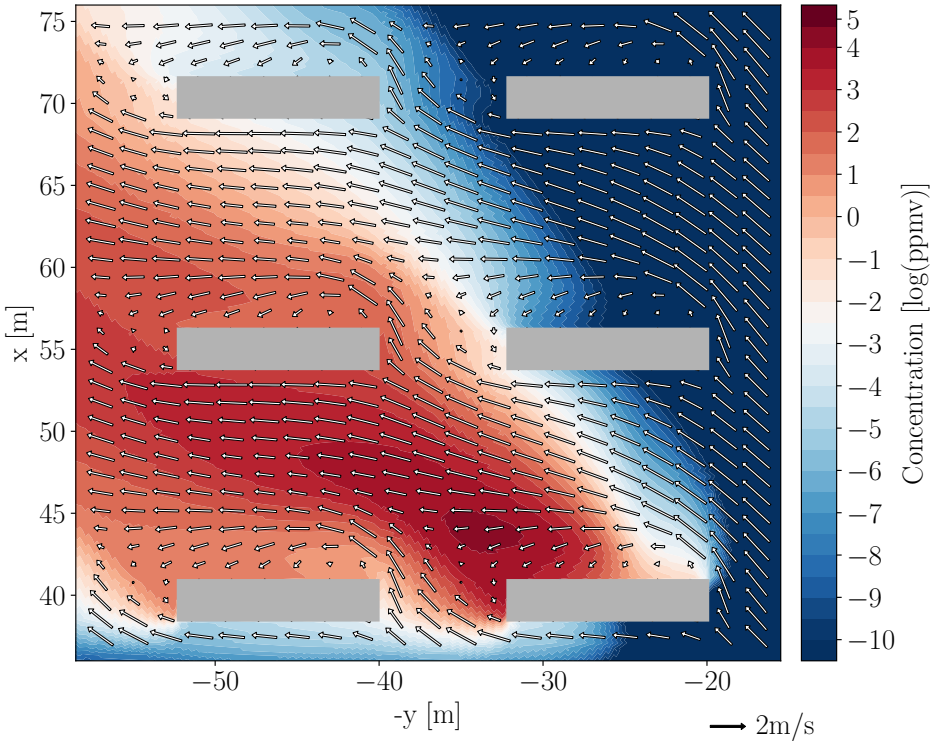

(c) Analysis W

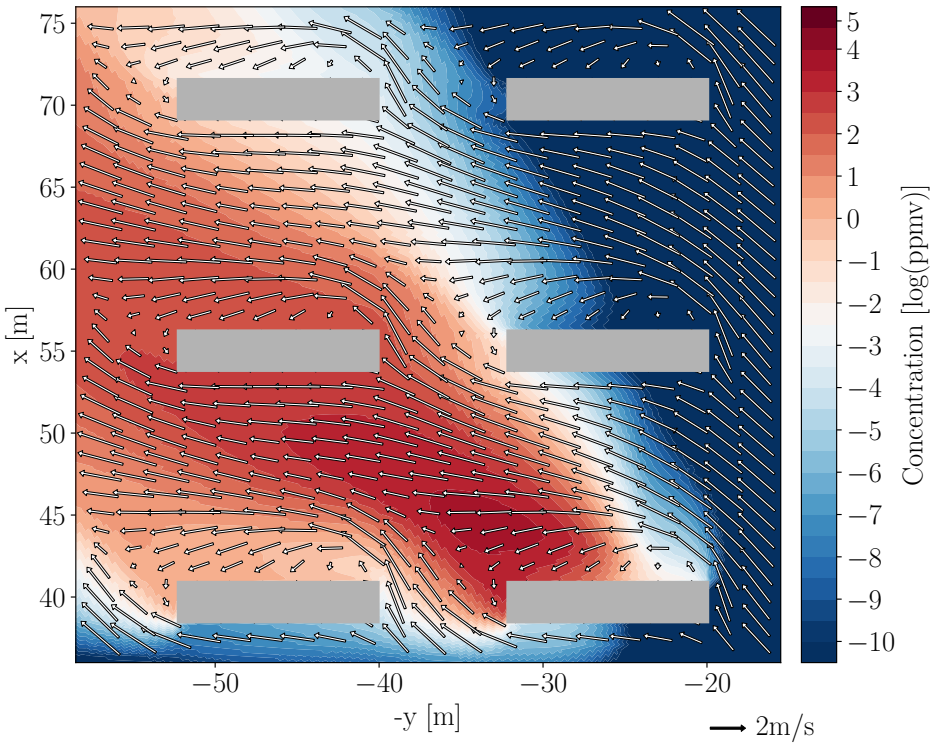

(d) Analysis C

Figure 6.13: Same as Figure 6.9 but for the Stable case.

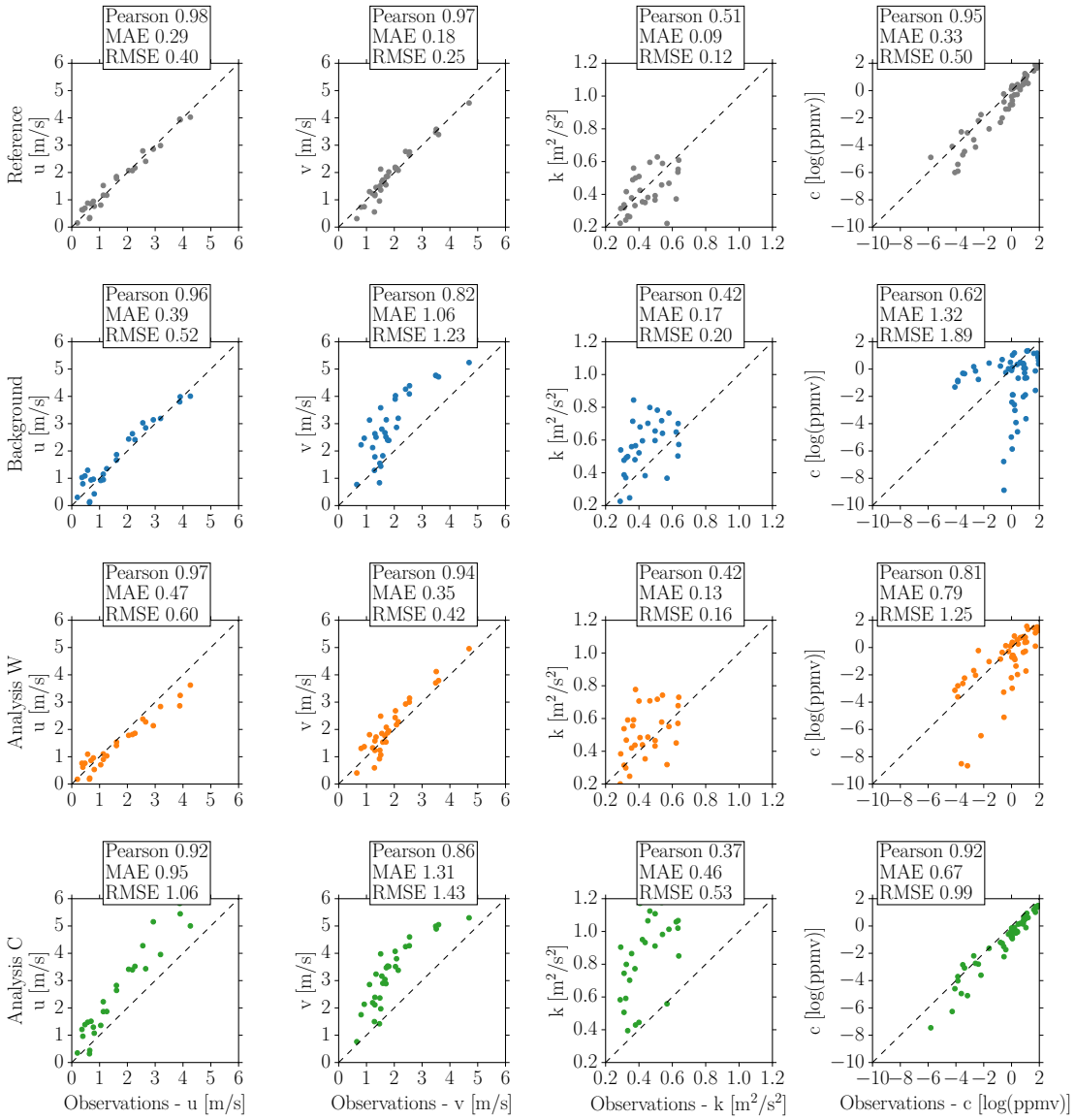

Figure 6.14: Same as Figure 6.10 but for the Stable case.

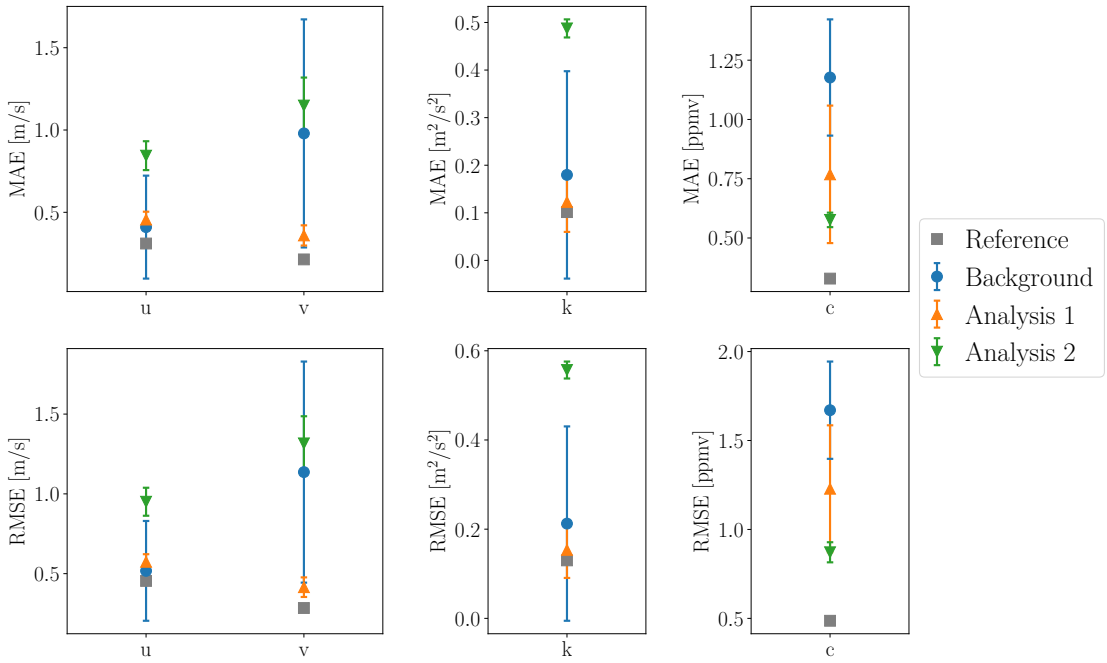

Figure 6.15: Same as Figure 6.11 but for the Stable case.

addition, the wind speed is globally overestimated. We can see that the erroneous wind speed and direction in the background simulation triggers a quite different behaviour of the pollutant plume. Here it is the contrary compared to the Neutral case: since the wind flow is more aligned with the containers in the background simulation and the wind flow is too fast, the velocity field is less altered by the presence of obstacles and the gas is more dispersed. This leads to a global underestimation of the concentrations in the background simulation. Moreover, due to the error of wind direction, the pollutant plume far from the source goes more to the left than the reference plume and tends to spread more. This explains that the concentrations are overestimated on the left of the plume and underestimated on the right.

We can verify in Figure 6.13b that the wind speed is less reduced in the container array and that the wind flow is nearly aligned with the streets. As a result, the gas is transported more to the left and substantial underestimation can be observed in the top-left corner.

We perform the DA experiments starting from the background described above. The optimal value of the BC is obtained after 5 IEnKS iterations in the first experiment, and 8 in the second one.

Similar to the results obtained in the Neutral case, the velocity field of Analysis W is more similar to the reference than the background and the velocity errors are significantly reduced (see Fig. 6.12c). There remains small errors of wind speed and direction such that the deviation of the plume to the left subsists. The errors for concentrations are still much smaller than for the background.

Figure 6.13c shows that near the source the same conclusions hold: the wind field is similar to the reference and the pollutant plume is more similar than the background, though still slightly different. In particular, the plume is less spread toward the right such that the concentration field in the bottom-left part of the figure is very similar to the reference simulation, though in the top-left corner the concentrations are underestimated.

Figure 6.12d shows that the velocity errors for Analysis C are aligned with the wind flow, which means that the wind direction has been corrected. A a result, the pollutant plume is dispersed in the correct direction. However, the wind speed is still overestimated such that the gas is more washed by the wind and the concentrations are globally underestimated. The behaviour near the source is also better captured in terms of region affected by the pollution, however the concentrations are somehow smaller than the reference (see Fig. 6.13d).

Figures 6.14 and 6.15 show a comparison of the results obtained in the Stable case for both experiments with the available observations. The results obtained in this Stable case are very similar to those obtained with the Neutral case. The u-component of velocity is already very well represented in the background, such that the IEnKS only allows to reduce the uncertainty when wind observations are assimilated. For the Stable case, as for the Neutral one, Analysis C leads to slightly worse estimations of u. Note that the analysis errors for u and v are then of the same order of magnitude (approximately 1m/s which is consistent with the fact that similar error statistics are considered for u and v.

Most of the background error comes from the v-component of velocity. This error is corrected very efficiently in the first experiment but not in the second one. In this case, the TKE is slightly overestimated in the background and the assimilation of wind observations allows to somehow reduce this error but not the assimilation of concentration observations.

Regarding the concentration, both Analysis W and C show errors that are significantly reduced. However, Analysis C gives better results in terms of agreement between observed and simulated values (see Fig. 6.14). We can observe in Figure 6.14 that low values of concentration are underestimated in the first analysis. This is consistent with the behaviour of the pollutant plume near the source presented above.

6.4.4 Additional tests

In addition to the results presented in the two previous sections, we have tested the IEnKS with other parametrisations.

In particular, we have evaluated the performances of the IEnKS with different background errors. We have performed the DA experiment with the unperturbed background – estimated from the PWIDS, SAMS, and SODAR observations – with the background perturbed with $\Delta\text{WD} = -10^\circ$ and with $\Delta\text{WS} = 10\text{m/s}$ (not shown). In all the cases, assimilating observations of the velocity components helps reduce the error and the uncertainty of the simulated velocity field. Due to the important sensitivity of the

plume dispersion to the wind field, the pollutant plume is generally also better captured. When concentration observations are assimilated, the mean error of concentrations significantly decreases, and especially within the urban canopy ($h < 2.5$m). Note that when the perturbation of the wind direction is reversed as compared to the results shown above ($\Delta\text{WD} = -10°$), the background error of the v-component of velocity is smaller than the error of u and assimilating concentration observations tends to correct the error of u but may worsen the v estimations. Introducing correlations between these two variables, or considering different error statistics for u and v in the background error covariance matrix, could help correct both components of velocity when assimilating concentration observations.

The analyses obtained in the different experiments described above depend on the background, even though this sensitivity is somehow small. It is consistent with the fact that the weight given to the observations is much larger than the one given to the background. This comes from the fact that the eigenvalues of the background error covariance matrix are of the order of magnitude of 25 whereas the eigenvalues of $\mathbf{R}$ are approximately 0.025. As a matter of fact, the part of the cost function associated with the background

$$\mathcal{J}^{\mathrm{b}} = \frac{1}{2}\mathbf{w}^{\mathrm{T}}\mathbf{w} \tag{6.18}$$

is typically 10 times smaller than the term associated with the observations

$$\mathcal{J}^{\mathrm{o}} = \frac{1}{2}\|\mathbf{y} - \mathcal{H} \circ \mathcal{M}(\mathbf{z}^{\mathrm{b}} + \mathbf{A}\mathbf{w})\|^2_{\mathbf{R}^{-1}}. \tag{6.19}$$

The influence of the radius of vertical correlation (see Eq. 6.7) has been assessed. A very large radius (typically 50m) is equivalent to assume that the error is a bias, nearly constant in the vertical, which is not representative of a typical background error as explained in Section 6.3.5. As a result, assimilating observations in the canopy helps correct the BC near the ground and the strong correlation tend to also modify the profile in the upper levels. This might lead to increase the error in the higher atmosphere where the background is typically small and no additional information is available (observations are generally available a low altitudes).

Finally, we have also evaluated the performances of the method when both wind and concentration observations are assimilated (not shown). In order to keep a similar number of observations in total, we have considered 15 observations: 4 of u, 4 of v, and 7 of concentration, in the Neutral and Stable case. The analyses obtained in these experiments are very similar to the Analyses W: both the wind and concentration fields are better estimated. In addition, the turbulence is corrected by the IEnKS. This confirms that assimilating wind observations is somehow more efficient than assimilating concentration observations only. Indeed, there is a causal connection between the velocity and concentration fields and once the velocity field is well known, the dispersion is necessarily better represented. In the present experiment, we add more information to

the Analysis W by assimilating concentration observations, which tend to correct the remaining variables that influence the concentration field, i.e. turbulence.

6.5 Conclusions

In this chapter, the IEnKS has been applied to a case of dispersion modelling in an urban area. These DA experiments differ from the application of wind resource assessment presented in Chapter 5 by the fact that the size of the control vector is smaller, though it includes turbulence variables. Moreover, the final outcome of interest here is the concentration of a tracer gas, which is nonlinearly related to the wind field and turbulence. The MUST campaign has been widely studied and has the great advantage to provide very numerous observations of wind velocity, turbulence, and gas concentration.

Among the several trials of gas release performed during the MUST campaign, we have here selected two trials, corresponding to stable and neutral stability conditions. For each of these two cases, we have performed two DA experiments assimilating either wind or concentration observations. For all the experiments, the IEnKS helps reduce the error and the uncertainty for the assimilated variables: either wind components or concentration. Since dispersion is largely driven by wind, when velocity observations are assimilated, the correction of the wind field through DA also leads to a better representation of pollutant dispersion. Consequently, the causality relation between wind and dispersion explains that assimilating observations of wind is more efficient to improve the overall dispersion simulation. On the other hand, assimilating concentration observations modifies the wind field in a way such that the error on u and v separately may increase. In general, the wind direction is rectified – it is the parameter that influences the most dispersion – and in turns the concentration field simulated with this new wind field is closer to the observations.

In the experiments presented in this chapter, the errors in the TKE profile are poorly corrected by the DA process. This could be explained by the fact that no information directly related to the turbulence is added, since we do not assimilate observations of turbulence. Moreover, even when concentration observations are assimilated, the error for the TKE is not much reduced. This suggests that in the cases studied here, dispersion is less sensitive to the inflow turbulence and that the turbulence is mostly created by the obstacles. We have seen that assimilating observations of both wind and concentration helps correct the TKE. One can imagine that assimilating observations of turbulence variables would be another solution to rectify the BC related to turbulence.

We have assessed the small sensitivity of the method to the background error, consistent with the larger confidence placed in the observations than the background. In this study, we assume that the observation errors are uncorrelated, however this assumption is probably incorrect especially for u and v. Consequently, it would be interesting to perform further sensitivity analyses regarding the observation error covariance matrix.

Moreover, we have here always worked with ensembles of 5 members and it would be beneficial to assess the evolution of the performances of the IEnKS with the ensemble size.

The two experiments presented here correspond to a similar (small) number of observations and one could consider evaluating the sensitivity of the results to the number and the position of the observations. Such an analysis could be particularly beneficial for experimental design.

Another perspective would be to apply the IEnKS to the remaining trials performed during the MUST campaign. In particular, the cases 2671934, 2672033, and 2672101 correspond to very stable atmospheric conditions such that the usual formulas to estimate the vertical profile of BC cannot be applied. As a result, these cases are known to be particularly difficult to simulate and it would be interesting to try recovering the BC using the IEnKS (Kumar et al., 2015).

Conclusions and perspectives

The present work is part of the research effort of the Centre d'Enseignement et de Recherche en Environnement Atmosphérique (CEREA) which performs several types of micrometeorological studies such as wind resource assessment and pollutant dispersion in built environments. Similarly, the dispersion of radioactive or chemical materials is of great interest for the Commissariat à l'énergie atomique et aux énergies alternatives (CEA). These micrometeorological applications require the accurate reconstruction of meteorological fields (wind, turbulence, etc.) over local-scale domains. When the domains under investigation contain complex geometrical features such as buildings or steep topography, the use of computational fluid dynamics (CFD) model is recommended. One of the counterparts of CFD models is their sensitivity to input parameters, and especially to the boundary conditions (BC) required at the open boundaries of the domains. Downscaling methods – which consist in extrapolating the results of mesoscale simulations to first estimate the BC – are generally used to force the local-scale simulations with mesoscale meteorology. However, such methods still present some errors and limitations. When field measurements of meteorological variables or pollutant concentrations are available, they represent a great source of information, not sufficiently exploited so far. Applying data assimilation (DA) methods, appropriate for micrometeorological applications, is a solution to take the available observations into account and improve simulations.

In the present work, we have first chosen two DA methods that seemed adapted to an usage with a CFD model in the context of local-scale atmospheric simulations: the back and forth nudging (BFN) algorithm and the iterative ensemble Kalman smoother (IEnKS). These two methods have been adapted here in order to take the BC into account, instead of the initial conditions (IC) as in their original derivations.

For the IEnKS, a very similar mathematical derivation can be applied, albeit replacing the IC by the BC in the control vector. While utilizing an ensemble to represent the background error statistics has several advantages – avoiding the use of the model adjoint, estimating the uncertainty, reducing the size of the problem, etc. – it requires an adequate definition of the initial ensemble. The initial – or background – ensemble represents the background error covariance matrix and can be built from the leading modes of this matrix. The problem then comes to estimate the background error covariance matrix. In the present work, we have proposed a method to estimate it, based on the statistical

analysis of the climatological covariances. These covariances are evaluated from long time series of mesoscale simulations or observations.

Regarding the BFN algorithm, a new implementation has been derived to correct the BC with the algorithm iterations. In particular, we have proposed to perform the backward integration with the forward model and positive time steps but with the velocity field reversed. This equivalency is exact when the model considered solves the shallow-water equations (SWE) and we have generalized this result to the CFD models.

The performances of the two DA methods have been evaluated on three different studies, gradually increasing complexity. At first, we have considered a simple model of atmospheric flow, based on the solution of the one-dimensional SWE. With this model, the atmosphere is represented by two layers of fluid: the atmospheric boundary layer (ABL) which is governed by the SWE and the free atmosphere above. This model has been used to develop the methods and assess their performances. In particular, the small size of the control vector has allowed us to compare the results obtained with the IEnKS and the BFN algorithm to the results given by 3D-Var, considered here as a reference method. Both methods have proved to greatly reduce the error of the BC and thus of the simulated system state. The simplicity of the model has also allowed us to perform several sensitivity analyses and to confirm that the behaviour of the two methods was in agreement with the theory. In particular, the 3D-Var and the IEnKS on one hand, and the BFN algorithm on the other hand solve fundamentally different DA problems.

The IEnKS and the BFN algorithm have then been tested with the atmospheric module of *Code_Saturne*. The second study corresponded to a real application of wind resource assessment for a domain with very complex topography. At first, we have considered a 2D slice and twin experiments, then we have performed twin experiments in 3D, and finally we have assimilated observations provided by a field campaign. The results obtained in this last configuration are validated with other observations, not assimilated. This second study, has highlighted some limits of the revised version of the BFN. In fact, the proposed method to perform the backward integrations is based on a linearity assumption that fails with *Code_Saturne* over steep topography. On the other hand, the IEnKS has proved to greatly enhance the precision of the BC with a small number of members and thus a reasonable number of model integrations. In addition, this ensemble-based method has the great advantage to provide an estimate of the uncertainty of the BC which is reduced through the DA process. We have highlighted in this study that using *Code_Saturne* for wind resource assessment does not necessarily improves the wind potential estimation if the BC provided by downscaling are incorrect. However, after the application of the IEnKS, the error and uncertainty of the wind potential are both greatly reduced.

Finally, we have studied a case of pollutant dispersion in a built environment, based on the Mock Urban Setting Test (MUST) field campaign with the IEnKS. Two different stability conditions have been considered (neutral and stable) and in both cases two

experiments have been performed to assess the ability of the method to assimilate either wind or concentration observations within the urban canopy. The estimation of the assimilated variables are better improved than the variables that are not assimilated. Due to the large influence of wind field on dispersion, when wind observations are assimilated the wind field is better represented and consequently the concentration field is also more accurate. As a result, assimilating wind measurements is somehow more efficient to improve the overall simulation. Assimilating both types of observations allows to also improve the estimation of inflow turbulence. In all the cases analysed, the IEnKS with a few ensemble members allow to greatly enhance the exactitude – i.e., the ensemble mean – as well as the accuracy – i.e., the ensemble spread – of the simulated pollutant dispersion, which the the main objective of this kind of studies.

While DA methods are widely used to correct the IC of large-scale atmospheric simulations, only a few past studies applied such methods to improve atmospheric simulations at local scale, and even fewer examples consider CFD models. The present work is thus original as it provides first examples of the application of DA methods for micrometeorological applications. Besides deriving new versions of two existing methods, adapted to the issue of BC estimation, we have shown that one of the methods (IEnKS) is very appropriate for micrometeorological studies in quasi-operational conditions. While the BFN algorithm has not been further studied in the present work, it does not seem to me that this DA method is fundamentally inappropriate for micrometeorological applications with CFD model. Indeed, several potential improvements have been put forward such as extruding the domain with flat borders or using a linearised version of the model for the backward integration.

The results obtained with the IEnKS are very promising and it would be very interesting to further improve this method. At first, we have highlighted that the initialisation of the ensemble is a crucial step that might be problematic. A perspective to improve this initialisation step comes with the evolution of the outputs of mesoscale models. Indeed, weather forecast agencies tend to provide ensembles of mesoscale simulations at a resolution increasingly fine. These ensembles could provide a very good starting point to construct the background ensemble of BC for the application of the IEnKS.

Another perspective for future works is related to the use of localisation to improve the performances of the IEnKS. The main idea of localisation is that most geophysical systems exhibit correlations that vanish with distance. A key approach to implement localisation – when the control variables correspond to the system state – is called "domain localisation" and comes to perform local analyses, taking into account only the observations within a given radius of influence. Such a method is hardly transposable to the present case where the control variables correspond to the BC. In fact, the area of influence of a given observation is less clear. A second approach of localisation, called "covariance localisation", consists in filtering the spurious correlations obtained in the

analysis error covariance matrix. This method has already been implemented with the IEnKS (Bocquet, 2016) but in studies where the control variables correspond to IC. It would be interesting to analyse how the localisation methods could be generalised in the micrometeorological context where the control variables are the BC.

All the studies performed in the present work considered constant BC and steady states obtained when these BC are prescribed. To broaden the application cases, one could consider unsteady BC. Two approaches could be considered in such a case. First, all the variables that define the unsteady BC could be included in a (very) large control vector. The IEnKS would then assimilate asynchronous observations and try to recover the "trajectory" of BC that best fits the observations. On the other hand, one could divide the time period under scrutiny into consecutive (short) periods during which the BC are considered constant. The methodology presented in the present work could then be applied as it is, for each of these "steady" sub-periods. In such a case, several cycles of analyses would be chained, so that the analysis ensemble of the previous cycle could be used as the background ensemble of the next cycle. Both inflation and localisation may be needed for unsteady studies.

For each of the present studies, we kept the same DA pattern: both the number and location of the assimilated observations were unchanged. It would be interesting to assess the sensitivity of the results to the number of observations as well as their location, both horizontally and vertically. Such analyses could be particularly useful to study best practices in terms of experimental design.

Eventually, we have here focused on local-scale atmospheric simulations and we performed all the simulations with the CFD model *Code_Saturne*. However, one of the great advantages of the IEnKS is its modularity. Indeed, this DA method is non-intrusive and can be quite easily adapted to other models of micrometeorology. One could imagine to use the IEnKS for several other fields of applications. For instance wildfire studies also require the precise estimation of the wind field in regions with possible complex terrain and can benefit from using DA (Rochoux et al., 2013, 2015). On the other hand, climate studies at regional scale face similar issues of high sensitivity to the resolution of the BC that are estimated through downscaling (Rummukainen, 2010) and the IEnKS could be used to improve their accuracy.

Bibliography

Abbott, M., 1966: *An introduction to the Method of Characteristics*. American Elsevier, New York, NY. 40, 187

Al-Yahyai, S., Y. Charabi, and A. Gastli, 2010: Review of the use of Numerical Weather Prediction (NWP) Models for wind energy assessment. *Renew. Sustain. Energy Rev.*, **14**, 3192–3198. 46

Albriet, B., K. Sartelet, S. Lacour, B. Carissimo, and C. Seigneur, 2010: Modelling aerosol number distributions from a vehicle exhaust with an aerosol CFD model. *Atmospheric Environ.*, **44**, 1126–1137. 42, 124

Alcrudo, F., and P. Garcia-Navarro, 1993: A high-resolution Godunov-type scheme in finite volumes for the 2D shallow-water equations. *Int. J. for Numer. Methods Fluids*, **16**, 489–505. 70

Angot, G., 2018: WRAPP - A comprehensive methodology to estimate the wind resource, production and wake effects. *Code_Saturne & NEPTUNE_CFD user meeting*. 48

Antoniou, I., H. E. Jorgensen, F. Ormel, S. G. Bradley, S. von Hünerbein, S. Emeis, and G. Warmbier, 2003: On the theory of SODAR measurement techniques (final reporting on WP1, EU WISE project NNE5-2001297). Tech. rep., RisøNational Laboratory, Roskilde, Denmark, 61 pp. 56

Apte, A., D. Auroux, and M. Ramaswamy, 2018: Observers for compressible Navier-Stokes equation. *SIAM J. on Control. Optim.*, **56**, 1081–1104. 92

Archambeau, F., N. Méchitoua, and M. Sakiz, 2004: Code Saturne: A Finite Volume Code for the computation of turbulent incompressible flows - Industrial Applications. *Int. J. on Finite Vol.*, **1**. 41

Arya, S. P., 1988: *Introduction to micrometeorology*. Academic Press, San Diego. 29, 31, 34

Asch, M., M. Bocquet, and M. Nodet, 2016: *Data assimilation: methods, algorithms, and applications*. Society for Industrial and Applied Mathematics. 58, 59, 64, 65

Audusse, E., M. O. Bristeau, and A. Decoene, 2006: 3D Free Surface Flows Simulations Using a Multilayer Saint-Venant Model. Comparisons with Navier-Stokes Solutions. *Numerical Mathematics and Advanced Applications: Proceedings of ENUMATH 2005, the 6th European Conference on Numerical Mathematics and Advanced Applications Santiago de Compostela, Spain, July 2005*, Springer Berlin Heidelberg, Berlin, Heidelberg, 181–189. 40

Auroux, D., 2008: The back and forth nudging algorithm applied to a shallow water model, comparison and hybridization with the 4D-VAR. *Int. J. for Numer. Methods Fluids*, **61**, 911–929. 68

Auroux, D., P. Bansart, and J. Blum, 2013: An evolution of the back and forth nudging for geophysical data assimilation: application to Burgers equation and comparisons. *Inverse Probl. Sci. Eng.*, **21**, 399–419. 59

Auroux, D., and J. Blum, 2005: Back and forth nudging algorithm for data assimilation problems. *Comptes Rendus Math.*, **340**, 873–878. 59, 68, 69, 72

Auroux, D., and J. Blum, 2008: A nudging-based data assimilation method: the Back and Forth Nudging (BFN) algorithm. *Nonlin. Process. Geophys.*, **15**, 305–319. 59, 68

Auroux, D., J. Blum, and M. Nodet, 2011: Diffusive Back and Forth Nudging algorithm for data assimilation. *Comptes Rendus Math.*, **349**, 849–854. 59, 68

Auroux, D., and S. Bonnabel, 2011: Symmetry-based observers for some water-tank problems. *IEEE Transactions on Autom. Control.*, **56**, 1046–1058. 92

Auroux, D., and M. Nodet, 2012: The Back and Forth Nudging algorithm for data assimilation problems : theoretical results on transport equations. *ESAIM: Control. Optimisation Calc. Var.*, **18**, 318–342. 59, 68

Ayotte, K. W., 2008: Computational modelling for wind energy assessment. *J. Wind. Eng. Ind. Aerodyn.*, **96**, 1571–1590. 46

Ayotte, K. W., and D. E. Hughes, 2004: Observations of Boundary-Layer Wind-Tunnel Flow over Isolated Ridges of Varying Steepness and Roughness. *Boundary-Layer Meteor.*, **112**, 525–556. 47

Badger, J., H. Frank, A. N. Hahmann, and G. Giebel, 2014: Wind-Climate Estimation Based on Mesoscale and Microscale Modeling: Statistical–Dynamical Downscaling for Wind Energy Applications. *J. Appl. Meteor. Climatol.*, **53**, 1901–1919. 48

Bahlali, M., 2018: Adaptation de la modélisation hybride eulérienne/lagrangienne stochastique de Code_Saturne à la dispersion atmosphérique de polluants à l'échelle micrométéorologique et comparaison à la méthode eulérienne. Ph.D. thesis, Université Paris-Est, 234 pp. 51, 125, 129, 137

Bahlali, M. L., E. Dupont, and B. Carissimo, 2018: A hybrid CFD RANS/Lagrangian approach to model atmospheric dispersion of pollutants in complex urban geometries. *Int. J. Environ. Pollut.*, **64**, 74–89. 51

Baik, J.-J., S.-B. Park, and J.-J. Kim, 2009: Urban Flow and Dispersion Simulation Using a CFD Model Coupled to a Mesoscale Model. *J. Appl. Meteor. Climatol.*, **48**, 1667–1681. 46

Balgovind, R., A. Dalcher, M. Ghil, E. Kalnay, R. Balgovind, A. Dalcher, M. Ghil, and E. Kalnay, 1983: A Stochastic-Dynamic Model for the Spatial Structure of Forecast Error Statistics. *Mon. Wea. Rev.*, **111**, 701–722. 132

Balogh, M., and A. Parente, 2015: Realistic boundary conditions for the simulation of atmospheric boundary layer flows using an improved k-ϵ model. *J. Wind. Eng. Ind. Aerodyn.*, **144**, 183–190. 46

Barcons, J., M. Avila, and A. Folch, 2018: A wind field downscaling strategy based on domain segmentation and transfer functions. *Wind. Energy*, **21**, 409–425. 47

Benamrane, Y., J.-L. Wybo, and P. Armand, 2013: Chernobyl and Fukushima nuclear accidents: what has changed in the use of atmospheric dispersion modeling? *J. Environ. Radioact.*, **126**, 239–252. 124

Benkhaldoun, F., and M. Seaid, 2010: Solving the shallow water equations using the finite volume modified method of characteristics. *Pap. presented at Fifth Eur. Conf. on Comput. Fluid Dyn. ECCOMAS CFD 2010, Lisbon (Portugal)*. 185, 189, 191, 192

Berre, L., H. Varella, and G. Desroziers, 2015: Modelling of flow-dependent ensemble-based background-error correlations using a wavelet formulation in 4D-Var at Météo-France. *Quart. J. Royal Meteor. Soc.*, **141**, 2803–2812. 64

Bertino, L., G. Evensen, and H. Wackernagel, 2003: Sequential Data Assimilation Techniques in Oceanography. *Int. Stat. Rev.*, **71**, 223–241. 130

Biltoft, C. A., 2001: Customer report for mock urban setting test. *DPG Document Number 8-CO-160-000-052. Prep. for Def. Threat. Reduct. Agency.* 57, 125

Bingöl, F., J. Mann, and D. Foussekis, 2009: Conically scanning lidar error in complex terrain. *Meteor. Zeitschrift*, **18**, 189–195. 56

Björck, Å., 1996: *Numerical Methods for Least Squares Problems*. Society for Industrial and Applied Mathematics. 76

Blocken, B., 2014: 50 years of Computational Wind Engineering: Past, present and future. *J. Wind. Eng. Ind. Aerodyn.*, **129**, 69–102. 46, 93

Blocken, B., 2015: Computational Fluid Dynamics for urban physics: Importance, scales, possibilities, limitations and ten tips and tricks towards accurate and reliable simulations. *Build. Environ.*, **91**, 219–245. 50

Blocken, B., Y. Tominaga, and T. Stathopoulos, 2013: CFD simulation of micro-scale pollutant dispersion in the built environment. *Build. Environ.*, **64**, 225–230. 50

Blocken, B., A. van der Hout, J. Dekker, and O. Weiler, 2015: CFD simulation of wind flow over natural complex terrain: Case study with validation by field measurements for Ria de Ferrol, Galicia, Spain. *J. Wind. Eng. Ind. Aerodyn.*, **147**, 43–57. 47, 93

Bocquet, M., 2016: Localization and the iterative ensemble Kalman smoother. *Quart. J. Royal Meteor. Soc.*, **142**, 1075–1089. 162

Bocquet, M., and P. Sakov, 2012: Combining inflation-free and iterative ensemble Kalman filters for strongly nonlinear systems. *Nonlin. Process. Geophys.*, **19**, 383–399. 76, 77

Bocquet, M., and P. Sakov, 2013: Joint state and parameter estimation with an iterative ensemble Kalman smoother. *Nonlin. Process. Geophys.*, **20**, 803–818. 64, 65

Bocquet, M., and P. Sakov, 2014: An iterative ensemble Kalman smoother. *Quart. J. Royal Meteor. Soc.*, **140**, 1521–1535. 65, 75, 76

Bonavita, M., L. Isaksen, and E. Hólm, 2012: On the use of EDA background error variances in the ECMWF 4D-Var. *Quart. J. Royal Meteor. Soc.*, **138**, 1540–1559. 64

Bonavita, M., L. Raynaud, and L. Isaksen, 2011: Estimating background-error variances with the ECMWF Ensemble of Data Assimilations system: some effects of ensemble size and day-to-day variability. *Quart. J. Royal Meteor. Soc.*, **137**, 423–434. 64

Bosanquet, C. H., and J. L. Pearson, 1936: The spread of smoke and gases from chimneys. *Transactions Faraday Soc.*, **32**, 1249. 49

Bouzereau, E., 2004: Représentation des nuages chauds dans le modèle météorologique "MERCURE" : Application aux panaches d'aéroréfrigérants et aux précipitations orographiques. Ph.D. thesis, Université Pierre et Marie Curie-Paris VI. 42

Buehner, M., and Coauthors, 2010a: Intercomparison of Variational Data Assimilation and the Ensemble Kalman Filter for Global Deterministic NWP. Part I: Description and Single-Observation Experiments. *Mon. Wea. Rev.*, **138**, 1550–1566. 64

Buehner, M., and Coauthors, 2010b: Intercomparison of Variational Data Assimilation and the Ensemble Kalman Filter for Global Deterministic NWP. Part II: One-Month Experiments with Real Observations. *Mon. Wea. Rev.*, **138**, 1567–1586. 64

Buehner, M., and Coauthors, 2015: Implementation of Deterministic Weather Forecasting Systems Based on Ensemble–Variational Data Assimilation at Environment Canada. Part I: The Global System. *Mon. Wea. Rev.*, **143**, 2532–2559. 65

Businger, J. A., 1988: A note on the Businger-Dyer profiles. *Boundary-Layer Meteor.*, **42**, 145–151. 35

Byrd, R. H., P. Lu, J. Nocedal, and C. Zhu, 1995: A Limited Memory Algorithm for Bound Constrained Optimization. *SIAM J. on Sci. Comput.*, **16**, 1190–1208. 81

Carta, J. A., S. Velázquez, and P. Cabrera, 2013: A review of measure-correlate-predict (MCP) methods used to estimate long-term wind characteristics at a target site. *Renew. Sustain. Energy Rev.*, **27**, 362–400. 44

Casey, M., and T. Wintergerste, 2000: *Best Practices Guidelines: ERCOFTAC Special Interest Group on "Quality and Trust in Industrial CFD"*. Ercoftac. 47

Castro, F. A., J. M. L. M. Palma, and A. Silva Lopes, 2003: Simulation of the Askervein Flow. Part 1: Reynolds Averaged Navier–Stokes Equations (k epsilon Turbulence Model). *Boundary-Layer Meteor.*, **107**, 501–530. 47

Castro, F. A., C. S. Santos, and C. Costa, 2010: Development of a meso-microscale coupling procedure for site assessment in complex terrain. *EWEC 2010 - European Wind Energy Conference & Exhibition*, EWEA - European Wind Energy Association. 46

Castro, M., J. Macías, and C. Parés, 2001: A Q -scheme for a class of systems of coupled conservation laws with source term. Application to a two-layer 1-D shallow water system. *ESAIM: Math. Model. Numer. Analysis*, **35**, 107–127. 189, 192

Cattin, R., B. Schaffner, and S. Kunz, 2006: Validation of CFD wind resource modeling in highly complex terrain. *2006 European Wind Energy Association Conference*. 47, 93

Chen, F., and Coauthors, 2011: The integrated WRF/urban modelling system: development, evaluation, and applications to urban environmental problems. *Int. J. Climatol.*, **31**, 273–288. 45

Clifton, A., D. Elliott, and M. Courtney, 2013: Ground-Based vertically profiling remote sensing for wind resource assessment. Tech. rep., International Energy Agency. 55

Cohn, S. E., 1997: An Introduction to Estimation Theory (gtSpecial IssueltData Assimilation in Meteology and Oceanography: Theory and Practice). *J. Meteor. Soc. Jpn. Ser. II*, **75**, 257–288. 130

Cohn, S. E., N. S. Sivakumaran, R. Todling, S. E. Cohn, N. S. Sivakumaran, and R. Todling, 1994: A Fixed-Lag Kalman Smoother for Retrospective Data Assimilation. *Mon. Wea. Rev.*, **122**, 2838–2867. 63

Davoine, X., and M. Bocquet, 2007: Inverse modelling-based reconstruction of the Chernobyl source term available for long-range transport. *Atmospheric Chem. Phys.*, **7**, 1549–1564. 124

Debreu, L., and E. Blayo, 2008: Two-way embedding algorithms: a review. *Ocean. Dyn.*, **58**, 415–428. 45

Defforge, C. L., B. Carissimo, M. Bocquet, P. Armand, and R. Bresson, 2018: Data assimilation at local scale to improve CFD simulations of atmospheric dispersion: application to 1D shallow-water equations and method comparisons. *Int. J. Environ. Pollut.*, **64**, 90–109. 28, 84, 94

Defforge, C. L., B. Carissimo, M. Bocquet, R. Bresson, and P. Armand, 2019a: Improving CFD atmospheric simulations at local scale for wind resource assessment using the iterative ensemble Kalman smoother. *J. Wind. Eng. Ind. Aerodyn.*, **189**, 243–257. 28, 95

Defforge, C. L., B. Carissimo, M. Bocquet, R. Bresson, and P. Armand, 2019b: Improving dispersion modelling in built environments with CFD using the iterative ensemble Kalman smoother. *To be submitted.*

Dhunny, A. Z., M. R. Lollchund, and S. D. Rughooputh, 2017: Wind energy evaluation for a highly complex terrain using Computational Fluid Dynamics (CFD). *Renew. Energy*, **101**, 1–9. 47

Du, S., 2001: A heuristic Lagrangian stochastic particle model of relative diffusion: model formulation and preliminary results. *Atmospheric Environ.*, **35**, 1597–1607. 50

Du Vachat, R., and L. Musson-Genon, 1982: Rossby similarity and turbulent formulations. *Boundary-Layer Meteor.*, **23**, 47–68. 35

Duraisamy, V. J., E. Dupont, and B. Carissimo, 2014: Downscaling wind energy resource from mesoscale to microscale model and data assimilating field measurements. *J. Physics: Conf. Ser.*, **555**, 012 031. 66, 103

Dutton, J. A., 1995: *Dynamics of atmospheric motion.* Dover Pub. 30

Duynkerke, P. G., 1988: Application of the E – epsilon Turbulence Closure Model to the Neutral and Stable Atmospheric Boundary Layer. *J. Atmospheric Sci.*, **45**, 865–880. 35

Ehrhard, J., I. Khatib, C. Winkler, R. Kunz, N. Moussiopoulos, and G. Ernst, 2000: The microscale model MIMO: development and assessment. *J. Wind. Eng. Ind. Aerodyn.*, **85**, 163–176. 47

Evensen, G., 1994: Sequential data assimilation with a nonlinear quasi-geostrophic model using Monte Carlo methods to forecast error statistics. *J. Geophys. Res.*, **99**, 10 143–10 162. 63

Evensen, G., P. J. van Leeuwen, G. Evensen, and P. J. van Leeuwen, 2000: An Ensemble Kalman Smoother for Nonlinear Dynamics. *Mon. Wea. Rev.*, **128**, 1852–1867. 63

Fagbenle, R., J. Katende, O. Ajayi, and J. Okeniyi, 2011: Assessment of wind energy potential of two sites in North-East, Nigeria. *Renew. Energy*, **36**, 1277–1283. 46

Foken, T., 2006: 50 Years of the Monin–Obukhov Similarity Theory. *Boundary-Layer Meteor.*, **119**, 431–447. 35

Foken, T., 2017: *Micrometeorology*. Springer, Berlin, Heidelberg, Berlin, Heidelberg. 29

Frank, H., and L. Landberg, 1997: Modelling the Wind Climate of Ireland. *Boundary-Layer Meteor.*, **85**, 359–377. 48

Franke, J., A. Hellsten, K. H. Schlunzen, and B. Carissimo, 2011: The COST 732 Best Practice Guideline for CFD simulation of flows in the urban environment: a summary. *Int. J. Environ. Pollut.*, **44**, 419. 47, 50

Franke, J., and Coauthors, 2004: Recommendations on the use of cfd in wind engineering. *Cost action C*, Vol. 14, C1. 93

Frey-Buness, F., D. Heimann, and R. Sausen, 1995: A statistical-dynamical downscaling procedure for global climate simulations. *Theor. Appl. Climatol.*, **50**, 117–131. 48

Frisch, U., and A. N. Kolmogorov, 1995: *Turbulence : the legacy of A.N. Kolmogorov*. Cambridge University Press, 296 pp. 38

García-Sánchez, C., and C. Gorlé, 2018: Uncertainty quantification for microscale CFD simulations based on input from mesoscale codes. *J. Wind. Eng. Ind. Aerodyn.*, **176**, 87–97. 97

Garratt, J., 1994: Review: the atmospheric boundary layer. *Earth-Science Rev.*, **37**, 89–134. 30, 134

Garuma, G. F., 2018: Review of urban surface parameterizations for numerical climate models. *Urban Clim.*, **24**, 830–851. 36

Goutal, N., and F. Maurel, 1997: *Proceedings of the 2nd workshop on dam-break wave simulation*. Electricité de France. Direction des études et recherches. 40, 186

Grimmond, C. S. B., 2006: Progress in measuring and observing the urban atmosphere. *Theor. Appl. Climatol.*, **84**, 3–22. 56

Gu, Y., and D. S. Oliver, 2007: An Iterative Ensemble Kalman Filter for Multiphase Fluid Flow Data Assimilation. *SPE J.*, **12**, 438–446. 76

Haltiner, G. J., and F. L. Martin, 1957: *Dynamical and Physical Meteorology*. McGraw-Hill Book Company. 30

Hamill, T. M., C. Snyder, T. M. Hamill, and C. Snyder, 2000: A Hybrid Ensemble Kalman Filter–3D Variational Analysis Scheme. *Mon. Wea. Rev.*, **128**, 2905–2919. 64

Hanna, S., R. Britter, E. Argenta, and J. Chang, 2012: The Jack Rabbit chlorine release experiments: Implications of dense gas removal from a depression and downwind concentrations. *J. Hazard. Mater.*, **213-214**, 406–412. 57

Hanna, S. R., and Coauthors, 2006: Detailed Simulations of Atmospheric Flow and Dispersion in Downtown Manhattan: An Application of Five Computational Fluid Dynamics Models. *Bull. Am. Meteor. Soc.*, **87**, 1713–1726. 124

Haussaire, J.-M., and M. Bocquet, 2016: A low-order coupled chemistry meteorology model for testing online and offline data assimilation schemes: L95-GRS (v1.0). *Geosci. Model. Dev.*, **9**, 393–412. 65

Holmes, N., and L. Morawska, 2006: A review of dispersion modelling and its application to the dispersion of particles: An overview of different dispersion models available. *Atmospheric Environ.*, **40**, 5902–5928. 48, 50

Homicz, G. F., 2002: Three-dimensional wind field modeling: a review. Tech. rep., Sandia National Laboratories. 47

Hurley, P., P. Manins, S. Lee, R. Boyle, Y. L. Ng, and P. Dewundege, 2003: Year-long, high-resolution, urban airshed modelling: verification of TAPM predictions of smog and particles in Melbourne, Australia. *Atmospheric Environ.*, **37**, 1899–1910. 50

Jardak, M., and O. Talagrand, 2018a: Ensemble variational assimilation as a probabilistic estimator - Part 1: The linear and weak non-linear case. *Nonlin. Process. Geophys.*, **25**, 565–587. 64

Jardak, M., and O. Talagrand, 2018b: Ensemble variational assimilation as a probabilistic estimator - Part 2: The fully non-linear case. *Nonlin. Process. Geophys.*, **25**, 589–604. 64

Jarraud, M., 2008: Guide to meteorological instruments and methods of observation (WMO-No. 8). Tech. rep., World Meteorological Organisation, Geneva, Switzerland, 716 pp. 56

Jung, Y.-R., W.-G. Park, and O.-H. Park, 2003: Pollution dispersion analysis using the puff model with numerical flow field data. *Mech. Res. Commun.*, **30**, 277–286. 50

Kain, J. S., and J. M. Fritsch, 1993: Convective Parameterization for Mesoscale Models: The Kain-Fritsch Scheme. *The Representation of Cumulus Convection in Numerical Models*, American Meteorological Society, Boston, MA, 165–170. 36

Kalman, R. E., 1960: A New Approach to Linear Filtering and Prediction Problems. *J. Basic Eng.*, **82**, 35. 62

Kalmikov, A., G. Dupont, K. Dykes, and C. Chan, 2010: Wind power resource assessment in complex urban environments: MIT campus case-study using CFD Analysis. *AWEA 2010 Windpower Conference*. 47, 93

Kalnay, E., 2003: *Atmospheric modeling, data assimilation, and predictability*. Cambridge university press, 341 pp. 58, 59, 65, 89

Kalnay, E., H. Li, T. Miyoshi, S.-C. Yang, and J. Ballabrera-Poy, 2007: 4-D-Var or ensemble Kalman filter? *Tellus A: Dyn. Meteor. Oceanogr.*, **59**, 758–773. 63

Kato, H., A. Yoshizawa, G. Ueno, and S. Obayashi, 2015: A data assimilation methodology for reconstructing turbulent flows around aircraft. *J. Comput. Phys.*, **283**, 559–581. 66

Kim, J., and R. LeVeque, 2008: Two-layer shallow water system and its applications. *Proc. Twelth Int.*. 185

Koohkan, M., 2012: Multiscale data assimilation approaches and error characterisation applied to the inverse modelling of atmospheric constituent emission fields . Ph.D. thesis, Université Paris-Est. https://pastel.archives-ouvertes.fr/pastel-00807468. 96

Krstic, M., L. Magnis, and R. Vazquez, 2009: Nonlinear Control of the Viscous Burgers Equation: Trajectory Generation, Tracking, and Observer Design. *J. Dyn. Syst. Meas. Control.*, **131**. 92

Krysta, M., M. Bocquet, B. Sportisse, and O. Isnard, 2006: Data assimilation for short-range dispersion of radionuclides: An application to wind tunnel data. *Atmospheric Environ.*, **40**, 7267–7279. 124

Kumar, P., A.-A. Feiz, S. K. Singh, P. Ngae, and G. Turbelin, 2015: Reconstruction of an atmospheric tracer source in an urban-like environment. *J. Geophys. Res. Atmospheres*, **120**, 12 589–12 604. 157

Kumar, P., M. Ketzel, S. Vardoulakis, L. Pirjola, and R. Britter, 2011: Dynamics and dispersion modelling of nanoparticles from road traffic in the urban atmospheric environment—A review. *J. Aerosol Sci.*, **42**, 580–603. 124

Kunsch, J., and D. Webber, 2000: Simple box model for dense-gas dispersion in a straight sloping channel. *J. Hazard. Mater.*, **75**, 29–46. 49

Kunz, R., I. Khatib, and N. Moussiopoulos, 2000: Coupling of mesoscale and microscale models—an approach to simulate scale interaction. *Environ. Model. & Softw.*, **15**, 597–602. 46

Kwak, K.-H., J.-J. Baik, Y.-H. Ryu, and S.-H. Lee, 2015: Urban air quality simulation in a high-rise building area using a CFD model coupled with mesoscale meteorological and chemistry-transport models. *Atmospheric Environ.*, **100**, 167–177. 46

Landberg, L., L. Myllerup, O. Rathmann, E. L. Petersen, B. H. Jørgensen, J. Badger, and N. G. Mortensen, 2003: Wind Resource Estimation-An Overview. *Wind. Energy*, **6**, 261–271. 46, 93, 94

Lateb, M., R. Meroney, M. Yataghene, H. Fellouah, F. Saleh, and M. Boufadel, 2016: On the use of numerical modelling for near-field pollutant dispersion in urban environments - A review. *Environ. Pollut.*, **208**, 271–283. 51, 56

Launder, B. E., and D. B. Spalding, 1974: The numerical computation of turbulent flows. *Comput. Methods Appl. Mech. Eng.*, **3**, 269–289. 39, 134

Le Dimet, F.-X., and O. Talagrand, 1986: Variational algorithms for analysis and assimilation of meteorological observations: theoretical aspects. *Tellus A: Dyn. Meteor. Oceanogr.*, **38**, 97–110. 63

Li, Y., I. M. Navon, P. Courtier, and P. Gauthier, 1993: Variational Data Assimilation with a Semi-Lagrangian Semi-implicit Global Shallow-Water Equation Model and Its Adjoint. *Mon. Wea. Rev.*, **121**, 1759–1769. 96

Lister, M., 1960: The numerical solution of hyperbolic partial differential equations by the method of characteristics. *Math. methods for digital computers*, **1**, 165–179. 40, 187

Liu, C., Q. Xiao, and B. Wang, 2008: An Ensemble-Based Four-Dimensional Variational Data Assimilation Scheme. Part I: Technical Formulation and Preliminary Test. *Mon. Wea. Rev.*, **136**, 3363–3373. 65, 76

Liu, Y., J.-M. Haussaire, M. Bocquet, Y. Roustan, O. Saunier, and A. Mathieu, 2017: Uncertainty quantification of pollutant source retrieval: comparison of Bayesian methods with application to the Chernobyl and Fukushima Daiichi accidental releases of radionuclides. *Quart. J. Royal Meteor. Soc.*, **143**, 2886–2901. 136

Liu, Y., S. Miao, C. Zhang, G. Cui, and Z. Zhang, 2012: Study on micro-atmospheric environment by coupling large eddy simulation with mesoscale model. *J. Wind. Eng. Ind. Aerodyn.*, **107-108**, 106–117. 46

Lorenc, A. C., 2003: The potential of the ensemble Kalman filter for NWP—a comparison with 4D-Var. *Quart. J. Royal Meteor. Soc.*, **129**, 3183–3203. 63

Makké, L., and Coauthors, 2016: A New Method for Fast Computation of Three-Dimensional Atmospheric Infrared Radiative Transfer in a Nonscattering Medium, with an Application to Dynamical Simulation of Radiation Fog in a Built Environment. *J. Atmospheric Sci.*, **73**, 4137–4149. 42

Mallet, V., and Coauthors, 2007: Technical Note: The air quality modeling system Polyphemus. *Atmospheric Chem. Phys.*, **7**, 5479–5487. 51

Maurizi, A., J. Palma, and F. Castro, 1998: Numerical simulation of the atmospheric flow in a mountainous region of the North of Portugal. *J. Wind. Eng. Ind. Aerodyn.*, **74-76**, 219–228. 47

McFarlane, N., 2011: Parameterizations: representing key processes in climate models without resolving them. *Wiley Interdiscip. Rev. Clim. Chang.*, **2**, 482–497. 36

Michioka, T., A. Sato, and K. Sada, 2013: Large-eddy simulation coupled to mesoscale meteorological model for gas dispersion in an urban district. *Atmospheric Environ.*, **75**, 153–162. 46

Mikkelsen, T., J. Mann, M. Courtney, and M. Sjöholm, 2008: Windscanner: 3-D wind and turbulence measurements from three steerable doppler lidars. *IOP Conf. Series: Earth Environ. Sci.*, **1**, 012 018. 56

Milliez, M., 2006: Modélisation micro-météorologique en milieu urbain : dispersion des polluants et prise en compte des effets radiatifs. Ph.D. thesis, ENPC, 228 pp. 42, 125, 135, 137

Milliez, M., and B. Carissimo, 2007: Numerical simulations of pollutant dispersion in an idealized urban area, for different meteorological conditions. *Boundary-Layer Meteor.*, **122**, 321–342. 125

Milliez, M., and B. Carissimo, 2008: Computational Fluid Dynamical Modelling of Concentration Fluctuations in an Idealized Urban Area. *Boundary-Layer Meteor.*, **127**, 241–259. 125

Mingham, C. G., and D. M. Causon, 1998: High-Resolution Finite-Volume Method for Shallow Water Flows. *J. Hydraul. Eng.*, **124**, 605–614. 192

Misaka, T., T. Ogasawara, S. Obayashi, I. Yamada, and Y. Okuno, 2008: Assimilation Experiment of Lidar Measurements for Wake Turbulence. *J. Fluid Sci. Technol.*, **3**. 66

Moltchanov, S., I. Levy, Y. Etzion, U. Lerner, D. M. Broday, and B. Fishbain, 2015: On the feasibility of measuring urban air pollution by wireless distributed sensor networks. *Sci. The Total. Environ.*, **502**, 537–547. 57

Monin, A. S., and A. M. Obukhov, 1954: Basic laws of turbulent mixing in the surface layer of the atmosphere. *Contrib. Geophys. Inst. Acad. Sci. USSR*, **151**. 33

Mons, V., L. Margheri, J.-C. Chassaing, and P. Sagaut, 2017: Data assimilation-based reconstruction of urban pollutant release characteristics. *J. Wind. Eng. Ind. Aerodyn.*, **169**, 232–250. 66

Mortensen, N. G., L. Landberg, I. Troen, and E. Lundtang Petersen, 1993: Wind Atlas Analysis and Application Program (WAsP). Vol. 2: User's guide. *Risø Natl. Lab.*, **666**, 1–137. 47

Muller, C. L., L. Chapman, C. Grimmond, D. T. Young, and X. Cai, 2013: Review. Sensors and the city: a review of urban meteorological networks. *Int. J. Climatol.*, **33**, 1585–1600. 56

Muñoz-Esparza, D., B. Kosović, J. Mirocha, and J. van Beeck, 2014: Bridging the Transition from Mesoscale to Microscale Turbulence in Numerical Weather Prediction Models. *Boundary-Layer Meteor.*, **153**, 409–440. 45

Nakayama, H., T. Takemi, and H. Nagai, 2012: Large-eddy simulation of urban boundary-layer flows by generating turbulent inflows from mesoscale meteorological simulations. *Atmospheric Sci. Lett.*, **13**, 180–186. 46

Noilhan, J., S. Planton, J. Noilhan, and S. Planton, 1989: A Simple Parameterization of Land Surface Processes for Meteorological Models. *Mon. Wea. Rev.*, **117**, 536–549. 36

Oettl, D., J. Kukkonen, R. A. Almbauer, P. J. Sturm, M. Pohjola, and J. Härkönen, 2001: Evaluation of a Gaussian and a Lagrangian model against a roadside data set, with emphasis on low wind speed conditions. *Atmospheric Environ.*, **35**, 2123–2132. 50

Oke, T. R., 2007: Siting and Exposure of Meteorological Instruments at Urban Sites. *Air Pollution Modeling and Its Application XVII*, Springer US, Boston, MA, 615–631. 56

Oldrini, O., P. Armand, C. Duchenne, C. Olry, J. Moussafir, and G. Tinarelli, 2017: Description and preliminary validation of the PMSS fast response parallel atmospheric flow and dispersion solver in complex built-up areas. *Environ. Fluid Mech.*, **17**, 997–1014. 45

Pahlow, M., M. B. Parlange, and F. Porté-Agel, 2001: On Monin–Obukhov Similarity In The Stable Atmospheric Boundary Layer. *Boundary-Layer Meteor.*, **99**, 225–248. 35

Palma, J., F. Castro, L. Ribeiro, A. Rodrigues, and A. Pinto, 2008: Linear and nonlinear models in wind resource assessment and wind turbine micro-siting in complex terrain. *J. Wind. Eng. Ind. Aerodyn.*, **96**, 2308–2326. 47, 93

Parra, M., J. Santiago, F. Martín, A. Martilli, and J. Santamaría, 2010: A methodology to urban air quality assessment during large time periods of winter using computational fluid dynamic models. *Atmospheric Environ.*, **44**, 2089–2097. 50

Pasquill, F., 1961: The estimation of the dispersion of windborne material. *Met. Mag.*, **90**, 33. 49

Pedlosky, J., 1979: *Geophysical fluid dynamics*. Springer-Verlag. 30, 40

Peterson, E. W., J. P. Hennessey, E. W. Peterson, and J. P. H. Jr., 1978: On the Use of Power Laws for Estimates of Wind Power Potential. *J. Appl. Meteor.*, **17**, 390–394. 99

Pielke, R. A., 2013: *Mesoscale meteorological modeling*. Academic Press, 743 pp. 31

Prandtl, L., 1925: Bericht uber Untersuchungen zur ausgebildeten Turbulenz. *Zs. angew. Math. Mech.*, **5**, 136–139. 39

Probst, O., and D. Cárdenas, 2010: State of the Art and Trends in Wind Resource Assessment. *Energies*, **3**, 1087–1141. 45, 46, 94

Ragland, K. W., 1973: Multiple box model for dispersion of air pollutants from area sources. *Atmospheric Environ.*, **7**, 1017–1032. 49

Raza, S., R. Avila, and J. Cervantes, 2001: A 3-D Lagrangian stochastic model for the meso-scale atmospheric dispersion applications. *Nucl. Eng. Des.*, **208**, 15–28. 50

Robins, A., 2003: Wind tunnel dispersion modelling some recent and not so recent achievements. *J. Wind. Eng. Ind. Aerodyn.*, **91**, 1777–1790. 50, 56

Rochoux, M., B. Delmotte, B. Cuenot, S. Ricci, and A. Trouvé, 2013: Regional-scale simulations of wildland fire spread informed by real-time flame front observations. *Proc. Combust. Inst.*, **34**, 2641–2647. 162

Rochoux, M. C., C. Emery, S. Ricci, B. Cuenot, and A. Trouvé, 2015: Towards predictive data-driven simulations of wildfire spread – Part II: Ensemble Kalman Filter for the state estimation of a front-tracking simulator of wildfire spread. *Nat. Hazards Earth Syst. Sci.*, **15**, 1721–1739. 162

Rodi, W., 1997: Comparison of LES and RANS calculations of the flow around bluff bodies. *J. Wind. Eng. Ind. Aerodyn.*, **69-71**, 55–75. 39

Rodrigues, C. V., J. M. Palma, and H. Rodrigues, 2016: Atmospheric Flow over a Mountainous Region by a One-Way Coupled Approach Based on Reynolds-Averaged Turbulence Modelling. *Boundary-Layer Meteor.*, **159**, 407–437. 45

Rummukainen, M., 2010: State-of-the-art with regional climate models. *Wiley Interdiscip. Rev. Clim. Chang.*, **1**, 82–96. 162

Sakov, P., J.-M. Haussaire, and M. Bocquet, 2018: An iterative ensemble Kalman filter in presence of additive model error. *Quart. J. Royal Meteor. Soc.*, **144**, 1297–1309. 57

Sakov, P., D. S. Oliver, and L. Bertino, 2012: An Iterative EnKF for Strongly Nonlinear Systems. *Mon. Wea. Rev.*, **140**, 1988–2004. 65, 75, 76

Sanz Rodrigo, J., D. Cabezón, I. Martí, P. Patilla, and J. Van Beeck, 2008: Numerical CFD modelling of non-neutral atmospheric boundary layers for offshore wind resource assessment based on Monin-Obukhov theory. *European Wind Energy Conference and Exhibition*, Brussels. 48

Sanz Rodrigo, J., and Coauthors, 2017: Mesoscale to microscale wind farm flow modeling and evaluation. *Wiley Interdiscip. Rev. Energy Environ.*, **6**, e214. 46, 47

Sherman, C. A., and C. A. Sherman, 1978: A Mass-Consistent Model for Wind Fields over Complex Terrain. *J. Appl. Meteor.*, **17**, 312–319. 47

Shimada, S., T. Ohsawa, S. Chikaoka, and K. Kozai, 2011: Accuracy of the Wind Speed Profile in the Lower PBL as Simulated by the WRF Model. *Sola*, **7**, 109–112. 101

Simões, T., and A. Estanqueiro, 2016: A new methodology for urban wind resource assessment. *Renew. Energy*, **89**, 598–605. 47, 93

Skamarock, C., and Coauthors, 2005: A Description of the Advanced Research WRF Version 3. *Tech. Rep.*, 88. 46, 97

Soetaert, K., and P. M. J. Herman, 1995: Estimating estuarine residence times in the Westerschelde (The Netherlands) using a box model with fixed dispersion coefficients. *Hydrobiol.*, **311**, 215–224. 49

Song, M., K. Chen, Z. He, and X. Zhang, 2014: Wind resource assessment on complex terrain based on observations of a single anemometer. *J. Wind. Eng. Ind. Aerodyn.*, **125**, 22–29. 66

Sousa, J., C. García-Sánchez, and C. Gorlé, 2018: Improving urban flow predictions through data assimilation. *Build. Environ.*, **132**, 282–290. 66

Srebric, J., V. Vukovic, and G. He, 2008: CFD boundary conditions for contaminant dispersion, heat transfer and airflow simulations around human occupants in indoor environments. *Build. Environ.*, **43**, 294–303. 124

Stocker, J., C. Hood, D. Carruthers, and C. McHugh, 2012: ADMS–Urban: developments in modelling dispersion from the city scale to the local scale. *Int. J. Environ. Pollut.*, **50**, 308. 45

Stohl, A., C. Forster, A. Frank, P. Seibert, and G. Wotawa, 2005: Technical note: The Lagrangian particle dispersion model FLEXPART version 6.2. *Atmospheric Chem. Phys.*, **5**, 2461–2474. 50

Stull, R. B., 1988: *An Introduction to Boundary Layer Meteorology*. Springer Netherlands, 670 pp. 37, 134

Tang, X.-Y., S. Zhao, B. Fan, J. Peinke, and B. Stoevesandt, 2019: Micro-scale wind resource assessment in complex terrain based on CFD coupled measurement from multiple masts. *Appl. Energy*, **238**, 806–815. 66

Tewari, M., H. Kusaka, F. Chen, W. J. Coirier, S. Kim, A. A. Wyszogrodzki, and T. T. Warner, 2010: Impact of coupling a microscale computational fluid dynamics model with a mesoscale model on urban scale contaminant transport and dispersion. *Atmospheric Res.*, **96**, 656–664. 46

Thouron, L., Y. Kim, B. Carissimo, C. Seigneur, and B. Bruge, 2019: Intercomparison of two modeling approaches for traffic air pollution in street canyons. *Urban Clim.*, **27**, 163–178. 42

Tominaga, Y., and T. Stathopoulos, 2013: CFD simulation of near-field pollutant dispersion in the urban environment: A review of current modeling techniques. *Atmospheric Environ.*, **79**, 716–730. 124

Tominaga, Y., and T. Stathopoulos, 2016: Ten questions concerning modeling of near-field pollutant dispersion in the built environment. *Build. Environ.*, **105**, 390–402. 49

Toro, E. F., 2009: *Riemann Solvers and Numerical Methods for Fluid Dynamics*. Springer Berlin Heidelberg, Berlin, Heidelberg. 192

Trémolet, Y., 2006: Accounting for an imperfect model in 4D-Var. *Quart. J. Royal Meteor. Soc.*, **132**, 2483–2504. 57

Tsuang, B.-J., 2003: Quantification on the source/receptor relationship of primary pollutants and secondary aerosols by a Gaussian plume trajectory model: Part I—theory. *Atmospheric Environ.*, **37**, 3981–3991. 50

Uchida, T., and Y. Ohya, 2008: Micro-siting technique for wind turbine generators by using large-eddy simulation. *J. Wind. Eng. Ind. Aerodyn.*, **96**, 2121–2138. 47

Umlauf, L., and H. Burchard, 2005: Second-order turbulence closure models for geophysical boundary layers. A review of recent work. *Cont. Shelf Res.*, **25**, 795–827. 39

Venkatesan, R., R. Mathiyarasu, and K. Somayaji, 2002: A study of atmospheric dispersion of radionuclides at a coastal site using a modified Gaussian model and a mesoscale sea breeze model. *Atmospheric Environ.*, **36**, 2933–2942. 50

Wang, B., L. Cot, L. Adolphe, S. Geoffroy, and S. Sun, 2017: Cross indicator analysis between wind energy potential and urban morphology. *Renew. Energy*, **113**, 989–1006. 47, 93

Wilby, R., and T. Wigley, 1997: Downscaling general circulation model output: a review of methods and limitations. *Prog. Phys. Geogr. Earth Environ.*, **21**, 530–548. 44

Wilks, D. S., and R. L. Wilby, 1999: The weather generation game: a review of stochastic weather models. *Prog. Phys. Geogr. Earth Environ.*, **23**, 329–357. 44

Winiarek, V., 2014: Dispersion atmosphérique et modélisation inverse pour la reconstruction de sources accidentelles de polluants. Ph.D. thesis, Université Paris-Est. 125, 132, 137

Winiarek, V., M. Bocquet, O. Saunier, and A. Mathieu, 2012: Estimation of errors in the inverse modeling of accidental release of atmospheric pollutant: Application to the reconstruction of the cesium-137 and iodine-131 source terms from the Fukushima Daiichi power plant. *J. Geophys. Res. Atmospheres.* 124

Witha, B., and Coauthors, 2019: WRF model sensitivity studies and specifications for the NEWA mesoscale wind atlas production runs. Tech. rep., NEWA - New European Wind Atlas. 46

Xia, Q., J. Niu, and X. Liu, 2014: Dispersion of air pollutants around buildings: A review of past studies and their methodologies. *Indoor Built Environ.*, **23**, 201–224. 56

Yamada, T., 2004: Merging CFD and atmospheric modeling capabilities to simulate airflows and dispersion in urban areas. *Comput. Fluid Dyn. J.*, **13**, 329–341. 45, 94

Yan, B., and Q. Li, 2016: Coupled on-site measurement/CFD based approach for high-resolution wind resource assessment over complex terrains. *Energy Convers. Manag.*, **117**, 351–366. 66

Yang, Y., M. Gu, S. Chen, and X. Jin, 2009: New inflow boundary conditions for modelling the neutral equilibrium atmospheric boundary layer in computational wind engineering. *J. Wind. Eng. Ind. Aerodyn.*, **97**, 88–95. 64, 93

Yee, E., and C. A. Biltoft, 2004: Concentration Fluctuation Measurements in a Plume Dispersing Through a Regular Array of Obstacles. *Boundary-Layer Meteor.*, **111**, 363–415. 125, 129, 134, 137

Zaïdi, H., E. Dupont, M. Milliez, B. Carissimo, and L. Musson-Genon, 2014: Effect of Atmospheric Stability on the Atmospheric Dispersion Conditions Over a Industrial Site Surrounded by Forests. *Air Pollution Modeling and its Application XXII*, Springer, 733–737. 42

Zajaczkowski, F. J., S. E. Haupt, and K. J. Schmehl, 2011: A preliminary study of assimilating numerical weather prediction data into computational fluid dynamics models for wind prediction. *J. Wind. Eng. Ind. Aerodyn.*, **99**, 320–329. 45, 66

Zeitlin, V., and F. Bouchut, 2010: A robust well-balanced scheme for multi-layer shallow water equations. *Discret. Continuous Dyn. Syst. - Ser. B*, **13**, 739–758. 192

Zou, X., F. Vandenberghe, M. Pondeca, and Y.-H. Kuo, 1997: Introduction to adjoint techniques and the MM5 adjoint modeling system. NCAR Tech. Note NCAR/TN-435-STR, 107 pp. 96

Appendix A

Supplementary information about the shallow water model of the atmospheric boundary layer

We have seen in Section 1.2.3 that the SWE ca be used as a simple model of the ABL. We provide in this appendix the theoretical derivation of the SWE for one, two, and multi-layer cases. Afterwards, we give the analytical solutions to the one-layer SWE and we present the method of characteristics, which is widely used to study these equations. In particular, we show how this method indicates the type of inputs – either IC or BC – required to solve the SWE in different configurations. In a last section, we briefly present the shallow-layer model used as a simple representation of the atmosphere in two layers in Chapter 4.

A.1 Derivation of the shallow-water equations

A.1.1 Governing equations for one layer

The SWE are derived from Navier-Stokes equations in the approximation of small fluid height compared to horizontal spatial scales.

Using the Einstein notation, the Navier-Stokes equations read:

$$\begin{cases} \frac{\partial \rho}{\partial t} + \frac{\partial \rho u_i}{\partial x_i} = 0 \\ \frac{\partial u_i}{\partial t} + u_j \frac{\partial u_i}{\partial x_j} = -\frac{1}{\rho}\frac{\partial p}{\partial x_i} + \frac{\partial R_{i,j}}{\partial x_j} + g_i + C_i \end{cases} \tag{A.1}$$

where u_i is the i-th component of the flow velocity, p is the pressure, ρ is the density, $R_{i,j}$ are the components of the stress tensor, g_i is i-th component of the gravity force, and C_i is the i-th component of the Coriolis force. The first equation expresses the conservation of mass and the second one the conservation of momentum.

The flow motion equations can be time-averaged to give the Reynolds-averaged Navier-Stokes equations (or RANS equations). The derivation of these equations uses the

Reynolds decomposition, which separates each of the flow variable into the time-averaged component and the fluctuating component (see Section 1.2.2). Due to the nonlinearity of the Navier-Stokes equation, the velocity fluctuations appear in the RANS equations in the Reynolds stress $R_{i,j}$. The closure problem aims at removing any reference to the fluctuating components by modelling the Reynolds stress as a function of the mean flow. The Boussinesq eddy viscosity assumption states that the momentum transfer caused by turbulent eddies can be modelled with an eddy (or turbulence) viscosity, ν_t.

For incompressible Newtonian fluids, the mass continuity equation reads:

$$\frac{\partial u_i}{\partial x_i} = 0 \tag{A.2}$$

and the Stokes' stress tensor is given by:

$$\frac{\partial R_{i,j}}{\partial x_j} = (\nu + \nu_t)\frac{\partial^2 u_i}{\partial x_j \partial x_j} \tag{A.3}$$

where $\nu = \frac{\mu}{\rho}$ is the kinematic viscosity and μ the dynamic viscosity.

The SWE are derived using the following assumptions:

- the 3-dimensional effects are negligible: $w \ll (u, v)$
- the pressure distribution is hydrostatic: $\frac{\partial p}{\partial z} = -\rho g$

We refer to η as the absolute height of the fluid surface, h is the fluid height, and z_f is the bottom topography:

$$\eta = h + z_f. \tag{A.4}$$

In what follows, u and v refer to the components of the vertically-averaged horizontal velocity.

The pressure at height z inside the fluid layer is:

$$p(z) = \rho_a g(H_a - \eta) + \rho g(\eta - z) \tag{A.5}$$

where ρ_a and H_a refer to atmospheric density and geopotential height, and g is the gravitational acceleration ($g = 9.81\mathrm{m/s}^2$). The atmosphere's height is assumed homogeneous along x- and y-axis such that the horizontal derivative of pressure reads:

$$\frac{\partial p}{\partial x_i} = (\rho - \rho_a)g\frac{\partial \eta}{\partial x_i} \tag{A.6}$$

for $x_i = x$ or y.

The above expression of the pressure gradient is replaced in the Navier-Stokes equations (A.1) and the assumptions listed above are used to derive the SWE. The non-conservative form of the 2-D SWE for one layer of fluid read:

$$\begin{cases} \frac{\partial h}{\partial t} + \frac{\partial hu}{\partial x} + \frac{\partial hv}{\partial y} = 0 \\ \frac{\partial u}{\partial t} + u\frac{\partial u}{\partial x} + v\frac{\partial u}{\partial y} = -g'\frac{\partial \eta}{\partial x} + \frac{1}{h}\frac{\partial hD_{xx}}{\partial x} + \frac{1}{h}\frac{\partial hD_{xy}}{\partial y} + fv + \frac{F_x}{h} + \frac{S_x}{h} \\ \frac{\partial v}{\partial t} + u\frac{\partial v}{\partial x} + v\frac{\partial v}{\partial y} = -g'\frac{\partial \eta}{\partial y} + \frac{1}{h}\frac{\partial hD_{yx}}{\partial x} + \frac{1}{h}\frac{\partial hD_{yy}}{\partial y} - fu + \frac{F_y}{h} + \frac{S_y}{h} \end{cases} \tag{A.7}$$

where D_{ij} include viscous, turbulent, and dispersion effects, S_i represents the surface friction and F_i the bottom friction, $g' = \frac{\rho-\rho_a}{\rho} g$ is the reduced gravity, and f is the Coriolis parameter.

When the fluid considered is water, $\rho_a \ll \rho$ such that $g' \approx g$. In the present work, we consider layers of air and this approximation is not valid; we need to keep g'. For local scale simulations, the Coriolis effect is usually negligible and we will also neglect the effect of diffusion and dispersion.
With these approximations, the equations can be written in the conservative form:

$$\begin{cases} \frac{\partial h}{\partial t} + \frac{\partial hu}{\partial x} + \frac{\partial hv}{\partial y} = 0 \\ \frac{\partial hu}{\partial t} + \frac{\partial}{\partial x}(hu^2 + \frac{1}{2}g'h^2) + \frac{\partial}{\partial y}(huv) = -g'h\frac{\partial z_f}{\partial x} + F_x + S_x \\ \frac{\partial hv}{\partial t} + \frac{\partial}{\partial x}(huv) + \frac{\partial}{\partial y}(hv^2 + \frac{1}{2}g'h^2) = -g'h\frac{\partial z_f}{\partial y} + F_y + S_y. \end{cases} \tag{A.8}$$

The non-conservative form can be obtained by expanding the derivatives using the product rule. However, the non-conservative SWE do not hold across a shock or hydraulic jump, such that the conservative form is preferred here.

A.1.2 Two-layer equations

We consider two layers superposed, both of them satisfying the SWE. The index '1' refers to the top layer and '2' to the bottom one (Fig. A.1). The continuity equation in (A.7) holds in each layer. However, the layers interact through the pressure expression. At height z in the bottom layer, the pressure is given by:

$$p_2(z) = \rho_a g(H_a - \eta_1) + \rho_1 g h_1 + \rho_2 g(\eta_2 - z).$$

Using the fact that $\eta_1 = z_f + h_2 + h_1$ and $\eta_2 = z_f + h_2$, defining the reduced gravities: $g'_1 = \frac{\rho_1-\rho_a}{\rho_1} g$ and $g'_2 = \frac{\rho_2-\rho_a}{\rho_2} g$, and noting that $\frac{\rho_1-\rho_a}{\rho_2} = g'_1 \frac{\rho_1}{\rho_2}$, the horizontal partial derivative along x_i reads:

$$\begin{aligned} &\frac{\partial p_2}{\partial x_i} = (\rho_1 - \rho_a) g \frac{\partial h_1}{\partial x} + (\rho_2 - \rho_a) g \frac{\partial h_2}{\partial x} + (\rho_2 - \rho_a) g \frac{\partial z_f}{\partial x} \\ \iff &\frac{1}{\rho_2}\frac{\partial p_2}{\partial x_i} = g'_1 \frac{\rho_1}{\rho_2}\frac{\partial h_1}{\partial x} + g'_2 \frac{\partial h_2}{\partial x} + g'_2 \frac{\partial z_f}{\partial x}. \end{aligned} \tag{A.9}$$

For the top layer, we assume that there is no surface friction with the atmosphere at rest but the bottom friction corresponds to the friction between the two fluid layers that are approximated by the Manning equation:

$$\overrightarrow{f}_1 = -\frac{n_1^2 g \|\overrightarrow{u_1} - \overrightarrow{u_2}\|(\overrightarrow{u_1} - \overrightarrow{u_2})}{h_1^{1/3}} \tag{A.10}$$

where n_1 is a Manning coefficient.

Similarly, the bottom friction for the lower layer is given by:

$$\overrightarrow{f}_2 = -\frac{n_2^2 g \|\overrightarrow{u_2}\|\overrightarrow{u_2}}{h_2^{1/3}}. \tag{A.11}$$

Replacing in A.8 and rearranging the terms, we obtain the system of conservative equations for 2 layers:

$$\begin{cases} \dfrac{\partial h_1}{\partial t} + \dfrac{\partial h_1 u_1}{\partial x} + \dfrac{\partial h_1 v_1}{\partial y} = 0 \\ \dfrac{\partial h_1 u_1}{\partial t} + \dfrac{\partial}{\partial x}(h_1 u_1^2 + \dfrac{1}{2} g_1' h_1^2) + \dfrac{\partial}{\partial y}(h_1 u_1 v_1) = -g_1' h_1 \dfrac{\partial}{\partial x}(\eta_2) + f_{1,x} \\ \dfrac{\partial h_1 v_1}{\partial t} + \dfrac{\partial}{\partial x}(h_1 v_1 u_1) + \dfrac{\partial}{\partial y}(h_1 v_1^2 + \dfrac{1}{2} g_1' h_1^2) = -g_1' h_1 \dfrac{\partial}{\partial y}(\eta_2) + f_{1,y} \\ \\ \dfrac{\partial h_2}{\partial t} + \dfrac{\partial h_2 u_2}{\partial x} + \dfrac{\partial h_2 v_2}{\partial y} = 0 \\ \dfrac{\partial h_2 u_2}{\partial t} + \dfrac{\partial}{\partial x}(h_2 u_2^2 + \dfrac{1}{2} g_2' h_2^2) + \dfrac{\partial}{\partial y}(h_2 u_2 v_2) = -h_2 \dfrac{\partial}{\partial x}(g_2' z_f - g_1' \dfrac{\rho_1}{\rho_2} h_1) + f_{2,x} - \dfrac{\rho_1}{\rho_2} f_{1,x} \\ \dfrac{\partial h_2 v_2}{\partial t} + \dfrac{\partial}{\partial x}(h_2 u_2 v_2) + \dfrac{\partial}{\partial y}(h_2 v_2^2 + \dfrac{1}{2} g_2' h_2^2) = -h_2 \dfrac{\partial}{\partial y}(g_2' z_f - g_1' \dfrac{\rho_1}{\rho_2} h_1) + f_{2,y} - \dfrac{\rho_1}{\rho_2} f_{1,y} \end{cases} \tag{A.12}$$

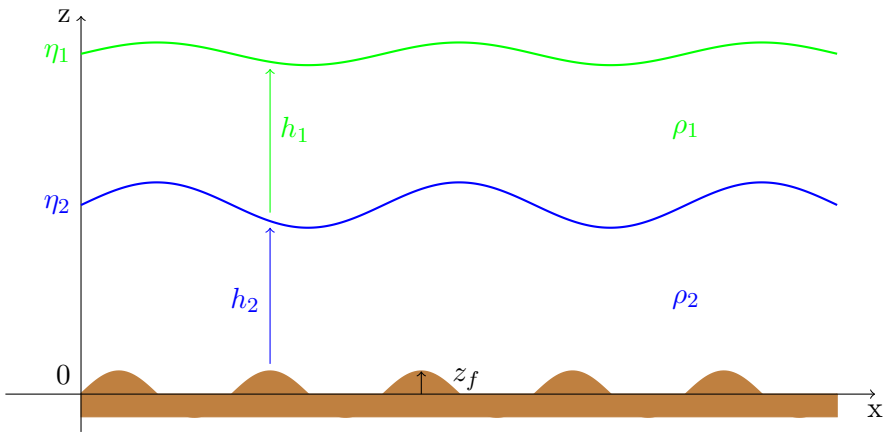

Figure A.1: Two-layers fluid.

A.1.3 Generalization to multi-layer case

We now consider a general case with N superposed layers governed by the SWE. The layers are numbered from top to bottom.

We first define the surface height of the n-th layer:

$$\eta_n = z_f + \sum_{k=n}^{N} h_k, \tag{A.13}$$

where h_k is the fluid height of the k-th layer. Note that all the subscripts refer to the

layer index. The reduced gravity for the n-th layer is

$$g'_n = \frac{\rho_n - \rho_a}{\rho_n} g, \tag{A.14}$$

where ρ_n is the fluid density of this layer. The friction forces between the n-th layer and the ones below and above are

$$\overrightarrow{F_n} = \overrightarrow{f_n} - \frac{\rho_{n-1}}{\rho_n} \overrightarrow{f_{n-1}} \tag{A.15}$$

where

$$\overrightarrow{f_k} = -\frac{n_k^2 g \|\overrightarrow{u_k} - \overrightarrow{u_{k+1}}\|}{h_k^{1/3}} (\overrightarrow{u_k} - \overrightarrow{u_{k+1}}) \tag{A.16}$$

with the convention that $f_0 = 0$, and $\overrightarrow{u_0} = \overrightarrow{u_{N+1}} = 0$. n_k is the Manning coefficient for the k-th layer, and $\overrightarrow{e_x}$ and $\overrightarrow{e_y}$ are the unit vectors along x and y. We also define the x- and y-components of these forces: $F_{n,x} = \overrightarrow{F_n} \cdot \overrightarrow{e_x}$ and $F_{n,y} = \overrightarrow{F_n} \cdot \overrightarrow{e_y}$.

We thus deduce the conservative form of SWE for any layer n, including friction forces (A.17) (Benkhaldoun and Seaid, 2010; Kim and LeVeque, 2008):

$$\begin{cases} \dfrac{\partial h_n}{\partial t} + \dfrac{\partial h_n u_n}{\partial x} + \dfrac{\partial h_n v_n}{\partial y} = 0 \\ \dfrac{\partial h_n u_n}{\partial t} + \dfrac{\partial}{\partial x}(h_n u_n^2 + \dfrac{1}{2} g'_n h_n^2) + \dfrac{\partial}{\partial y}(h_n u_n v_n) = -h_n \dfrac{\partial}{\partial x}(g'_n \eta_{n+1} + \displaystyle\sum_{k=1}^{n-1} (g'_k \frac{\rho_k}{\rho_n} h_k)) + F_{n,x} \\ \dfrac{\partial h_n v_n}{\partial t} + \dfrac{\partial}{\partial x}(h_n u_n v_n) + \dfrac{\partial}{\partial y}(h_n v_n^2 + \dfrac{1}{2} g'_n h_n^2) = -h_n \dfrac{\partial}{\partial y}(g'_n \eta_{n+1} + \displaystyle\sum_{k=1}^{n-1} (g'_k \frac{\rho_k}{\rho_n} h_k)) + F_{n,y} \end{cases} \tag{A.17}$$

where u_n, v_n are velocity-components for the n-th layer and z_f is the topography.

A.2 Theoretical resolution of the 1D shallow-water equations

A.2.1 Bernoulli equation

The 1D SWE with topography and without friction can be solved analytically. The non-conservative, stationary 1D SWE for one layer with topography read:

$$\begin{cases} \dfrac{\partial hu}{\partial x} = 0 \\ u \dfrac{\partial u}{\partial x} + g' \dfrac{\partial h}{\partial x} = -g' \dfrac{\partial z_f}{\partial x}. \end{cases} \tag{A.18}$$

The momentum equation in (A.18) can be rewritten as follows:

$$\frac{\partial}{\partial x}(h + \frac{u^2}{2g'} + z_f) = 0 \iff \frac{\partial}{\partial x}(\mathcal{H}_s + z_f) = 0, \tag{A.19}$$

where $\mathcal{H}_s \equiv h + \frac{u^2}{2g'}$ is the specific charge. According to the continuity equation, the discharge $q = hu$ is conserved over the domain and the specific charge can also be expressed as: $\mathcal{H}_s = h + \frac{q^2}{2g'h^2}$.

The analytical solution is thus obtained with the Bernoulli equation (Goutal and Maurel, 1997):

$$\frac{q^2}{2g'h^2} + h + z_f = \mathcal{H}_0 \iff \frac{u^2}{2g'} + h + z_f = \mathcal{H}_0, \tag{A.20}$$

which stands that the sum of the specific charge and the topography height is conserved over the domain.

A.2.2 Subcritical, critical and supercritical regimes

The regime of a flow is determined by the value of the Froude number, which is the ratio of the flow inertia to the external forces:

$$Fr \equiv \frac{u}{\sqrt{gh}}. \tag{A.21}$$

If $Fr < 1$ the flow is subcritical, if $Fr = 1$ it is critical, and if $Fr > 1$ the flow is supercritical. Figure A.2 shows the profile of $\mathcal{H}_s$ versus h. The minimum of $\mathcal{H}_s$ is reached for the critical height $h_c \equiv (\frac{q^2}{g'})^{\frac{1}{3}}$ for which $Fr = 1$ and $\mathcal{H}_s(h_c) = \frac{3}{2}h_c$. For $h < h_c$, the regime is supercritical and for $h > h_c$ the regime is subcritical.

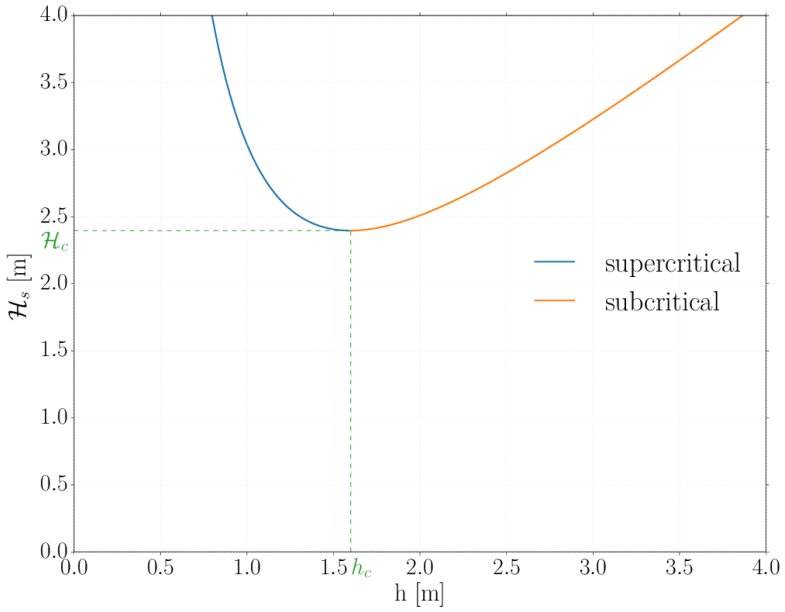

Figure A.2: Profile of the specific charge $\mathcal{H}_s$ versus fluid height h in the case where $g' = 0.981\text{m/s}^2$ and $q = 2.0\text{m}^2/\text{s}$.

A.3 The method of characteristics

In addition to Bernoulli equation, the 1D SWE can be solved using the method of characteristics (Abbott, 1966; Lister, 1960). We present here the derivation of this method in the case of unidimensional domain without topography, with only one layer of fluid, and without taking the Coriolis effect nor the friction forces into account.

The continuity and momentum equations (A.19) without topography can be written as follows with $\mathbf{X} = \begin{pmatrix} h \\ u \end{pmatrix}$ and $\mathbf{M} = \begin{pmatrix} u & h \\ g' & u \end{pmatrix}$:

$$\frac{\partial \mathbf{X}}{\partial t} + \mathbf{M}\frac{\partial \mathbf{X}}{\partial x} = 0. \tag{A.22}$$

The eigenvalues of $\mathbf{M}$ are the roots of

$$\begin{aligned} & det(\mathbf{M} - \lambda \mathbf{I}) = 0 \\ \iff & (u - \lambda - \sqrt{g'h})(u - \lambda + \sqrt{g'h}) = 0. \end{aligned} \tag{A.23}$$

Consequently, $\mathbf{M}$ has two real eigenvalues: $\alpha_+ = u + c$ and $\alpha_- = u - c$ where $c = \sqrt{g'h}$ is the wave speed. $\mathbf{M}$ is diagonalizable and can be decomposed as follows:

$$\mathbf{M} = \mathbf{P}^{-1}\mathbf{D}\mathbf{P}, \tag{A.24}$$

with $\mathbf{D} = \begin{pmatrix} \alpha_+ & 0 \\ 0 & \alpha_- \end{pmatrix}$ and $\mathbf{P} = \begin{pmatrix} g' & c \\ g' & -c \end{pmatrix}$.

We deduce from this decomposition that:

$$\begin{aligned} & \frac{\partial \mathbf{X}}{\partial t} + \mathbf{P}^{-1}\mathbf{D}\mathbf{P}\frac{\partial \mathbf{X}}{\partial x} = 0 \\ \Leftrightarrow\ & \mathbf{P}\frac{\partial \mathbf{X}}{\partial t} + \mathbf{D}\mathbf{P}\frac{\partial \mathbf{X}}{\partial x} = 0. \end{aligned} \tag{A.25}$$

Defining $\mathbf{P}_1 = \begin{pmatrix} g' & c \end{pmatrix}$ and $\mathbf{P}_2 = \begin{pmatrix} g' & -c \end{pmatrix}$, equation (A.25) reads:

$$\begin{cases} \mathbf{P}_1 \left(\dfrac{\partial \mathbf{X}}{\partial t} + \alpha_+ \dfrac{\partial \mathbf{X}}{\partial x} \right) = 0 \\ \mathbf{P}_2 \left(\dfrac{\partial \mathbf{X}}{\partial t} + \alpha_- \dfrac{\partial \mathbf{X}}{\partial x} \right) = 0 \end{cases} \tag{A.26}$$

Using the fact that $\mathrm{d}(g'h) = \mathrm{d}(c^2) = 2c\mathrm{d}c$, the system of equations (A.26) becomes:

$$\begin{cases} \left(\dfrac{\partial}{\partial t} + \alpha_+ \dfrac{\partial}{\partial x} \right)(u + 2c) = 0 \iff \left. \dfrac{\mathrm{d}R_+}{\mathrm{d}t} \right|_{\mathcal{C}_+} = 0 \\ \left(\dfrac{\partial}{\partial t} + \alpha_- \dfrac{\partial}{\partial x} \right)(u - 2c) = 0 \iff \left. \dfrac{\mathrm{d}R_-}{\mathrm{d}t} \right|_{\mathcal{C}_-} = 0 \end{cases} \tag{A.27}$$

These equations indicate that the Riemann invariants $R_+ = u + 2c$ and $R_- = u - 2c$ are conserved along the curves $\mathcal{C}_+$ and $\mathcal{C}_-$ defined by

$$(\mathcal{C}_+) : \frac{\mathrm{d}x}{\mathrm{d}t} = \alpha_+ = u + c \tag{A.28a}$$

$$(\mathcal{C}_-) : \frac{\mathrm{d}x}{\mathrm{d}t} = \alpha_- = u - c \tag{A.28b}$$

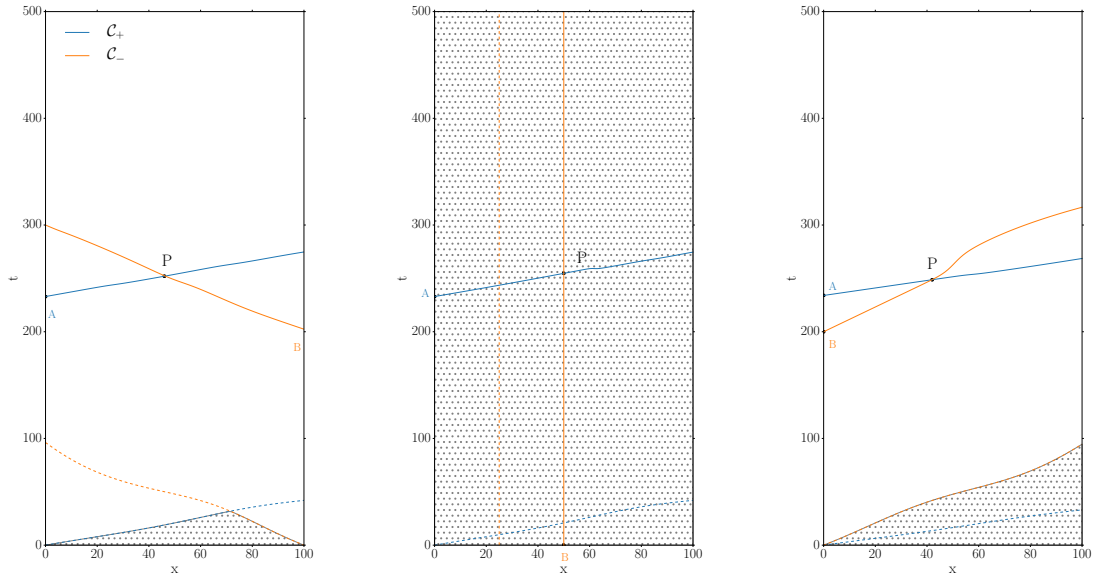

(a) Subcritical case (b) Critical case (c) Supercritical case

Figure A.3: Characteristic curves $\mathcal{C}_+$ (blue lines) and $\mathcal{C}_-$ (orange lines) in the subcritical (a), critical (b), and supercritical (c) cases over a bump. The dotted area corresponds to the region influenced by IC.

In the previous demonstration, the state vector was $\mathbf{X} = \begin{pmatrix} h \\ u \end{pmatrix}$. It would be equivalent to work with $\mathbf{X}' = \begin{pmatrix} h \\ q \end{pmatrix}$ or $\mathbf{X}'' = \begin{pmatrix} q \\ u \end{pmatrix}$. In particular, the same Riemann invariants and the same characteristic curves are obtained.

Figure A.3 shows two members of the family of characteristic curves $\mathcal{C}_+$ (blue lines) and two curves $\mathcal{C}_-$ (orange lines) for the subcritical (a), critical (b), and supercritical case (c). These curves are obtained from the integration of a shallow-layer model without topography in an unsteady situation. In all cases, $\alpha_+ > u$ such that the curves $\mathcal{C}_+$ transport information downstream faster than u. The dashed lines delimit the area that is influenced by the IC (dotted regions). In the rest of the spatio-temporal domain, the characteristic curves transport information from the BC.

A.3.1 Prescription of BC

On Figure A.3, the full lines represent the characteristic curves $\mathcal{C}_+$ (blue) and $\mathcal{C}_-$ (orange) that intersect at the point P ($x = 50$ and $t = 250$). On each characteristic curve, a Riemann invariant is conserved and the state of the system in P, i.e. the value of

$\mathbf{X}_P = \begin{pmatrix} h_P \\ u_P \end{pmatrix}$, is the solution of

$$\begin{cases} u_P + 2\sqrt{g'h_P} = R_+ = R_A \\ u_P - 2\sqrt{g'h_P} = R_- = R_B, \end{cases} \tag{A.29}$$

where R_A (resp. R_B) is the value of the Riemann invariant R_+ (resp. R_-) in A (resp. B). In the subcritical and supercritical cases (Fig.A.3a and A.3c), the values of the Riemann invariants in A and B are given by BC. In the critical case (Fig. A.3b), the Riemann invariant in A corresponds to BC and in B to IC.

In the subcritical case (Fig. A.3a), as $Fr < 1$, the eigenvalue α_- is negative such that the characteristic curves $\mathcal{C}_-$ transport information upstream (orange line). Consequently the state of the system in P is determined by two BC: one upstream (A) and one downstream (B).

In the critical case (Fig. A.3b), the curves $\mathcal{C}_-$ are vertical because $\alpha_- = 0$, such that any point in the domain is influenced by IC and the upstream BC.

The supercritical case (Fig. A.3c) is similar to the subcritical case because IC influence only a small part of the domain. However, $Fr > 1$ so $\alpha_- > 0$ and both characteristic curves transport information from upstream to downstream. The state in P is determined by two upstream BC.

As a conclusion, to ensure the uniqueness of the solution to the 1D SWE, two conditions must be prescribed that depend of the flow regime.

- If the flow is subcritical: two BC, one upstream and one downstream.
- If the flow is critical: one upstream BC and one IC.
- If the flow is supercritical: two upstream BC.

A.3.2 Phase speeds for two-layer systems

The method of characteristics can be applied to one-dimensional two-layer flows, especially for the discretization, by means of finite volume schemes, of the system of partial differential equations governing the flow (Benkhaldoun and Seaid, 2010; Castro et al., 2001):

$$\begin{cases} \dfrac{\partial h_1}{\partial t} + \dfrac{\partial h_1 u_1}{\partial x} = 0 \\ \dfrac{\partial h_1 u_1}{\partial t} + \dfrac{\partial}{\partial x}(h_1 u_1^2 + \dfrac{1}{2} g_1' h_1^2) = -g_1' h_1 \dfrac{\partial}{\partial x}(h_2 + z_f) + f_1 \\ \dfrac{\partial h_2}{\partial t} + \dfrac{\partial h_2 u_2}{\partial x} = 0 \\ \dfrac{\partial h_2 u_2}{\partial t} + \dfrac{\partial}{\partial x}(h_2 u_2^2 + \dfrac{1}{2} g_2' h_2^2) = -h_2 \dfrac{\partial}{\partial x}(g_2' z_f - g_1' \dfrac{\rho_1}{\rho_2} h_1) + f_2 - \dfrac{\rho_1}{\rho_2} f_1 \end{cases} \tag{A.30}$$

where the subscripts 1 and 2 refers to the top and bottom layer respectively (Fig. A.1). This system can be rewritten in a more compact form:

$$\begin{cases} \dfrac{\partial W_1}{\partial t} + \dfrac{\partial F(W_1)}{\partial x} = B_{1,2}(W_1)\dfrac{\partial W_2}{\partial x} + \Phi_1 \\ \dfrac{\partial W_2}{\partial t} + \dfrac{\partial F(W_2)}{\partial x} = B_{2,1}(W_2)\dfrac{\partial W_1}{\partial x} + \Phi_2 \end{cases} \tag{A.31}$$

where W_1 and W_2 are the vectors of conserved variables, F and Φ are the flux and source terms:

$$W_i(x,t) = \begin{pmatrix} h_i(x,t) \\ q_i(x,t) \end{pmatrix},\ i = 1,2, \tag{A.32a}$$

$$F(W_i) = \begin{pmatrix} h_i u_i \\ h_i u_i^2 + \frac{1}{2} g_i' h_i^2 \end{pmatrix}, \tag{A.32b}$$

$$B_{1,2}(W_1) = \begin{bmatrix} 0 & 0 \\ -g_1' h_1 & 0 \end{bmatrix}, \tag{A.32c}$$

$$B_{2,1}(W_2) = \begin{bmatrix} 0 & 0 \\ -g_1' r h_2 & 0 \end{bmatrix}, \tag{A.32d}$$

$$\Phi_1 = \begin{pmatrix} 0 \\ -g_1' h_1 \frac{\partial z_f}{\partial x} + f_1 \end{pmatrix}, \tag{A.32e}$$

$$\Phi_2 = \begin{pmatrix} 0 \\ -g_2' h_2 \frac{\partial z_f}{\partial x} + f_2 - r f_1 \end{pmatrix}, \tag{A.32f}$$

where $r = \frac{\rho_1}{\rho_2}$.

The calculation of the eigenvalues of the two-layer system (A.31) is not trivial. If the two layers were uncoupled, the eigenvalues of the Jacobian matrix $\frac{\partial F}{\partial W}$ would give the eigenvalues of each separate system. Similar to the one-layer system (A.22), the eigenvalues would be

$$u_i \pm \sqrt{g' h_i},\ i = 1,2 \tag{A.33}$$

where $u_i = \frac{q_i}{h_i}$ is the averaged velocity of the i-th layer.

The two layers being coupled, the eigenvalues are more difficult to calculate. The system (A.31) can be rewritten as follows:

$$\frac{\partial \mathbf{W}}{\partial t} + \mathcal{A}(\mathbf{W})\frac{\partial \mathbf{W}}{\partial x} = \Phi(x, \mathbf{W}), \tag{A.34}$$

where

$$\mathbf{W} = \begin{bmatrix} W_1 \\ W_2 \end{bmatrix} \tag{A.35a}$$

$$\Phi(x, \mathbf{W}) = \begin{bmatrix} \Phi_1(x, W_1) \\ \Phi_2(x, W_2) \end{bmatrix} \tag{A.35b}$$

$$\mathcal{A}(\mathbf{W}) = \begin{bmatrix} A(W_1) & -B_{1,2}(W_1) \\ -B_{2,1}(W_2) & A(W_2) \end{bmatrix} \tag{A.35c}$$

$$A(W_i) = \frac{\partial F}{\partial W_i} = \begin{bmatrix} 0 & 1 \\ -\frac{q_i^2}{h_i^2} + g_i' h_i & 2\frac{q_i}{h_i} \end{bmatrix} \tag{A.35d}$$

From equation (A.34), it is clear that the eigenvalues of the system are those of the matrix $\mathcal{A}(\mathbf{W})$, which are the solutions of the characteristic equation:

$$\left(\lambda^2 - 2u_1\lambda + u_1^2 - g_1' h_1\right)\left(\lambda^2 - 2u_2\lambda + u_2^2 - g_2' h_2\right) = (\frac{g_1'}{g_2'} r) g_1' h_1 g_2' h_2. \tag{A.36}$$

We define $r' = \frac{g_1'}{g_2'} r = \frac{\rho_1 - \rho_a}{\rho_2 - \rho_a}$.

For $r' \ll 1$, the eigenvalues of the system (A.34) approach (A.33). In the case $r' \approx 1$ and $u_1 \approx u_2$, a first-order approximation of the eigenvalues is given in Benkhaldoun and Seaid (2010), where gh_1, gh_2, and r are formally replaced with $g_1' h_1$, $g_2' h_2$, and r':

$$\lambda_{ext}^{\pm} = U_m \pm \sqrt{g_1' h_1 + g_2' h_2}, \tag{A.37a}$$

$$\lambda_{int}^{\pm} = U_c \pm \sqrt{(1 - r') \frac{g_1' h_1 g_2' h_2}{g_1' h_1 + g_2' h_2} \left(1 - \frac{(u_2 - u_1)^2}{(1 - r')(g_1' h_1 + g_2' h_2)}\right)}, \tag{A.37b}$$

where the mean and convective velocities are defined by

$$U_m = \frac{g_1' h_1 u_1 + g_2' h_2 u_2}{g_1' h_1 + g_2' h_2}, \tag{A.38a}$$

$$U_c = \frac{g_1' h_1 u_2 + g_2' h_2 u_1}{g_1' h_1 + g_2' h_2}. \tag{A.38b}$$

The two external eigenvalues $\lambda_{ext}^{\pm}$ are related to the barotropic component of the flow and the two internal eigenvalues $\lambda_{int}^{\pm}$ are related to the baroclinic component. These eigenvalues are real only if the following inequality on the Richardson number Ri is satisfied:

$$Ri \equiv (1 - r') \frac{g_1' h_1 + g_2' h_2}{(u_2 - u_1)^2} > 1. \tag{A.39}$$

This inequality is a necessary condition for the system (A.34) to be hyperbolic and thus have real solutions.

A.4 Shallow-layer model for micrometeorology

A.4.1 Finite-volume method for shallow-layer flows

The SWE for each layer (A.17) are solved by a second-order accurate finite-volume scheme of Godunov type approach. The fluxes at interfaces between cells are computed using a HLLE (Harten, Lax, van Leer, and Einfeldt) Riemann solver with pressure-based wave-speed estimate (Mingham and Causon, 1998; Toro, 2009). The interface fluxes are directly constructed from a suitable averaged interface state, which is obtained from the fastest leftward and rightward moving characteristics. The model also includes:

- the possibility of simulating a multi-layer flow;
- bottom and inter-layer friction, using Manning's equation;
- the possibility to prescribe a topography.

In the presence of topography, the left and right values of interface fluxes may differ and, in order to estimate the Riemann state, a well-balanced numerical scheme with non-negative height reconstruction has been used as in Zeitlin and Bouchut (2010). To solve the multi-layer shallow-layer problem, we have used a splitting method with an upwinding dispersive correction scheme (Zeitlin and Bouchut, 2010).

The CFL condition is defined by

$$\Delta t \leq \frac{\Delta x}{a^{SCHR}}. \tag{A.40}$$

where a^{SCHR} is the sum of the speed involved in the CFL condition for nonnegativity of the hydrostatic reconstruction scheme (a^{HR}) (Benkhaldoun and Seaid, 2010; Castro et al., 2001), and the speed associated with the dispersive correction scheme (a^{J})(Zeitlin and Bouchut, 2010):

$$a^{SCHR} = a^{HR} + a^{J}. \tag{A.41}$$

The speed a^{HR} is estimated as follows:

$$a^{HR} = \max(|\lambda^{\pm}_{ext}|, |\lambda^{\pm}_{int,k}|) \tag{A.42a}$$

$$\lambda^{\pm}_{ext} = U_m \pm \sqrt{\sum_{k=1}^{N} g'_k h_k} \tag{A.42b}$$

$$\lambda^{\pm}_{int,k} = U_{c,k} \pm \sqrt{g'_k \frac{h_k h_{k+1}}{h_k + h_{k+1}} [1 - \frac{(u_k - u_{k+1})^2}{g'_k (h_k + h_{k+1})}]} \text{ for } 1 \leq \mathrm{k} < \mathrm{N} \tag{A.42c}$$

$$U_m = \frac{\sum_{k=1}^{N} g'_k h_k u_k}{\sum_{k=1}^{N} g'_k h_k} \tag{A.42d}$$

$$U_{c,k} = \frac{g'_k h_k u_{k+1} + g'_{k+1} h_{k+1} u_k}{g'_k h_k + g'_{k+1} h_{k+1}}. \tag{A.42e}$$

A.4.2 Validation of the shallow water model

Subcritical, critical, and supercritical regime

The behaviour of the model in subcritical, critical, and supercritical regimes has been tested over a small bump centred on $x = 80$ and with a maximum height of 0.5m (black line in Fig. A.4). A constant value of flow rate is prescribed on the left of the domain (q_L) and a constant fluid height is prescribed on the right for subcritical and critical cases and on the left for the supercritical case (h_R). The values of q_L and h_R are given in Table A.1 and $g' = 0.1g = 0.981\text{m}^2/\text{s}$ which corresponds to a layer of air slightly denser than the atmosphere above ($\rho = 1.11\rho_a$). After a transition regime, the simulated system reaches a stationary state that is considered as the result of the simulation.

Regime	**Fr**	$\mathbf{q}_L$	$\mathbf{h}_R$
Subcritical	0.4	2.0	3.0
Critical	1	2.0	2.309
Supercritical	2	2.0	1.0

Table A.1: Values of prescribed BC.

The simulated profiles are compared with the analytical solution obtained from the resolution of the Bernoulli equation (A.20), the value of H_0 being determined on the right of the domain ($H_0 = \frac{q_L^2}{2g'h_R^2} + h_R$).

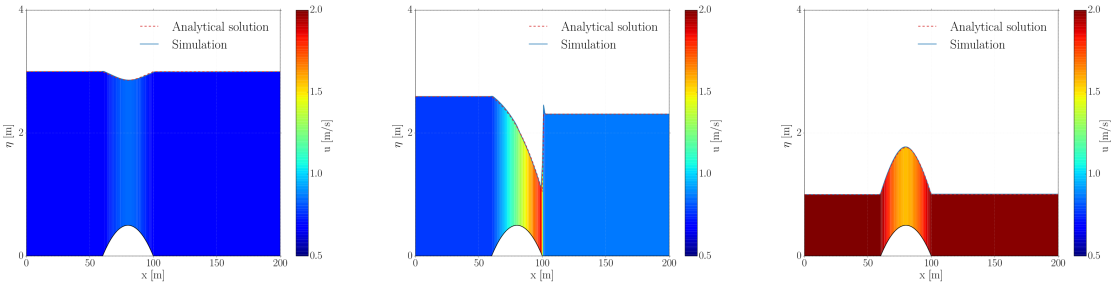

(a) Subcritical case (b) Critical case (c) Supercritical case

Figure A.4: Analytical solution and numerical simulation of the behaviour of subcritical, critical, and supercritical flows over a bump.

Figure A.4a shows the behaviour of a subcritical flow over a bump. The flow is subcritical so it corresponds to a case where $Fr < 1 \iff u < \sqrt{g'h}$. Consequently, in the conservation of momentum equation, the second term of the right-hand side predominates and there is an approximate balance between the variation of height and the variation of topography: $\frac{\partial h}{\partial x} \approx -\frac{\partial z_f}{\partial x}$. Where the topography increases, the height decreases and vice-versa. The vertical velocity adjusts to ensure continuity, leading to an acceleration over the bump. It is in agreement with the fact that if z_f increases, the

specific charge $\mathcal{H}_s$ has to decrease. In the subcritical regime, $\frac{\partial \mathcal{H}_s}{\partial h} > 0$ (Fig. A.2), and h has to decrease to reduce the specific charge.

On the contrary, if the flow is supercritical as on Figure A.4c, the Froude number is greater than 1. Consequently, the first term in the equation of momentum conservation predominates and the convection balances the variation of topography: $u\frac{\partial u}{\partial x} \approx -g'\frac{\partial z_f}{\partial x}$. Where the topography increases, the velocity decreases and – due to continuity – the height increases over the bump. Here again, the observed increase of height over the bump is in agreement with the fact that $\frac{\partial \mathcal{H}_s}{\partial h} < 0$ in the supercritical regime such that the height has to increase to reduce the specific charge and compensate the increase of topography.

Figure A.4b shows the case where the flow is critical over the bump with a hydraulic jump after.

Hydraulic jump Let us derive the necessary conditions to obtain this particular situation where the flow is exactly critical at the top of the bump and thus transits from a subcritical regime before the bump to a supercritical regime after the bump. Just after the bump, a hydraulic jump occurs to allow the flow to come back to a subcritical regime and satisfy the downstream boundary condition. Consequently, there are 4 different states:

- upstream, before the bump (subcritical): h_1, u_1
- above the bump (critical): h_c, u_c
- after the bump and before the jump (supercritical): h_2, u_2
- downstream, after the jump: h_3, u_3

First, the critical regime is reached over the bump if the specific charge at this point is equal to the critical specific charge: $\mathcal{H}_c = \mathcal{H}_s(h = h_c) = \frac{3}{2}h_c$. The conservation of $\mathcal{H}_s + z_f$ implies that the specific charge before and after the bump must be $\mathcal{H}_1 = \mathcal{H}_2 = \mathcal{H}_c + z_{f,max}$ where $z_{f,max}$ is the height of the bump. Two different heights (h^+ and h^-) are solution of the equation

$$\mathcal{H}_s(h) = \mathcal{H}_1 = \mathcal{H}_2 \iff h + \frac{q^2}{2g'h^2} = \mathcal{H}_1 = \mathcal{H}_2. \tag{A.43}$$

For the sake of simplicity, we ordinate these solutions: $h^+ > h^-$. The greater solution (h^+) corresponds to a subcritical flow and the smaller one (h^-) to a supercritical flow. We thus deduce that $h_1 = h^+$ and $h_2 = h^-$.

While the specific charge is conserved between the upstream condition and the top of the bump, the hydraulic jump triggers a loss of charge. Consequently, the downstream specific charge is smaller than the upstream one: $\mathcal{H}_2 > \mathcal{H}_3$. The specific charge decreases with h in the supercritical regime and since we assume that the topography is flat after the bump ($z_2 = z_3$), we deduce that $h_2 < h_3$. This justifies that, in order to observe a

stationary jump the flow must be supercritical before the jump (h_2, u_2) and then transits towards a subcritical regime after the jump (h_3, u_3).

Therefore flow transits from a subcritical regime before the bump where the height is equal to $h_1 = h^+$ to a supercritical regime with a fluid height $h_2 = h^-$. At the top of the bump the flow is critical. To have a hydraulic jump, the downstream boundary condition on height must ensure that the flow is subcritical downstream.

The heights and velocities before (h_2, u_2) and downstream (h_3, u_3) the jump must satisfy the conservation of mass:

$$h_2 u_2 = h_3 u_3 = q \tag{A.44}$$

and the conservation of momentum flux:

$$h_2 u_2^2 + \frac{1}{2} g h_2^2 = h_3 u_3^2 + \frac{1}{2} g h_3^2. \tag{A.45}$$

From these two equations, one can derive the Bélanger equation which relates the two heights from either side of the hydraulic jump:

$$h_3 = \frac{h_2}{2}\left(\sqrt{1 + 8\frac{q^2}{g' h_2^3}} - 1\right). \tag{A.46}$$

If the height prescribed downstream corresponds to a subcritical regime satisfying the Bélanger equation, a hydraulic jump occurs after the bump to make the junction between the supercritical regime just after the bump and the subcritical regime downstream imposed by the BC.

In the present example, we have:

$$q = 2.0\text{m}^2/\text{s} \tag{A.47a}$$

$$z_{f,max} = 0.5\text{m} \tag{A.47b}$$

$$h_c = \left(\frac{q^2}{g'}\right)^{\frac{1}{3}} = 1.597\text{m} \tag{A.47c}$$

$$\mathcal{H}_c = \frac{3}{2} h_c = 2.396\text{m} \tag{A.47d}$$

$$\mathcal{H}_1 = \mathcal{H} =_2= \mathcal{H}_c + z_{f,max} = 2.896\text{m} \tag{A.47e}$$

$$h_1 = h^+ = 2.593\text{m and } h_2 = h^- = 1.051\text{m} \tag{A.47f}$$

$$h_3 = 2.309\text{m}. \tag{A.47g}$$

These theoretical values are verified numerically as shown on Figure A.4b.

Wind fields over topography show regions of speed up over the peaks of topography and lower velocities in valleys. This corresponds to subcritical case (Fig. A.4a) consequently only this case will be studied in what follows.

Validation with and without friction

For a simple, flat, and slanted bottom, it is possible to verify the performance of the model to simulate friction forces by comparing the numerical simulation to the analytical solution. In stationary regime for unidimensional domain with only one layer of fluid and friction forces, the equation of momentum conservation reads:

$$\frac{\mathrm{d}}{\mathrm{d}x}(hu^2 + \frac{1}{2}g'h^2) = -g'h\frac{\mathrm{d}z_f}{\mathrm{d}x} - \frac{n^2gu^2}{h^{1/3}}. \tag{A.48}$$

Using the continuity equation that ensures the spatial conservation of the discharge: $\frac{dq}{dx} = 0$, a first-order differential equation on h can be derived:

$$(g' - \frac{q^2}{h^3})\frac{\mathrm{d}h}{\mathrm{d}x} = -g'\frac{\mathrm{d}z_f}{\mathrm{d}x} - g\frac{n^2q^2}{h^{10/3}}. \tag{A.49}$$

The solution to this equation gives an analytical solution for comparison with the results of numerical simulations (Fig. A.5). Different values of the Manning coefficient are tested, in particular $n = 0$ to verify that $\mathcal{H}_s + z_f$ is conserved.

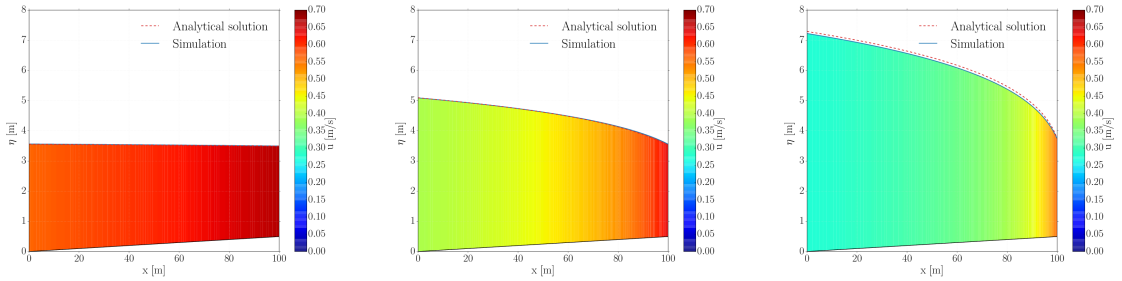

(a) $n = 0$ (b) $n = 0.02$ (c) $n = 0.05$

Figure A.5: Analytical solution and numerical simulation of the height and horizontal velocity of fluid over a slanted bottom, with and without friction.

Appendix B

Supplementary information about the BFN algorithm

B.1 Effect of boundary conditions and forcing on wave equation

B.1.1 Generalisation of d'Alembert solution of wave equation

The so-called d'Alembert formula gives the unique solution to the Cauchy problem:

$$\begin{cases} \dfrac{\partial^2 \phi}{\partial t^2} - c^2 \dfrac{\partial^2 \phi}{\partial x^2} = 0 \\ \text{with initial conditions } \phi(x,0) = f(x) \text{ and } \dfrac{\partial \phi}{\partial t}(x,0) = g(x) \end{cases} \tag{B.1}$$

Here we adapt the d'Alembert formula for the case where the solution is subject to BC instead of IC.

At first, we will consider a transport equation constrained BC , whose unique solution is given by Lemma 1. We use the following notation: $\partial_t f = \frac{\partial f}{\partial t}$ and $\partial_x f = \frac{\partial f}{\partial x}$.

Lemma 1 (Duhamel formula for BC problem)**.** *We consider the transport equation with BC in* $x = a \in \mathbb{R}_+$

$$\begin{cases} \partial_t \psi + c \partial_x \psi = f(x,t),\ t \geq 0,\ x \geq a \\ \psi(a,t) = \psi_a(t),\ t \geq 0. \end{cases} \tag{B.2}$$

There is a unique solution $\psi \in \mathcal{C}^1([a, +\infty[\times [a, +\infty[)$ *given by*

$$\psi(x,t) = \psi_a\left(t - \frac{x-a}{c}\right) + \frac{1}{c}\int_a^x f\left(s, t + \frac{s-x}{c}\right) \mathrm{d}s. \tag{B.3}$$

Proof. If $f \equiv 0$ then the solution is obtained with the method of characteristics. We define the family of characteristic curves $\mathcal{C}$ of equation

$$t = t_0 + \frac{x-a}{c}, \tag{B.4}$$

for any fixed (a, t_0) in $\mathbb{R}^2_+$. These curves satisfy

$$\frac{\mathrm{d}x}{\mathrm{d}t} = c. \tag{B.5}$$

The function ψ is constant along each of these characteristics:

$$\begin{aligned} \mathrm{d}\psi_{|(\mathcal{C})} &= \partial_t \psi \mathrm{d}t + \partial_x \psi \mathrm{d}x && \text{(B.6)} \\ &= \partial_t \psi \mathrm{d}t + \partial_x \psi c \mathrm{d}t && \text{(B.7)} \\ &= (\partial_t \psi + c\partial_x \psi)\mathrm{d}t && \text{(B.8)} \\ &= 0. && \text{(B.9)} \end{aligned}$$

For any $(x, t) \in \mathbb{R}^2_+$, there is a $t_0 = t - \frac{x-a}{c}$ such that the corresponding characteristic goes through (x, t) and (a, t_0). Consequently,

$$\psi(x, t) = \psi\left(a, t_0\right) = \psi_a\left(t - \frac{x-a}{c}\right). \tag{B.10}$$

Now, if $f \neq 0$ we can note that

$$\begin{aligned} &\frac{1}{c}\partial_t \psi + \partial_x \psi = \frac{1}{c} f \\ \iff &\frac{\mathrm{d}\psi}{\mathrm{d}x}|_{(\mathcal{C})} = \frac{1}{c} f. \end{aligned}$$

The integration between a and x, along $\mathcal{C}$, of the previous equation gives:

$$\begin{aligned} &\psi\left(x, t_0 + \frac{x-a}{c}\right) = \psi\left(a, t_0\right) + \frac{1}{c}\int_a^x f\left(s, t_0 + \frac{s-a}{c}\right)\mathrm{d}s \\ \iff &\psi\left(x, t\right) = \psi_a\left(t - \frac{x-a}{c}\right) + \frac{1}{c}\int_a^x f\left(s, t + \frac{s-x}{c}\right)\mathrm{d}s. \end{aligned}$$

□

In other words, Duhamel's formula states that the value of ϕ for any (x, t), is equal to the value of the BC at the extremity of the characteristic ($\mathcal{C}$: $\frac{\mathrm{d}x}{\mathrm{d}t} = c$) plus the integral of the forcing function f along this characteristic between the boundary and (x, t).

Now that we have the solution to a forced transport equation constrained by BC, we can prove the d'Alembert theorem which gives the solution to wave equations with BC.

Theorem 1 (d'Alembert formula for BC problem)**.** *Consider $g \in \mathcal{C}^2(\mathbb{R}_+)$ and $h \in \mathcal{C}^1(\mathbb{R}_+)$, then there is a unique solution $\phi \in \mathcal{C}^2(\mathbb{R}_+ \times \mathbb{R}_+)$ to the Cauchy problem*

$$\begin{cases} \partial_t^2 \phi - c^2 \partial_x^2 u = 0,\ t \geq 0,\ x \geq 0 \\ \phi(a, t) = f(t),\ \partial_x \phi(a, t) = g(t),\ t \geq 0 \text{ and } a \in \mathbb{R}_+ \end{cases} \tag{B.11}$$

which is given by the following formula:

$$\phi(x, t) = \frac{f\left(t + \frac{x-a}{c}\right) + f\left(t - \frac{x-a}{c}\right)}{2} + \frac{c}{2}\int_{t-\frac{x-a}{c}}^{t+\frac{x-a}{c}} g(s)\mathrm{d}s. \tag{B.12}$$

Proof. Let us consider ϕ a solution of equation (B.11) of class $\mathcal{C}^2(\mathbb{R}_+ \times \mathbb{R}_+)$. We define $\psi = \partial_t\phi + c\partial_x\phi$ such that

$$\begin{aligned}\partial_t\psi - c\partial_x\psi &= (\partial_t - c\partial_x)(\partial_t + c\partial_x)\phi \\ &= (\partial_t^2 - c^2\partial_x^2)\phi \\ &= 0.\end{aligned}$$

Consequently, ψ is solution of the Cauchy problem

$$\begin{cases}\partial_t\psi - c\partial_x\psi = 0 \\ \psi(a,t) = f'(t) + cg(t).\end{cases} \tag{B.13}$$

Using Lemma 1 where we formally replace c by $-c$, we know that there is a unique solution, given by:

$$\psi(x,t) = f'\left(t + \frac{x-a}{c}\right) + cg\left(t + \frac{x-a}{c}\right). \tag{B.14}$$

As $\partial_t\phi + c\partial_x\phi = \psi$ and $\phi(a,t) = f(t)$, the Lemma 1 gives the expression of ϕ:

$$\begin{aligned}\phi(x,t) &= f\left(t - \frac{x-a}{c}\right) + \frac{1}{c}\int_a^x \psi\left(s, t + \frac{s-x}{c}\right)\mathrm{d}s \\ &= f\left(t - \frac{x-a}{c}\right) + \frac{1}{2}\int_a^x \frac{2}{c}f'\left(t + \frac{2s-x-a}{c}\right)ds + \int_a^x g\left(t + \frac{2s-x-a}{c}\right)\mathrm{d}s \\ &= \frac{f\left(t + \frac{x-a}{c}\right) + f\left(t - \frac{x-a}{c}\right)}{2} + \frac{c}{2}\int_{t-\frac{x-a}{c}}^{t+\frac{x-a}{c}} g(s)\mathrm{d}s\end{aligned} \tag{B.15}$$

Reciprocally, it is easy to verify that the formula (B.12) is a solution of class $\mathcal{C}^2(\mathbb{R}_+ \times \mathbb{R}_+)$ for the problem (B.11).

□

We can understand d'Alembert formula with characteristics $\mathcal{C}_+$: $\frac{\mathrm{d}x}{\mathrm{d}t} = c$ and $\mathcal{C}_-$: $\frac{\mathrm{d}x}{\mathrm{d}t} = -c$, as shown on Figure B.1 whose intersection with the boundary delimits the section of the border (between $t - \frac{x-a}{c}$ and $t + \frac{x-a}{c}$) that influences the solution at (x,t). In fact, d'Alembert formula stands that for any (x,t) the value of ϕ is obtained by

$$\phi(x,t) = \overline{\phi(a,t)} + (x-a)\overline{\partial_x\phi_{|a}}, \tag{B.16}$$

where $\overline{\phi(a,t)}$ and $\overline{\partial_x\phi_{|a}}$ are the average values of f and g over the boundary section between in $t + \frac{x-a}{c}$ and $t - \frac{x+a}{c}$. The average boundary value is

$$\overline{\phi(a,t)} = \frac{f\left(t + \frac{x-a}{c}\right) + f\left(t - \frac{x-a}{c}\right)}{2}, \tag{B.17}$$

and the average space derivative is

$$\overline{\partial_x\phi_{|a}} = \frac{1}{\left(t - \frac{x-a}{c}\right) - \left(t + \frac{x-a}{c}\right)}\int_{t-\frac{x-a}{c}}^{t+\frac{x-a}{c}} g(s)\mathrm{d}s = \frac{c}{2(x-a)}\int_{t-\frac{x-a}{c}}^{t+\frac{x-a}{c}} g(s)\mathrm{d}s. \tag{B.18}$$

.

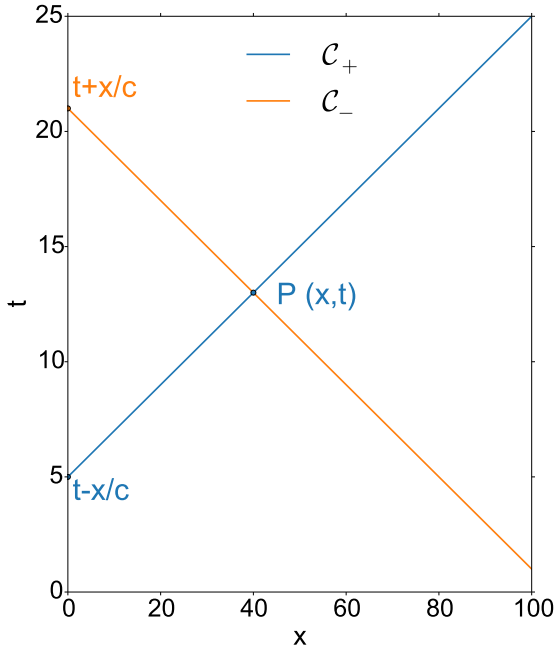

Figure B.1: Graphical explanation of d'Alembert formula in the case $a = 0$. The two characteristic lines passing through P (x, t) transport the BC from $t - \frac{x}{c}$ and $t + \frac{x}{c}$.

B.1.2 The forced wave equation with homogeneous BC

In this section we consider a forcing term $F \in \mathcal{C}^0(\mathbb{R}_+ \times \mathbb{R}_+)$ and we seek the solution ϕ to the forced wave equation

$$\frac{\partial^2 \phi}{\partial t^2} - c^2 \frac{\partial^2 \phi}{\partial x^2} = F, \tag{B.19}$$

on $[a, +\infty[\times[a, +\infty[$, subject to the homogeneous BC: $\phi(x = a, t) = 0$ and $\frac{\partial \phi}{\partial x}(x = a, t) = 0$.

We first seek a Green's function $G(x, t; y, \tau)$ that obeys the simpler problem where the forcing term is replaced by δ-functions in both space and time variables:

$$\left(\frac{\partial^2}{\partial t^2} - c^2 \frac{\partial^2}{\partial x^2} \right) G = \delta(x - y)\delta(t - \tau) \tag{B.20}$$

The Green's function must satisfy the same BC than ϕ:

$$G(x = a, t; y, \tau) = 0 \quad \text{and} \quad \frac{\partial G}{\partial x}(x = a, t; y, \tau) = 0 \tag{B.21}$$

Knowing G, the solution of the problem (B.19) is given by the convolution of the Green's function with the forcing function:

$$\phi(x, t) = \int_a^\infty \int_0^\infty F(y, \tau) G(x, t; y, \tau) \mathrm{d}y \mathrm{d}\tau. \tag{B.22}$$

To find the Green's function, we will consider the Fourier transform with respect to time, and its inverse, defined as follows:

$$\widetilde{f}(\xi) = \int_{-\infty}^{\infty} f(t) e^{-i\xi t} \mathrm{d}t \quad \text{and} \quad f(t) = \frac{1}{2\pi} \int_{-\infty}^{\infty} \widetilde{f}(\xi) e^{-i\xi t} \mathrm{d}\xi. \tag{B.23}$$

We take the Fourier transform with respect to time of the equation (B.20):

$$\begin{aligned} -\xi^2\widetilde{G} - c^2\frac{\partial^2\widetilde{G}}{\partial x^2} &= \delta(x-y)e^{-i\xi\tau} \\ \iff \frac{\partial^2\widetilde{G}}{\partial x^2} + \frac{\xi^2}{c^2}\widetilde{G} &= \frac{-1}{c^2}\delta(x-y)e^{-i\xi\tau}. \end{aligned} \tag{B.24}$$

The function $\widetilde{G}(x,\xi;y,\tau)$ is thus the solution of a second order partial differential equation (PDE), subject to the BC:

$$\widetilde{G}(x=a,\xi;y,\tau)=0 \quad \text{and} \quad \tfrac{\partial\widetilde{G}}{\partial x}(x=a,\xi;y,\tau)=0 \tag{B.25}$$

To solve this PDE, we first consider the associate homogeneous equation and then we will use the method based on the variation of parameters to find a particular solution to (B.24). The general solution is then the sum of the homogeneous and the particular solutions.

The **homogeneous equation** corresponding to equation (B.24) is:

$$\frac{\partial^2\widetilde{G}_h}{\partial x^2} + \frac{\xi^2}{c^2}\widetilde{G}_h = 0, \tag{B.26}$$

which is solved by

$$\widetilde{G}_h(x,\xi;y,\tau) = \lambda_1(\xi;y,\tau)e^{i\frac{\xi}{c}x} + \gamma_1(\xi;y,\tau)e^{-i\frac{\xi}{c}x}, \tag{B.27}$$

where λ_1 and γ_1 are constants with respect to x.

Now we consider the inhomogeneous equation (B.24) and we use the method of variation of parameters to seek a particular solution of the form:

$$\widetilde{G}_0(x,\xi;y,\tau) = \lambda(x,\xi;y,\tau)e^{i\frac{\xi}{c}x} + \gamma(x,\xi;y,\tau)e^{-i\frac{\xi}{c}x} \tag{B.28}$$

We deduce that $\partial_x\lambda$ and $\partial_x\gamma$ must satisfy the following system of equation:

$$\begin{cases} e^{i\frac{\xi}{c}x}\dfrac{\partial\lambda}{\partial x} + e^{-i\frac{\xi}{c}x}\dfrac{\partial\gamma}{\partial x} = 0 \\ i\dfrac{\xi}{c}e^{i\frac{\xi}{c}x}\dfrac{\partial\lambda}{\partial x} - i\dfrac{\xi}{c}e^{-i\frac{\xi}{c}x}\dfrac{\partial\gamma}{\partial x} = \dfrac{-1}{c^2}\delta(x-y)e^{-i\xi\tau}. \end{cases} \tag{B.29}$$

The solutions of this system are:

$$\begin{cases} \dfrac{\partial\lambda(x,\xi;y,\tau)}{\partial x} = \dfrac{-\delta(x-y)}{2i\xi c}e^{-i\frac{\xi}{c}x}e^{-i\xi\tau} \\ \dfrac{\partial\gamma(x,\xi;y,\tau)}{\partial x} = \dfrac{\delta(x-y)}{2i\xi c}e^{i\frac{\xi}{c}x}e^{-i\xi\tau}. \end{cases} \tag{B.30}$$

If we integrate between 0 and x we obtain the expression of λ:

$$\begin{aligned} \lambda(x,\xi;y,\tau) &= \int_0^x \frac{-\delta(s-y)}{2i\xi c}e^{-i\frac{\xi}{c}s}e^{-i\xi\tau}\mathrm{d}s + C_1(\xi;y,\tau) \\ &= \begin{cases} \dfrac{-e^{-i\frac{\xi}{c}y}e^{-i\xi\tau}}{2i\xi c} + C_1'(\xi;y,\tau) & \text{if } x \geq y \\ C_1'(\xi;y,\tau) & \text{otherwise} \end{cases} \\ &= -\Theta(x-y)\frac{e^{-i\frac{\xi}{c}y}e^{-i\xi\tau}}{2i\xi c} + C_1'(\xi;y,\tau), \end{aligned}$$

where $\Theta(x)$ is the Heaviside step function, defined for any $x \in \mathbb{R}$ by

$$\Theta(x) = \begin{cases} 0 & \text{if } x \leq 0, \\ 1 & \text{if } x > 0. \end{cases} \tag{B.31}$$

Similarly,

$$\gamma(x, \xi; y, \tau) = \Theta(x - y) \frac{e^{i\frac{\xi}{c}y} e^{-i\xi\tau}}{2i\xi c} + C_2'(\xi; y, \tau). \tag{B.32}$$

Eventually, the **particular solution** is given by

$$\widetilde{G}_0(x, \xi; y, \tau) = \frac{-\Theta(x - y) e^{-i\xi\tau}}{\xi c} \sin\left(\frac{\xi}{c}(x - y)\right) + C_1'(\xi; y, \tau) e^{i\frac{\xi}{c}x} + C_2'(\xi; y, \tau) e^{-i\frac{\xi}{c}x}. \tag{B.33}$$

The general solution is the sum of the solution to the homogeneous equation and the particular solution:

$$\widetilde{G}(x, \xi; y, \tau) = \widetilde{G}_h + \widetilde{G}_0 = \frac{-\Theta(x - y) e^{-i\xi\tau}}{\xi c} \sin\left(\frac{\xi}{c}(x - y)\right) + C_1''(\xi; y, \tau) e^{i\frac{\xi}{c}x} + C_2''(\xi; y, \tau) e^{-i\frac{\xi}{c}x}, \tag{B.34}$$

where $C_1'' = C_1' + \lambda_1$ and $C_2'' = C_2' + \gamma_1$.

Since y is defined on $[a, +\infty[$, $\Theta(a - y) = 0$ for any y. As a result, to satisfy the prescribed BC, C_1'' and C_2'' must satisfy:

$$C_1'' e^{i\frac{\xi}{x}a} + C_2'' e^{-i\frac{\xi}{x}a} = 0 \tag{B.35a}$$

$$C_1'' e^{i\frac{\xi}{x}a} - C_2'' e^{-i\frac{\xi}{x}a} = 0. \tag{B.35b}$$

We deduce that $C_1'' = C_2'' = 0$.

Consequently the solution to the problem given by equation (B.24) and BC (B.25) is

$$\widetilde{G}(x, \xi; y, \tau) = -\Theta(x - y) \frac{e^{-i\xi\tau}}{\xi c} \sin\left(\frac{\xi}{c}(x - y)\right). \tag{B.36}$$

To recover the Green's function G, we have to compute the inverse Fourier transform of $\widetilde{G}$, which is defined by

$$G(x, t; y, \tau) = \frac{1}{2\pi} \int_{-\infty}^{\infty} -\Theta(x - y) \frac{e^{-i\xi\tau}}{\xi c} \sin\left(\frac{\xi}{c}(x - y)\right) e^{i\xi t} \mathrm{d}\xi. \tag{B.37}$$

To compute this inverse Fourier transform, let us define the function

$$u(t) = \int_{-\infty}^{\infty} \frac{\sin\left(\frac{\xi}{c}(x - y)\right)}{,} \xi e^{i\xi t} \mathrm{d}\xi \tag{B.38}$$

such that

$$G(x, t; y, \tau) = \frac{-\Theta(x - y)}{2\pi c} u(t - \tau). \tag{B.39}$$

We first compute the derivative of u:

$$\begin{aligned} u(t) &= \int_{-\infty}^{\infty} \frac{\sin\left(\frac{\xi}{c}(x-y)\right)}{\xi} i\xi e^{i\xi t} \mathrm{d}\xi \\ &= \int_{-\infty}^{\infty} \frac{e^{i\frac{\xi}{c}(x-y)} - e^{-i\frac{\xi}{c}(x-y)}}{2i} i e^{i\xi t} \\ &= \frac{1}{2}\int_{-\infty}^{\infty} e^{i\xi\left(t+\frac{(x-y)}{c}\right)} - e^{i\xi\left(t-\frac{(x-y)}{c}\right)} \mathrm{d}\xi \\ &= \pi\left[\delta\left(t+\frac{(x-y)}{c}\right) - \delta\left(t-\frac{(x-y)}{c}\right)\right]. \end{aligned} \tag{B.40}$$

The last result is obtained using the fact that the inverse Fourier transform of $e^{-i\xi\alpha}$ is $\frac{1}{2\pi}\int_{-\infty}^{\infty} e^{-i\xi\alpha}e^{it\xi}\mathrm{d}\xi = \delta(t-\alpha)$.

To obtain the expression of $u(t)$, we integrate u between 0 and t. Since $u(0) = \int_{-\infty}^{+\infty} \frac{\sin(\xi\frac{x-y}{c})}{\xi}\mathrm{d}\xi = \pi$, we get

$$\begin{aligned} u(t) &= \int_0^{\mathrm{t}} \pi\left[\delta\left(s+\frac{(x-y)}{c}\right) - \delta\left(s-\frac{(x-y)}{c}\right)\right]\mathrm{d}s + u(0) \\ &= \pi\left[\Theta\left(t+\frac{(x-y)}{c}\right) - \Theta\left(t-\frac{(x-y)}{c}\right) + 2\Theta\left(-(x-y)\right)\right]. \end{aligned}$$

Replacing in the expression of G (B.39) and using the fact that $\Theta\left(x-y\right)\Theta\left(-(x-y)\right) = 0$, we obtain

$$G(x,t;y,\tau) = \frac{\Theta(x-y)}{2c}\left[\Theta\left(t-\tau-\frac{(x-y)}{c}\right) - \Theta\left(t-\tau+\frac{(x-y)}{c}\right)\right]. \tag{B.41}$$

Using this Green's function in equation (B.22), the solution of the forced wave equation can be written as

$$\begin{aligned} \phi(x,t) &= \int_a^{\infty}\int_0^{\infty} F(y,\tau)\frac{\Theta(x-y)}{2c}\left[\Theta\left(t-\tau-\frac{(x-y)}{c}\right) - \Theta\left(t-\tau+\frac{(x-y)}{c}\right)\right]\mathrm{d}y\mathrm{d}\tau \\ &= \frac{1}{2c}\int_a^x \left[\int_0^{t-\frac{(x-y)}{c}} F(y,\tau)\mathrm{d}\tau - \int_0^{t+\frac{(x-y)}{c}} F(y,\tau)\mathrm{d}\tau\right]\mathrm{d}y \\ &= \frac{-1}{2c}\int_a^x \int_{t-\frac{(x-y)}{c}}^{t+\frac{(x-y)}{c}} F(y,\tau)\mathrm{d}\tau\mathrm{d}y \\ &= \int_a^x \left[\frac{c}{2}\int_{t-\frac{(x-y)}{c}}^{t+\frac{(x-y)}{c}} \frac{-1}{c^2}F(y,\tau)\mathrm{d}\tau\right]\mathrm{d}y. \end{aligned} \tag{B.42}$$

Comparing with equation (B.12), we can see that for any $y < x$, the term

$$\frac{c}{2}\int_{t-\frac{(x-y)}{c}}^{t+\frac{(x-y)}{c}} \frac{-1}{c^2}F(y,\tau)\mathrm{d}\tau$$

corresponds to the d'Alembert solution to the unforced wave equation with inhomogeneous BC given by

$$\phi(x=y,t) = 0 \quad \text{and} \quad \frac{\partial\phi}{\partial x}(x=y,t) = \frac{-1}{c^2}F(y,t). \tag{B.43}$$

Hence, the solution (B.42) of the forced wave equation can be viewed as the superposition of the influences of the forcing term $\frac{-1}{c^2}F$, which acts similarly to a BC (here on the space derivative of ϕ) for each $y < x$.

B.1.3 Application to the shallow-water equations

Linearisation of shallow-water equations

We consider the decomposition of the state variables u and h around the constant mean state $\begin{pmatrix} H \\ U \end{pmatrix}$:

$$\begin{cases} u = U + u' \\ h = H + h' \end{cases} \tag{B.44}$$

where u' and h' are the perturbations around the mean, such that $u' \ll U$ and $h' \ll H$. Replacing in the 1D SWE without topography (A.22) and neglecting the terms of second order in u' or h', we get

$$\begin{cases} \dfrac{\partial h'}{\partial t} + U\dfrac{\partial h'}{\partial x} + H\dfrac{\partial u'}{\partial x} = 0. \\ \dfrac{\partial u'}{\partial t} + U\dfrac{\partial u'}{\partial x} + g\dfrac{\partial h'}{\partial x} = 0. \end{cases} \tag{B.45}$$

For the sake of simplicity, we omit the apostrophe in what follows.

We perform a change of variable

$$\begin{cases} X = x - Ut \\ \tau = t \end{cases} \tag{B.46}$$

such that, for any functional A,

$$\partial_x A = \partial_X A \tag{B.47}$$

$$\partial_t = -U\partial_X A + \partial_\tau A. \tag{B.48}$$

The linearised SWE (B.45) thus become:

$$\begin{cases} \dfrac{\partial h}{\partial \tau} + H\dfrac{\partial u}{\partial X} = 0 & \text{(B.49a)} \\ \dfrac{\partial u}{\partial \tau} + g\dfrac{\partial h}{\partial X} = 0 & \text{(B.49b)} \end{cases}$$

Then we combine equations (B.49a) and (B.49b) as follows

$$\frac{\partial(\text{B.49a})}{\partial \tau} - H\frac{\partial(\text{B.49b})}{\partial X} \Rightarrow \frac{\partial^2 h}{\partial \tau^2} - gH\frac{\partial^2 h}{\partial X^2} = 0$$
$$\frac{\partial(\text{B.49b})}{\partial \tau} - g\frac{\partial(\text{B.49a})}{\partial X} \Rightarrow \frac{\partial^2 u}{\partial \tau^2} - gH\frac{\partial^2 u}{\partial X^2} = 0$$

We can define the state vector $\phi(X,\tau) = \begin{pmatrix} h(X,\tau) \\ u(X,\tau) \end{pmatrix}$ which then satisfies the wave equation

$$\frac{\partial^2 \phi}{\partial \tau^2} - c^2\frac{\partial^2 \phi}{\partial X^2} = 0 \tag{B.50}$$

with $c^2 = gH$. We have shown that the linearised unidimensional SWE can be written as a wave equation.

Linearised shallow-water equations with forcing

We have previously proved that the Cauchy problem with prescribed BC admits a unique solution (see Appendix B.1.1). For the linearised SWE, we consider the following Cauchy problem:

$$\begin{cases} \dfrac{\partial^2 \phi}{\partial t^2} - c^2 \dfrac{\partial^2 \phi}{\partial X^2} = 0 \\ \phi(X = -Ut, t) = f(t) \text{ and } \dfrac{\partial \phi}{\partial X}(X = -Ut, t) = g(t) \end{cases} \tag{B.51}$$

where $X = x - Ut$.

Since the point where the BC is applied depends on t, the formula derived above should not be used directly. However, in the case of subcritical flow we have $U \ll c$ such that $c + U \approx c$ and $c - U \approx c$. Using these approximations, the expression of ϕ is given by the modified d'Alembert formula (B.12), by formally replacing 'x' by $X = x - Ut$ and 'a' by $-Ut$:

$$\begin{aligned} \phi(X,t) &= \frac{f\left(t + \frac{X+Ut}{c}\right) + f\left(t - \frac{X+Ut}{c}\right)}{2} + \frac{c}{2}\int_{t-\frac{X+Ut}{c}}^{t+\frac{X+Ut}{c}} g(s)\mathrm{d}s \\ \iff \phi(x,t) &= \frac{f\left(t + \frac{x}{c}\right) + f\left(t - \frac{x}{c}\right)}{2} + \frac{c}{2}\int_{t-\frac{x}{c}}^{t+\frac{x}{c}} g(s)\mathrm{d}s \end{aligned} \tag{B.52}$$

Similarly, we can deduce from equation (B.42) the solution to the linearised SWE with forcing:

$$\begin{aligned} \phi(X,t) &= \int_{-Ut}^{X} \left[\frac{c}{2} \int_{t-\frac{(X-Y)}{c}}^{t+\frac{(X-Y)}{c}} \frac{-1}{c^2} F(Y,\tau)\mathrm{d}\tau \right] \mathrm{d}Y \\ \iff \phi(x,t) &= \int_{0}^{x} \left[\frac{c}{2} \int_{t-\frac{(x-y)}{c}}^{t+\frac{(x-y)}{c}} \frac{-1}{c^2} F(y,\tau)\mathrm{d}\tau \right] \mathrm{d}y, \end{aligned} \tag{B.53}$$

where we performed the change of variable $y = Y + Ut$ in the integral.

The major advantage of linear theory is that the general solution to the linearised SWE with forcing and inhomogeneous BC is the superposition of the solution with forcing and homogeneous BC (B.53) and of the solution without forcing and with inhomogeneous BC (B.52).

Effect of nudging on the shallow-water equations

Let us start again from the 1D SWE (B.45), adding nudging terms $K_h(h_{obs} - h)$ and $K_u(u_{obs} - u)$ to the continuity and momentum equations respectively. Here again, the lowercase variables refer to the perturbations around the mean state in the linearised SWE. K_h (resp. K_u) is the nudging coefficient on h (resp. u) and h_{obs} (resp. u_{obs}) is the

vector of observed fluid height (resp. velocity). Performing the same change of variables and combination of the equations as previously, the wave equation B.50 becomes:

$$\frac{\partial^2\phi}{\partial\tau^2} - c^2\frac{\partial^2\phi}{\partial X^2} = \frac{\partial}{\partial\tau}\begin{pmatrix}K_h(h_{obs}-h)\\K_u(u_{obs}-u)\end{pmatrix} - \frac{\partial}{\partial X}\begin{pmatrix}HK_u(u_{obs}-u)\\gK_h(h_{obs}-h)\end{pmatrix} \tag{B.54}$$

At first, we consider the case where $K_h = 0$ and we focus on the wave equation relative to u:

$$\frac{\partial^2 u}{\partial\tau^2} - c^2\frac{\partial^2 u}{\partial X^2} = \frac{\partial}{\partial\tau}\left[K_u(u_{obs}-u)\right] \tag{B.55}$$

This is a forced wave equation where the forcing is $F(X,\tau) = \partial_\tau\left[K_u(u_{obs}-u)\right]$. From the change of variables (B.46), we obtain $\partial_\tau = \partial_t + U\partial_x$ and consequently

$$F(x,t) = (\partial_t + U\partial_x)\left[K_u(u_{obs}-u)\right]. \tag{B.56}$$

If the steady state is reached, $\partial_t = 0$ such that the forcing is of the same sign than $U\frac{\partial}{\partial x}\left[K_u(u'_{obs}-u')\right]$. We assume that:

- $U > 0$,
- there is only one observation,
- the effect of nudging is only local, i.e. $K_u = k\delta(x - x_{obs})$ where δ is the Kronecker delta and x_{obs} the abscissa of the observation.

Consequently $K_u(u_{obs}-u)$ is zero everywhere except for $x = x_{obs}$, where it is positive if $u_{obs} > u$ (and negative otherwise). $\frac{\partial}{\partial x}\left[K_u(u_{obs}-u)\right]$ is thus non-zero only for $x = x_{obs}$ where it is positive if $u_{obs} > u > 0$ (case 1) or if $u_{obs} < u < 0$ (case 2) (upstream calculation of the gradient) and negative otherwise (cases 3 and 4). We have previously shown that a forcing term has the same effect at any (x_0, t_0) than BC of the form

$$\partial_x u(x = y, t_0) = \frac{-1}{c^2}F(y, t_0) \tag{B.57}$$

for all $y < x_0$. In our example, the forcing triggered by the nudging induces that the velocity is constant everywhere ($\partial_x u' = 0$) except at $x = x_{obs}$ where it decreases in cases 1 and 2 ($\frac{-1}{c^2}F(y,t_0) < 0$), and increases in cases 3 and 4 ($\frac{-1}{c^2}F(y,t_0) > 0$).

We have verified numerically this influence of nudging on the profile of u in the four different cases. The steady profiles of u obtained with nudging are shown in Figure B.2. We notice that in all cases, the downstream value of u is further from the true state than upstream. If the upstream velocity is prescribed as a Dirichlet BC ($u_L = u^{\mathrm{b}}$), u on the first half of the domain is equal to the u^{b} and on the second half, the error $u - u^{\mathrm{t}}$ is greater. Thus nudging has a counter-productive effect. In fact the nudging acts similarly to an intern BC, so the system is over-constrained. A solution to this problem of over-constraint would be to *release* the upstream BC on u and prescribe a Neumann BC: $\partial_x u = 0$.

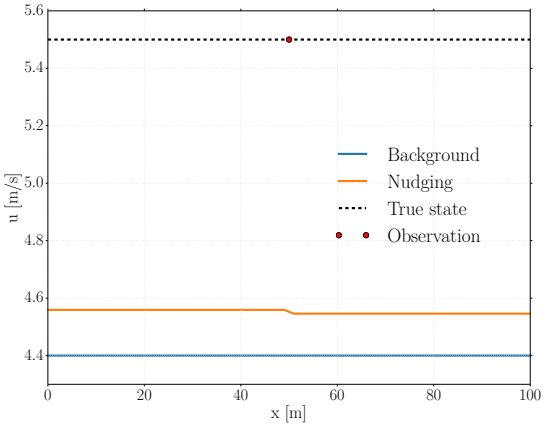

(a) Case 1: $u^{\mathrm{t}} > u^{\mathrm{b}} > 0$

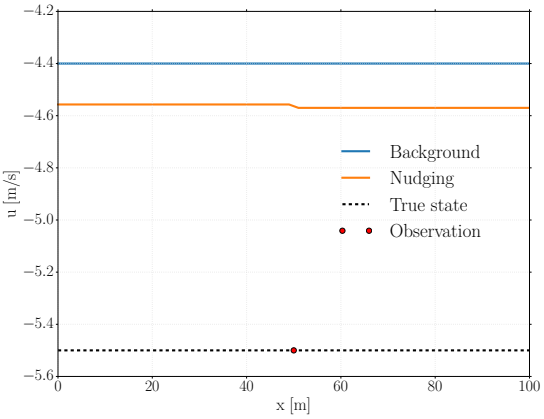

(b) Case 2: $u^{\mathrm{t}} < u^{\mathrm{b}} < 0$

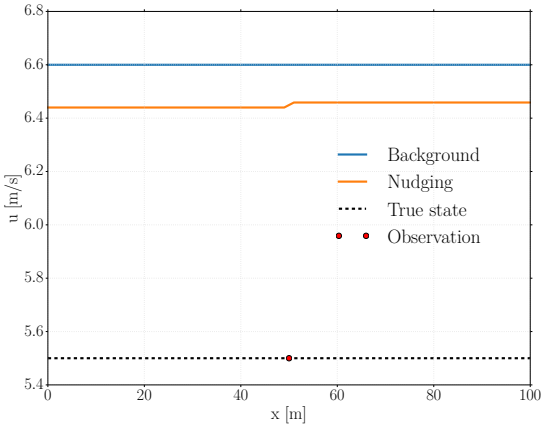

(c) Case 3: $u^{\mathrm{b}} > u^{\mathrm{t}} > 0$

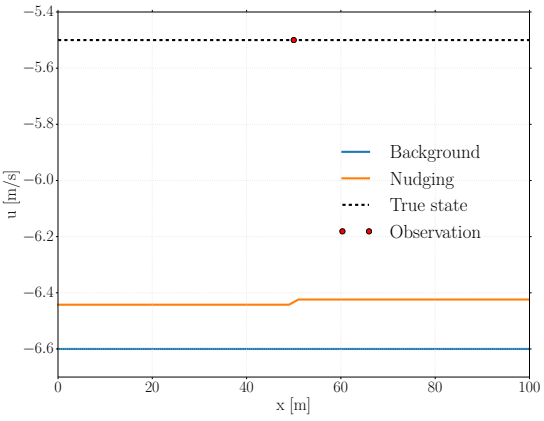

(d) Case 4: $u^{\mathrm{b}} < u^{\mathrm{t}} < 0$

Figure B.2: Effect of nudging on u for different cases.

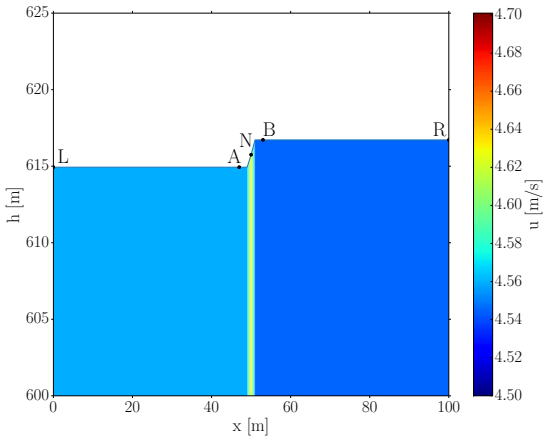

Figure B.3: Profile of the fluid height and velocity contours at the end of the forward integration with nudging (steady state reached). The location of the points (L, A, N, B, R) used in the demonstration are also shown.

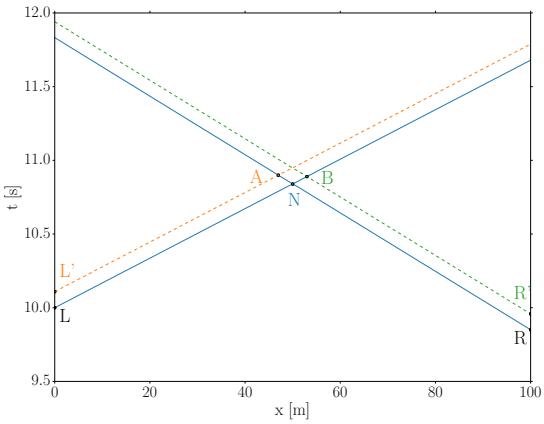

Figure B.4: Characteristic curves that intersect on the points A, N, and B.

Understanding the effect of forcing with the method of characteristics

Another approach to understand the effect of nudging on the SWE is to use the method of characteristics. Let us consider the case 1 mentioned above: the background value of u is smaller than the true value and $U > 0$. We further assume that the steady state is reached. We consider 5 points in the domain as shown on Figure B.3:

- L on the left boundary ($h_L = 614.9$m,$u_L = 4.56$m/s)
- A just before the observation ($h_A = 614.9$m,$u_A = 4.56$m/s)
- N at the observation location and where nudging is applied ($h_N = 615.8$m,$u_N = 4.63$m/s)
- B just after the observation ($h_B = 616.7$m,$u_B = 4.55$m/s)
- R on the right boundary ($h_R = 616.7$m,$u_R = 4.55$m/s)

Figure B.4 shows the characteristic curves that intersect at point A, B, and N. Since we consider a steady state, there is no variation in time, i.e. along the vertical axis. Consequently the system is in the same state in L and L', and in R and R'. Along the characteristic curves, the Riemann invariants $R_+ = u + 2\sqrt{g'h}$ and $R_- = u - 2\sqrt{g'h}$ are

conserved. We deduce the following equalities:

$$u_N^s + 2\sqrt{g'h_N^s} = u_L + 2\sqrt{g'h_L} \tag{B.58a}$$
$$u_N^s - 2\sqrt{g'h_N^s} = u_R - 2\sqrt{g'h_R} \tag{B.58b}$$
$$u_A + 2\sqrt{g'h_A} = u_L + 2\sqrt{g'h_L} \tag{B.58c}$$
$$u_A - 2\sqrt{g'h_A} = u_N - 2\sqrt{g'h_N} \tag{B.58d}$$
$$u_B + 2\sqrt{g'h_B} = u_N + 2\sqrt{g'h_N} \tag{B.58e}$$
$$u_B - 2\sqrt{g'h_B} = u_R - 2\sqrt{g'h_R} \tag{B.58f}$$

where u_N^s and h_N^s are the solutions from the conservation of Riemann invariants. u_N and h_N define the state of the system after applying nudging:

$$\begin{cases} u_N = u_N^s + \delta_u \\ 2\sqrt{g'h_N} = 2\sqrt{g'h_N} - \delta_h \end{cases} \tag{B.59}$$

where δ_u and δ_h represent the effects of nudging term on u and h. If the nudging only applies to u and if $u^{\mathrm{t}} > u^{\mathrm{b}}$, then $\delta_u > 0$. From equation (B.45), we deduce that $\delta h > 0$.

Replacing equation B.59 in equations B.58 gives us:

$$\begin{cases} u_A + 2\sqrt{g'h_A} = u_N^s + 2\sqrt{g'h_N^s} \\ u_A - 2\sqrt{g'h_A} = u_N^s - 2\sqrt{g'h_N^s} + \delta_u + \delta_h \end{cases} \iff \begin{cases} u_A = u_N^s + \dfrac{\delta_u + \delta_h}{2} \\ 2\sqrt{g'h_A} = 2\sqrt{g'h_N^s} - \dfrac{\delta_u + \delta_h}{2}. \end{cases} \tag{B.60}$$

Similarly

$$\begin{cases} u_B = u_N^s + \dfrac{\delta_u - \delta_h}{2} \\ 2\sqrt{g'h_B} = 2\sqrt{g'h_N^s} + \dfrac{\delta_u - \delta_h}{2}. \end{cases} \tag{B.61}$$

These equations are numerically verified here.

Consequently, due tu nudging, $u_A > u_B$ and $h_A < h_B$. If the value of u_L is prescribed by the BC, the steady state with nudging will be such that $u_A = u_L$ and $u_B < u_L$. As a result, the distance from the true state, and thus the error, is larger in B than in A where it is equal to the background error: the nudging has a counter-productive effect. As suggested in the previous section, if the BC on u is a Neumann condition, the effect of nudging can propagate upstream and downstream and the solution gets closer to the true state.

B.2 Proving the convergence of the BFN algorithm

B.2.1 Evolution of the Riemann invariants

The 1D SWE without topography and with nudging are given below:

$$\begin{cases} \partial_t h + h\partial_x u + u\partial_x h = \mathbf{K}_h(h^o - \mathcal{H}_h(h)) \end{cases} \tag{B.62a}$$
$$\begin{cases} \partial_t u + u\partial_x u + g'\partial_x h = \mathbf{K}_u(u^o - \mathcal{H}_u(u)) \end{cases} \tag{B.62b}$$

where $\mathbf{K}_h$ and $\mathbf{K}_u$ are the nudging matrices, h^o and u^o the observation vectors, and $\mathcal{H}_h$ and $\mathcal{H}_u$ are the observation operators. In what follows we assume that the observation operators are linear and that the nudging matrices are proportional to the transpose of $\mathcal{H}_h$ and $\mathcal{H}_u$:

$$\mathbf{K}_h = k_h \mathcal{H}_h^{\mathrm{T}} \quad \text{and} \quad \mathbf{K}_u = k_u \mathcal{H}_u^{\mathrm{T}} \tag{B.63}$$

where k_h and k_u are positive scalars.

Due to nudging, the Riemann invariants are not conserved any more. To determine how these quantities evolve along the characteristics

$$\mathcal{C}_+ : \frac{\mathrm{d}x}{\mathrm{d}t} = u + \sqrt{g'h} \tag{B.64a}$$

$$\mathcal{C}_- : \frac{\mathrm{d}x}{\mathrm{d}t} = u - \sqrt{g'h} \tag{B.64b}$$

we combine equations (B.62a) and (B.62b) as follows:

$$\begin{cases} \text{(B.62b)} + \sqrt{\dfrac{g'}{h}} \times \text{(B.62a)} \\ \text{(B.62b)} - \sqrt{\dfrac{g'}{h}} \times \text{(B.62a)} \end{cases} \iff \begin{cases} \dfrac{\mathrm{d}\left(u + 2\sqrt{g'h}\right)}{\mathrm{d}t}|_{\mathcal{C}_+} = \mathbf{K}_u(u^o - \mathcal{H}(u)) + \sqrt{\dfrac{g'}{h}}\mathbf{K}_h(h^o - \mathcal{H}(h)) \\ \dfrac{\mathrm{d}\left(u - 2\sqrt{g'h}\right)}{\mathrm{d}t}|_{\mathcal{C}_-} = \mathbf{K}_u(u^o - \mathcal{H}(u)) - \sqrt{\dfrac{g'}{h}}\mathbf{K}_h(h^o - \mathcal{H}(h)) \end{cases} \tag{B.65}$$

In what follows we only consider the characteristic $\mathcal{C}_+$ but similar derivation can be obtained along $\mathcal{C}_-$. The observations h^o and u^o are random variables whose means correspond to the true state (h^{t}, u^{t}) and the observation errors (ϵ_h and ϵ_u) follow normal distributions with variances σ_h^2 and σ_u^2 respectively:

$$h^o(i) = h^{\mathrm{t}}(i) + \epsilon_h(i),\ \epsilon_h \sim \mathscr{N}(0, \sigma_h^2) \tag{B.66}$$

$$u^o(i) = u^{\mathrm{t}}(i) + \epsilon_u(i),\ \epsilon_u \sim \mathscr{N}(0, \sigma_u^2). \tag{B.67}$$

B.2.2 Convergence of BFN algorithms for linearised SWE

At first, we consider the SWE linearised around the constant mean state $\begin{pmatrix} H \\ U \end{pmatrix}$ (see Eq. B.45). In this linearised approximation, the characteristic equations become

$$\mathcal{C}_\pm : \frac{\mathrm{d}x}{\mathrm{d}t} \approx U \pm \sqrt{g'H}, \tag{B.68}$$

and the Riemann invariants

$$R_\pm = u' \pm \sqrt{\frac{g'}{H}}h'. \tag{B.69}$$

In this section we omit the apostrophe such that lower-case variables refer to perturbations. Assuming that the truth and the background have the same average state $\begin{pmatrix} H \\ U \end{pmatrix}$, the nudging does not impact the characteristic equations. Consequently, characteristics are straight lines with constant slope that are identical with and without nudging. The

evolution of Riemann invariants with nudging along the characteristic curves, derived in equation (B.65), becomes

$$\begin{cases} \dfrac{\mathrm{d}\left(u+\sqrt{\frac{g'}{H}}h\right)}{\mathrm{d}t}|_{\mathcal{C}_+} = \mathbf{K}_u\left(u^o-\mathcal{H}(u)\right)+\sqrt{\dfrac{g'}{H}}\mathbf{K}_h\left(h^o-\mathcal{H}(h)\right), \\ \dfrac{\mathrm{d}\left(u-\sqrt{\frac{g'}{H}}h\right)}{\mathrm{d}t}|_{\mathcal{C}_-} = \mathbf{K}_u\left(u^o-\mathcal{H}(u)\right)-\sqrt{\dfrac{g'}{H}}\mathbf{K}_h\left(h^o-\mathcal{H}(h)\right). \end{cases} \tag{B.70}$$

Since we assume that $\mathbf{K}_h = k_h\mathcal{H}^{\mathrm{T}}$ and $\mathbf{K}_u = k_u\mathcal{H}^{\mathrm{T}}$, the right hand sides of above equations are zero except if an observation is available at i. Consequently, while $\mathcal{C}_+$ is out of the area of influence of any observation, the Riemann invariant is conserved:

$$u(i+1)+\sqrt{\frac{g'}{H}}h(i+1) = u(i)+\sqrt{\frac{g'}{H}}h(i), \tag{B.71}$$

where i and $i+1$ are two consecutive points along $\mathcal{C}_+$. And if an observation is available at i, the Riemann invariant at $i+1$ is given by

$$u(i+1)+\sqrt{\frac{g'}{H}}h(i+1) = u(i)+\sqrt{\frac{g'}{H}}h(i)+\left(k_u[u^o(i)-u(i)]+\sqrt{\frac{g'}{H}}k_h[h^o(i)-h(i)]\right)\delta t, \tag{B.72}$$

where δt is the time increment between i and $i+1$. Note that δt does not depend on i because $\mathcal{C}$ has a constant slope. This relation of recurrence can be easily solved assuming that $k_u = k_h = k$.

When the characteristic reaches the right boundary, it has crossed N observations and the expression of the Riemann invariant at the border is equal to

$$u(L)+\sqrt{\frac{g'}{H}}h(L) = u^{\mathrm{t}}(0)+\sqrt{\frac{g'}{H}}h^{\mathrm{t}}(0)+(1-k\delta t)^N\left[u(0)+\sqrt{\frac{g'}{H}}h(0)-u^{\mathrm{t}}(0)-\sqrt{\frac{g'}{H}}h^{\mathrm{t}}(0)\right] +k\delta t\sum_{j=0}^{N-1}(1-k\delta t)^j\epsilon(N-1-j) \tag{B.73}$$

where $\epsilon = \epsilon_u+\sqrt{\frac{g'}{H}}\epsilon_h$. The last term of right-hand side corresponds to the stochastic part which has zero mean and the other terms correspond to the deterministic part of $u+\sqrt{\frac{g'}{H}}h$.

We have previously seen that the equations governing the backward integration of the BFN are the same than the forward equations, albeit replacing u by $\widetilde{u} = -u$. Consequently we can easily deduce the expressions of $\widetilde{u}-\sqrt{\frac{g'}{H}}\widetilde{h}$ along $\widetilde{\mathcal{C}_-}$, which is identical to $\mathcal{C}_+$:

$$\widetilde{u}(0)-\sqrt{\frac{g'}{H}}\widetilde{h}(0) = \widetilde{u}^{\mathrm{t}}(L)-\sqrt{\frac{g'}{H}}\widetilde{h}^{\mathrm{t}}(L)+(1-\widetilde{k}\delta t)^N\left[\widetilde{u}(L)-\sqrt{\frac{g'}{H}}\widetilde{h}(L)-\widetilde{u}^{\mathrm{t}}(L)+\sqrt{\frac{g'}{H}}\widetilde{h}^{\mathrm{t}}(L)\right] +\widetilde{k}\delta t\sum_{j=0}^{N-1}(1-\widetilde{k}\delta t)^j\widetilde{\epsilon}(N-1-j) \tag{B.74}$$

where $\widetilde{\epsilon} = \epsilon_u - \sqrt{\frac{g'}{H}}\epsilon_h$.

We first consider that the observations are perfect ($\epsilon_h = \epsilon_u = 0$). If we refer to the j-th BFN cycle with superscript '(j)', the relations between forward and backward states are as follows:

$$\begin{aligned} h^{(j+1)}(0) &= \widetilde{h}^{(j)}(0), \quad & u^{(j+1)}(0) &= -\widetilde{u}^{(j)}(0) \\ \widetilde{h}^{(j)}(L) &= h^{(j)}(L), \quad & \widetilde{u}^{(j)}(L) &= -u^{(j)}(L) \end{aligned} \tag{B.75}$$

Combining equations (B.73), (B.74), and (B.75) we deduce that

$$u^{(j+1)}(0) + \sqrt{\frac{g'}{H}}h^{(j+1)}(0) - \left(u^{\mathrm{t}}(0) + \sqrt{\frac{g'}{H}}h^{\mathrm{t}}(0)\right) = (1-k\delta t)^N(1-\widetilde{k}\delta t)^N\left[u^{(j)}(0) + \sqrt{\frac{g'}{H}}h^{(j)}(0) - u^{\mathrm{t}}(0) - \sqrt{\frac{g'}{H}}h^{\mathrm{t}}(0)\right] \tag{B.76}$$

Iterating (B.76), we obtain the expression of the errors on $u + \sqrt{\frac{g'}{H}}h$ at any BFN cycle p:

$$u^{(p)}(0) + \sqrt{\frac{g'}{H}}h^{(p)}(0) - \left(u^{\mathrm{t}}(0) + \sqrt{\frac{g'}{H}}h^{\mathrm{t}}(0)\right) = (\Gamma)^p\left[u^{(0)}(0) + \sqrt{\frac{g'}{H}}h^{(0)}(0) - u^{\mathrm{t}}(0) - \sqrt{\frac{g'}{H}}h^{\mathrm{t}}(0)\right] \tag{B.77}$$

where $\Gamma = (1-k\delta t)^N(1-\widetilde{k}\delta t)^N$.

From this relation, we deduce the conditions that $k\delta t$ and $\widetilde{k}\delta t$ must be smaller than 1 to ensure that the error vanishes. This proves that, under this condition, $u^{(p)}(0) + \sqrt{\frac{g'}{H}}h^{(p)}(0)$ converges toward the true state $u^{\mathrm{t}}(0) + \sqrt{\frac{g'}{H}}h^{\mathrm{t}}(0)$ with BFN iterations.

We can perform the same derivation along $\mathcal{C}_-$ – which comes to formally replace '$\sqrt{\frac{g'}{H}}$' by '$-\sqrt{\frac{g'}{H}}$' – we obtain that

$$u^{(p)}(0) - \sqrt{\frac{g'}{H}}h^{(p)}(0) \underset{p\to+\infty}{\longrightarrow} u^{\mathrm{t}}(0) - \sqrt{\frac{g'}{H}}h^{\mathrm{t}}(0). \tag{B.78}$$

We deduce from these two conclusions that:

$$u^{(p)}(0) \underset{p\to+\infty}{\longrightarrow} u^{\mathrm{t}}(0), \tag{B.79a}$$

$$h^{(p)}(0) \underset{p\to+\infty}{\longrightarrow} h^{\mathrm{t}}(0). \tag{B.79b}$$

Similarly, we could prove that the state of the system along the right boundary converge toward the true state with BFN iterations:

$$u^{(p)}(L) \underset{p\to+\infty}{\longrightarrow} u^{\mathrm{t}}(L), \tag{B.80a}$$

$$h^{(p)}(L) \underset{p\to+\infty}{\longrightarrow} h^{\mathrm{t}}(L). \tag{B.80b}$$

This demonstration is bases on the invariance of the characteristics with nudging, which means that the background and the true state correspond to the same mean state.

If this assumption is not satisfied, the characteristics are perturbed by nudging and the characteristics in the nudged system do not correspond to the true characteristics any more. We consider in the present work that the departure of the perturbed characteristics from the unperturbed ones is small enough such that the previous demonstration is still valid.